The Synthesis and Magnetochemistry of Transition and Lanthanide Metal Compounds

A thesis submitted to The University of Manchester for the degree of PhD in the Faculty of Engineering and Physical Sciences

2012

Charlene Amanda Smith

School of Chemistry

Synthesis and Magnetochemistry of Transition and Lanthanide Metal Compounds

Table of Contents

Table of Contents 2

List of Abbreviations and Physical Constants 7

List of Structures 11

List of Figures 13

List of Tables and Schemes 20

List of Publications 23

Colour Scheme for Atoms of Compounds 24

Abstract 25

Declaration 26

Copyright Statements 26

Acknowledgements 28

Chapter One Introduction to Coordination Chemistry and Magnetochemistry of the Lanthanides. 29

1.1 Introduction to the Principles of Lanthanide(III) Co-ordination Chemistry 30

1.2 Background to Cyclopentadienyl Complexes 34

1.3 Lanthanide Bis(cyclopentadienyl) halide Complexes. 36

1.4 Single-Molecule Magnets 38

1.5 Magnetic Behaviour in Lanthanide Complexes 40

1.6 Monometallic Lanthanide Compounds 44

1.7 Polymetallic Lanthanide Clusters 47

1.8 Lanthanide Complexes of tris-Cyclopentadienide Ligands. 50

1.6 Project Proposal. 53

Chapter Two Organometallic Sulfur-Bridged Lanthanide(III) Methylcyclopentadienyl Compounds 54

2.1 Introduction to Lanthanide-Thiolate Chemistry 55

2.2 Results and Discussion 58

2.2.1 Syntheses and Structure of Lanthanide(III) Methylcyclopentadienide Thiolates 58

2.2.2 Magnetic Studies for Compounds **2.2** and **2.3** 65

2.2.2.1 d.c. and a.c. Magnetic Susceptibility Measurements 65

2.3 Conclusions 73

Chapter Three Monometallic Lanthanide(III) Alkoxide Chemistry 75

3.1 Introduction to Lanthanide Alkoxide Chemistry 76

3.1.2 Synthetic Routes to Lanthanide Alkoxides 78

3.1.3 Lanthanide(III) Siloxide Compounds 82

3.1.4 Introduction 84

3.2. Results and Discussion 85

3.2.1 Synthesis and Structure of Monometallic Lanthanide(III) Siloxide Complexes. 85

3.2.2 Magnetic Studies for Compounds **3.4**, **3.5**, **3.6**, **3.7** and **3.8** 95

3.2.2.1 Background 95

3.2.2.2 d.c. and a.c. Magnetic Susceptibility Measurements 97

3.2.3 Low Temperature Optical Absorption Spectroscopy 109

3.2.3.1 Background to 4*f* Electronic Absorption Spectroscopy 109

3.2.3.2 Introduction and Aims 111

3.2.3.3 Optical Absorption Studies for Lanthanide(III) Compounds **3.4**, **3.5**, **3.8**. 112

3.2.4 Conclusions to Variable Temperature Optical Spectroscopy and Further Discussion 122

3.3 Overall Conclusions 125

Chapter Four Synthesis, Structure and Magnetochemistry of 3*d* Transition Metal Compounds 128

4.1 Introduction to 3*d* Transition Metal Metallocenes 129

4.2 From Metal-Organic to Organometallic Cluster Chemistry 133

4.3 Organometallic Sulfur-Bridged Transition Metal Compounds 137

4.4 Background and Aims 139

4.5 Results and Discussion 141

4.5.1 The Synthesis and Structure of the trimetallic Manganese(II) Siloxide Complex 141

4.5.2 Magnetic Studies for Compound **4.7** 146

4.5.2.1 d.c. Magnetic Susceptibility Measurements 146

4.5.3 The Synthesis and Structure of the Hetero-Cubane Manganese(II) Thiolate Complex. 148

4.5.4 Magnetic Studies for Compound **4.8** 154

4.5.4.1 d.c. Magnetic Susceptibility Measurements 154

4.5.5 The Synthesis and Structure of the Chromium(II) Thiolate-Bridged dimer 156

4.5.6 Magnetic Studies for Compound **4.9** 160

4.6 Organometallic Synthesis with Selenium-Bridging Ligands 161

4.7 Organometallic Manganocene Reactions with Amido- Bridging Ligands 166

4.8 Conclusions 171

Chapter Five Thesis Review and Future Work 175

5.1 Thesis Review 176

5.2 Future Work 180

Chapter Six Experimental Section 183

Chapter Seven References 203

Appendices 222

Appendix One 223

Appendix Two 252

Appendix Three 263

Appendix Four

Word Count: 47,459

List of Abbreviations and Physical Constants

η^n-L	Ligand of hapticity n
μ^n-L	Ligand bridging n atoms
α, β, γ	Crystallographic unit cell angles
a, b, c	Crystallographic unit cell length
a.c.	Alternating current
BtaH	Benzotriazole
Cp	Cyclopentadienyl
Cp’	Substituted cyclopentadienyl
D	Axial Zero-field splitting parameter
d.c.	Direct current
dppfe	1,1-bis(diphenylphosphino)ferrocene
E	Main group element
EPR	Electron Paramagnetic Resonance
EtOH	Ethanol
g	*g*-value

H	Magnetic Field or Spin Hamilitonian
Hfac	Anion of hexafluoroacetylacetone
H_2hmi	(2-hydroxy-3-methoxyphenyl)methylene (isonicotino)hydrazine
*i*PrOH	*iso*-Propanol
J	Total angular momentum quantum number
J/Hz	Exchange interaction coupling constant
k_B	Boltzmann constant = 0.69503877 cm^{-1} K^{-1}
KO*i*Pr	Potassium *iso*-propoxide
L	Orbital angular momentum quantum number
LDA	Lithium diisopropylamide
LF	Ligand Field
Ln	Lanthanide
M	Metal
m	Multiplet
Me_2pm	2-amino-4,6-dimethylpyrimidine
Me_3NO	Trimethylamine-N-oxide
MeCN	Acetonitrile

Cp^{Me}	Methycyclopentadienyl
MeOH	Methanol
^{n}BuLi	*n*-Butyllithium
$NaO^{t}Bu$	Sodium *tert*- butoxide
NMR	Nuclear magnetic resonance
H_2Pc	Phthalocyanine
POMs	Polyoxometallates
R	Alkyl or Aryl
R1	Unweighted residual factor
S	Total spin angular momentum quantum number
s	singlet
$SaoH_2$	Salicylaldoxime or 2-hydroxybenzaldehyde oxime
SMM	Single Molecule Magnet
SQUID	Superconducting Quantum Interference Device
T/K	Temperature/Kelvin
T_B	Blocking temperature for reversal of magnetisation
THF	Tetrahydrofuran

TMEDA	Tetramethylethylenediamine
tu	Thiourea
U_{eff}/cm^{-1}	Effective Energy Barrier to Magnetisation Reversal
V	Unit Cell Volume
wR2	Weighted residual factor
Z	The number of molecules in the asymmetric unit
ZFS	Zero Field Splitting
δ/ppm	Chemical shifts in parts per million
ρ_{calcd}	Calculated density
υ/s^{-1}	Frequency
χ_M	Molar Magnetic Susceptibility

List of Structures

$[Mn_{12}O_{12}(O_2CMe)_{16}(H_2O)_4]$ (**1.1**) 38

$[Mn_6O_2$ (sao) $_6(O_2CPh)_2(EtOH)_2]$ (**1.2**) 39

$[Dy_5O(OiPr)_{13}]$ (**1.3**) 42

$\{[(Me_3Si)_2N]_2(THF)Ln\}_2(\mu\text{-}\eta^2\text{:}\eta^2\text{-}N_2)$ (Ln = Gd (**1.4**),Dy (**1.5**) 44

$[K(18\text{-crown-}6)]\{[(Me_3Si)_2N]_2(THF)Ln\}_2(\mu\text{-}\eta^2\text{:}\eta^2\text{-}N_2)$ (Ln = Gd (**1.6**), Dy (**1.7**) 44

$[Pc_2Tb]^-$ (**1.8**) 45

$[Pc_2Dy]^-$ (**1.9**) 45

$[ErW_{10}O_{36}]^{9-}$ (**1.10**) 46

$Dy_2(hmi)_2(NO_3)_2(MeOH)_2]$ (**1.11**) 49

$[Dy_2(hmi)_2(NO_3)_2(MeOH)_2]_\infty(MeCN).(2MeCN)$ (**1.12**) 49

$[Cp_2Ln\{_2\text{-NH-4,6-}Me_2pm\}]_2$, (Ln = Gd(**1.13**), Dy(**1.14**), Yb(**1.15**)**,** Nd(**1.16**)) 50

$[\{Cp_2Dy(\mu\text{-bta})\}_2]$ (**1.17**) 51

$(Ph_3SiS\text{-}Li)$ (**2.1**) 58

$[(MeCp)_2Dy(\mu\text{-}SSiPh_3)]_2$ (**2.2**) 59

$[(MeCp)_2Gd(\mu\text{-}SSiPh_3)]_2$ (**2.3**) 59

$[Ln(OSiPh_3)(THF)_3](THF)$ (Ce (**3.1**), Ln (**3.2**), Yt (**3.3**) 83

[$Ln(OSiPh_3)(THF)_3$] (Ln = Dy(**3.4**), Er(**3.5**), Ho(**3.6**), Gd(**3.7**), Tb(**3.8**)) 87-91

[$Mn_3(Me_3CCO_2)_6(Me_3CCO_2H)_5]\cdot2(Me_3CCO_2H)$ (**4.1**) 135

[(Cp)Mn{2-NH(4,6-Me_2pm)}·Mn{2-N-(4,6-Me_2pm)}]$_4$ (**4.2**) 136

[$Mn_4(\mu\text{-}O)\{N(H)Ar^2)_4]_2$ (**4.3**) 136

$Mn_4(SPh)_{4(}CO)_{12}$ (**4.4**) 138

[$Mn(CO)_3]_2(\mu\text{-}SPh)_2(\mu\text{-}$dppfe)(**4.5**) 138

[$Cr(NCS)_2(tu)_2$](**4.6**) 139

$Cp_2Mn_3(\mu\text{-}OSiPh_3)_4$] (**4.7**) 144

[$CpMn(\mu\text{-}SSiPh_3)]_4$ (**4.8**) 151

[$CpCr(\mu\text{-}SSiPh_3)]_2$ (**4.9**) 158

Me_3SiCH_2Se-Li (**4.10**) 162

List of Figures

Figure 1.1 Illustration to show the cubic set of 4*f* orbitals. 32

Figure 1.2 (a) The $[Mn_{12}O_{12}(O_2CMe)_{16}(H_2O)_4]$(**1.1**) complex (b) Diagram outlining the ZFS of a $S = 10$ ground state with negative *D.* 38-39

Figure 1.3 The $[Mn_6O_2(sao)_6(O_2CPh)_2(EtOH)_2]$ (**1.2**) complex. 39

Figure 1.4 (a) Low energy electronic structure of Dy(III) ions, with the crystal field splitting (b) the degenerate population of m_J states for Dy(III) 41

Figure 1.5 Structure of $[Dy_5O(OiPr)_{13}]$ (**1.3**) (a), (b) a view of (**1.3**) conveying the pseudo fourfold axis. 42

Figure 1.6 Structure of the $\{[(Me_3Si)_2N]_2(THF)Ln\}_2(\mu\text{-}\eta^2\text{:}\eta^2\text{-}N_2)^-$ (Ln = Gd (**1.6**), THF) anion hydrogen atoms omitted for clarity. 44

Figure 1.7 (a) The structure of the phthalocyanine molecule (b) double-decker complexes Ln = Tb, Dy, Ho, Er, Tm and Yb 45

Figure 1.8 The structure of polyoxometalate, $[ErW_{10}O_{36}]^{9-}$ (**1.10**) and its coordination geometry. 46

Figure 1.9 Diagram to show the (2-hydroxy-3-methoxyphenyl)methylene (isonicotino)hydrazine, (H_2hmi) pro-ligand. 48

Figure 1.10 (a) The molecular structure of the complex $[Dy_2(hmi)_2(NO_3)_2(MeOH)_2]$ (**1.11**)(b) 2D network of complex $[Dy_2(hmi)_2(NO_3)_2(MeOH)_2]_\infty$(**1.12**) 49

Figure 2.1 Molecular structure of $[LnL_2(\mu\text{-}SBu_t)]_2$, (Ln = Eu, Gd). 56

Figure 2.2 Molecular structure of **2.2**, with the hydrogen atoms omitted for clarity. Selected distances/Å and angles/° 60

Figure 2.3 Molecular structure of **2.3**, with the hydrogen atoms omitted for clarity. selected distances/Å and angles° 64

Figure 2.4 Magnetic data plot showing the temperature dependence of χ_M and $\chi_M T$ for compound **2.2** 65

Figure 2.5 (a) *M vs. H* data plot (b) *M* vs. *H*/*T* at varying temperatures between 1.8 K and 10 K, for compound **2.2.** 66

Figure 2.6 (a) Out-of-phase (χ_M'') and in-phase (χ_M') (b) χ_M vs T data plots for compound **2.2** 67

Figure 2.7 Cole-Cole plot based on the a.c. susceptibility measurements of **2.2** 68

Figure 2.8 Magnetization relaxation time (τ) versus T^{-1} for **2.2** under zero static field. 69

Figure 2.9 Temperature dependence $\chi_M T$ for compounds **2.3** 70

Figure 2.10 Magnetisation vs. field data plot at varying temperatures between 2 K and 9 K, for compound **2.3** 71

Figure 3.1 Illustration of the progressive increasing pK_a values for common alkoxide pro- ligands. 77

Figure 3.2 Triphenylsilanol pro-ligand, exhibiting moderate basicity and therefore allows for a more labile O-H bond. 78

Figure 3.3 Structure representing the lanthanide siloxide complex with the general formula, $[Ln(OSiPh_3)(THF)_3](THF)$. 83

Figure 3.4 Molecular structure of **3.4**, with the hydrogen atoms omitted for clarity. Selected distances/Å and angles° 87

Figure 3.5 Molecular structure of **3.5**, with the hydrogen atoms omitted for clarity. Selected distances/Å and angles°. 88

Figure 3.6 Molecular structure of **3.6**, with the hydrogen atoms omitted for clarity. Selected distances/Å and angles° 89

Figure 3.7 Molecular structure of **3.7**, with the hydrogen atoms omitted for clarity. Selected distances/Å and angles° 90

Figure 3.8 Molecular structure of **3.8**, with the hydrogen atoms omitted for clarity. Selected distances/Å and angles° 91

Figure 3.9 Diagram to illustrate the splitting of the spin-orbit coupled (*J*) ground state by the crystal field for $[LnPc_2]^-$ 96

Figure 3.10 Magnetic data plot showing the temperature dependence of χ_M and $\chi_M T$ for compounds **3.4** (Dy) **, 3.5**(Er), **3.6**(Ho), **3.8**(Tb) for the field strength *H* 1 kG 97

Figure 3.11 Magnetisation vs. field data plot at 2 K for compounds **3.4** (Dy), **3.5**(Er), **3.6**(Ho), **3.8**(Tb). 98

Figure 3.12 Out-of-phase (χ_M'') (a) and in-phase (χ_M') (b), χ_M vs. T data plots for compound **3.5** 99

Figure 3.13 Frequency dependent (υ/Hz) out-of-phase (χ_M'') (a) and in-phase (χ_M') (b), χ_M vs υ data plot for compound **3.5** 100

Figure 3.14 Cole-Cole plot based on the a.c. susceptibility measurements of **3.4** between 1.8 and 5 K. 101

Figure 3.15 Magnetization relaxation time (τ) versus T^{-1} for **3.5.** 101

Figure 3.16 The out-of-phase and in-phase a.c. magnetic susceptibility data plots for compound **3.4.** 102

Figure 3.17 Q-band ($\sim$ 34 GHz) solid-phase experimental EPR spectrum for compound **3.8**. 103

Figure 3.18 Comparative analysis of known Gd(III) containing compounds. 102

Figure 3.19 EPR simulation for **3.7.** 106

Figure 3.20 A list of lanthanide(III) ions alongside their associated colours (a), in addition to energy level diagram for the late trivalent rare earth series. 111

Figure 3.21 Diagram illustrating the copper disk sample holder (a), alongside photographic representation of the cold finger to which the copper disk is mounted (b), whilst under vacuum (c), and the spectrometer set-up (d). 113

Figure 3.22 Optical measurements for $[Er(Hfac)_3(H_2O)_2]$. 114

Figure 3.23 Variable temperature visible spectra for **3.5** (a) and variable temperature NIR spectra for **3.5**. 115

Figure 3.24 Multi-gauss fit data (pink) for compound **3.5** at 12 K in the visible region (a) and NIR region (b). Observed absorption bands for **3.5** simulated onto energy level diagram for Er(III) (c) 116

Figure 3.25 Multi-gauss fit (green) data for compound **3.8** in the NIR. Observed absorption bands for **3.8** simulated onto energy level Diagram for Tb(III)(c). 117

Figure 3.26 Variable temperature visible spectra for **3.4** (a) and variable temperature NIR spectra for **3.5** (b). 119

Figure 3.27 Multi–gauss fit data (blue) for compound **3.4** at 9 K in the visible region (a) and NIR (b). Observed absorption bands for **3.4** simulated onto energy level diagram for Dy(III) (c). 120

Figure 3.28 NIR spectrum for the triphenylsilanol pro-ligand Ph_3SiOH. 121

Figure 3.29 Visible spectra for compound 3.5 (a), simulated next to an energy level diagram for Er(III)- doped glass for fibre amplifers. 123

Figure 4.1 Scheme to show the proposed representation of complex dicyclopentadienyliron 129

Figure 4.2 Representation of the sandwich metallocene complexes, $[(\eta^5\text{-}C_5H_5)_2M]$. 129

Figure 4.3 Generic MO diagram for the series of first row metallocenes. 131

Figure 4.4 Atypical zig-zag structure adopted by manganocene. 132

Figure 4.5 Structure of the trimetallic manganese(II) compound, $[Mn_3(Me_3CCO_2)_6(Me_3CCO_2H)_5]\cdot 2(Me_3CCO_2H)$ (**4.1**). 135

Figure 4.6 Molecular structures of compounds $Mn_4(SPh)_{4(}CO)_{12}$ (**4.4**)(a) and $[Mn(CO)_3]_2(\mu\text{-}SPh)_2(\mu\text{-}dppfe)$(**4.5**) (b). 139

Figure 4.7 Subunit structure of $[Cr(NCS)_2(tu)_2]$(**4.6**)(a), alongside a section of the repeating units for compound **4.6**. 142

Figure 4.8 ^{1}H NMR spectrum for compound **4.7** in deuterated benzene, (d_6-C_6D_6). 142

Figure 4.9 Molecular structure of **4.7**, with the hydrogen atoms omitted for clarity. 144

Figure 4.10 Magnetic data plot showing the temperature dependence of χ_M and $\chi_M T$ for compound **4.7.** 146

Figure 4.11 Spin-Hamiltonian model used to derive the exchange coupling constant *J* 147

Figure 4.12 Molecular structure of **4.8**, with the hydrogen atoms omitted for clarity. Selected distances/Å and ang 151

Figure 4.13 Space filling diagrams for compound **4.7** (a) and **4.8** (b). 152

Figure 4.14 Magnetic data plot showing the temperature dependence of χ_M and $\chi_M T$ for compound **4.8.** 154

Figure 4.15 Molecular structure of **4.9**, with the hydrogen atoms omitted for clarity. Selected distances/Å and angles/° 158

Figure 4.16 Solution phase ^{77}Se NMR spectrum of **4.11** in d_6 -C_6D_6 indicating a prominent peak at 320.93 ppm. 163

List of Tables and Schemes

Table 1.1 Magnetic properties of the rare earth ions. 33

Table 2.1 Crystallographic data and summary of structural refinement for compounds **2.2** and **2.3.** 61

Table 3.1 Crystallographic data and summary of structural refinement for compounds **3.4-3.6.** 92-93

Table 3.2 Table to show the relevant magnetic parameters to derive the magnetic susceptibility values for compounds **3.4**-**3.7**, with the expected value for **3.7** 97

Table 3.3 Comparative spin-Hamiltonian constants for a range of trigonal, Gd(III)-doped compounds with compound **3.7** 107

Table 3.4 Selected energies of the lowest spin-orbit Kramers doublets taken from the values which correspond to the electronic absorptions associated with the relevant energy level term symbol. 124

Table 4.1 Crystallographic data and summary of structural refinement for compound **4.7** 145

Table 4.2 Crystallographic data and summary of structural refinement for compound **4.8**. 153

Table 4.3 Crystallographic data and summary of structural refinement for compound **4.9.** 159

Table 4.4 List of amido- bridging benzotriazoles and pyrazoles utilised. 161-170

Scheme 1.1 Synthesis of [Cp_3Ln](a), and schematic representation for the molecular 34

Scheme 1.2 A sequence of synthetic reactions for the preparation of Cp_2LnCl complexes. 37

Scheme 1.3 Reaction scheme illustrating the synthesis of [$Cp_2Ln\{2\text{-}NH\text{-}4,6\text{-}Me_2pm\}]_2$. 50

Scheme 1.4 Reaction scheme illustrating the formation of the dysprosium dimer, [$\{Cp_2Dy(\mu\text{-}bta)\}_2$] (**1.17**). 51

Scheme 2.1 Synthesis of the monolithiated thiolate ligand lithium triphenylsilylthiolate. 58

Scheme 2.2 Synthesis of the dimetallic sulfur-bridged lanthanide compound. 59

Scheme 3.1 Scheme illustrating lanthanide metal alcoholysis using a catalyst. 79

Scheme 3.2 General scheme for a lanthanide protonolysis exchange reaction. 79

Scheme 3.3 A scheme to illustrate the formation of lanthanide alkoxides utilising lanthanide halide precursors. 80

Scheme 3.4 A scheme to show the formation of *aryl*-oxides utilising ammonia gas and lanthanide halide precursors. 80

Scheme 3.5 A scheme to show the formation of lanthanide alkoxides from lanthanide amide precursors. 81

Scheme 3.6 Scheme displaying the two synthetic routes adopted by Evans to produce the $[Ln(OSiPh_3)(THF)_3](THF)$. 83

Scheme 3.7 Scheme to show the synthesis of $[Ln(OSiPh_3)(THF)_3](THF)$ compounds utilising the organometallic precursor methylcyclopentadienyl lanthanide. 85

Scheme 4.1 Scheme to show the traditional synthetic route for developing oxygen- bridged-metal clusters that are also SMMs 134

Scheme 4.2 A scheme to show the organometallic synthesis for developing SMM clusters. 135

Scheme 4.3 A scheme to the reaction manganocene to yield $[(Cp)Mn\{2\text{-}NH(4,6\text{-}Me_2pm)\}\cdot Mn\{2\text{-}N\text{-}(4,6\text{-}Me_2pm)\}]_4$ (**4.2**). 136

Scheme 4.4 A scheme to show the reaction of manganocene to yield $[Mn_4(\mu\text{-}O)\{N(H)Ar^2)_4]_2$ (**4.3**). 136

Scheme 4.5 Synthesis of the trimetallic oxygen-bridged compound **4.7**. 141

Scheme 4.6 Synthesis of the hetero-cubane$[CpMn(\mu\text{-}SSiPh_3)]_4$ (**4.8**) tetramer. 148

Scheme 4.7 Synthesis of the chromium(II) thiolate bridged dimer $[CpCr(\mu\text{-}SSiPh_3)]_2$ (**4.9**). 156

Scheme 4.8 Insertion reaction of elemental Se into the organic (trimethylsilyl)methyllithium organolithium . 162

Scheme 4.9 Scheme outlining the reaction of transition and lanthanide metal precursors with ligand (**4.11**) 164

Scheme 4.10 General synthetic method implemented to conduct reactions of manganocene with benzotriazole. 167

List of Publications:

F. Tuna, C. A. Smith, M. Bodensteiner, L. Ungur, L. F. Chibotaru, E. J. L. McInnes, R. E. P. Winpenny, D. Collison and R. A. Layfield. "A high anisotropy barrier in a sulphur-bridged organo-dysprosium single-molecule magnet". *Angew. Chem. Int. Ed*. 2012 **51**

DOI:10.1002/anie.201202497

C. A. Smith , F. Tuna , M. Bodensteiner , M. Helliwell , D. Collison and R. A. Layfield "Exchange-coupled oxygen- and sulfur-bridged cyclopentadienyl-manganese(II) cages" *Dalton Trans.,* 2013, **42**, 71.

DOI: 10.1039/C2DT32262E

Colour Scheme for the Atoms of Structures

Carbon = Black

Nitrogen = Blue

Red = Oxygen

Silicon = Turquoise

Sulfur = Yellow

Bromine = Brown

Phosphorus = Dark orange

Manganese = Green

Iron = Orange

Chromium = Deep red

General Lanthanides = Dark green

Dysprosium = Purple

Gadolinium = Light Green

Erbium = Pink

Holmium = Light Pink

Terbium = Silvery Purple

ABSTRACT OF THESIS, submitted by: Charlene A. Smith to **THE UNIVERSITY OF MANCHESTER** for the degree of **DOCTOR OF PHILOSOPHY** and entitled: **The Synthesis and Magnetochemistry of Transition and Lanthanide Metal Compounds.** Month and Year of Submission: September 2012.

The introductory Chapter to this thesis outlines fundamental aspects of 4*f* lanthanide(III) coordination chemistry, in particular compounds that possess the intriguing properties of slow relaxation of magnetisation, (or the ability to behave as single-molecule magnets, SMMs). The recent renaissance into the study of the magnetic behaviour of 4*f*-coordination complexes has led to the consideration of utilising organometallic precursors for the development of novel lanthanide containing compounds, which may possess interesting magnetic properties, subsequently forming the basis of Chapter Two. In Chapter Two, the syntheses and structures of the novel lithiated thiolate ligand, lithium triphenylsilylthiolate, (Ph_3SiS-Li) (**2.1**), and the sulfur-bridged, dimetallic dysprosium(III) and gadolinium(III) complexes $[(MeCp)_2Dy(\mu\text{-}SSiPh_3)]_2$ (**2.2**) and $[(MeCp)_2Gd(\mu\text{-}SSiPh_3)]_2$ (**2.3**), are described in detail. The structural and physical properties of these compounds are analysed through NMR, elemental analysis and SQUID magnetometry, alongside supporting theoretical calculations to reveal that compound **2.2** is the first dimetallic, sulfur-bridged SMM reported, giving an energy barrier to the reversal of magnetisation of U_{eff} = 192 ± 5 K.[56b]

Chapter Three reports on the structural development of a series of lanthanide monomers, exhibiting the general motif $[Ln(OSiPh_3)_3(THF)_3]$ (where Ln = Dy(**3.4**), Er(**3.5**), Ho(**3.6**), Gd(**3.7**), Tb(**3.8**)), exploiting the siloxide ligand Ph_3SiOH through two novel synthetic routes. This Chapter also provides new analytical insight to these complexes by exploring their magnetic properties through a series of SQUID measurements and through the analysis of their electronic properties using air sensitive, variable temperature optical absorption spectroscopy. Compounds **3.4** and **3.5** were revealed to be SMMs, with **3.5** having a much higher thermal barrier to the reversal of magnetisation, U_{eff} = ~ 28 K, than **3.4**, which are supported by theoretical analysis.

Chapter Four describes the utility of ligand **2.1** and Ph_3SiOH in the context of 3*d* transition metal cyclopentadienyl chemistry, outlining the syntheses and structures of three distinct compounds; the trimetallic, $[Cp_2Mn_3(\mu\text{-}OSiPh_3)_4]$(**4.7**), the hetero-cubane tetramer $[CpMn(\mu\text{-}SSiPh_3)]_4$ (**4.8**) and the dimetallic thiolate-bridged $[CpCr(\mu\text{-}SSiPh_3)]_2$ (**4.9**) compound. These compounds were formed in reactions exploiting organometallic manganocene and chromocene precursors. Magnetic susceptibility measurements were conducted on these compounds to gain further insight into their structural properties. The magnetic exchange coupling constants for Mn(II) compounds **4.7** and **4.8** were J = - 4.4 cm^{-1} and J = - 3.0 cm^{-1} respectively. Furthermore, having demonstrated the use of metal-cyclopentadienyl building blocks in the synthesis of novel SMMs, Chapter Five discusses the possibility of further advancement on the development of this class of magnetic molecules.

Declaration

No portion of the work referred to in the thesis has been submitted in support of an application for another degree or qualification of this or any other university or other institute of learning.

Copyright Statement

i. The author of this thesis (including any appendices and/or schedules to this thesis) owns certain copyright or related rights in it (the "Copyright") and s/he has given The University of Manchester certain rights to use such Copyright, including for administrative purposes.

ii. Copies of this thesis, either in full or in extracts and whether in hard or electronic copy, may be made only in accordance with the Copyright, Designs and Patents Act 1988 (as amended) and regulations issued under it or, where appropriate, in accordance with licensing agreements which the University has from time to time. This page must form part of any such copies made.

iii. The ownership of certain Copyright, patents, designs, trademarks and other intellectual property (the "Intellectual Property") and any reproductions of copyright works in the thesis, for example graphs and tables ("Reproductions"), which may be described in this thesis, may not be owned by the author and may be owned by third parties. Such Intellectual Property and Reproductions cannot and must not be made

available for use without the prior written permission of the owner(s) of the relevant Intellectual Property and/or Reproductions.

iv. Further information on the conditions under which disclosure, publication and commercialisation of this thesis, the Copyright and any Intellectual Property and/or Reproductions described in it may take place is available in the University IP Policy (see http://documents.manchester.ac.uk/DocuInfo.aspx?DocID=487), in any relevant Thesis restriction declarations deposited in the University Library, The University Library's regulations (see http://www.manchester.ac.uk/library/aboutus/regulations) and in The University's policy on presentation of Theses.

Acknowledgements

Primarily I would like to thank my supervisors Richard Layfield and David Collison, for their constant support and encouragement throughout this work, and also Richard Winpenny and Eric McInnes for their additional help and guidance for which I am exceptionally grateful.

Many thanks to all those who have provided useful suggestions and have contributed to my work. In particular, Floriana Tuna for conducting the SQUID magnetometer measurements. To Rebecca Docherty and Stephen Sproules for their work on the EPR data and Madeline Helliwell for her help and support with single crystal X-ray diffraction.

I would also like to thank Michael Bodensteiner, based at the University of Regensburg for his assistance with X-ray crystallography, and Liviu Chibotaru based at the University of Leuven for his work on the *ab initio* theoretical calculations.

Thanks are given to the University of Manchester and the EPSRC for funding.

Finally, I would like to thank my Family, close friends, all the MChem students, PhD students and postdoctoral workers past and present from the Manchester Molecular Magnetism group for helping me get through the ups and downs of life as a PhD student.

Chapter One

Introduction to the Coordination Chemistry and Magnetochemistry of the Lanthanides.

1.1 Introduction to the Principles of Lanthanide(III) Co-ordination Chemistry[1-4]

The lanthanide elements are a section of the Periodic Table also known as the rare earth metals and typically possess 4*f* orbitals that are progressively filled. The electropositive nature of the lanthanide metals is similar to that of the alkali and alkaline earth metals, and results in the formation of primarily ionic lanthanide(III) compounds, with the +3 oxidation state being the most stable.[1] The majority of lanthanide ions adopt the +3 oxidation state because the removal of the fourth electron requires a large ionisation energy, which cannot be compensated by chemical bond formation. Therefore, +4 oxidation states are largely inaccessible as a result of the 'core' 4*f* electrons being strongly shielded except for Ce(IV) . For Eu and Yb, +2 oxidation states are favoured due to the presence of a half filled (7-electrons) and a filled (14-electrons) 4*f* shell respectively. The 4*f* electrons added along the lanthanide series starting with cerium(III) $4f^1$ all the way through to lutetium(III) $4f^{14}$ are unable to shield each other effectively from the progressive addition of nuclear charge, resulting in what is known as the lanthanide contraction. It is this phenomenon that greatly affects the coordination geometry of the complexes they form.

The electronic states of lanthanide ions can be derived from the Russell-Saunders (*L*-*S*) coupling method, using Hund's rules, to give the ground state term symbol $^{2S+1}L_J$ for the lanthanide in question, (Table 1.1 and caption). The interaction between the *f*-orbitals and the ligand electrons in lanthanide complexes is small, and therefore

the difference between the energy levels in lanthanide complexes and the free lanthanide ion also relatively small.

Due to prominent spin-orbit coupling and the very small crystal field splitting, the 'spin-only' formula for determining μ_{eff} does not apply to the majority of 4*f* complexes except for complexes with Eu(II), Gd(III), Yb(II) and Lu(III) ions. Therefore, the effective magnetic moments, μ_{eff} for these elements are reliant upon the quantum number *J*, (where *J* represents the total angular momentum and is given by *J = L+S*, *L+S-1*,…., *L-S* Equation 1.1).

$$\mu_{eff} \propto \sqrt{J(J+1)} \quad (a)$$

where the Landé g value is the constant of proportionality and varies for each 4f ion. g is given by:

$$g = 1 + \frac{S(S+1) + J(J+1) - L(L+1)}{2J(J+1)} \quad (b)$$

Equation 1.1 The effective magnetic moment (a) and Landé *g* value (b) for lanthanide ions.

The spin-orbit coupling that exists within these lanthanide ions occurs as a result of the angular momentum associated with the spin of an electron as part of an atom, coupling with that being generated by its orbital motion and increases with increasing nuclear charge. A formulation of this model, represented in Equation 1.1,

is further illustrated in Table 1.1, and it is these electronic properties across the *f*-elements that lead to interesting magnetochemistry and optical properties. However, 4*f* ions Eu(III) and Sm(III) are exempt from this model because they both have low-lying excited states. The *f*-orbitals are unusual because they can be represented by two sets of 4*f* orbitals. Illustrated in Figure 1.1 is the cubic set, which is commonly assigned to atoms that are x, y, and z symmetry related (i.e. degenerate), for example those conforming to octahedral (O_h) and tetrahedral (T_d) point groups. The other set is known as the general set and there are three orbitals that contribute to both sets, these are the f_z^3, $f_z(x^2\text{-}y^2)$, f_{xyz}.

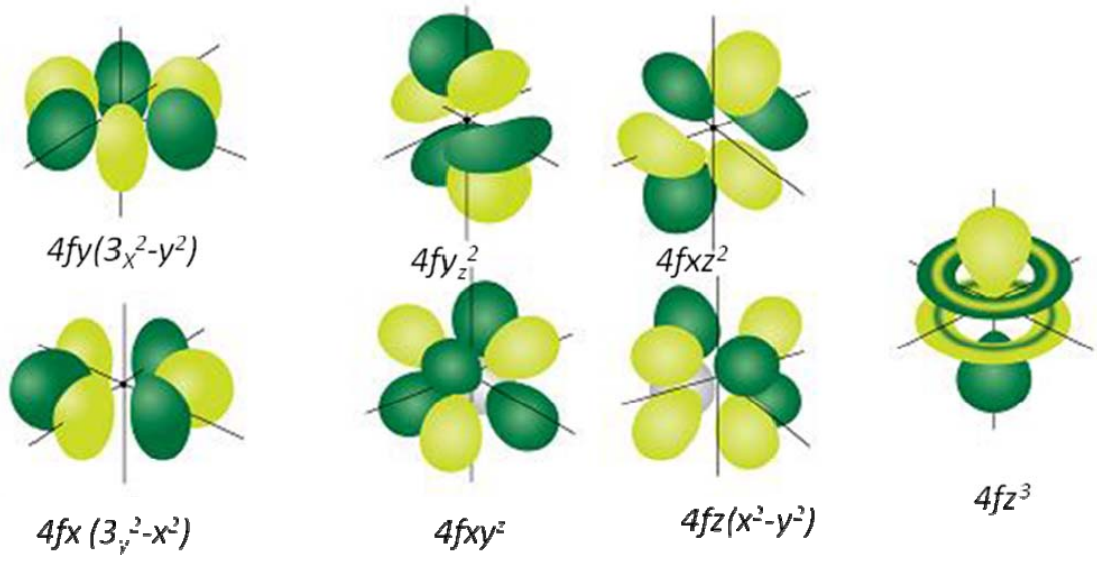

Figure 1.1 Illustration to show the general set of 4*f* orbitals. [4b]

Table 1.1 Magnetic properties of the rare earth ions.[4]

Ln	4*f* configuration	ground state term symbol	*g*	$g\sqrt{(J(J+1))}$
La^{3+}	$4f^0$	$^1S_0$	0	0
Ce^{3+}	$4f^1$	$^2F_{5/2}$	6/7	2.54
Pr^{3+}	$4f^2$	$^3H_4$	4/5	3.58
Nd^{3+}	$4f^3$	$^4I_{9/2}$	8/11	3.62
Pm^{3+}	$4f^4$	$^5I_4$	3/5	2.68
Sm^{3+}	$4f^5$	$^6H_{5/2}$	2/7	0.84
Eu^{3+}	$4f^6$	$^7F_0$	1	0.0
Gd^{3+}	$4f^7$	$^8S_{7/2}$	2	7.94
Tb^{3+}	$4f^8$	$^7F_6$	3/2	9.72
Dy^{3+}	$4f^9$	$^6H_{15/2}$	4/3	10.63
Ho^{3+}	$4f^{10}$	$^5I_8$	5/4	10.60
Er^{3+}	$4f^{11}$	$^4I_{15/2}$	6/5	9.59
Tm^{3+}	$4f^{12}$	$^3H_6$	7/6	7.57
Yb^{3+}	$4f^{13}$	$^2F_{7/2}$	8/7	4.54

J = L+S, L+S-1,…., L-S

(Where L = atomic orbital angular momentum quantum number, S = total spin quantum number and J = the total angular momentum, which is used to derive the required ground state term symbol $^{(2S+1)}L_J$*).*

1.2 Background to Cyclopentadienyl Complexes.

The first reported organometallic lanthanide complexes were the tris(cyclopentadienyls) lanthanides, [$LnCp_3$] reported by Wilkinson and Birmingham in 1954.[5] These complexes are conveniently prepared by the reaction of sodium cyclopentadienide, NaCp, with anhydrous $LnCl_3$ in THF. The resulting solvated product, [$LnCp_3(THF)$] remains in solution, and is readily separated from the insoluble NaCl by-product. The electrostatic interaction between the Ln-Cp bonds arising from the ionic bonding nature, make these complexes highly unstable in air and moisture, and it is therefore imperative to handle these complexes in a strictly anhydrous environment. The initial [$LnCp_3(THF)$] product, can be easily desolvated by heating *in vacuo*, and the pure homoleptic compound is obtained by sublimation, Scheme 1.1.

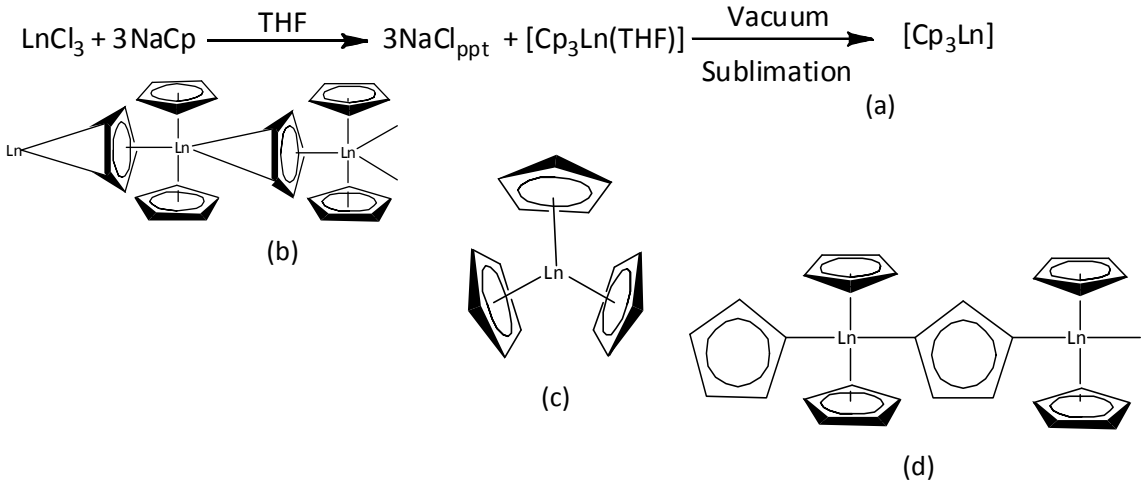

Scheme 1.1 Synthesis of [Cp_3Ln](a), and schematic representation for the molecular structures of a homoleptic, ionic [Cp_3Ln] derivatives, $[(\eta^5\text{- Cp})_2Ln(\mu\text{- }\eta^5{:}\eta^x\text{–Cp})]_\infty$ (b), $Ln(\eta^5\text{-Cp}_3)$(c), $[(\eta^5\text{- Cp})_2Ln(\mu\text{- }\eta^1{:}\eta^1\text{–Cp})]_\infty$ (d), exhibiting formal coordination numbers of 11, 9 and 8 respectively.[1]

There are three observed structural types of [Cp_3Ln] depending on the radius of the lanthanide cation, Scheme1.1. As a direct result of the lanthanide contraction the larger cations, e.g. lanthanum, adopt a polymer structure where each atom is coordinated to three η^5-Cp ligands and has a η^2 interaction with one other Cp ligand, Scheme 1.1(b). Samarium which has an intermediate cation size tends to adopt a monomeric structure, Scheme 1.1(c), whilst those lanthanides(III) towards the end of the series e.g. lutetium, possessing the smallest ionic radius, adopt a polymeric structure with each lanthanide atom coordinated to two η^5- Cp ligands and two μ_2-Cp ligands, Scheme 1.1(d). The monomeric structure is the preferred geometry for lanthanides(III) complexes with ligands bearing bulky substituents.[1,3]

Organometallic lanthanide(III) complexes are significantly sensitive to air and moisture in part owing to their ionic nature.[2] There is an abundance of organo-lanthanide chemistry concerning the cyclopentadienyl, Cp, ligand and its various derivatives. The lower basicity of Cp ligands compared to that of R- ligand substituents (R = alkyl ligand), results in Cp being far less reactive than alkyl ligands in heteroleptic complexes. As a result of the typically large lanthanide 4*f* ions, these cations tend to prefer formal coordination numbers in the range of 8-12 to accommodate their size, because more anions can pack around the large cation. However, low coordination numbers are achieved with very sterically bulky ligands.[1] Therefore, [Cp_3Ln] precursors facilitate the coordination of Ln-R bonds (R = alkyl ligand), since the Cp ligand allows the highly shielded 4*f* ions to be effectively

induced. In addition, physical characteristics such as ligand field effects are energetically large within *d* block ions, but are much smaller in the chemistry of lanthanides.

The *tris*-(methycyclopentadienyl) lanthanide complex $[(MeCp)_3Ln]$, Scheme 1.1, has a methyl group on each of the three η^5-Cp rings which enhances the solubility of this complex in organic solvents, which is the reason why $[(MeCp)_3Ln]$ features heavily in the following chapters. However, there are some notable differences between $[(MeCp)_3Ln]$ and $[Cp_3Ln]$ complexes. Generally, the compounds derived from methylcyclopentadienyl tend to crystallise as thin platelets, while the cyclopentadienyl complexes often form prisms and methylcyclopentadienyl compounds are also much more sensitive to moisture and oxidation than the cyclopentadienyls.[5,6]

1.3 Lanthanide Bis(cyclopentadienyl) halide Complexes.

The bis(cyclopentadienyl) lanthanide halides are useful intermediates in the area of organolanthanide chemistry, exploiting Cp' derivatives as auxiliary ligands. The reaction of 2MCp (M = alkali metal) with $LnCl_3$ in THF gives the $[Cp_2LnCl]_n$ compound, although this metathesis reaction may lead to the formation of heterometallic 'ate' complexes $[Cp_2Ln(\mu\text{-}Cl)_2M]$, and elimination of the alkali metal can be difficult. Synthetic routes are outlined in Scheme 1.2.[7,8]

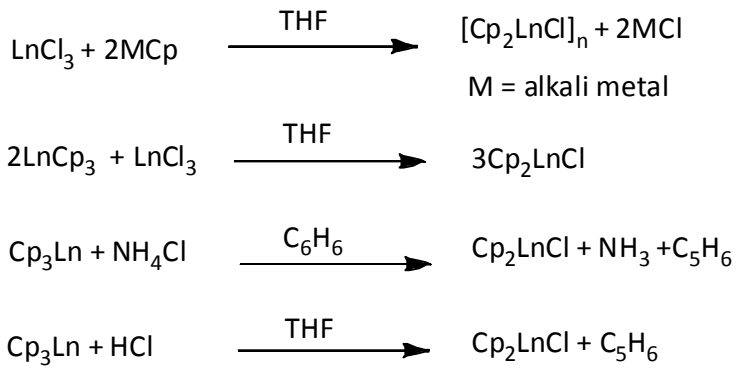

Scheme 1.2 A sequence of synthetic reactions for the preparation of Cp_2LnCl complexes

The synthetic route illustrated in Scheme 1.2, reacting $LnCl_3$ with two equivalents of $LnCp_3$ by a ligand redistribution reaction, emphasises the stability of Cp_2LnCl and the relative lability of lanthanide complexes. The resulting unsolvated Cp_2LnCl fragment is Lewis acidic and can readily form chloride-bridged compounds, where the coordination environments of the Ln results in the formation of either a dimer or oligomer. Various complexes can be formed by utilising the Cp_2LnCl precursor, depending on the size of the Ln cation, and as with Cp_3Ln precursors the structures are determined by a combination of the steric requirements and the necessity to minimise inter-ligand repulsion effects. Hence, the size of the decreasing lanthanide(III) radius along the series, is influential for determining the coordination environments of the complex.

1.4 Single-Molecule Magnets.

Since the discovery of single-molecule magnets (SMMs), there has been growing interest into the development of polymetallic complexes of paramagnetic *d*-transition and lanthanide metals which display SMM behaviour. For the *d* block, this extraordinary class of molecules exhibit a magnetic bistability that is solely of molecular origin and occurs from a combination of a high ground state electron spin (*S*), resulting from the magnetic exchange interactions between the individual ions within the cluster, and a large negative zero-field splitting, (*D*) within this ground state. The first and best known SMM is the dodecametallic, mixed valence manganese(III/IV) cluster $[Mn_{12}O_{12}(O_2CMe)_{16}(H_2O)_4]$ (**1.1**), commonly referred to as Mn_{12} which exhibits a ground state of $S = 10$ (Figure 1.2).[9] Magnetic hysteresis within SMMs is observed at very low temperatures. The temperature at which this retention of magnetisation is lost is defined as the blocking temperature, T_B and is ca. 4 K for Mn_{12}. Therefore, if SMMs are to be utilised in areas such as data storage and quantum information processing for example, SMMs need to be synthesised with higher blocking temperatures.[10-12]

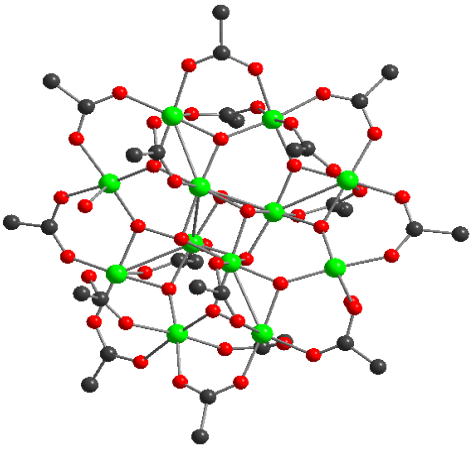

(a)

Figure 1.2 (a) The $[Mn_{12}O_{12}(O_2CMe)_{16}(H_2O)_4]$(**1.1**) complex consisting of eight Mn(III), four Mn(IV), connected through bridging oxo-ligands, with sixteen acetates and four water ligands (1.1a).[9]

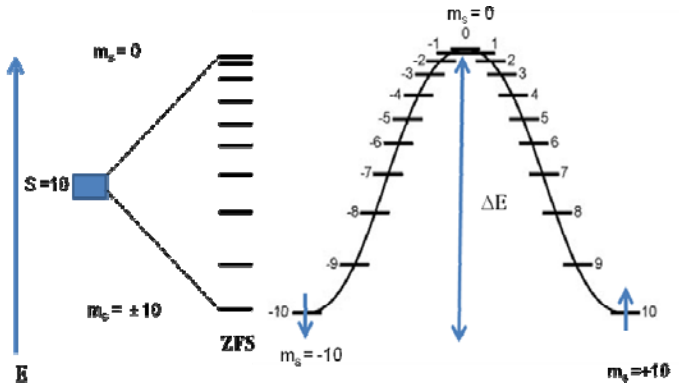

(b)

1.2(b) Diagram outlining the ZFS of an *S* = 10 ground state with negative *D,* where the population of the lowest energy m_s levels (+/-) are represented by the up and down arrows and are equally populated in the zero field. ΔE signifies the energy barrier between m_s=+ 10 and m_s = -10.

A further example of 3*d* transition metal SMM clusters can be seen in the form of the hexametallic Mn(III) complex $[Mn_6O_2(sao)_6(O_2CPh)_2(EtOH)_2]$(**1.2**), ($saoH_2$= salicylaldoxime), where the metal centres are bridged by oxygen donor ligands, commonly observed within this types of structure, (Figure 1.3).[13] However, the blocking temperature at which the magnetisation is reversed for this compound, reported in 2007, is only 4.5 K, suggesting that there is still scope for the discovery of new SMMS with higher blocking temperatures.

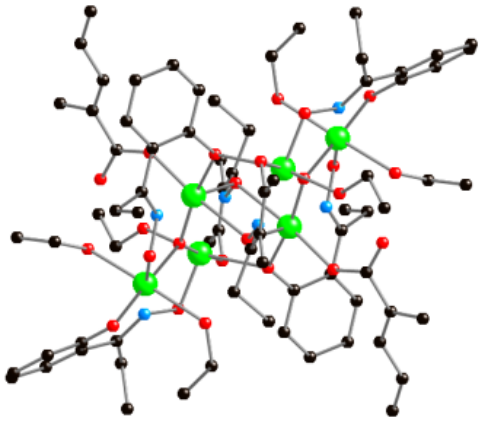

Figure 1.3 The $[Mn_6O_2$ (sao) $_6(O_2CPh)_2(EtOH)_2]$ (**1.2**) complex.[13]

1.5 Magnetic Behaviour in Lanthanide Complexes

The large magnetic anisotropy within lanthanide ions has made complexes of the 4*f* ions ideal candidates for the development of new types of SMMs. Previous limited interest in investigating lanthanide systems for the development of SMMs, was largely due to very weak exchange interactions when they are in their most stable trivalent oxidation state. After the first SMM **1.1**, was discovered high spin, strongly coupled 3*d* transition metal clusters were initially considered to have the most potential for the development of SMMs. However, it has been confirmed over recent years that the *f*-elements can also be used, depending on the interaction between the electron density of the 4*f* ions and the crystal field environments in which it is placed. The parameters which determines the magnetic properties of 3*d* metal complexes cannot be applied to 4*f* ions.[14,15] When observing the individual properties of the lanthanides ions, using Dy(III) as an example, the spin orbit coupled ground state $^{6}H_{15/2}$ ground term symbol is more informative when considering how useful 4*f* ions are for single-molecule magnetism, than simply representing the electronic structure by the number of valence electrons ($4f^{9}$), Figure 1.4(a). The spin orbit coupled quantum number *J*, is of great importance because the spin orbit coupling energy is generally larger than the effect of the crystal field for *f*-elements. However, the crystal field effects are integral for the development of SMMs that utilise *f*-elements. In contrast with transition metals, the *f*-block metals rely on the interaction of the ground state spin orbit *J* state with the crystal field to derive the magnetic anisotropy barrier, with opposite orientations of the spin ground state. Continuing to use Dy(III) as an example because of its large spin-orbit coupling, this

observation is shown in Figure 1.4(b), with the ground state for the free ion being 16-fold degenerate, ($2J_{Dy}$ +1), and is made up of magnetic states, denoted by m_J. [14d, 15]

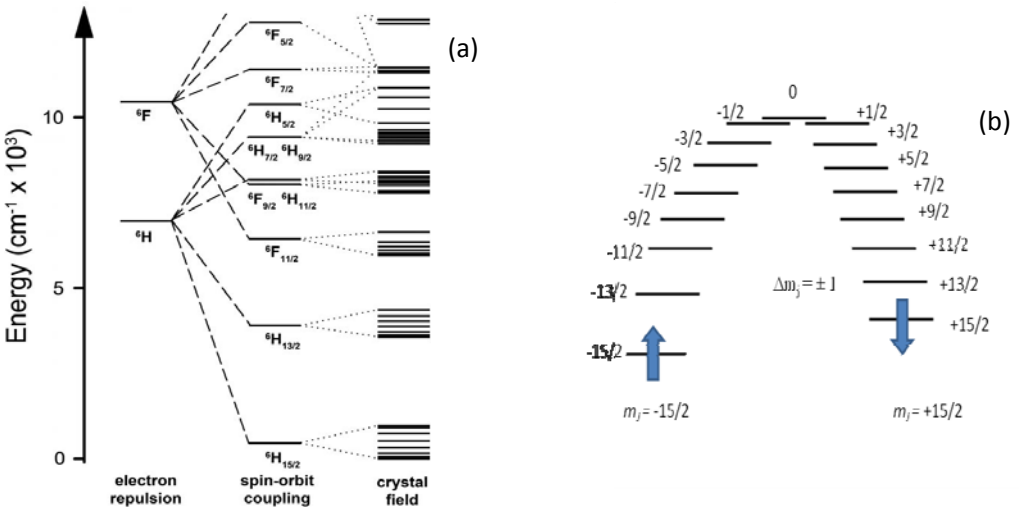

Figure 1.4 Low energy electronic structure of Dy(III) ions, with the crystal field splitting modelled on the $Dy[Me_3Si)_2N]_3$ complex (a),[15b] and the degenerate population of m_J states for Dy(III)(b).

Consequently, the observed splitting of spins states in conjunction with the strong spin- orbit coupling interaction directly associates the orientation of the spin to the strength and symmetry of the ligand field. As a result it is possible to increase the single ion anisotropy by selecting or modifying the coordination environment of the lanthanide ion to the ligand in question. For this model to be used effectively, when considering which *f*-element to be used in single-molecule magnetism, two factors must occur. Firstly, the ground state should be doubly degenerate and have a high value of $\pm m_J$ quantum number. This is imperative because SMMs collectively are defined by their bistability in the ground state, (a singlet ground state is of virtually no use magnetically).[15] The other component for a strong anisotropy within

lanthanide ions is a separation between the bistable $\pm m_J$ ground state and the first excited $\pm m_J$ state. If these two instances occur simulatlaneously, the magnetic ground state should be sustained and the magnetic relaxation should be significantly slowed at temperatures below the first excitation energy.

A recent development in the quest for discovering novel lanthanide SMMs example can be found through the synthesis of a $\{Dy_5\}$ square-based pyramid, Figure 1.5.[16] This oxo-centered $\{Dy_5\}$ pyramid exists as part of a family of lanthanides with the general formula $[Ln_5(\mu\text{-}O)(\mu_3\text{-}OR)_4(\mu_2\text{-}OR)_4(OR)_5]$ where, R = *i*Pr, Ln = Nd[17,18], Eu[19], Gd[17], Er[17,20], Yb[21]; R = ^{t}Bu, Ln = La[22], Nd[23]. The $[Dy_5O(O\textit{i}Pr)_{13}]$ (**1.3**), square-based pyramid was conveniently prepared by the reaction of KO*i*Pr, with $DyCl_3$ in *i*PrOH/toluene with a stoichiometric amount of H_2O, which gave two different crystal systems, one of which is isostructural to the previously reported $\{Er_5\}$ compound,[19] however the other has a different unit cell.

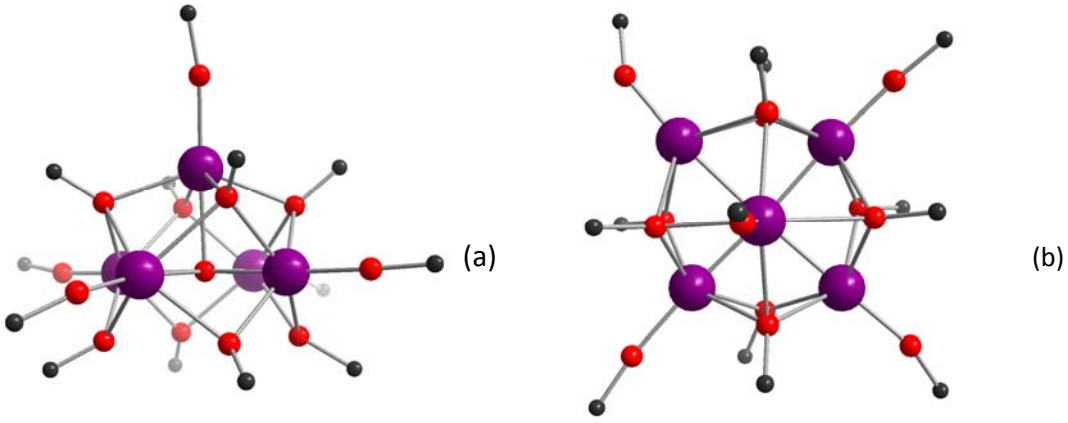

Figure 1.5 Structure of $[Dy_5O(O\textit{i}Pr)_{13}]$ (**1.3**) (a), alongside a view of illustrating the pseudo fourfold axis (b), (*i*Pr groups are trimmed for clarity).[16]

Magnetic measurements conducted on both polymorphs revealed identical properties. The room temperature molar magnetic susceptibility $\chi_M T$, is 70.5 cm^3 K mol^{-1} and is in good agreement with that expected for five uncoupled Dy^{III} ions, which is 70.8 cm^3 K mol^{-1}, calculated for $^6H_{15/2,}$ S = 5/2, L = 5, J = 15/2, g = 4/3,[16b] and decreases rapidly below 30 K. The results of the magnetic measurements conducted for the $\{Dy_5\}$ square-based pyramid confirmed that **1.3** is an SMM, with a thermal energy barrier to magnetization relaxation U_{eff} of around 530 K. In the context of *d*- or *f*-block clusters, this is undoubtedly the largest barrier recorded, surpassing the 86 and 200 K reported for a $\{Mn^{III}_6\}$[13] and a $\{Dy_6\}$[24] cluster, respectively. The only molecular species that exceeds this value is that of Ishikawa's $[Ln(Pc)_2]^{n-}$ (where Pc = dianion of phthalocyanine) single-ion magnets, and with the addition of chemical and redox modification have reached energy barriers of 790 K.[14a-d,15a]

Further examples of lanthanide containing compounds, which were also found to be SMMs possessing extremely high blocking temperatures, were reported by Long and Evans.[25] By exploiting the concept that some lanthanide complexes display a useful combination of high anisotropy and spin ground state interaction (*J*), Long *et al*. pursued the reduction of $\{[(Me_3Si)_2N]_2(THF)Ln\}_2(\mu\text{-}\eta^2\text{:}\eta^2\text{-}N_2)$ (Ln = Gd (**1.4**),Dy (**1.5**)) with potassium graphite in THF to produce two isostructural dimetallic N_2^{3-} radical-bridged complexes, $[K(18\text{-crown-6})]\{[(Me_3Si)_2N]_2(THF)Ln\}_2(\mu\text{-}\eta^2\text{:}\eta^2\text{-}N_2)$ (Ln = Gd (**1.6**), Dy (**1.7**)), Figure 1.6. In this instance, according to Long, the desired strong exchange coupling required to achieve SMMs with high blocking temperatures, was through

the use of radical bridging ligands with diffuse spin orbitals that can penetrate the core electron density of the lanthanide ions, where the 4*f* spin orbitals are deeply immersed within the core because of the significant radial extent 4*f* ions.

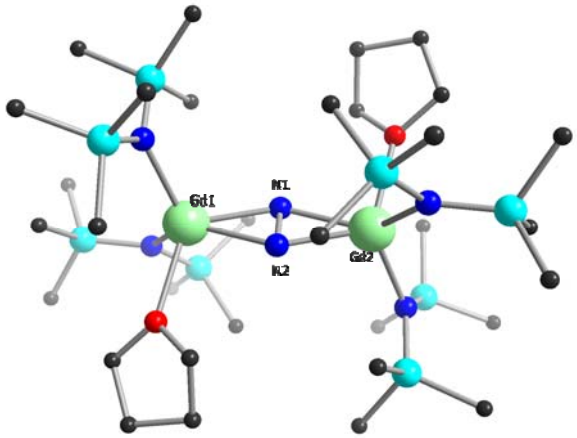

Figure 1.6 Structure of the $\{[(Me_3Si)_2N]_2(THF)Ln\}_2(\mu\text{-}\eta^2\text{:}\eta^{2\text{-}}N_2)^-$ (Ln = Gd (**1.6**)) anion hydrogen atoms omitted for clarity.[25a]

The d.c. magnetization experiments were made for **1.7** at 2.0 K with a sweep rate of ~0.0016 T/s to reveal significant hysteretic behaviour, indicating slow magnetic relaxation on the timescale set for this particular measurement. The magnetic hysteresis loops collected on **1.7** up to 8.3 K is one of the highest blocking temperatures reported for this type of magnetic experiment.[25]

1.6. Monometallic Lanthanide Compounds

Ishikawa et al. have reported some of the most intriguing results in the area of single-ion magnets (SIMs), where magnetic studies concerning the behaviour of

single-ion lanthanide compounds were conducted on a series of monometallic lanthanide complexes with phthalocyanine (Pc), ligands. Out of the six phthalocyanine double-decker complexes, $[Pc_2Ln]^-$ (Ln = Tb, Dy, Ho, Er, Tm and Yb), the Ishikawa group discovered the first SIM were compounds $[Pc_2Tb]^-$ (**1.8**) and $[Pc_2Dy]^-$ (**1.9**), exhibiting considerable retention of the magnetisation relaxation, whilst the others complexes in this series did not (Figure 1.7).[14a-c,15a]

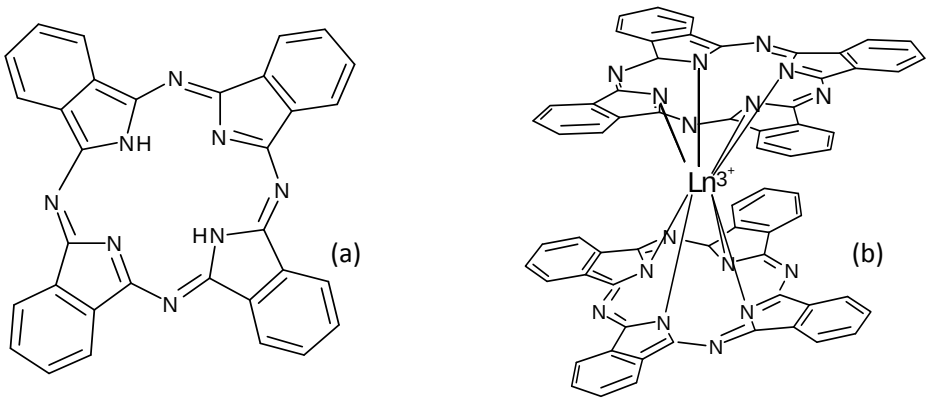

Figure 1.7 The structure of the phthalocyanine molecule (a) and an illustration to show how the lanthanide metal ion co-ordinates to phthalocyanine to form double-decker complexes (b). Ln = Tb, Dy, Ho, Er, Tm and Yb.

In addition, the slow relaxation of magnetization as a single-molecule property in compounds **1.8** and **1.9** results from a mechanism different from that of transition metal cluster SMMs,[9a,26a-h] and the temperature ranges for which the magnetization relaxations are observed for these systems are significantly higher than any other single-ion transition metal complex, (SIM).

Coronado and co-workers have reported that polyoxometalate (POM) complexes of lanthanide ions, form monolanthanide SIMs.[26i] The main focus of their work was the magnetic properties of the sodium salt of $[ErW_{10}O_{36}]^{9-}$ **1.10**, and was the first example of a POM displaying SMM behaviour. Although the ligands encapsulating the central single-ion of compounds **1.8**/**1.9** and **1.10** differ, the POMs encapsulate the lanthanide ion in a similar "sandwich" manner, to that of Ishikawa's monomers. Compounds **1.8** and **1.9** were initially assumed to adopt a cubic D_{4d} symmetry. However they were later found to have a different high symmetry point group by Magnani et al., stating that C_4 point group symmetry is actually observed,[26j] whereas, **1.10** is square anti-prismatic and adopts D_{4d} symmetry. This lanthanide POM comprises two anionic $[W_5O_{18}]^{6-}$ moieties encapsulating the Er^{3+} (Figure 1.8). In order to balance the charge the anionic clusters are surrounded by sodium cations, which are octahedrally coordinated by water molecules.

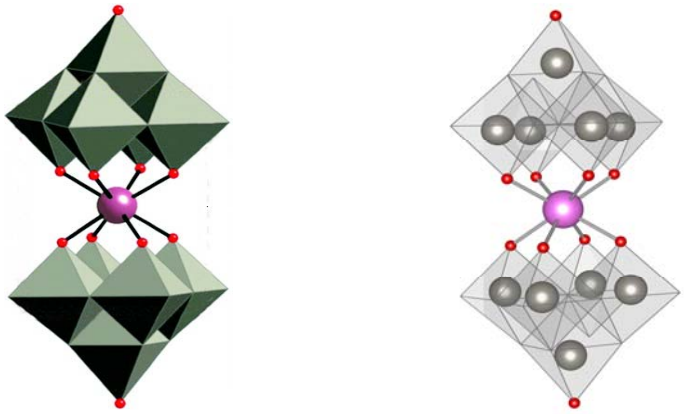

Figure 1.8 The structure of polyoxometalate, $[ErW_{10}O_{36}]^{9-}$ (**1.10**) and its coordination geometry.[26j]

The coordination environment of these single lanthanide-based systems plays a vital role in determining whether they exhibit SMM behaviour. This is highlighted by a comparison of the geometric features of the $[ErW_{10}O_{36}]^{9-}$ polyanion with those of its erbium double-decker counterpart $[Pc_2Er]^{-}$. Small geometrical differences between these two systems results in no slow relaxation properties being observed for the Er-containing phthalocyanine complex as opposed to the $[ErW_{10}O_{36}]^{9-}$ polyanion.

1.7 Polymetallic Lanthanide Clusters

With regards to the magnetism in lanthanide-containing compounds, those containing dysprosium (Dy) ions have received the most attention.[27,28] There is a growing number of homometallic metal clusters to accompany the breadth mixed metal clusters reported.[29-33] This is largely because of the difficulty to induce magnetic interactions between the metal ions of lanthanide based systems as a result of the strongly shielded unpaired electrons in the 4*f* orbitals. Consequently, the choice of ligand to incorporate within these lanthanide reactions is very influential, as the magnetic interactions between 4*f* metal ions can be achieved through the communication of the overlapping ligands.

Po-Heng Lin and co-workers have reported on the use of the pro-ligand (2-hydroxy-3-methoxyphenyl)methylene(isonicotino)hydrazine (H_2hmi), in reactions with dysprosium(III), because of this has the ability to it act as a rigid chelate (Figure 1.9).[34] The planarity of ligands of this nature provides O,N,O,O- based multichelating sites, which are compatible for lanthanide ion complex formation.[35,36] By reacting penta-aqua dysprosium nitrate, $Dy(NO_3)_3.5H_2O$, with H_2hmi in methanol (in the presence of triethylamine) in a 3:1 mixture of acetonitrile and methanol (in the presence of pyridine), pale orange crystals of $[Dy_2(hmi)_2(NO_3)_2(MeOH)_2]$ **1.11** and $[Dy_2(hmi)_2(NO_3)_2(MeOH)_2]_\infty(MeCN).(2MeCN)$ **1.12** were produced after two days, Figure 1.9. Phenoxide-bridged dysprosium dimers are the result of these reactions, where the positioning of the pyridyl groups aids the formation of an extended network that can control the arrangement of the SMM units in the three-dimensional structure of **1.12.** However, with regards to complex **1.12**, the pyridyl N-atoms further coordinate to the Dy atoms of the adjacent complexes forming a two- dimensional network of the dimetallic Dy complexes.

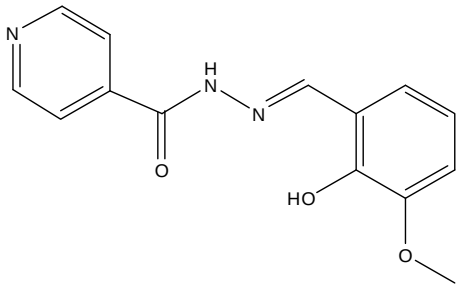

Figure 1.9 Diagram to show the (2-hydroxy-3-methoxyphenyl)methylene (isonicotino)hydrazine, (H_2hmi) pro-ligand.

The magnetic properties of **1.11** and **1.12** are exactly the same as expected, since they possess identical coordination environments, with **1.12** exhibiting identical repeating dimetallic dysprosium units of **1.11**. At room temperature, the $\chi_M T$ values of 30.4 and 30.0 cm^3 K mol^{-1} for **1.11** and **1.12** respectively, compare very well with the expected values of 28.34 cm^3 K mol^{-1} for two non-interacting dysprosium(III) ions. For both complexes the $\chi_M T$ product remains roughly constant before reaching a minimum value of 29.3 cm^3 K mol^{-1} at 23 K. $\chi_M T$ then sharply increases to a maximum value of 38.4 cm^3 K mol^{-1} for **1.11** and 36.6 cm^3 $Kmol^{-1}$ at 1.8 K. The increase of $\chi_M T$ at low temperature suggests the presence of intramolecular ferromagnetic interactions between metal centres. The oxygen donor bridging ligands of compounds **1.11** and **1.12** promote ferromagnetic exchange between the Dy(III) ions, and after a series of magnetic measurements were conducted on **1.12** the results showed that this compound possessed one of the largest energy barriers, at 71 K, reported for a lanthanide complex at the time, (Figure 1.10).[34]

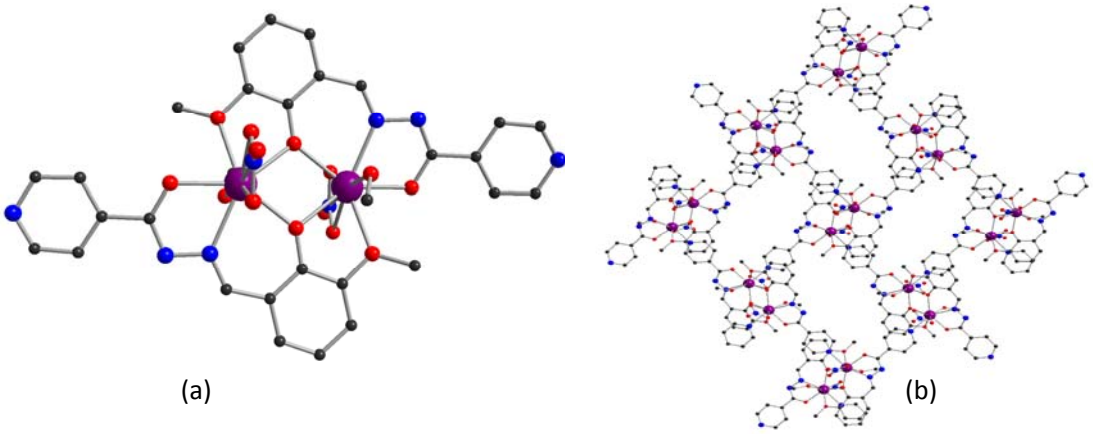

(a) (b)

Figure 1.10 The molecular structure of the complex $[Dy_2(hmi)_2(NO_3)_2(MeOH)_2]$ (**1.11**)(a), alongside the 2D network of complex $[Dy_2(hmi)_2(NO_3)_2(MeOH)_2]_\infty$ (**1.12**) (b) as viewed along the *c* axis. [34]

1.8 Lanthanide Complexes of tris-Cyclopentadienide Ligands.

The ionic character of the metal-ligand bond in tris-cyclopentadienyl lanthanide ligands (Cp_3Ln), gives these compounds the potential to be utilized as Brønsted bases in the synthesis of Ln-containing imido or amido clusters from their primary amines.[36,37] However, the magnetic interactions that occur between the metal atoms within compounds of this type have received comparatively little attention. Layfield et al. have reported on the structural and magnetic properties of the dimeric species $[Cp_2Ln\{_2\text{-NH-4,6-Me}_2pm\}]_2$, where Ln = Gd(**1.13**), Dy(**1.14**), Yb(**1.15**), and Nd(**1.16**), and are formed from the mono-deprotonation of 2-amino-4,6-dimethylpyrimidine by the corresponding Cp_3Ln.[37]

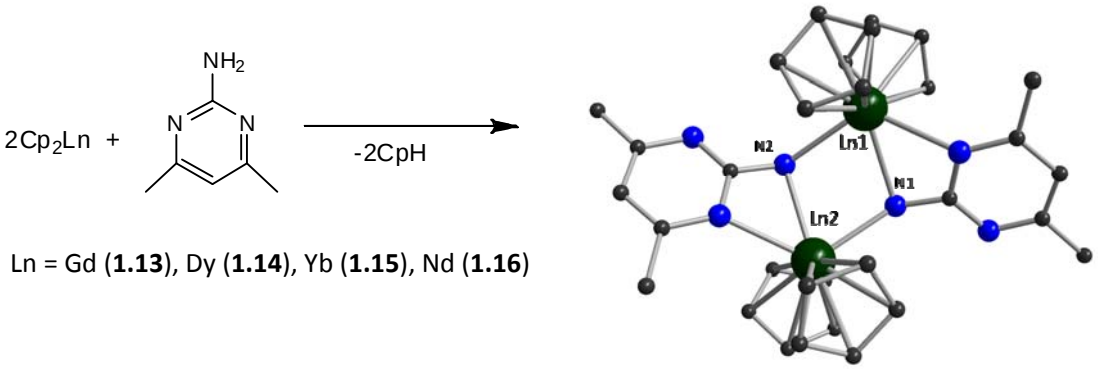

Ln = Gd (**1.13**), Dy (**1.14**), Yb (**1.15**), Nd (**1.16**)

Scheme 1.3 Reaction scheme illustrating the synthesis of $[Cp_2Ln\{2\text{-NH-4,6-Me}_2pm\}]_2$.

Addition of a toluene solution of Cp_3Ln to 2-amino-4,6-dimethylpyridine at -78° C, followed by slowly warming the reaction to room temperature and storing the resulting solution overnight produced complexes **1.13-1.16** (Scheme 1.3). Each of the resulting dimers listed in Scheme 1.2 contains two Ln^{3+} cations bridged by two [μ-2-N(H)-4,6-Me_2pm] ligands to give a butterfly-like $[Ln_2N_2]$ central core. Each Ln(III) is chelated to the amidopyrimidine ligand via an ortho- nitrogen atom, whilst also

being bonded to two terminal Cp ligands. As a result, this type of bonding leads to a formal coordination number of nine for each Ln(III) centre.

However favourable aspects of the cyclopentadienyl ligand (such as providing an ideal ligand environment to satisfy the coordination environments of large trivalent lanthanide ions), has led to further investigations into its utility for the production of organometallic lanthanide complexes for SMMs. Layfield et al. have reported on the synthesis and magnetic properties of organometallic dimers of dysprosium [{$Cp_2Dy(\mu\text{-bta})\}_2$] (btaH = 1*H*-1,2,3-benzotriazole), **1.17** (Scheme 1.4), and [{$Cp_2Dy[\mu\text{-}N(H)pmMe_2]\}_2$] **1.14** ($NH_2pmMe_2$ = 2-amino-4-6-dimethylpyrimidine).[39] Compound **1.17** was prepared by a deprotonation reaction between [Cp_3Dy] and benzotriazole.

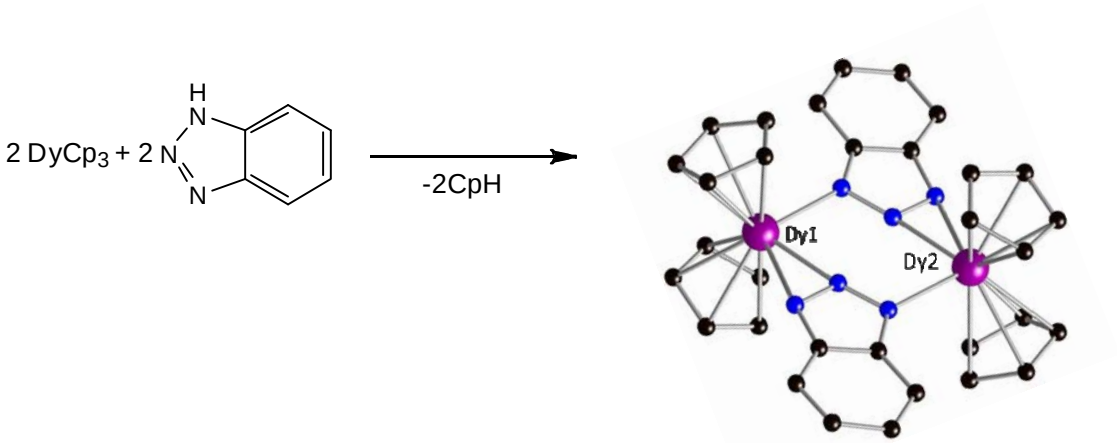

Scheme 1.4 Reaction scheme illustrating the formation of the dysprosium dimer, [{$Cp_2Dy(\mu\text{-bta})\}_2$] (**1.17**).

The molecular structure of **1.17** is made up of a non-centrosymmetric dimer where the two dysprosium atoms are bridged by two $[bta]^-$ ligands, allowing the two dysprosium atoms to be complexed by two terminal η-Cp ligands, whereas

compound **1.14** exists as an amido–bridged dimer containing nine co-ordinate Dy(III) centres. Whilst the structural motif of [{$Cp_2Ln(\mu\text{-}En)\}_2$] (E*n* = heteroatom group) has become commonly represented throughout organolanthanide chemistry[7b,36] compound **1.17** is the first example of this type to contain $[bta]^-$ as the bridging ligand.

Magnetic measurements were conducted on compounds **1.17** and **1.14** to reveal similar results in both magnetisation against the field and susceptibility against temperature measurements. For compounds **1.17** and **1.14** the $\chi_M T$ values at room temperature gave values of 27.2 and 28.1 cm^3 K mol^{-1} respectively, which are compatible with expected values of 28.34 cm^3 $Kmol^{-1}$ for non-interacting Dy(III) ions, (S = 5/2). When subjected to cooling, a gradual decrease in $\chi_M T$ is observed and it then drops more rapidly below 30 K to reach 16.2 (for compound **1.17**) and 13.1 cm^3 K mol^{-1} for **1.14**. The gradual decline of $\chi_M T$ with T is essentially due to crystal field effects.

For compound **1.17** the Dy ions were found to interact weakly electronically with each other and in fact the slow relaxation seen for **1.17** is due to single ion factors, which is unusual compared to other reports on dimetallic dysprosium SMMs.[40] The same cannot be said for **1.14** which is not considered an SMM. Therefore, this suggests the strength of the magnetic interaction between the Dy(III) ions cannot be determined with complete certainty. Hence, the intrinsic properties leading to axial

anisotropy in different 4*f* ions, is influential in the development of new lanthanide SMMs

1.9 Project Proposal.

There is considerable scope for developing monometallic and polymetallic complexes of lanthanide metals utilising organometallic synthesis. Most of this chemistry is dominated by either oxygen or nitrogen bridging ligands. Consequently the capacity for synthesising further 4*f* compounds, exploiting different chalcogen bridging ligands such as those incorporating sulfur, is extensive, whilst oxygen bridging compounds of this nature are still of importance. The work conducted by Layfield et al.[39] to produce the $[\{Cp_2Dy(\mu\text{-bta})\}]_2]$ dimer has set the precedent for subsequent reactions of this nature, albeit with different groups of bridging ligands. Hence, extending the family of organometallic lanthanide compounds, to be exploited as SMMs, will form an integral part of this thesis. In addition to dysprosium, further lanthanides thought to exhibit intriguing comparable behaviour will also be explored such as Er(III), Tb(III), Ho(III) and Gd(III) and will be utilised in conjunction with chalcogen-based ligands.

Therefore, the aims of this research are to synthesise a series of novel lanthanide metal compounds, utilising chalcogen-bridging ligands, and to investigate the effects ligand substitution has on the structural and magnetic properties of these compounds, ultimately in a bid to create new SMMs.

Chapter Two

Organometallic Sulfur-Bridged Lanthanide(III) Methylcyclopentadienyl Compounds

2.1 Introduction to Lanthanide-Thiolate Chemistry.

Over recent years there has been considerable interest in the employment of sulfur-containing ligands for organometallic synthesis. The utility of these ligands in industrially related or enzyme-catalysed processes has been widely reported.[41,42] Furthermore, there are many examples of these compounds being exploited as precursors with intriguing physical properties.[43,44] In 1997, Brennan, Melman and Emge highlighted the convenience of lanthanide thiolates [$Ln(SPh)_3$; Ln = Pr, Nd, Gd] to be utilised as precursors in reactions with elemental sulfur to give crystalline octametallic $Ln_8S_6(SPh)_{12}(THF)_8$ compounds.[43a]

Although there is a profusion of lanthanide co-ordination chemistry utilising 'hard' oxygen and nitrogen donor ligands, there are considerably fewer reported lanthanide compounds incorporating sulfur donor ligands. This gap in lanthanide(III) thiolate chemistry is mainly due to trivalent lanthanide ions generally behaving as hard Lewis acids, therefore the ability of soft S-donor ligands to coordinate to hard trivalent lanthanide precursors is relatively low. However, relative to more conventional O, N, or C based anions, these singly charged more electropositive chalcogenolate ligands should also be highly susceptible to displacement from Ln coordination sphere in the context of reacting lanthanide thiolate precursors with thiolate ligands.[43a]

Examples of sulfur ligation within *f*-block complexes do however exist in the form of dithiocarbamates[45] and dithiophosphinates[46,] where dithiocarbamates have been

known since 1908 when neodymium complexes were formed exploiting this class of ligands. However, the first structurally characterised lanthanide thiolate complexes were reported almost a century later in 1985 by Aspinall et al.[47]

Under stringent air and moisture sensitive conditions $[LnL_2(\mu\text{-}Cl)(THF)]_2$ (Ln = Eu, Gd, L = $N(SiMe_3)_2$)[48] was reacted with two equivalents of $LiSBu^t$ in THF, leading to the formation of $[LnL_2(\mu\text{-}SBu^t)]_2$, (Ln = Eu, Gd), Figure 2.1. These reactions have set the precedent for the synthesis of subsequent lanthanide thiolate compounds and a substantial growth of interest into their properties.[49]

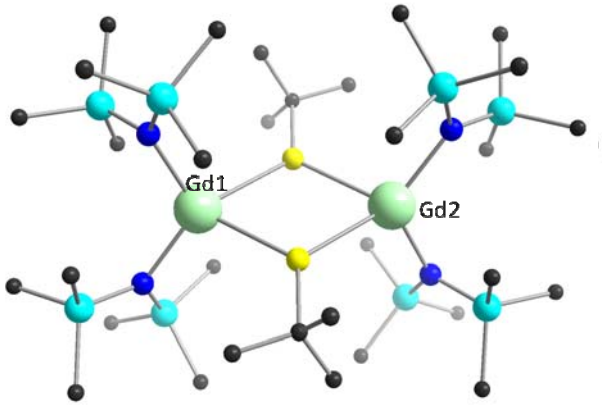

Figure 2.1 Molecular structure of $[LnL_2(\mu\text{-}SBu_t)]_2$, (Ln = Eu, Gd), with hydrogen atoms removed for clarity.[47]

The magnetic properties of polymetallic lanthanide compounds detailed in Section 1.1, has led to the development of new 4*f* polymetallic compounds, in particular expanding the family of organometallic SMM complexes. In this section, alternative ligand environments to the widely exploited hard O- and N-donor ligands have been explored. 'Soft' donor ligands, such as sulfur could lead to improved relaxation of

magnetisation times. The use of these soft donor ligands may have two influential effects. Firstly, these sulfur donor ligands could enhance the magnetic exchange between the Ln(III) ions due to the greater radial extension of the sulfur orbitals, which are considerably more than O- and N-donor ligands and secondly very different crystal field environments may occur. Therefore, since crystal field effects are the principal interaction which governs the slow relaxation of magnetisation in Ln-SMMs, there is great attraction to developing these postulates further. In addition, there has been very little reported in the literature on the magnetic properties of lanthanide-sulfur bridged compounds. Hence, this chapter will report on the synthesis, structure and magnetic properties of the lithium triphenylsilylthiolate pro-ligand (Ph_3SiS-Li) (**2.1**) and the organometallic, isostructural dimers, $[(MeCp)_2Dy(\mu\text{-}SSiPh_3)]_2$ (**2.2**) and $[(MeCp)_2Gd(\mu\text{-}SSiPh_3)]_2$ (**2.3**), with compound **2.2** being the first sulfur-bridged SMM.

2.2 Results and Discussion.

2.2.1 Syntheses and Structure of Lanthanide(III) Methylcyclopentadienide Thiolates.

The preparation of the novel lithiated-sulfur based ligand, lithium triphenylsilylthiolate (Ph_3SiS-Li) (**2.1**), is illustrated in Scheme 2.1 and produced yields of 87% as a white precipitate.

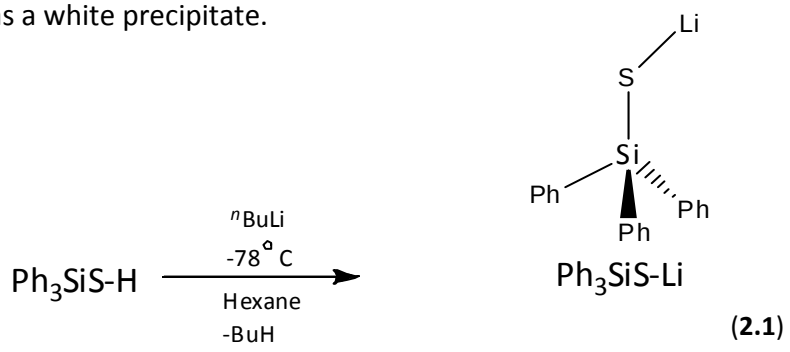

(**2.1**)

Scheme 2.1 Synthesis of the monolithiated thiolate ligand lithium triphenylsilylthiolate.

Deprotonation of the initial triphenylsilanethiol pro-ligand, using *n*-butyllithium, (^{n}BuLi), enabled metalation to yield compound **2.1**. Characterisation of **2.1** by elemental analysis compared well with the expected figures (*vide infra*; Chapter Six, 6.7) and solution phase ^{1}H NMR spectroscopy, in deuterated THF, showed evidence of proton coupling patterns expected for the phenyl groups, along with assigned lithium chemical shifts in the ^{7}Li NMR spectra (*vide infra;* Chapter Six, 6.7). Ligand **2.1** was subsequently utilised in a reaction with tris-(methylcyclopentadienyl)lanthanide(III) precursors, $(MeCp)_3Dy$ and $(MeCp)_3Gd$ in toluene, to give compounds $[(MeCp)_2Dy(\mu\text{-}SSiPh_3)]_2$ (**2.2**) and $[(MeCp)_2Gd(\mu\text{-}SSiPh_3)]_2$ (**2.3**) by means of transmetalation, Scheme 2.2**.** The sulfur-bridged dimers **2.2** and

2.3 were crystallised by slow cooling of a saturated toluene solution to result in the formation of colourless needle-shaped single crystals suitable for X-ray crystallography.

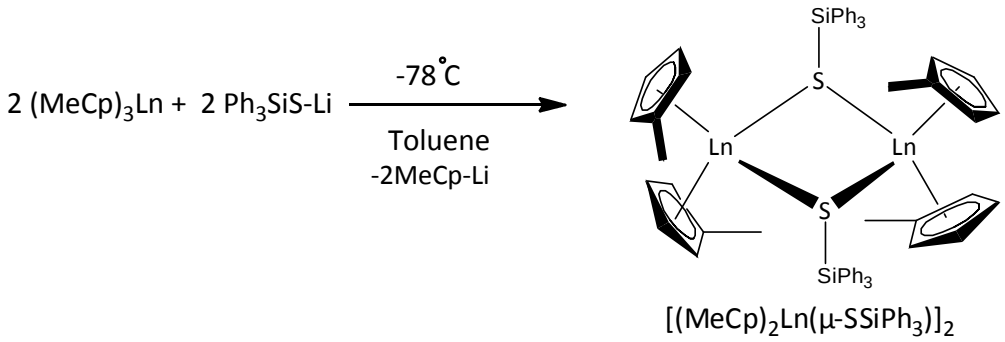

Ln = Dy (**2.2**), Gd (**2.3**)

Scheme 2.2 Synthesis of the dimetallic sulfur-bridged lanthanide compound.

Accurate elemental analysis on compounds **2.2** and **2.3**, proved initially difficult to obtain because of the severe air and moisture sensitivity of these compounds, however after numerous repeats elemental analytical data that compared well with calculated values of **2.2** and **2.3** were obtained. Both **2.2** and **2.3** are very soluble in non-polar hydrocarbon solvents, and are highly susceptible to deterioration upon exposure to air and moisture. Therefore, obtaining crystals of a sufficient quality suitable for X-ray diffraction proved somewhat difficult. Particularly close attention was paid to the quantity of solvent and temperature in order to achieve adequate crystallinity for further analysis. The sensitivity of these compounds to air and moisture is such that once dried *in vacuo,* these fragile, ultra thin needle-like, colourless crystals show visible signs of deterioration once subjected to trace air

exposure, and begin to turn a dark yellow/orange in colour in addition to becoming much more powdery in texture. Table 2.1 gives the crystallographic data and summary of structural refinement for compound **2.2**.

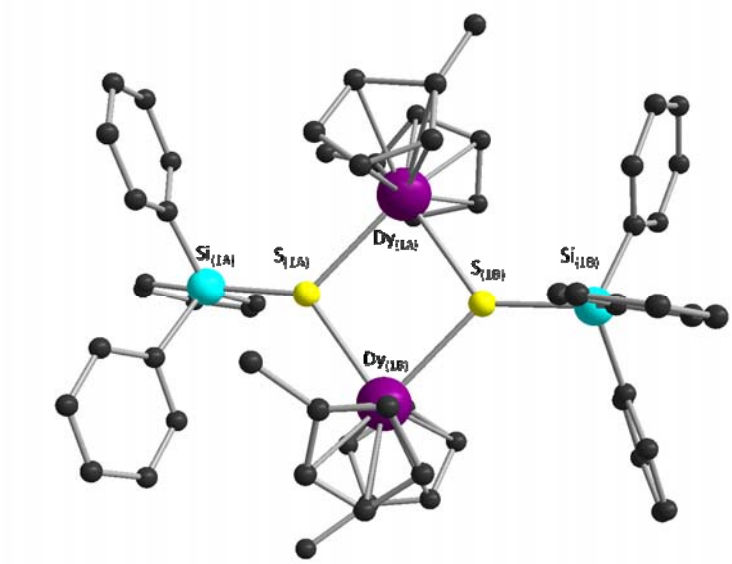

Figure 2.2 Molecular structure of **2.2**, with the hydrogen atoms omitted for clarity. Selected distances/Å and angles/°: $Dy_{(1A)}$-$S_{(1A)}$ 2.750(15), $Dy_{(1B)}$-$S_{(1B)}$ 2.776(16), $Dy_{(1A)}$-$C_{(1A)}$ 2.693(10), $Dy_{(1A)}$-$C_{(7A)}$ 2.666(6), $Dy_{(1A)}$-$C_{(10A)}$2.621(8), $S_{(1A)}$-$Si_{(1A)}$ 2.123(2), $Si_{(1A)}$-$C_{(13A)}$ 1.878(6), $Si_{(1A)}$-$C_{(19A)}$ 1.878(6), $S_{(1A)}$-$Dy_{(1A)}$-$S_{(1B)}$ 78.57(5), $Dy_{(1A)}$-$S_{(1A)}$-$Dy_{(1B)}$ 101.43(6), $Si_{(1A)}$-$S_{(1A)}$-$Dy_{(1A)}$ 129.50(8), $C_{(13A)}$-$Si_{(1A)}$-$C_{(19A)}$ 108.7(2), $C_{(13A)}$-$Si_{(1A)}$-$C_{(25A)}$ 103.1(3), $C_{(19A)}$-$Si_{(1A)}$-$C_{(25A)}$ 118.4(4), $S_{(1A)}$-$Si_{(1A)}$-$C_{(13A)}$ 111.19(18), $S_{(1A)}$-$Si_{(1A)}$-$C_{(19A)}$ 108.32(19), $S_{(1A)}$-$Si_{(1A)}$-$C_{(25A)}$ 107.0(3)

Table 2.1 Crystallographic data and summary of structural refinement for compounds **2.2** and **2.3.**

Empirical Formula	$C_{67}H_{56}Dy_2S_2Si_2$ (**2.2**)	$C_{67}H_{66}Gd_2S_2Si_2$ (**2.3**)
Formula Weight (g /mol^{-1})	1316.52	1306.02
Temperature (K)	100(2)	123(1)
Crystal System	Monoclinic	Monoclinic
Space Group	$P2_1/n$	$P2_1/n$
Colour	Colourless	Colourless
a (Å)	9.722(19)	9.7437(2)
b (Å)	18.864(4)	18.8921(6)
c (Å)	15.410(3)	15.4871(5)
α (deg)	90	90
β (deg)	96.55(3)	96.694(2)
γ (deg)	90	90
Volume (Å^3)	2807.8(10)	2831.41(14)
Z	2	2
ρ_{calcd}, (kg m^{-3})	1.557	1.532
R1 [I>2.0 σ(I)][a]	0.0400	0.0469
wR2 (all data) [a]	0.1183	0.1299

[a] $R1 = \Sigma (||F_0| - |F_c|| / \Sigma|F_0|)$. [b] $wR2 = [\Sigma[w(F_0^2 - Fc^2)^2] / \Sigma[w(F_0^2)^2]]^{1/2}$

Complex **2.2** crystallises in the centrosymmetric space group $P2_1/n$ as a dimeric compound, with a centre of symmetry, point group C_i. The molecular structure consists of two dysprosium atoms that are bridged by two $[\mu\text{-}Ph_3SiS]^-$ ligands, with each dysprosium atom being complexed by two terminal MeCp ligands, Figure 2.2. The Dy-S bridging bond lengths within complex **2.2**, are 2.750(15) Å and 2.776(16) Å, which results in a $Dy_{(1A)}\cdots Dy_{(1B)}$ separation of 4.277(8) Å. These bond distances are relatively consistent with expected Dy-S bond and Dy···Dy separation distances of those previously reported Dy-S bridging dimers, and are considered relatively long.[50,51] Furthermore, the Dy···Dy distance and Dy-S bonds will be of great significance when considering the extent of magnetic interaction between the Dy(III) ions within the core of this complex, (*vide infra*). The Dy-C distances of $Dy_{(1A)}$ and $Dy_{(1B)}$ are within the range of 2.599(15) Å- 2.670(11) Å, which are typical of dysprosium cyclopentadienides.[39] In addition, the dysprosium sites in complex **2.2** are formally eight coordinate, where the two central Dy(III) metals reside in pseudo-tetrahedral geometries with respect to the centroids of the MeCp ligands and the sulfur atoms, giving local C_2v symmetry at the lanthanide (considering the S-donor atoms and the centroids of the MeCp groups). The S-Si bonds are 2.123(2) Å for $S1_{(A)}$ and $S1_{(B)}$.

The bond angles between the two $[(MeCp)_2Ln]$ units and the bridging sulfur ligand, $Dy_{(1A)}\text{-}S_{(1A)}\text{-}Dy_{(1B)}$ and $Dy_{(1B)}\text{-}S_{(1B)}\text{-}Dy_{(1A)}$, are 101.43(6)˚ and complex **2.2** displays relatively obtuse bonding angles between $Si_{(1A)}\text{-}Dy_{(1A)}\text{-}S_{(1B)}$ and $Si_{(1A)}\text{-}Dy_{(1B)}\text{-}S_{(1A)}$

because of the presence of the sterically bulky phenyl groups residing on the silicon atom within the triphenylsilanethiolate ligand, giving an angle of 128.93(8)°.

The crystal structure of **2.3** containing the slightly larger Gd(III) than Dy(III), is essentially isostructural with that of **2.2**, and crystallises in the same centrosymmetric space group, $P2_1/n$, with a centre of symmetry, point group C_i (Table 2.1 gives the crystallographic data and summary of structural refinement for compound **2.3**), Figure 2.3. Both compounds were prepared under the same reaction conditions, with compound **2.3** also yielding colourless crystals from a saturated solution of toluene. The effect of the larger radius of the Gd(III) ion on the structure between compounds **2.2** and **2.3** is minimal. However, there are some noticeable differences. The $Gd_{(1A)}\cdots Gd_{(1B)}$ separation of 4.316(5) Å is marginally longer than that of Dy···Dy, suggesting there may be weaker electronic and magnetic interaction between the Gd(III) metal centres. The Gd-S bond distances are 2.775(14) Å and 2.796(15) Å, which are in the same range as those reported for compound **2.2**, taking into account the values of the standard deviations. In addition, the Gd-C bond length of $Gd_{(1A)}$ and $Gd_{(1B)}$ range between 2.622(14) Å and 2.707(14) Å, which again are slightly more extended than the Dy-C lengths observed in compound **2.2**. The bond angles that exist between $Gd_{(1A)}$-$S_{(1A)}$-$Gd_{(1B)}$ and $Gd_{(1B)}$-$S_{(1B)}$-$Gd_{(1A)}$ compare well to those of **2.2**, exhibiting almost the same angle of 101.53(5)° similarly with the bond angles between $Si_{(1A)}$- $S_{(1B)}$ -$Gd_{(1A)}$ and the $Si_{(1A)}$-$S_{(1A)}$ -$Gd_{(1B)}$, which give an angle of 129.1(7)°.

Although the geometric structures and chemical properties of a set of Ln(III) compounds are essentially the same, the different electronic structures of each makes the magnetic properties unique. Thurs, the effect of the spin-orbit coupling in Dy(III) is large, but is absent in Gd(III).

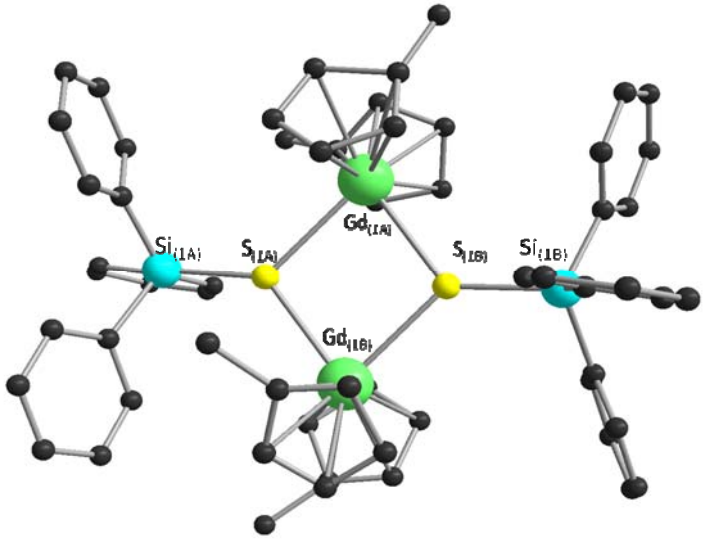

Figure 2.3 Molecular structure of **2.3**, with the hydrogen atoms omitted for clarity. Selected distances/Å and angles°: $Gd_{(1A)}$-$S_{(1A)}$ 2.775(14), $Gd_{(1B)}$-$S_{(1B)}$ 2.796(15), $Gd_{(1A)}$-$C_{(1A)}$ 2.707(14), $Gd_{(1A)}$-$C_{(7A)}$ 2.686(7), $Gd_{(1A)}$-$C_{(10A)}$ 2.637(8), $S_{(1A)}$-$Si_{(1A)}$ 2.124(2), $Si_{(1A)}$-$C_{(13)}$ 1.880(5), $Si_{(1A)}$-$C_{(19A)}$ 1.867(5), $Si_{(1A)}$-$C_{(25A)}$ 1.883(14), $S_{(1A)}$-$Gd_{(1A)}$-$S_{(1B)}$ 78.47(4), $Gd_{(1A)}$-$S_{(1A)}$-$Gd_{(1B)}$ 101.53(4), $Si_{(1A)}$-$S_{(1A)}$-$Gd_{(1A)}$ 129.11(7), $C_{(13A)}$-$Si_{(1A)}$-$C_{(19A)}$ 108.8(2), $C_{(13A)}$-$Si_{(1A)}$-$C_{(25A)}$ 103.2(4), $C_{(19A)}$-$Si_{(1A)}$-$C_{(25A)}$ 118.4(4), $S_{(1A)}$-$Si_{(1A)}$-$C_{(13A)}$ 110.86(17), $S_{(1A)}$-$Si_{(1A)}$-$C_{(19A)}$ 107.95(19), $S_{(1A)}$-$Si_{(1A)}$-$C_{(25A)}$ 107.6(4)

2.2.2 Magnetic Studies for Compounds 2.2 and 2.3

2.2.2.1 d.c. and a.c. Magnetic Susceptibility Measurements

Direct current (d.c.), magnetic susceptibility measurements were conducted on polycrystalline samples of compounds **2.2** and **2.3** in a temperature range of 1.8-300 K in an applied field of 1 kG. SQUID measurements were conducted by the University of Manchester EPR/ SQUID service.

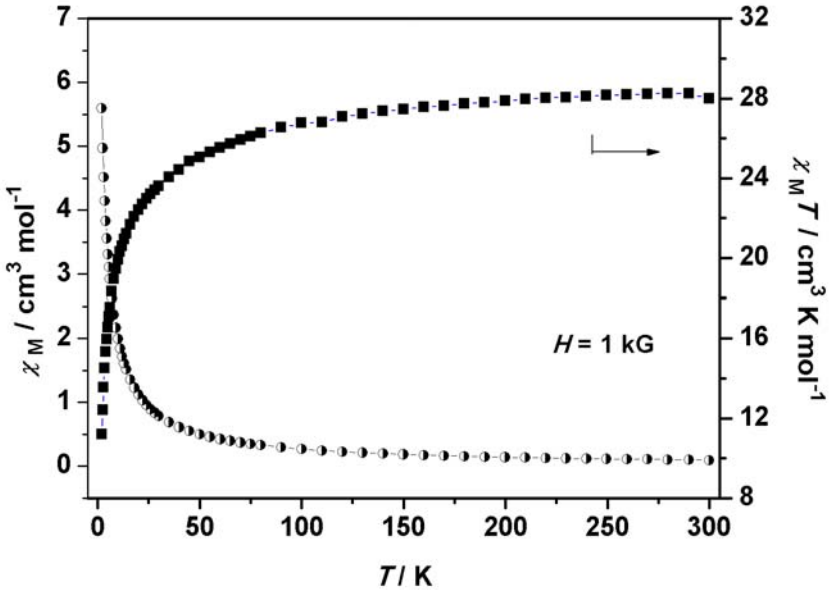

Figure 2.4 Magnetic data plot showing the temperature dependence of χ_M and $\chi_M T$ for compound **2.2** for the field strength *H = 1 kG*

The d.c. $\chi_M T$ (where χ_M is the molar magnetic susceptibility) value of 27.9 cm^3 K mol^{-1} at 300 K is in good agreement with the expected value of 28.34 cm^3 K mol^{-1} for two non-interacting dysprosium(III) ions (S = 5/2, L = 5, J = 15/2, g = 4/3; ground term symbol $^6H_{15/2}$). Subjected to cooling, $\chi_M T$ decreases gradually, then more

dramatically below 70 K until reaching 11.2 cm^3 K mol^{-1} at 2 K. This decline of $\chi_M T$ with T is primarily a result of crystal field effects (i.e. thermal depopulation of the Dy(III) Stark sub levels of the term, $^6H_{15/2}$) giving weak antiferromagnetic exchange, Figure 2.4.

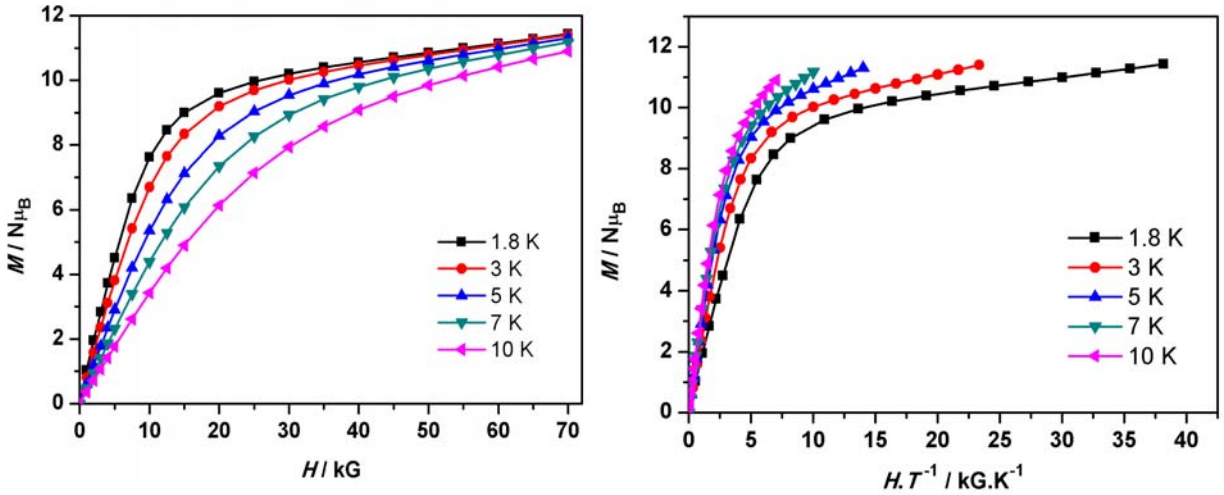

(a) (b)

Figure 2.5 *M vs. H* data plot (a) and *M* vs. *H/T(b),* at varying temperatures between 1.8 K and 10 K, for compound **2.2.**

The magnetisation versus field data plot for compound **2.2**, Figure 2.5 (a), indicates that below 10 K there is a rapid increase in magnetisation at low magnetic field. At a higher magnetic field the magnetisation increases linearly, approaching ~ 11.4 $N\mu_B$, without showing clear saturation up to a field of approximately 70 kG, which suggests large magnetic anisotropy within this compound i.e. the presence of low lying excited states due to an increase in spin state density. This is further supported by a non-superposition on a single master-curve of *M* versus *H/T,* Figure 2.5 (b).

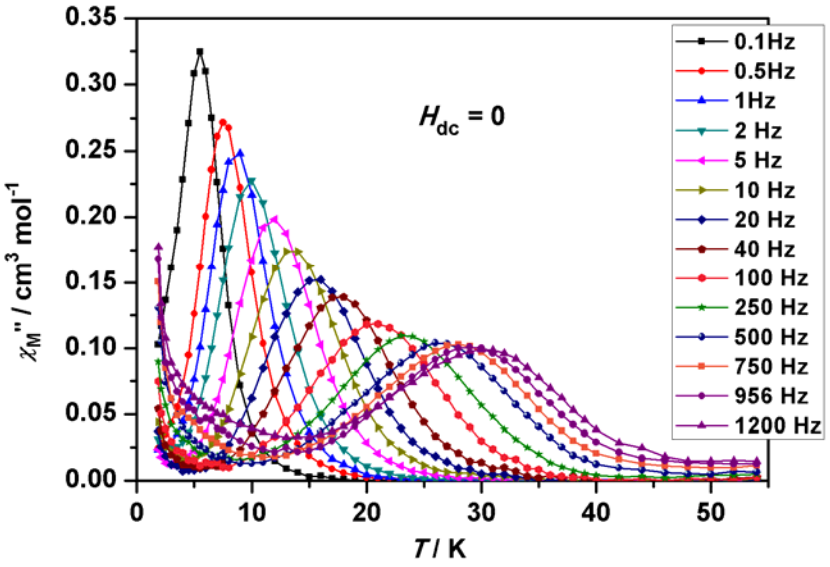

(a)

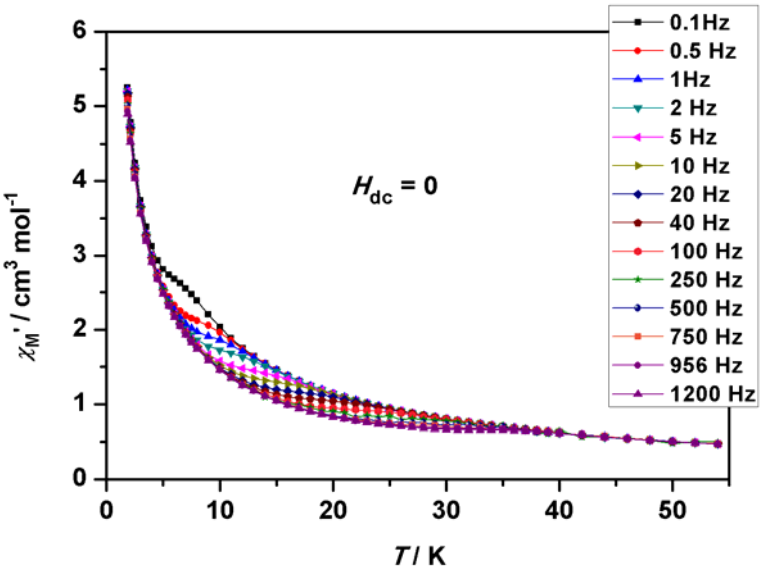

(b)

Figure 2.6 Out-of-phase (χ_M'') (a) and in-phase (χ_M') (b), χ_M vs T data plots for compound **2.2** at different frequencies between 0.1 and 1200 Hz in an oscillating field of 1.55 G.

From the low temperature a.c. (alternating current), magnetic susceptibility data plots illustrated in Figure 2.6, it is clear there are frequency dependent maxima below 32 K in both the in-phase (χ_M') and out-of phase (χ_M'') components of susceptibility recorded with zero-d.c. field, indicating slow relaxation of magnetisation, i.e. SMM behaviour.

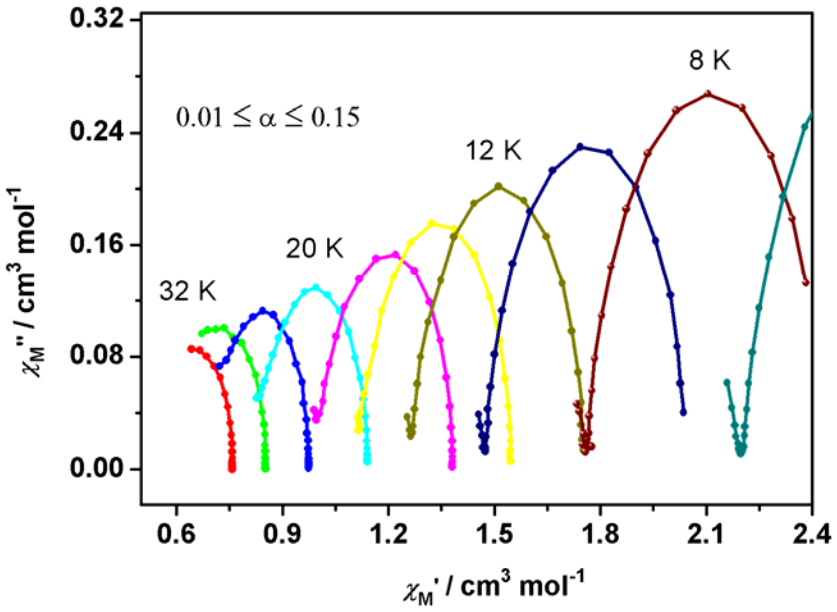

Figure 2.7 Cole-Cole plot based on the a.c. susceptibility measurements of **2.2** between 8 and 32 K. The solid lines travelling through the experimental values represent best fits.[7b]

Figure 2.7 illustrates Cole-Cole data plots (χ_M'' versus χ_M'), at fixed temperatures between 8 K and 32 K with a zero applied d.c.-field and an a.c.-magnetic field of 1.55 G, oscillating at frequencies between 0.1 and 1200 Hz. The solid lines are a best fit from a generalised Debye model, with α parameters $0.01 \leq \alpha \leq 0.15$, which indicates a narrow distribution of relaxation times (τ).[26g,52] Magnetisation relaxation times can be observed from a plot of the a.c. data as ln τ versus $1/T$, Figure 2.8. Form Figure

2.8, it is apparent that 20 K is the temperature above which the relaxation process becomes thermally activated and the data above 20 K obey the Arrhenius law $\tau = \tau_0$ *exp* ($\Delta E/K_B T$) with ΔE = 192 ± 5 K (or U_{eff} = 133 ± 3.5 cm^{-1}) and $\tau_0 = 2.38 \times 10^{-7}$ s, where ΔE is the energy barrier for relaxation of the magnetisation and τ_0 is the pre-exponential.

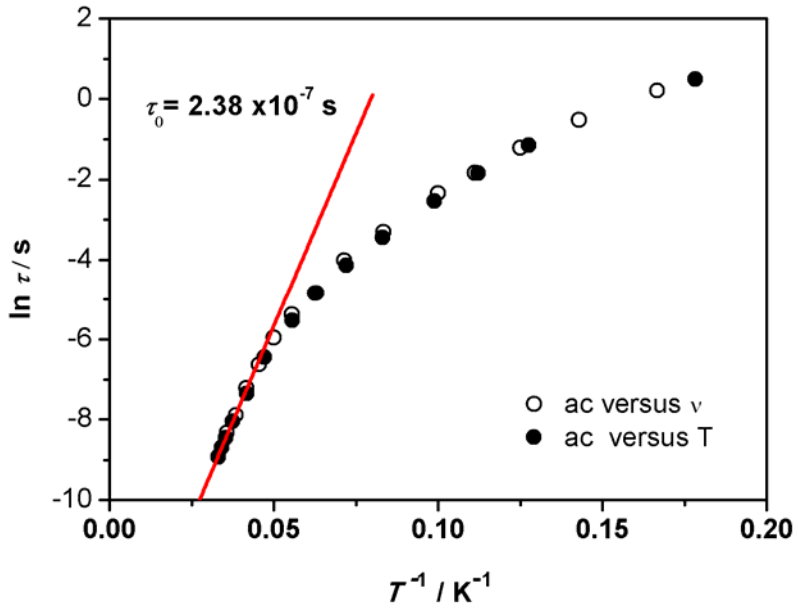

Figure 2.8 Magnetization relaxation time (τ) versus T^{-1} for **2.2** under zero static field, from data collected in frequency (opaque dots) and temperature (transparent dots), variation regimes and best fit to the Arrhenius law of the thermally activated regime (solid red line).

The energy barrier of **2.2** is one of the largest reported for a polymetallic lanthanide compound, surpassing that of the compound **1.17** (Section **1.8**), previously reported by the Layfield group,[39] although still lower than that observed for monometallic $[Pc_2Tb]^-$, **1.8**[14,15] and Murugesu and co-workers, **1.12**.[34,40]

Compound **2.3** exhibits weak antiferromagnetic exchange coupling between the Gd(III) ions through the bridging [μ-SSiPh$_3$] ligands, which is in good agreement with that expected for exchange coupled gadolinium compounds, stemming from the apparent core-like character of the valence 4*f* orbitals. The $\chi_M T$ value of 15.5 cm^3 K mol^{-1} at 300 K, is in good agreement with the expected value for two non-interacting Gd(III) free ions of 15.75 cm^3 K mol^{-1} (S = 7/2, L = 0, J = 7/2, g = 2; ground term symbol $^8S_{7/2}$).[53] The value of $\chi_M T$ remains steady, showing no signs of decreasing until a sharp decrease at 30 K from which point the $\chi_M T$ value reaches 6.7 cm^3 K mol^{-1} at 2 K, Figure 2.9.

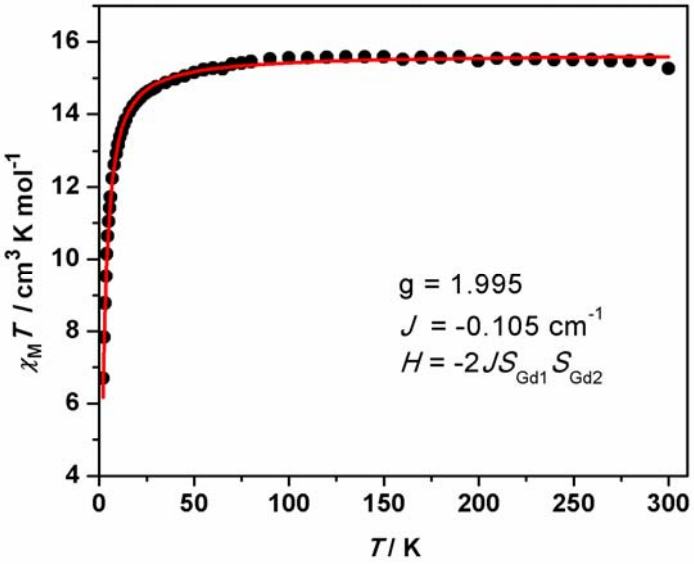

Figure 2.9 Temperature dependence $\chi_M T$ for compounds **2.3**, where the red line is the theoretical fit of the experimental data using the magnetic parameters shown in the data.

The relatively long Gd···Gd distance of **2.3** results in the weakly antiferromagnetic interaction observed in Figure 2.9. In the Gd(III) ion, the spin–orbit coupling effect is absent in the first order for the $^8S_{7/2}$ ground state of the 4f^7 core, as a result, this allows for the exchange coupling J to be readily determined, Figure 2.9.

The magnetisation versus field data plot for compound **2.3** is illustrated in Figure 2.10, where the magnetisation appears to saturate at 2 K. However, there is no evidence of slow relaxation down to 1.8 K, as there was no out-of-phase signal observed in the a.c. magnetic susceptibility.

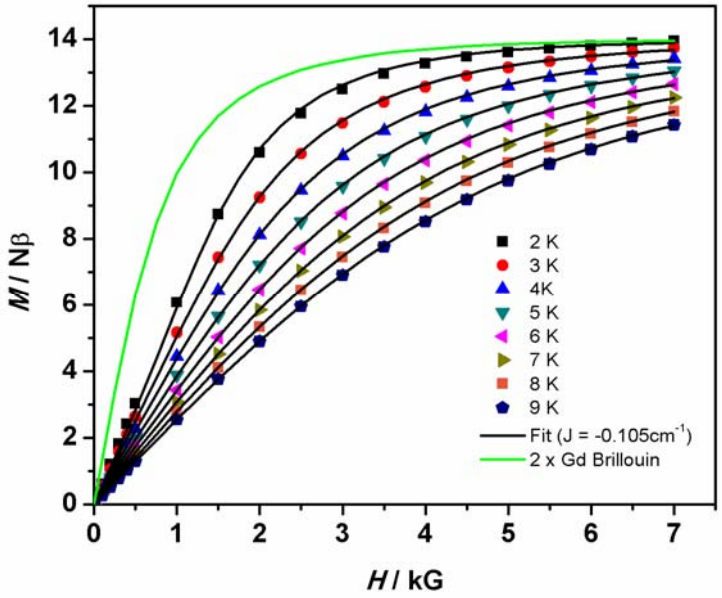

Figure 2.10 Magnetisation vs. field data plot at varying temperatures between 2 K and 9 K, for compound **2.3.** The solid green line represents the Brillouin function for two non-interacting Gd(III) ions.

To gain further insight into the origin of the barrier reversal of magnetisation the magnetisation reversal of compound (**2.2**), *ab initio* calculations,[54] were conducted using MOLCAS 7.6,[55] and compared against other known SMMs that exhibited structures closely related to that of **2.2**, (compounds $(Cp_2Dy(\mu\text{-}Cl)]_n$(**2.4**) and $[Cp_2Dy(thf)(\mu\text{-}Cl)]_2$(**2.5**)).[39,56a] The calculations can be found in Appendix 1, and it must be emphasised that these studies were carried out in collaboration with Prof. L. Chibotaru, based at the University of Leuven, Belgium. Studies on the local

magnetic properties on individual Dy(III) ions were computed using the Single_Aniso module,[57] while the magnetic properties of the dimers were simulated by the Poly-_Aniso method.[58] Through subsequent analysis of these complex data, it may become possible to postulate further as to why there are significant variations between the barrier to reversal of magnetisation of these compounds, when there are seemingly close structurally and chemically.

Furthermore, these compounds highlight the importance of symmetry in the context of magnetism. Crystal field effects are generally more of a minor contribution when compared to the large effect of the spin orbit coupling energy in the context of the overall electronic structure of **2.2** and **2.3**. However, in this context, the interaction of the ground spin orbit coupled *J* state with the crystal field generates the magnetic anisotropy barrier separating opposite orientation of the spin ground state (Chapter One; Section 1.6). Therefore, the symmetry at the individual Ln sites of **2.2** is of great importance in determining the observed U_{eff} value. Hence, the large separation in the crystal field for compounds such as **2.2**, is a significant contribution to the large energy barrier experienced be **2.2**, (Appendix One).

2.3 Conclusions

Following the isolation of the novel lithiated sulfur-bridging ligand, **2.1**, lithium triphenylsilylthiolate, successful attempts to isolate isostructural sulfur-bridged compounds $[(MeCp)_2Dy(\mu\text{-}SSiPh_3)]_2$ (**2.2**) and $[(MeCp)_2Gd(\mu\text{-}SSiPh_3)]_2$ (**2.3**) were achieved. Although the general structural motif that represents these compounds, $[Cp'Ln(\mu\text{-}E)]_2$ (Cp' = Cp, MeCp) is not uncommon across the lanthanide series,[7] those bridged by soft donor ligands are quite rare. Compounds **2.2** and **2.3** incorporate lanthanides that reside in towards the end of the lanthanide series and so formal coordination numbers of eight are observed because of the slightly smaller radii of these elements. The synthesis of these highly reactive and air sensitive compounds confirms the ability to utilise soft donor ligands in combination with lanthanide(III) precursors in order to achieve enhanced magnetic and electronic communication between the ligands and the core metal centres. The existence of the lanthanide contraction naturally results in the decrease in Ln-S and Ln-C bonds along the series of lanthanides. However, the bond lengths for **2.2** and **2.3** give virtually the same values. It is clear from both the structural analysis and the magnetic data that consideration for the symmetry aspects which reside within both compound **2.2** and **2.3**, should be significantly employed, when determining responsible factors for observed values of slow reversal of magnetization. Since Gd(III) ions make no orbital angular momentum contribution, $L = 0$, which makes compound **2.3** an ideal counterpart to **2.2** to highlight the intrinsic magnetic characteristics of **2.2**.

Furthermore, compound **2.2** is currently the only reported dimetallic sulfur-bridged SMM.[56b]

Chapter Three

Monometallic Lanthanide(III) Alkoxide Chemistry

3.1 Introduction to Lanthanide Alkoxide Chemistry

Alkoxide ligands and their derivatives are very significant in the context of inorganic chemistry because of their ability to form strong metal-oxygen bonds in addition to a flexible organic moiety, which result in variations in solubility and in steric and electronic factors.[59] Over the past two decades there has been significant interest into incorporating these ligands within lanthanide compounds. Progressively over this time lanthanide alkoxide reagents have become established in organic synthesis,[60] whereby utilising these reagents as well-defined monometallic precatalysts and catalytically active species allows for enhanced facilitation of the synthetic process in question. Furthermore, the kinetic liability of the Ln-O(R) bond within these compounds can be significantly beneficial within these catalytic transformations and are considered to be a more robust alternative to cyclopentadienide complexes in the context of catalysts.[59,60] Due to the inherent chemical properties of both the lanthanide cations and the alkoxide ligand, prospective synthesis encompassing lanthanide alkoxides has been known to prove at times challenging, albeit these reactions offer an array of promising applications, especially in the development of monomeric lanthanide alkoxides.[59b,61] A significant disadvantage of these reactions is their susceptibility to oligomerize, as a result of the 'large' oxophillic lanthanide metal reacting with common R-OH (R = alkyl groups) alcohols. Alkoxides tend to behave as bridging ligands and the extent of oligomerization depends on the bulk of the coordinating OR-ligand. Moreover, the electronic properties of the ligand also contribute to the degree of oligomerization.

To highlight this, Figure 3.1 illustrates a series of alkoxide ligands in order of increasing pK_a value, which is generally directly proportional to the susceptibility towards hydrolysis of the resulting alkoxide complex in question.[59a,62]

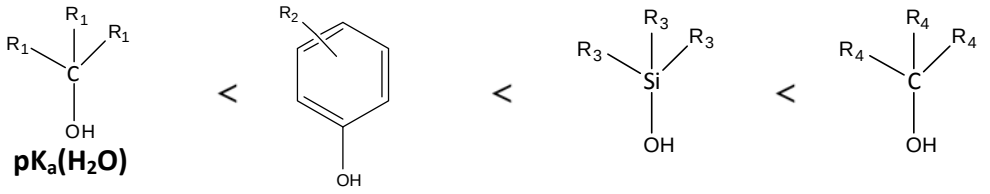

$pK_a(H_2O)$	5.4	10.0	13.6	18
	$R_1 = CF_3$	$R_2 = H$	$R_3 = Et$	$R_4 = {}^tBu$

Figure 3.1 Illustration of the progressive increasing pK_a values for common alkoxide and siloxide pro-ligands.[59a]

The lanthanide alkoxides derived from less bulky alkoxide ligands such as methanol or ethanol are commonly insoluble oligomeric substances and their structures are undetermined.[59b] In contrast, bulkier alkoxide ligands incorporating O*i*Pr and O^{t}Bu groups generally exhibit pentametallic or trimetallic species, respectively.[63,64] Often, additional co-ligands are incorporated, depending on the method of preparation, leading to the presence of O^{2-}, OH^- (derived from H_2O ligands), or Cl^- (from LnX_3 precursors) ions, which results in high coordination numbers for the metal, hence forming robust clusters.

There has been a significant number of reports on sterically hindered siloxide ligands where the strong silicon-oxygen bond is kinetically stable with respect to Si-O bond cleavage.[65-68] Furthermore, the lower basicity of siloxide ligands prevents undesired bridging modes. It is as a result of these inherent properties of the siloxy ligand has led to this derivative of alkoxide being the main focus of this Chapter (Figure 3.2).

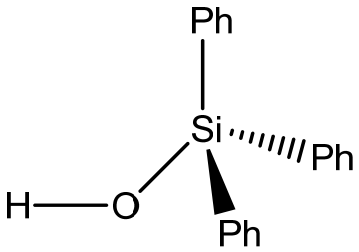

Figure 3.2 Triphenylsilanol pro-ligand, exhibiting moderate basicity and therefore allows for a more labile O-H bond.

3.1.2 Synthetic Routes to Lanthanide Alkoxides.

There is a range of synthetic routes to preparing lanthanide(III) alkoxides. Generally these reactions incorporate a variety of anionic ligands such as alkoxides, halides or amides. There is a number of synthetic routes that have been reported utilising Ln metal (Ln^o) with excess alcohol (HOR) in the presence of $HgCl_2$ [1,69,70] or $Hg(C_6F_5)_2$[71-74] as widely used catalysts to clean the metal surface and to facilitate the reaction (Scheme 3.1).[1,69,70] The reaction proceeds once the metal is activated to form the alkoxide complex as a result of incorporating the alcohol (Scheme 3.1). Reactions of

this nature can take place with a variety of alcohols; however *iso*-propanol ($HOCHMe_2$) is a common preference for these reactions, in order to achieve solubility and remove the salt residue. Furthermore, this synthetic methodology can be used to synthesise lanthanide aryloxide ($Ln(OAr)_3$).[71-77]

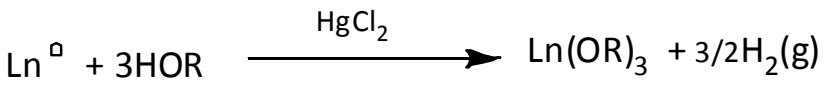

Scheme 3.1 Scheme illustrating lanthanide metal alcoholysis using a catalyst.

When the initial $Ln(OR)_3$ precursor is commercially available alcoholysis can occur by a protonolysis exchange reaction, Scheme 3.2. However, the low solubility of the lanthanide species makes this route disadvantageous. As a result, the extent of ligand substitution is entirely dependent on the reaction conditions. Utilising a slight excess of alcohol or applying moderate heating may facilitate the proton exchange needed to complete the reaction, but can give inconsistent results.[59]

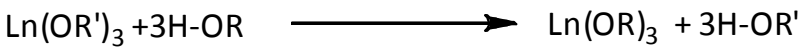

Scheme 3.2 General scheme for a lanthanide protonolysis exchange reaction.

Another frequently utilised synthetic route to generating lanthanide alkoxide complexes, involves halide metathesis, usually in the form of LnX_3 (X = Cl, Br, I).[2,78-82] The use of these halide complexes in their anhydrous form is favourable in order to

prevent the possibility of side reactions. Scheme 3.3 illustrates the typical metathesis for alkoxides utilising halide lanthanide precursors and alkali metal alkoxides. However, the insolubility of the lanthanide chloride in most solvents can be counteracted by exploiting the synthetic methodology illustrated in Scheme 3.4. In this instance ammonia gas is condensed onto the LnX_3 precursor in order to achieve dissolution, which is followed by the addition of the required alkali metal (A^o) and the necessary alcohol. In practice, this type of metathesis is exclusive to generating aryloxy derivatives, because less bulky alkyl substituted groups can lead to the incorporation of the alkali metal into the product.

$$LnX_3 + 3M'(OR) \longrightarrow Ln(OR)_3 + 3M'X$$

Scheme 3.3 A scheme to illustrate the formation of lanthanide alkoxides utilising lanthanide halide precursors.

$$LnX_3 + 3A^{\circ} \xrightarrow[-3AX]{NH_3/-78^{\circ}} Ln(NH_2)_3 \xrightarrow[-3H_2N]{3HOAr/tol} Ln(OAr)_3$$

Scheme 3.4 A scheme to show the formation of *aryl*-oxides utilising ammonia gas and lanthanide halide precursors.

The process of amide alcoholysis for the formation of lanthanide alkoxides is regarded as the most versatile route. The tris-amido $Ln(NR_2)_3$ complex, which is formed from the halide, illustrated in Scheme 3.5, proceeds to react with the excess

alcohol to form the alkoxide.[59b,83,84] In general, alkali metal amides, ANR_2 (where A = alkali metal, R = $SiMe_3$), are utilised prolifically in this area owing to their ability to preserve the monomeric characteristics of the lanthanide amide precursor. The crystallographic structure of the $Ln(NR_2)_3$ typically exhibits a distorted trigonal planar geometry with a variety of silyl amide ligands.[85-86] The exchange process that takes place once the lanthanide amide is formed occurs readily in a number of solvents and the reaction is generally conducted at low temperature.

$$LnX_3 + 3ANR_2 \longrightarrow Ln(NR_2)_3 + 3AX$$

$$Ln(NR_2)_3 + 3H\text{-}OR \longrightarrow Ln(OR)_3 + 3H\text{-}NR_2$$

Scheme 3.5 A scheme to show the formation of lanthanide alkoxides from lanthanide amide precursors.

With regard to the nature of the bonding within complexes that have the general structural motif $[Ln(OR)_x]_n$, the lone pairs of electrons on the substituted oxygen allows for the stabilisation of a range of binding modes. This can range from terminal, doubly bridging, triply bridging and the exceptionally rare quadruply bridging interactions, which in turn have an influence of the amount of steric and electronic saturation at each metal centre present. In addition, substituted aryl groups that are incorporated into lanthanide alkoxide complexes lead to unexpected π-interactions assisted by the presence of aromatic rings. Monometallic complexes can be stabilised by an array of bulky alkoxides where they generally possess

trigonal planar, tetrahedral, trigonal bipyramidal and octahedral coordination ligand geometries encompassing the metal. Monometallic lanthanide alkoxide complexes exhibiting octahedral geometry will be the main feature within this chapter.[87]

3.1.3 Lanthanide(III) Siloxide Compounds.

Prolific in the field of monometallic lanthanide(III) alkoxide compounds and their derivatives, is the work of Evans and co-workers, particularly throughout the early to mid-nineties.[86-88] In their attempts to expand the ever increasing family of monometallic lanthanide(III) alkoxide compounds, silylamide precursors were predominantly utilised because of the flexibility of this route. As the steric requirements of lanthanide silylamide precursors are significantly reduced when compared to that of precursors incorporating the Cp ligand, this synthetic route was favoured as it allows for the isolation of alkoxide compounds accommodating much bulkier ligands. These include sterically hindered siloxide ligands such as the triphenylsiloxide pro-ligand (Figure 3.2). Evans and co-workers were the first to report on the synthesis of the oxygen bonded tris-siloxide, tris-THF complexes of lanthanum, cerium and yttrium adopting an octahedral geometry, $[Ln(OSiPh_3)_3(THF)_3](THF)$, outlining two synthetic routes. The first route exploits anhydrous nitrates as ideal precursors to derive the homoleptic siloxy complexes, Scheme 3.6(a). The other route utilises a lanthanide oxo-alkoxide precursor, formed

from a nitrate, which in turn reacts with the siloxy ligand in order to produce the octahedral lanthanide siloxide complex, Scheme 3.6(b).

$$(NH_4)_x\,Ln(NO_3)_{3+x} + (3+x)\,NaOSiPh_3(THF) \xrightarrow{THF} [Ln(OSiPh_3)_3(THF)_3](THF) + (3+x)\,NaNO_3 + xHOSiPh_3 + xNH_3 \quad \text{(a)}$$

$$Y_5(OiPr)_{13}O + \text{excess } HOSiPh_3 \xrightarrow{THF} [Y(OSiPh_3)_3(THF)_3](THF) + HO\textit{i}Pr \quad \text{(b)}$$

Scheme 3.6 Scheme displaying the two synthetic routes adopted by Evans to produce the $[Ln(OSiPh_3)(THF)_3](THF)$. The production of the precursor $(NH_4)_xLn(NO_3)_{3+x}$ is outlined in the literature.[88]

Ln = Ce (**3.1**), Ln (**3.2**), Yt (**3.3**)

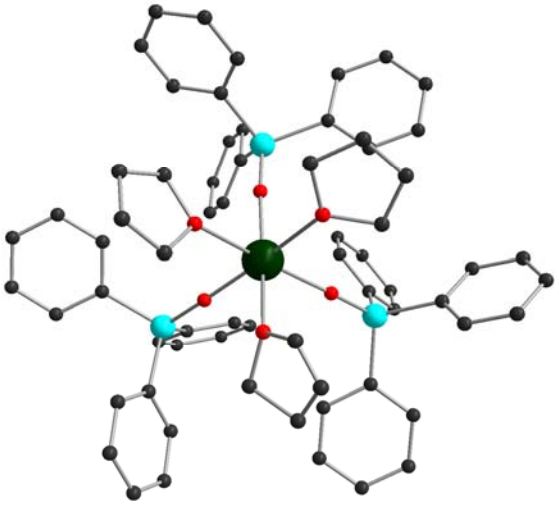

Figure 3.3 Structure representing the lanthanide siloxide complex with the general formula, $[Ln(OSiPh_3)(THF)_3](THF)$.

The synthesis of a series of monometallic lanthanide compounds with the general formula [Ln(OSiPh$_3$)(THF)$_3$], (Figure 3.3) will form the basis of this chapter with the extensive analysis of their optical properties and magnetochemistry.

3.1.4 Introduction

When considering the reaction of organometallic precursors, such as the lanthanide metallocenes reported in Chapter Two, with triphenylsilanol, (which is analogous to the triphenylsilanethiol pro-ligand before lithiation), it was assumed that directly analogous compounds to those of **2.1** and **2.2** were to be made. The preliminary aims proposed for the reaction of [Ln(MeCp)$_3$] with Ph$_3$SiOH, were to synthesise a series of oxygen-bridged dimetallic lanthanide metal complexes to accompany the compounds reported in Chapter Two, and exhibiting the expected general formula [(MeCp)$_2$Ln(μ-OSiPh$_3$)]$_2$ (Ln = Dy, Gd). However, upon the initial reaction of [Er(MeCp)$_3$] with Ph$_3$SiOH in THF, followed by [Dy(MeCp)$_3$] and [Gd(MeCp)$_3$], under the same reaction conditions, monometallic complexes of [Ln(OSiPh$_3$)(THF)$_3$](THF) were consistently produced. The formation of all three compounds displaying the same conformation suggests that replacing the sulfur atom for oxygen within the pro-ligand Ph$_3$SiOH directly affects the co-ordination chemistry of these compounds. Subsequently a family of monometallic triphenylsiloxy lanthanide complexes was produced, [Ln(OSiPh$_3$)(THF)$_3$] (Ln = Dy(**3.4**), Er(**3.5**), Ho(**3.6**), Gd(**3.7**), Tb(**3.8**)), along with analysis of their magnetic and electronic properties.

3.2. Results and Discussion

3.2.1 Synthesis and Structure of Monometallic Lanthanide(III) Siloxide Complexes.

Two novel synthetic routes were undertaken in order to derive the monometallic lanthanide siloxide complexes described in Section 3.1.4, which are outlined in Scheme 3.7. Scheme 3.7(a) illustrates the utility of an organometallic precursor, whilst Scheme 3.7 (b) details a more traditional route.

$$(MeCp)_3Ln + 3Ph_3SiOH \xrightarrow[THF]{RT} [Ln(OSiPh_3)_3(THF)_3](THF) + 3CpMeH \quad \text{(a)}$$

Ln = Dy, Er, Gd

$$LnCl_3 + 3Ph_3SiOH \xrightarrow[THF]{3NaO^tBu \quad \Delta} [Ln(OSiPh_3)_3(THF)_3](THF) + 3NaCl + 3HO^tBu \quad \text{(b)}$$

Ln = Dy (**3.4**), Er (**3.5**), Ho (**3.6**), Gd (**3.7**) Tb (**3.8**)

Scheme 3.7 Scheme to show the synthesis of $[Ln(OSiPh_3)(THF)_3](THF)$ compounds utilising the organometallic precursor methylcyclopentadienyl lanthanide(a). Scheme to show the synthesis of $[Ln(OSiPh_3)(THF)_3](THF)$ from lanthanide halides (b).

Both the methylcyclopentadienyl ligand and the sodium *tert*-butoxide proved effective Lewis bases for the deprotonation of the siloxide ligand. However, in a one-pot synthesis, upon reflux in THF, the synthetic method outlined in Scheme 3.8 proved a much more direct route, without having to synthesise each of the lanthanide MeCp precursors prior to the conducting the desired reaction, because the lanthanide chlorides used are commercially available. All the reactions were carried out under strict anaerobic conditions, using Schlenk line techniques to produce yields ranging between 21-55 %. Contrasting colours across compounds **3.4**-**3.8** were observed. Compound **3.4** produced yellow single crystals, **3.5** and **3.6** gave pale pink and deep pink crystals respectively and compounds **3.7** and **3.8** both provided colourless crystals, all of which were suitable for X-ray crystallography. The crystallographic data clearly account for the addition lattice THF, (Table 3.1). However upon rigorous drying of these crystals *in vacuo* the THF in the lattice is consequently removed, revealing an apparent C_{3v}, pseudo three-fold symmetry (*vide infra*). Crystal structures for compounds **3.4**-**3.8** were constructed by X-ray crystallography, and accompanied by good elemental analysis, with all five compounds crystallising in the non-centrosymmetric space group $P2_1$. The six bonded oxygen ligands construct *fac*-octahedral geometry, from three bonded THF molecules and three triphenylsilyl groups. Compared with compounds **2.2** and **2.3**, monometallic complexes **3.4**-**3.8**, are moderately stable when subjected to air or moisture. This is most likely due to the presence of oxygen as part of the coordinating ligands within these compounds, as opposed to sulfur, which makes

these compounds inherently more stable. Since compounds **3.4**-**3.8** are all isostructural; a common analysis of their structures is permitted, illustrated in Figures 3.4 through to Figure 3.8 along with the relevant bond lengths and angles.

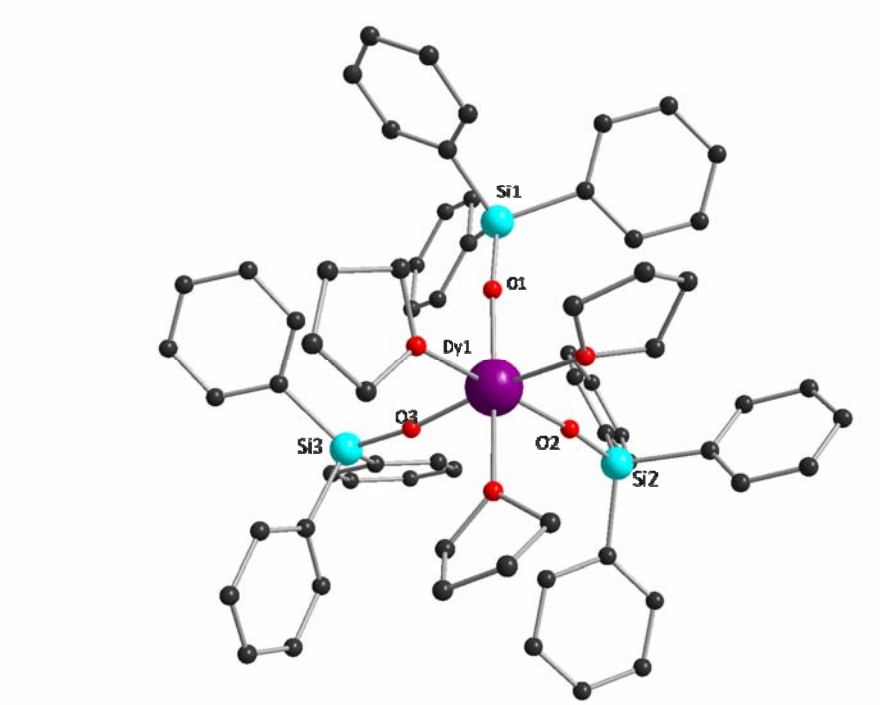

Figure 3.4 Molecular structure of **3.4**, with the hydrogen atoms omitted for clarity. Selected distances/Å and angles°: Dy1-O1 2.138(5), Dy1-O2 2.133(4), Dy1-O3 2.124(4), Dy1-O4 2.467(5), Dy1-O5 2.429(5), Dy1-O6 2.453(5), Si1-O1 1.603(5), Si2-O2 1.595(4), Si3-O3 1.596(4), O1-Dy1-O3 101.27(19), O1-Dy1-O2 101.38(18), O3-Dy1-O2 101.37(17), O1-Dy1-O5 90.1(2), O3-Dy1-O5 87.03(17), O2-Dy1-O5 164.00(18), O1-Dy1-O6 164.2(2), O3-Dy1-O6 90.61(19), O2-Dy1-O6 86.16(17), O5-Dy1-O6 80.1(2), O1-Dy1-O4 85.47(19), O3-Dy1-O4 166.69(16), O2-Dy1-O4 88.36(17), O5-Dy1-O4 81.45(17), O6-Dy1-O4 80.91(19), O1-Si1-C1 110.2(3), O1-Si1-C7 112.7(3), O1-Si1-C13 110.5(3), O2-Si2-C25 112.1(3), O2-Si2-C31 111.0(3), O3-Si3-C37 110.6(3), O3-Si3-C43 110.8(3), O3-Si3-C49 110.1(3).

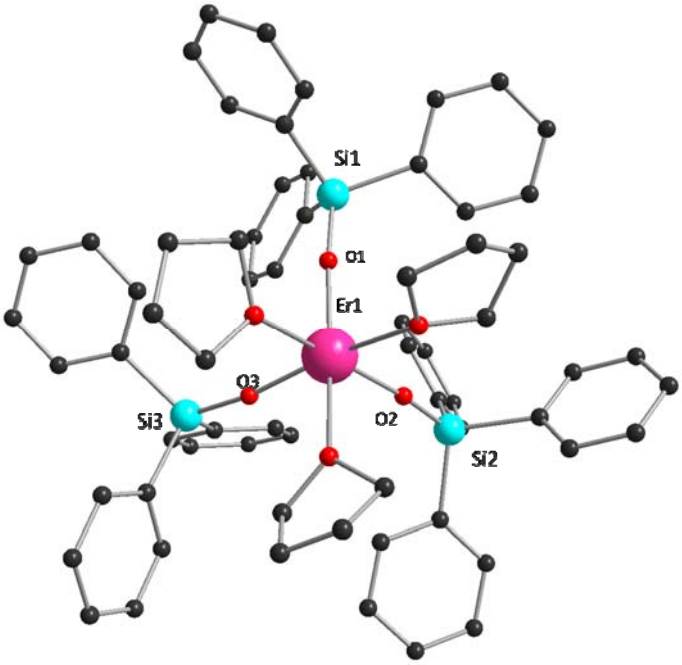

Figure 3.5 Molecular structure of **3.5**, with the hydrogen atoms omitted for clarity. Selected distances/Å and angles°: Er1-O1 2.080(19), Er1-O2 2.071(19), Er1-O3 2.11(2), Er1-O4 2.43(2), Er1-O5 2.34(2), Er1-O6 2.41(2), Si1-O1 1.65(2), Si2-O2 1.65(2), Si3-O3 1.56(2), O1-Er1-O3 100.8(8), O1-Er1-O2, 101.7(8), O3-Er1-O2 100.8(8), O1-Er1-O5 90.0(8), O3-Er1-O5 86.4(8), O2-Er1-O5 165.8(7), O1-Er1-O6 164.4(8), O3-Er1-O6 90.8(8), O2-Er1-O6 86.5(7), O5-Er1-O6 80.3(8), O1-Er1-O4 87.0(8), O3-Er1-O4 166.8(8), O2-Er1-O4 89.5(8), O5-Er1-O4 83.0(8), O6-Er1-O4 79.7(8), O1-Si1-C1 110.4(12), O1-Si1-C7 113.5(11), O1-Si1-C13 108.7(11), O2-Si2-C25 110.3(10), O2-Si2-C31 108.8(11), O3-Si3-C37 112.3(11), O3-Si3-C43 112.6(11), O3-Si3-C49 112.3(12).

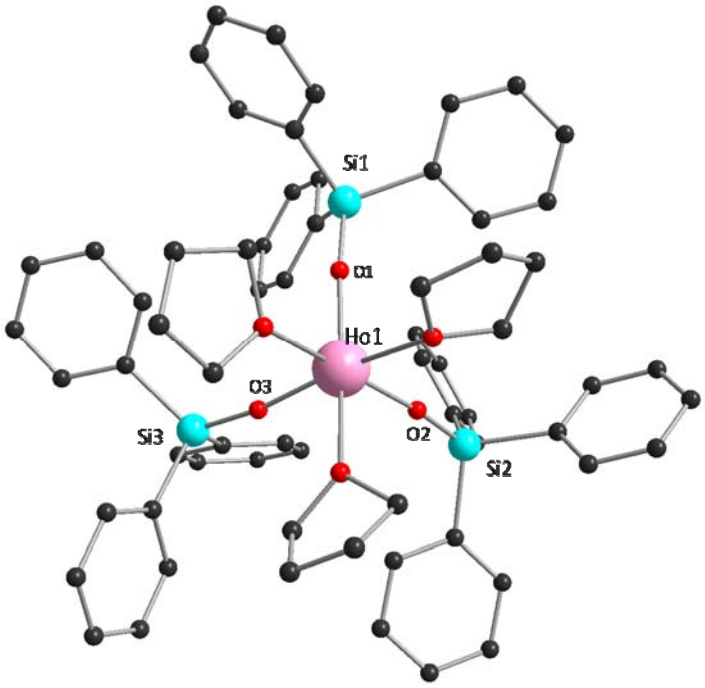

Figure 3.6 Molecular structure of **3.6**, with the hydrogen atoms omitted for clarity. Selected distances/Å and angles°: Ho1-O1 2.092(13), Ho1-O2 2.11(1), Ho1-O3 2.094(11), Ho1-O4 2.476(12), Ho1-O5 2.383(12), Ho1-O6 2.418(12), Si1-O1 1.623(14), Si2-O2 1.581(10), Si3-O3 1.587(12), O1-Ho1-O3 101.4(4), O1-Ho1-O2, 100.9(4), O3-Ho1-O2 100.2(4), O1-Ho1-O5 89.8(5), O3-Ho1-O5 88.2(4), O2-Ho1-O5 164.7(4), O1-Ho1-O6 164.5(5), O3-Ho1-O6 90.4(4), O2-Ho1-O6 86.8(4), O5-Ho1-O6 80.4(5), O1-Ho1-O4 85.8(4), O3-Ho1-O4 166.4(4), O2-Ho1-O4 89.7(4), O5-Ho1-O4 89.7(4), O6-Ho1-O4 80.7(4), O1-Si1-C1 (1) 110.3(7), O1-Si1-C7 112.6(7), O1-Si1-C13 109.2(7), O2-Si2-C25 110.9(7), O2-Si2-C31 113.4(7), O3-Si3-C37 108.7(7), O3-Si3-C43 110.3(8), O3-Si3-C49 106.4(8).

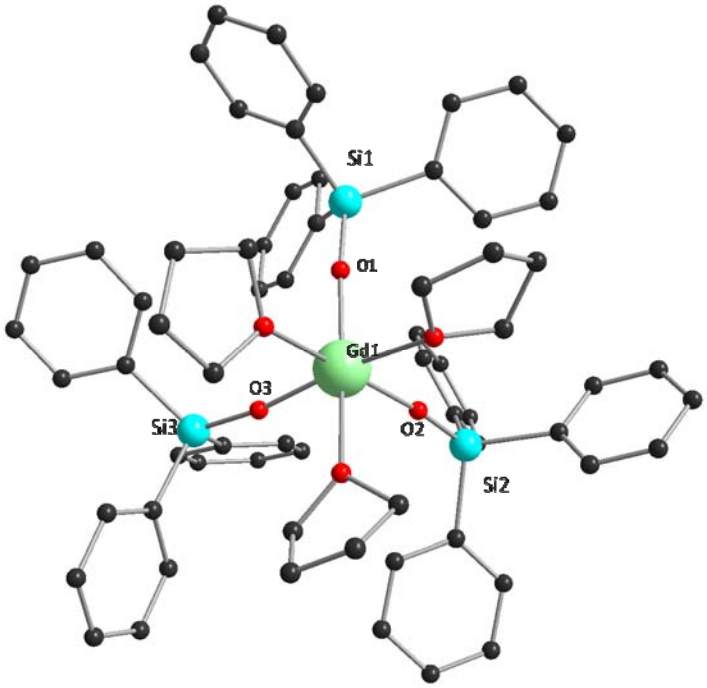

Figure 3.7 Molecular structure of **3.7**, with the hydrogen atoms omitted for clarity. Selected distances/Å and angles°: Gd1-O1 2.169(3), Gd1-O2 2.155(3), Gd1-O3 2.147(3), Gd1-O4 2.494(3), Gd1-O5 2.453(3), Gd1-O6 2.478(3), Si1-O1 1.589(3), Si2-O2 1.585(3), Si3-O3 1.593(3), O1-Gd1-O3 100.54(13), O1-Gd1-O2, 100.83(12), O3-Gd1-O2 101.37(12), O1-Gd1-O5 90.75(13), O3-Gd1-O5 87.48(12), O2-Gd1-O5 163.77(12), O1-Gd1-O6 165.17(13), O3-Gd1-O6 90.71(13), O2-Gd1-O6 86.21(12), O5-Gd1-O6 80.04(12), O1-Gd1-O4 86.16(12), O3-Gd1-O4 166.73(12), O2-Gd1-O4 88.44(11), O5-Gd1-O4 80.95(12), O6-Gd1-O4 80.96(12), O1-Si1-C1 110.4(2), O1-Si1-C7 112.8(2), O1-Si1-C13 110.5(2), O2-Si2-C25 112.10(19), O2-Si2-C31 111.25(19), O3-Si3-C37 110.7(2), O3-Si3-C43 111.10(19), O3-Si3-C49 109.5(2).

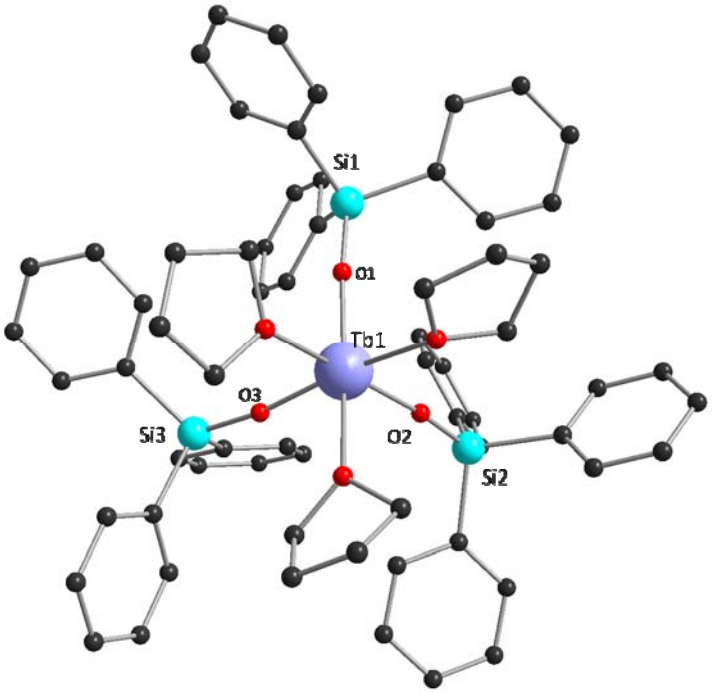

Figure 3.8 Molecular structure of **3.8**, with the hydrogen atoms omitted for clarity. Selected distances/Å and angles°: Tb1-O1 2.153(4), Tb1-O2 2.144(4), Tb1-O3 2.137(4), Tb1-O4 2.467(4), Tb1-O5 2.433(4), Tb1-O6 2.463(5), Si1-O1 1.592(4), Si2-O2 1.586(4), Si3-O3 1.584(4), O1-Tb1-O3 101.94(15), O1-Tb1-O2, 101.04(16), O3-Tb1-O2 101.83(15), O1-Tb1-O5 90.25(16), O3-Tb1-O5 86.87(15), O2-Tb1-O5 163.86(14), O1-Tb1-O6 164.08(16), O3-Tb1-O6 90.09(17), O2-Tb1-O6 86.44(15), O5-Tb1-O6 79.91(15), O1-Tb1-O4 85.17(14), O3-Tb1-O4 166.31(15), O2-Tb1-O4 88.07(14), O5-Tb1-O4 81.36(14), O6-Tb1-O4 81.02(16), O1-Si1-C1 110.7(3), O1-Si1-C7 112.3(2), O1-Si1-C13 110.7(2), O2-Si2-C25 111.8(2), O2-Si2-C31 111.1(2), O3-Si3-C37 110.5(2), O3-Si3-C43 110.8(2), O3-Si3-C49 109.9(3).

Table 3.1 Crystallographic data and summary of structural refinement for compounds **3.4-3.6.**

Compound	**3.4**	**3.5**	**3.6**
Empirical Formula	$C_{70}H_{77}O_7Si_3Dy$	$C_{70}H_{77}O_7Si_3Er$	$C_{70}H_{77}O_7Si_3Ho$
Formula Weight (g mol^{-1})	1277.09	1281.85	1279.52
Temperature (K)	100(2)	100(2)	100(2)
Crystal System	Monoclinic	Monoclinic	Monoclinic
Space Group	$P2_1$	$P2_1$	$P2_1$
Colour	Yellow	Pink	Pale Pink
a (Å)	14.3149(5)	14.365(3)	14.252(4)
b (Å)	16.4391(6)	16.388(3)	16.368(2)
c (Å)	14.5519(5)	14.466(3)	14.446(3)
α (deg)	90	90	90
β (deg)	113.532(4)	113.831(18)	113.51(3)
γ (deg)	90	90	90
Volume $Å^3$	3.139.41(19)	3.115.1(11)	3090.2(12)
Z	2	2	2
ρ_{calcd} (kg m^{-3})	1.351	1.367	1.375
R1 [I>2.0 σ(I)][a]	0.0540	0.0803	0.0886
wR2 (all data) [a]	0.1380	0.1783	0.1860

Table 3.1 Crystallographic data and summary of structural refinement for compounds **3.7** and **3.8**

Compound	**3.7**	**3.8**
Empirical Formula	$C_{70}H_{77}O_7Si_3Gd$	$C_{70}H_{77}O_7Si_3Tb$
Formula Weight (g mol^{-1})	1271.84	1273.51
Temperature (K)	100(2)	100(2)
Crystal System	Monoclinic	Monoclinic
Space Group	$P2_1$	$P2_1$
Colour	Colourless	Colourless
a (Å)	14.2640(11)	14.3081(8)
b (Å)	16.4606(12)	16.3981(6)
c (Å)	14.5368(11)	14.5255(7)
α (deg)	90	90
β (deg)	113.6550(10)	113.764(6)
γ (deg)	90	90
Volume $Å^3$	3126.4(4)	3119.1(3)
Z	2	2
ρ_{calcd} (kg m^{-3})	1.351	1.356
R1 [I>2.0 σ(I)][a]	0.0378	0.0372
wR2 (all data) [a]	0.0825	0.0787

[a] $R1 = \Sigma (||F_0| - |F_c||/ \Sigma|F_0|$.[b] $wR2 = [\Sigma[w(F_0^2 - F_c^2)^2]/ \Sigma[w(F_0^2)^2]]^{1/2}$

The family of isostructural lanthanide siloxide monomers listed **3.4**-**3.8**, are all six co-ordinate at the central metal. The mean Ln-O($OSiPh_3$) bond lengths are 2.131 Å (**3.4**), 2.086 Å (**3.5**), 2.098 Å (**3.6**), 2.157 Å (**3.7**) and 2.144 Å (**3.8**). Similarly, the Ln-(OC_4H_8) mean bond lengths which are 2.449 Å (**3.4**), 2.474 Å (**3.5**), 2.425 Å (**3.6**), 2.474 Å (**3.7**) and 2.454 Å (**3.8**), also compare very closely with each other. The small range of mean bond distances that do exist across the Ln-O($OSiPh_3$) bonds, decreases in order of increasing Ln(III) atomic number owing to the occurrence of the lanthanide contraction with compound **3.5** [Er(III)] exhibiting the shortest distance and compound **3.7** [Tb(III)] consequently giving the longest. Incidentally, the O-Ln-O bond angles consisting of *cis* orientated ligands, as a result of the *facial* octahedral geometry, give an average close to ~90.0 °, which complies well with the geometry. However, the bond angles associated with the THF ligands display angles which are considerably less than 90° and conversely the coupled -$OSiPh_3$ ligands are a lot more than 90°. These values compare well to those previously reported for the O-Ce-O bond lengths of [Ce($OSiPh_3$)$(THF)_3$](THF).[88]

The sterically bulky phenyl groups within the -$OSiPh_3$ ligand account for the obtuse bond angles between the O-Si-C angles in each of the five compounds with averages ranging between 110.2 and 111.2°.

3.2.2 Magnetic Studies for Compounds 3.4, 3.5, 3.6, 3.7 and 3.8

3.2.2.1 Background

The pseudo three-fold symmetry C_{3v}, in which these complexes reside, occurs once the mother liquors have been removed and the crystals are subjected to robust drying *in vacuo*. This process removes the fourth THF present in the lattice. Much of the intriguing magnetic properties that occur in compounds that are found to be SMMs/SIMs are owed to their symmetry. For instance, the remarkable slow relaxation process exhibited by Ishikawa's monometallic $(Bu_4N)[Tb(Pc)_2]$ compound or Coronado's $Na_9[Er(W_5O_{18})]_2$ is attributed to their fourfold symmetry, C_{4v}.[14-15,26i-j] Furthermore, rare earth ethyl sulfate complexes, in particular the whole series of lanthanide enneahydrates, $Ln(C_2H_5SO_4)_3.9H_2O$, have been investigated in the context of magnetic behaviour for over five decades as a result of their three-fold, C_{3h} symmetry.[89] Hence, in reference to the symmetry of these compounds, it would appear that the geometry of these monomers partly affects the strength of the ligand field splitting, whereby the bigger the separation, the slower the relaxation of magnetisation, therefore the symmetry determines the mixing of the m_J states. The C_{3v} high symmetry of these complexes, should provide an ideal environment to achieve greatly slowed relaxation for reversal of magnetisation.[14-15] Further evidence that the influence of the crystal field may have on the strength of the magnetic behaviour of these high symmetry single-ion lanthanide complexes, can be explained by observing the energy level diagram for Ishikawa's single-ion sandwich complexes.[14] This was determined from an analysis of the variable temperature

NMR spectrum, which can be used to measure the magnetism of the sample in solution. Figure 3.9, illustrates the splitting of the spin-orbit coupled (*J*) ground state by the crystal field for $[LnPc_2]^-$.[14] Here, an indication of how the symmetry can affect the strength of the crystal field is given, where the Tb(III) (**1.8**) complex has the lowest state assigned to $m_J \pm 6$, (which equates to the highest and lowest value in the $J = 6$ ground state). The observed energy separation from $m_J = \pm 6$ to $m_J = \pm 5$ exceeds 400 cm^{-1}, and it is this large energy separation of the ground $m_J = \pm 6$ state from the lowest excited state that provides ideal conditions for strong SMM behaviour.[14] In contrast, the apparent 'step-wise' transition from one m_J state the next m_J state (i.e ±1) observed for **1.8**, is not observed for the Dy(III) (**1.9**) complex where the lowest state is represented by $m_J = \pm 13/2$, which is the second largest in the $m_J = \pm 15/2$ ground state. This suggests a more complex regime is implemented where there is a 'mixing' of the states, although the separation between the energy levels is arranged more evenly than for **1.8**. Therefore, these cannot be 'rate-determining' for **1.9**, and requires much less energy for relaxation of the magnetisation. Hence, **1.9** is a weaker SMM.[14,15a, 26j]

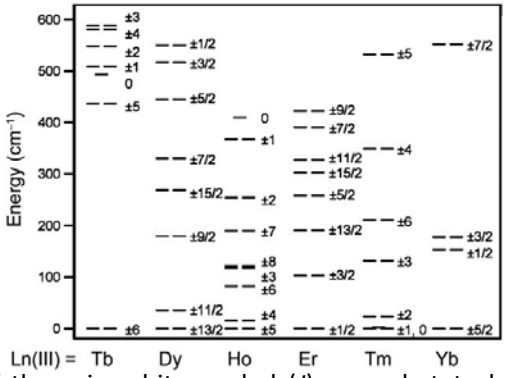

Figure 3.9 The splitting of the spin-orbit coupled (*J*) ground state by the crystal field for $[LnPc_2]^-$ [14d]

3.2.2.2 d.c. and a.c. Magnetic Susceptibility Measurements

Direct current (d.c.) magnetic susceptibility measurements were performed on polycrystalline samples of compounds **3.4**, **3.5**, **3.6** and **3.8** in a temperature range of 2-300 K in an applied field of 1 kG.

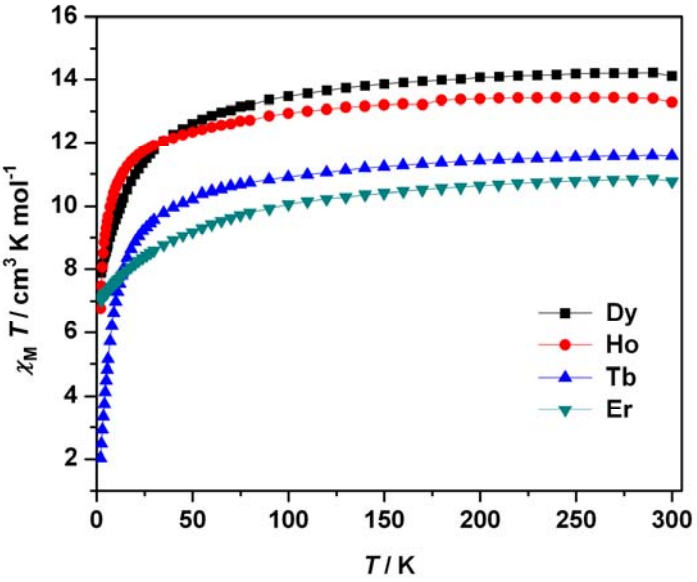

Figure 3.10 Data plot showing the temperature dependence of χ_M and $\chi_M T$ for compounds **3.4** (Dy) **, 3.5**(Er), **3.6**(Ho), **3.8**(Tb) for the field strength H = 1 kG

	Ground State Term Symbol	*S*	*g*	$\chi_M T$ cm^3 K mol^{-1}
Dy(III)	$^6H_{15/2}$	5/2	4/3	**14.17**
Ho(III)	$^5I_8$	2	5/4	**14.07**
Er(III)	$^4I_{15/2}$	3/2	6/5	**11.50**
Tb(III)	$^7F_6$	3	3/2	**11.82**
Gd(III)	$^8S_{7/2}$	7/2	2	**≈ 7.88**

Table 3.2 The relevant magnetic parameters to derive the magnetic susceptibility values for compounds **3.4**-**3.8**, with the expected value for **3.7**.

The d.c. $\chi_M T$ values for the compounds listed in Table 3.2, at 300 K, are all in good agreement with the expected values for monometallic lanthanide(III) ions.[53] The magnetisation versus field data plots at 2 K, Figure 3.11, reveal that compounds **3.4, 3.5** and **3.6** show a rapid increase in magnetisation at low magnetic field, gradually increasing more linearly at higher fields, although **3.4** increases at a slower rate at higher fields. In contrast, compound **3.8** experiences a slower accession at low magnetic fields with all compounds showing no clear saturation points.

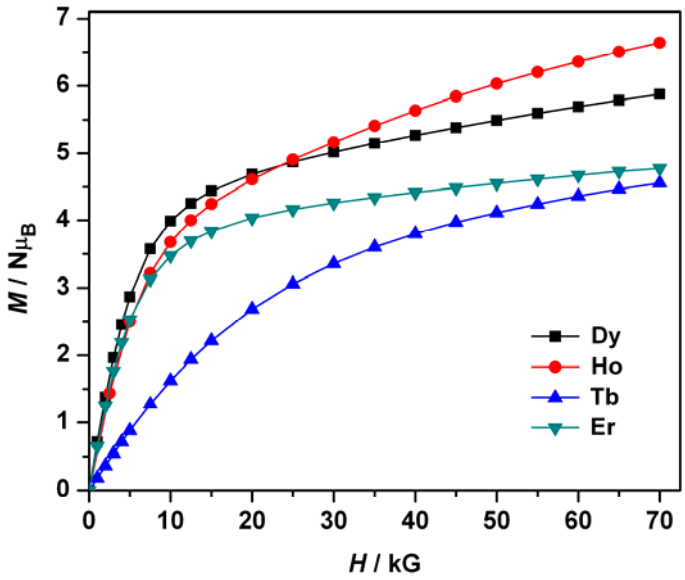

Figure 3.11 Magnetisation vs. field data plot at 2 K for compounds **3.4** (Dy), **3.5**(Er), **3.6**(Ho), **3.8**(Tb).

The temperature dependent in-phase and out-of-phase a.c. magnetic susceptibility data plots for compound **3.5** clearly show characteristics indicative of an SMM, Figure 3.12, in an oscillating field of H_{ac} = 1.55 G in an applied field of H_{dc} = 1 kG. The in-phase and out-of-phase components of the a.c. susceptibility show a frequency dependence up to about 6 K, where the frequency dependency maxima in the χ_M"

data plot are exhibited below 5 K. The frequency dependency maxima observed in both data plots demonstrates clear evidence of slow relaxation, (hence an SMM).

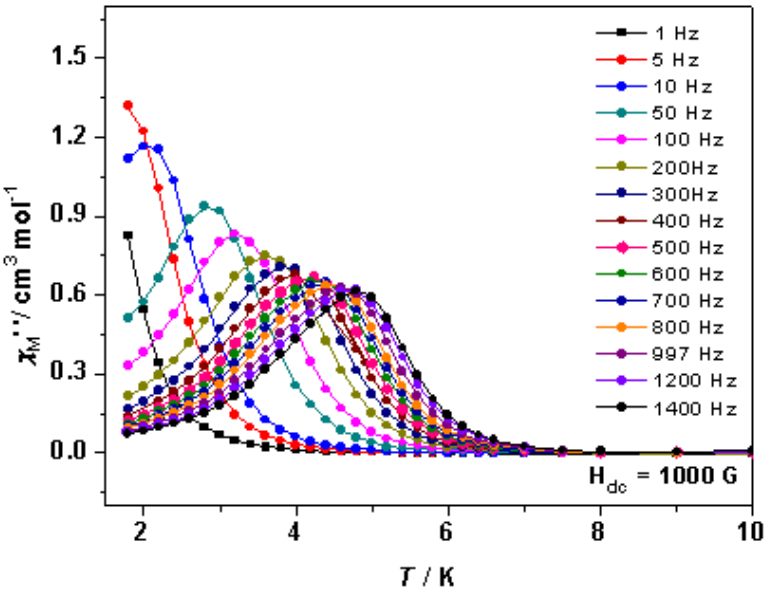

(a)

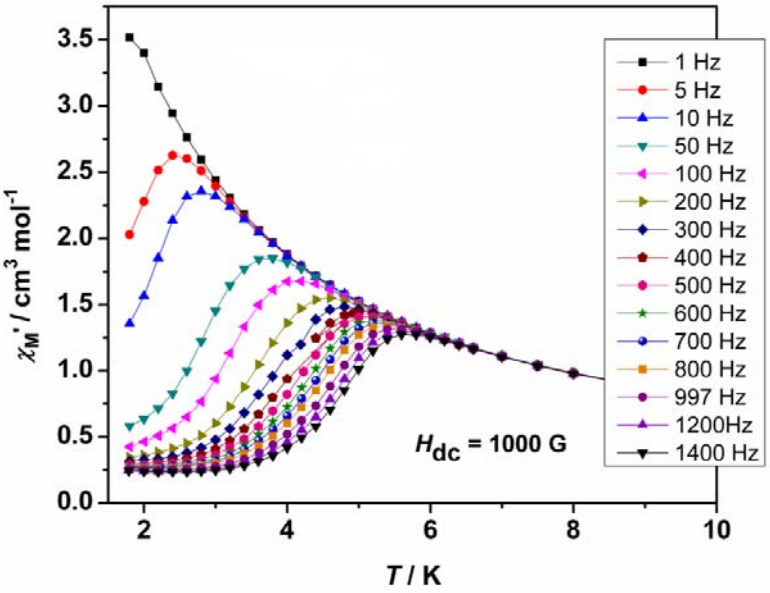

(b)

Figure 3.12 Out-of-phase (χ_M'') (a) and in-phase (χ_M') (b), χ_M vs. T data plots for compound **3.5** at different frequencies between 1 and 1400 Hz, in an oscillating field of 1.55 G.

Frequency dependent in-phase and out-of-phase a.c. magnetic susceptibility plots conducted at temperatures in the range of 1.8-6 K, Figure 3.13, provide further evidence to suggest that compound **3.5** is an SMM, again displaying frequency dependent maxima when lower frequencies are applied at lower temperatures.

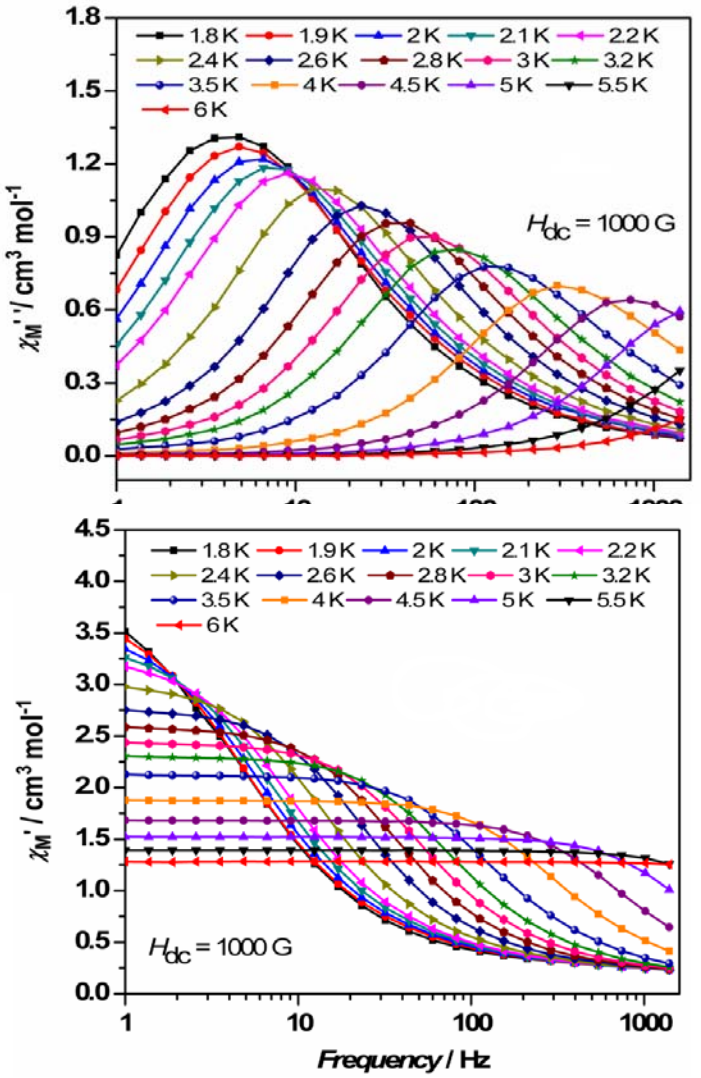

Figure 3.13 Frequency dependent (υ/Hz) out-of-phase (χ_M'') (a) and in-phase (χ_M') (b), χ_M vs. υ data plot for compound **3.5** at temperatures in the range of 1.8-6 K.

Semi-circular Cole-Cole plots of χ_M'' vs. χ_M' at a range of temperatures below 5 K were obtained. The data plots were fitted by a generalised Debye model using parameters α = <0.2, indicating a small distribution relaxation times in compound **3.5**.

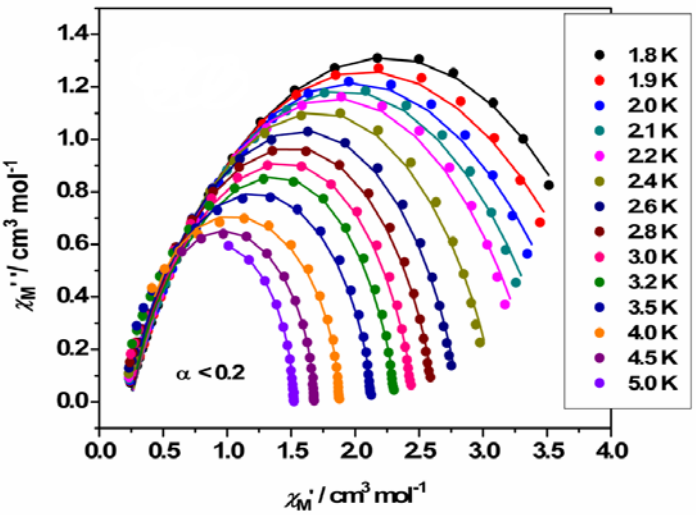

Figure 3.14 Cole-Cole plot based on the a.c. susceptibility measurements of **3.5** between 1.8 and 5 K. The solid lines travelling through the experimental values represent best fits.

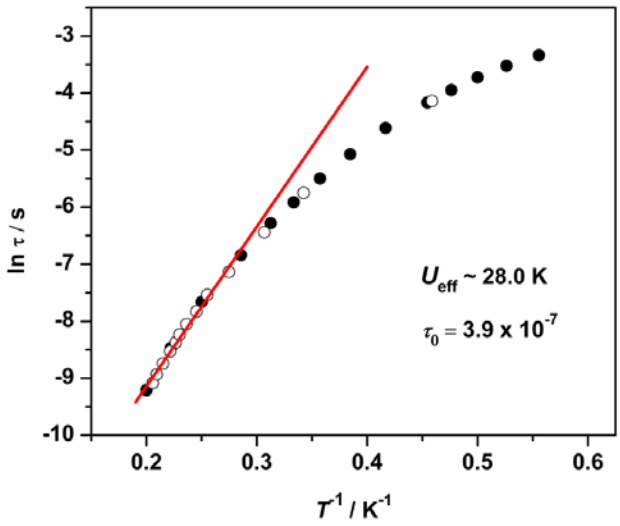

Figure 3.15 Magnetization relaxation time (τ) versus T^{-1} for **3.5** under zero static field, from data collected in frequency (opaque dots) and temperature (transparent dots), variation regimes and best fit to the Arrhenius law of the thermally activated regime (solid red line).

Above 4.5 K the relaxation of compound **3.5** becomes thermally activated and the Arrhenius plot of Inτ vs. 1/*T* is linear, Figure 3.15 and obeys the Arrhenius law $\tau = \tau_0 \, exp \, (\Delta E/K_B T)$ resulting in an energy barrier to magnetization reversal of U_{eff} = ~28.0 K, where the pre-exponential factor is $\tau_0 = 3.9 \times 10^{-7}$ s.

Alongside compound **3.5**, the dysprosium siloxide monomer, **3.4**, also shows the magnetic behaviour of an SMM, however much less prominently than compound **3.5**. The out-of-phase and in-phase components of a.c. magnetic susceptibility for **3.4** exhibited in Figure 3.16 clearly show frequency dependent maxima in both phases, although the rate of relaxation is much faster than that of **3.5** and is therefore a weaker SMM compared to **3.4**.

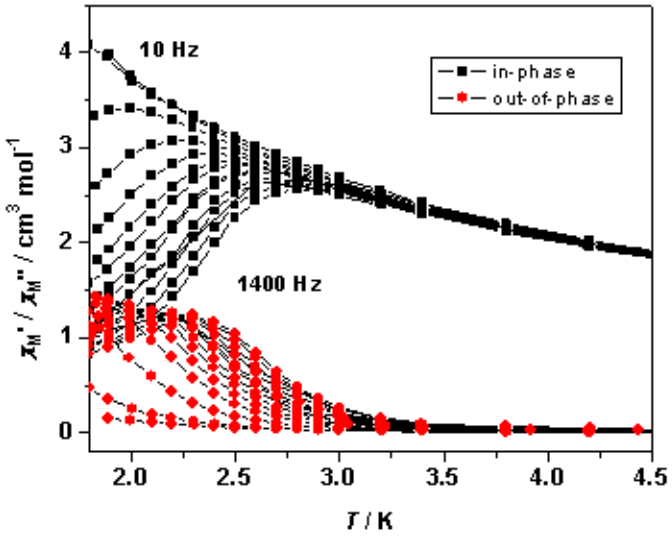

Figure 3.16 The out-of-phase and in-phase a.c. magnetic susceptibility data plots for compound **3.4.**

Attempts to conduct magnetic susceptibility measurement on compound **3.7**(Gd III) proved unsuccessful as the quantity of the sample available was very small and its static nature proved repeatedly difficult to handle in a glove box compared to its analogous counterparts. Consequently, because Gd(III) is isotropic, $^{8}S_{7/2}$, electron paramagnetic resonance, (EPR), measurements were conducted by the University of Manchester EPR service, in the solid phase at room temperature, 293 K, Figure 3.17.

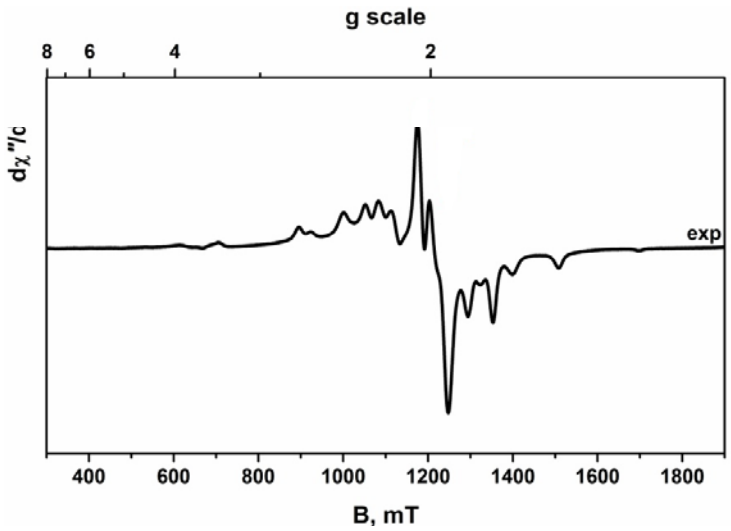

Figure 3.17 Q-band (~ 34 GHz) EPR spectrum for compound **3.7** as a polycrystalline powder.

The spin-Hamiltonian parameters previously reported for well characterised, three-fold symmetric Gd(III) sites in compounds or where Gd(III) is doped into lattices,[90a] were used to provide comparative EPR spectral simulations with the experimental EPR data of **3.7**, Figure 3.18.[90b] Inspection of the spectra in Figure 3.18 indicates a series of spectral simulations is needed to extract the parameters, because the spectrum of **3.7** is in a wide field range, (as for Gd(III) in Al_2O_3), but with an intense central region, (as for Gd(III) in lanthanum ethylsulfate).

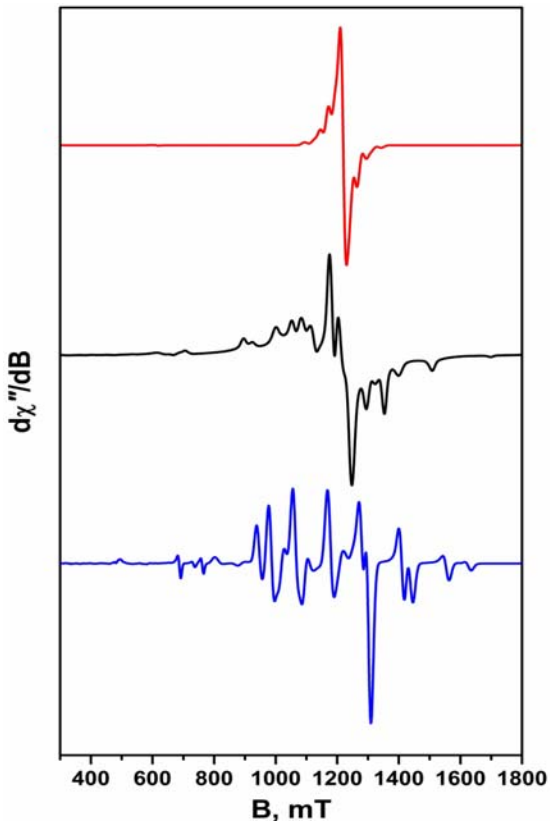

Figure 3.18 Comparative analysis of known Gd(III)-containing compounds, with the black spectrum representing the experimental data for **3.7**. Red simulation is based on Gd(III) in lanthanum ethylsulfate, with spin-Hamiltonian parameters: g = 1.99, D = 204.7 × 10^{-4} cm^{-1}; b04 = -3.96 × 10^{-4} cm^{-1}; b06 = 0.63 × 10-4 cm-1; |b66| = 3.5 × 10^{-4} cm^{-1}. Blue simulation based on Gd(III) in Al_2O_3, with spin-Hamiltonian parameters: g = 1.99, D = 1032.9 × 10^{-4} cm^{-1}; b04 = 26.0 × 10^{-4} cm^{-1}; b34 = 18.3 × 10^{-4} cm^{-1}; b06 = 0.63 × 10-4 cm^{-1}; b36 = 1.0 × 10^{-4} cm^{-1}; |b66| = 5.0 × 10^{-4} cm^{-1}.[90b] See text below for a description of the B_{kc}^{q} parameters.

Spectrum simulation for **3.7** can be attempted because the half-filled *f*-shell electron configuration, which generates a S = 7/2 spin ground state, exhibits slow electronic relaxation in a similar manner to that of high spin Mn(II) and Fe(III) ions with S =

5/2.[90c] Hence, aspects of these *d*-block ion Hamiltonian parameters can be used to present a spectrum at room temperature for **3.7**. This complicated regime stems from the contribution of a small zero-field splitting (ZFS; $D << hv$), expected for Gd(III), and the broad lines and single frequency of the experimental spectrum in Figure 3.17 that make any quantitative interpretation difficult. Therefore, initially a simulation has been produced based on the following spin-Hamiltonian:

$$\hat{H} = \mu_B \mathbf{B} \cdot \mathbf{g} \cdot \mathbf{S} + \mathbf{S} \cdot \mathbf{D} \cdot \mathbf{S}$$

The first term corresponds to the electronic Zeeman interaction and the second term represents the ZFS, where *D* is a traceless tensor parameterised by (a):

$$\hat{H}_{ZFS} = D\left[\hat{S}_z^2 - \frac{1}{3}S(S+1)\right] + \frac{1}{2}E(\hat{S}_x^2 + \hat{S}_y^2) \quad \text{(a)}$$

Here, *D* is the axial zero-field splitting parameter, $D = -3/2\ D_{zz}$ and *E* is the rhombicity parameter, $E = (D_{xx} + D_{yy})/2$. In systems with three-fold symmetry, $E = 0$, therefore the last term in the equation (a) is omitted. Figure 3.19, represents two proposed simulations for compound **3.7**, where the blue simulation uses $D = 700 \times 10^{-4}\ cm^{-1}$ for an isotropic *g* value of 2. An improved simulation is represented in red, which was derived by including higher order terms for ZFS in the spin-Hamiltonian. These components are necessary in high spin systems, and have been explored for Fe(III) and Gd(III)-doped materials of high symmetry, Table 3.3.[90]

Therefore the ZFS is can now be described as:

$$\hat{H}_{ZFS} = \sum_{k=2,4,6}\sum_{q=-k}^{k} B_k^q \hat{O}_k^q = \sum_{k=2,4,6}\sum_{q=-k}^{k} f_k b_k^q \hat{O}_k^q \quad \text{(b)}$$

In the equation (b) the term $\hat{O}_k^q$ for k = 2, 4, 6 are known as extended Stevens' operators and their associated coefficients B_k^q are always real (Appendix Three). Subsequently, the coefficients are scaled by a factor f_k, which are defined as $\frac{1}{3}$ for second-order, $\frac{1}{60}$ for fourth-order, and $\frac{1}{1260}$ for sixth-order terms. Hence, b_k^q values are directly introduced into the simulation program, and the allowed value of q are defined by symmetry. Therefore, the resulting spin-Hamiltonian used to simulate the Gd(III) ions in C_{3v} symmetry is, (c):

$$\hat{H} = \mu_B \mathbf{B}\cdot\mathbf{g}\cdot\mathbf{S} + \frac{1}{3}b_2^0\hat{O}_2^0 + \frac{1}{60}\left[b_4^0\hat{O}_4^0 + b_4^3\hat{O}_4^3\right] + \frac{1}{1260}\left[b_6^0\hat{O}_6^0 + b_6^3\hat{O}_6^3 + b_6^6\hat{O}_6^6\right]$$

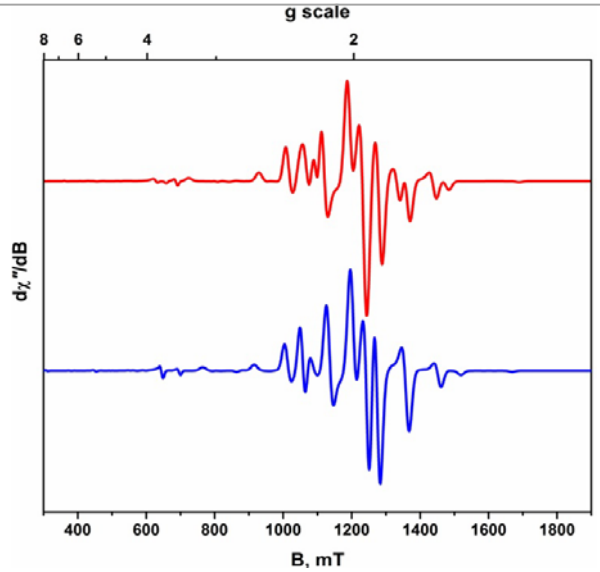

Figure 3.19 EPR simulation for **3.7**, with parameters: g = 2.00; D = 700 × 10^{-4} cm^{-1}; $b04$ = 15 × 10^{-4} cm^{-1}; $b34$ = 500 × 10^{-4} cm^{-1}; $b06$ = 4 × 10^{-4} cm^{-1}; $b36$ = -1 × 10^{-4} cm^{-1}; $|b66|$ = 10 × 10^{-4} cm^{-1}; W = 100 × 10^{-4} cm^{-1}, (in red and the best fit obtained with these parameters), and blue simulation for **3.7** with parameters: g = 2.00; D = 700 × 10^{-4} cm^{-1}; W = 100 × 10^{-4} cm^{-1}.

Gd(III) Compounds	*g*	b_2^0	b_4^0	b_4^3	b_4^4	b_6^0	b_6^3	b_6^6
1	~2	700	15	500	-	4	-1	10
2	1.992	± 347.6	±4.42	±72.8	±72.8	±0.98	-	23.8
3	1.995	1033	26	366	-	1	-	5
4	1.992	-136.6	24.54	-693.2	-	-0.28	-2.9	-0.6
5	1.992	80.1	8.36	14	-	1.26	-20	13

Table 3.3 Comparative spin-Hamiltonian parameters for a range of trigonal, Gd(III)-doped compounds with compound **3.7,** and are given in units of 10^{-4} cm^{-1}. **1** = $[Gd(OSiPh_3)_3(THF)_3]$**3.7**, **2** = Gd(III) in $RbZnF_3$,[90d] **3** = Gd(III) in Al_2O_3 (alumina),[90c] **4** = Gd(III) in BaF_2,[90h] **5** = Gd(III) $RbCaF_3$.[90e]

For the simulation in blue, (Figure 3.19), using only *D,* the outer region of the spectrum around the central $m_s = \pm ½$ transition (g ~ 2), has too much intensity and the highest field feature at 1650 mT is not aligned with the corresponding peak in the experimental spectrum at 1700 mT, Figure 3.17. However, the fourth and sixth order of the axial terms gave a reduction in the intensity of this region of the spectrum (i.e. the 'wings' of the spectrum), and correctly reproduce the resonant field at 1700 mT. The trigonal term $\hat{O}_4^3$ is quite large and subsequently affects the resonant positions between the principal axes, therefore the experimental peak positions had to be finely tuned. Furthermore, the small effect expected from the $\hat{O}_6^3$ and $\hat{O}_6^6$ terms meant that the parameters were very difficult to sufficiently determine due to the line-shape in the polycrystalline sample, which is was

susceptible to unresolved hyperfine coupling of ^{155,157}Gd (I = 3/2, 30.5% abundance). The simulation and the accuracy of the spin-Hamiltonian parameters would be greatly improved by conducting high-field measurements (> 130 GHz), to resolve the various EPR transitions that are irregularly spaced at Q-band. This would most likely sharpen the signal and improve the resolution of the spectral lines greatly. Hence, the second order operator, commonly known as the axial zero-field splitting parameter is related by, $D = b_2^0$, and the axial fourth-order parameter F is related by, $F = 3b_4^0$. The latter parameter can be related to some on-going theoretical calculations which explore the relationship between the crystal fields of these highly symmetric monomers with the magnetic data outlined in Section 3.2.2.2.

To summarise briefly, compounds **3.4**–**3.8** are essentially identical structurally, where the only interchangeable variable is the metal, and as the magnetic data show, this clearly has a significant impact on the magnetic properties. However, compounds **3.4**(Dy) and **3.5**(Er) exhibit magnetic behaviour that is characteristic of SMMs, with compound **3.5** being a stronger SMM. Due to the large spin orbit coupling in Dy(III) and even Tb(III) ions, it was expected, prematurely, that along with having a large magnetic anisotropy, these compounds would to some extent exhibit SMM behaviour and in the case of compound **3.4**, show much slower relaxation than observed.[14d,28b] However, it was compound **3.5** possessing the Er(III) ion, which showed a greater energy barrier to magnetization reversal. Therefore, to comprehend the observed magnetic data further, theoretical and optical absorption

studies were conducted to determine the source of the SMM behaviour in compound **3.5**.

3.2.3 Low Temperature Optical Absorption Spectroscopy

3.2.3.1 Background to 4*f* Electronic Absorption Spectroscopy

The optical spectroscopy of trivalent rare earth ions have long been the subject of great interest because of their intriguing electronic absorption properties. Much of this interest stems from the ability of these rare earths to have desirable spectroscopic applications in optical communications.[91] Over recent years there has been an escalating demand for high speed information transfer, which is driving the changeover from electrical to optical communication systems. This amplification of telecommunication signals is currently achieved by erbium-doped glass fibre amplifiers, which has led to the growth of investigating the optical absorption and luminescence spectroscopy of erbium(III) based compounds.[91-33]

There are three type of electronic transitions observed for lanthanide systems. These consist of the 4*f*-4*f* transitions, n*f*(n+1)*d* transitions and the ligand-metal transitions. The *f-f* transitions are similar to the *d-d* transitions of transition metal ions, whereby they are electric dipole forbidden by the Laporte selection rule, (as these transitions are of the same parity). However, interactions with the ligand field or vibrational states mix in electronic states of different parity (or symmetry) and so *f-f* transitions become possible. However, since the radial extent of 4*f*-orbitals is

relatively small, the intensity of *f-f* transitions are much weaker than *d-d* transitions, and the absorptions are a lot more sharper.[2]

The electronic spectra of lanthanide complexes give evidence of some interaction of the crystal field with the *f*-electrons, which is manifested by the slight shifting of absorptions bands to lower frequencies, and is experienced by rare earth complexes relative to their free ions. This is as result of the nephelauxetic effect, which occurs when the complex experiences a very small degree of metal-ligand covalent bonding.[2] Furthermore, crystal field effects are also observed within lanthanide complexes as a result of hypersensitive transitions.[2] Ligand environment and the chemical nature of the ligand play an influential role in the intensities of these transitions. However, this does not apply to all the *f-f* transitions. Whilst Er(III) and Nd(III) exhibit the greatest effects of hypersensitivity, Ce(III), Gd(III) and Yb(III) are completely devoid of this hypersensitive transition. The hypersensitive interactions which are sensitive to the symmetry of the crystal field usually have $\Delta J \pm 2$ (Figure 3.18).[2]

Comparatively, *f-d* transitions are Laporte allowed and produce much broader and higher intensities than *f-f* transitions. Ligand-metal transitions can also be Laporte allowed and similarly to *f-d* transitions have high intensities, but are much broader. Hence, the resulting colours of these complexes are much more intense and are observed in the visible region of the spectrum.[1-2] Figure 3.20 shows the series of lanthanide(III) ions with their corresponding colours and an energy level diagram

showing the relevant term symbol states for the second half of the trivalent lanthanides of the 4*f* series.

Ln	Colour
La^{3+}	Colourless
Ce^{3+}	Colourless
Pr^{3+}	Green
Nd^{3+}	Lilac
Pm^{3+}	pink
Sm^{3+}	Pale yellow
Eu^{3+}	Colourless
Gd^{3+}	Colourless
Tb^{3+}	very pale pink
Dy^{3+}	yellow
Ho^{3+}	yellow
Er^{3+}	pink
Tm^{3+}	pale green
Yb^{3+}	Colourless

(a)

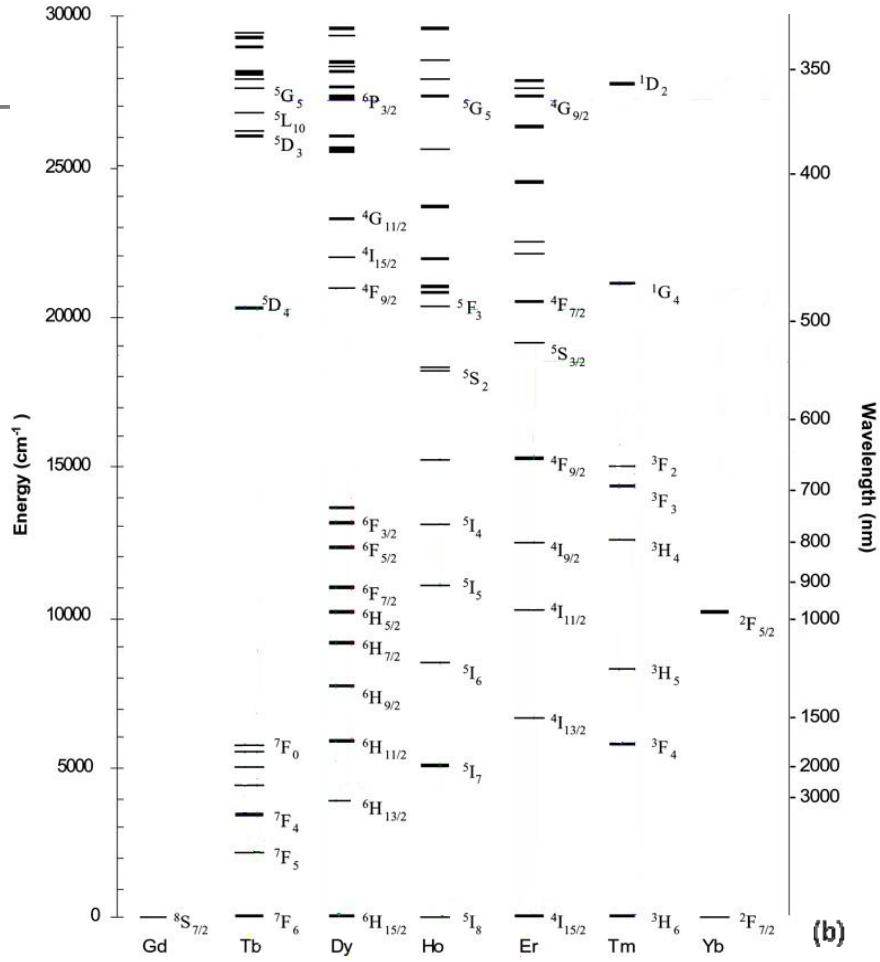

Figure 3.20 A list of lanthanide(III) ions alongside their associated colours (a), in addition to the energy level diagram for the late trivalent rare earth series labelled with the dominant Russell-Saunders $^{2S+1}L_J$ terms (b).[94]

3.2.3.2 Introduction and Aims

The disparity in magnetic behaviour between compound **3.5**, encapsulating the Er(III) ion, and compounds **3.4**(Dy), **3.6**(Ho), **3.7**(Gd) and **3.8**(Tb), made compound **3.5** subject to *ab initio* theoretical calculations (Appendix Four), to further

comprehend the slow relaxation properties experienced by **3.5**, compared to the other single-ion siloxides in this series. Preliminary theoretical *ab initio* studies conducted by Prof. Chibotaru, University of Leuven, Belgium have attempted to decipher the relationship between the results of the magnetic susceptibility data compiled for **3.4**-**3.8** with the effects of the crystal field on their electronic states, therefore preliminary low temperature electronic absorption spectroscopy measurements were conducted. Interestingly, although there has been a vast amount of attention focusing on the magnetism of SIM complexes with high symmetry, such as the compounds detailed in Section 1.6 and 3.2.2.1,[14-15,26i,31] there is currently comparatively little reported on the electronic properties of these compounds, with the exception of a selective range of lanthanide ethyl sulfates in the early 1960s. These studies were aimed at improving the relevant crystal field parameters through the use of optical spectra.[95-97] Consequently, the preliminary optical measurements outlined in the following sections will also address this gap in analytical data.

3.2.3.3 Optical Absorption Studies for Lanthanide(III) Compounds 3.4, 3.5, 3.8.

Visible, (~390-750 nm) and near-infrared (NIR), (~800-2500 nm), optical absorption spectroscopy was conducted on polycrystalline samples of **3.4**(Dy), **3.5**(Er) and **3.8**(Tb). A specially adapted sample holder allowed for a range of low temperature and room temperature measurements to be performed by isolating the sample in

question *in vacuo*. As a result of the air sensitive nature of these lanthanide alkoxides, the novel 'sample holder' had to be developed which was: compatible with the instrument, able to sustain the sample under low pressure and was able to keep the sample free from air and moisture long enough to mount the sample in the instrument once prepared in the glove box, where it would be eventually secured in an inert atmosphere under vacuum. A schematic diagram of the instrument and sample-holder is shown in Figure 3.21.

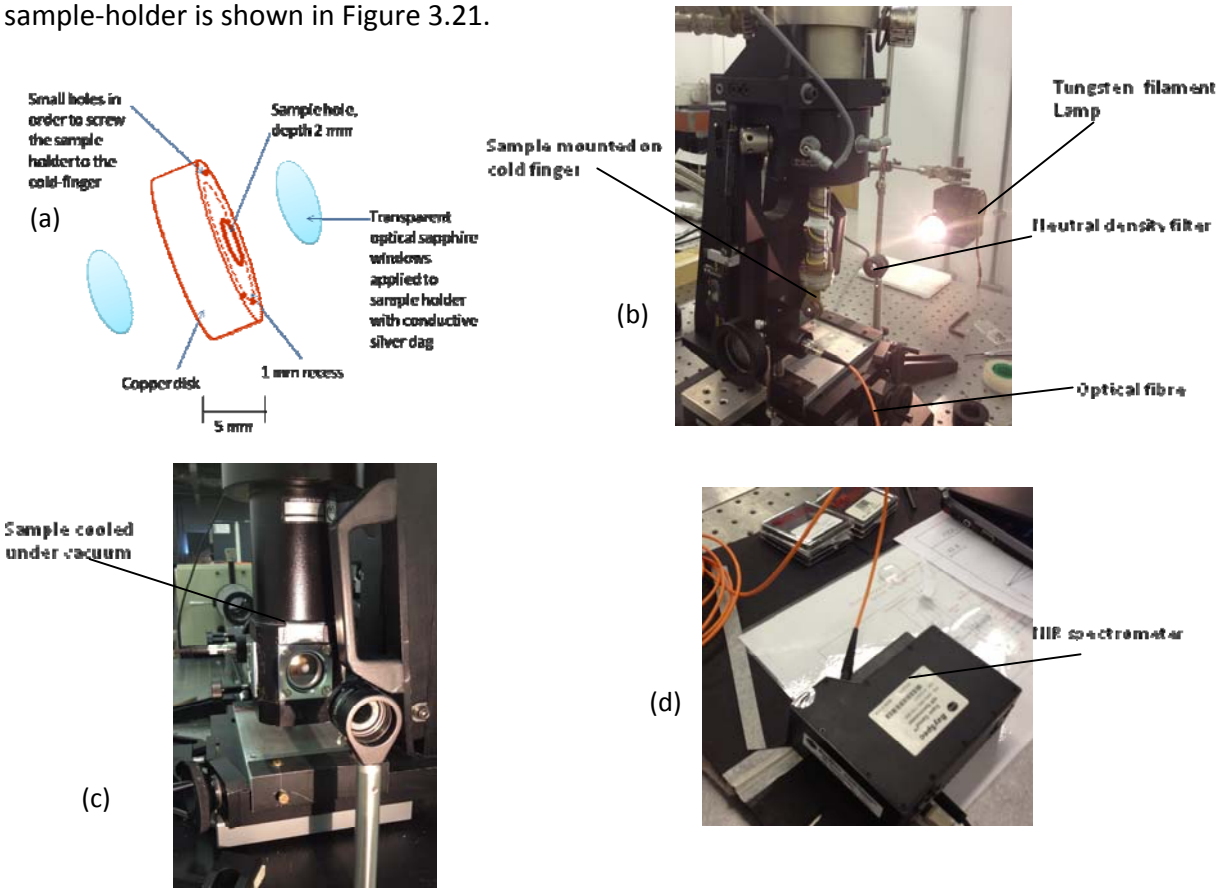

Figure 3.21 Diagram illustrating the copper disk sample holder (a), alongside photographic representation of the cold finger to which the copper disk is mounted (b), whilst under vacuum (c), and the spectrometer set-up (d).

To test this novel set-up, visible and NIR spectroscopic measurements were initially conducted on a known air stable Er(III) sample, $[Er(Hfac)_3(H_2O)_2]$ (Hfac = anion of hexafluoroacetylacetone), where absorption bands in the visible region have been previously reported, Figure 3.22.[98] The expected absorption bands for $[Er(Hfac)_3(H_2O)_2]$ were identified once a background dark scan had been subtracted from the scan of absorbed light by the sample, ensuring the efficiency of this application. Hence, a series of variable temperature optical measurements were performed on the air sensitive compounds.

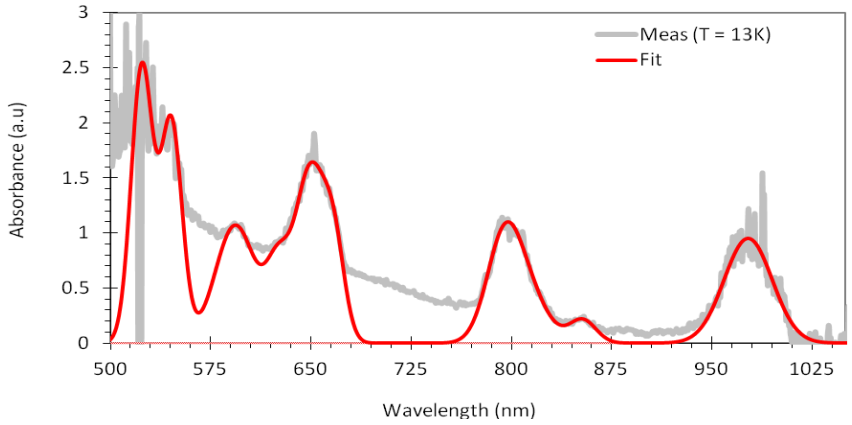

Figure 3.22 Optical measurements for $[Er(Hfac)_3(H_2O)_2]$ at 13 K (grey) superimposed with the multi-gauss fit data (red), where absorption is given by the Beer-Lambert Law $A = \log_{10}(I_0/I)$, (where I_0 = initial intensity of light and I = intensity of light after it passes through the sample).

Optical measurements were performed on compound **3.5**(Er), in a temperature range 12-300 K, Figure 3.23, first detecting absorption in the visible region of the spectrum then in the NIR. Figure 3.24 shows the multi-gauss fit at 12 K in the visible

and NIR region along with the corresponding ground-state absorption (GSA), bands which are in good agreement with the principal absorption peaks observed for the corresponding Er(III) energy levels.

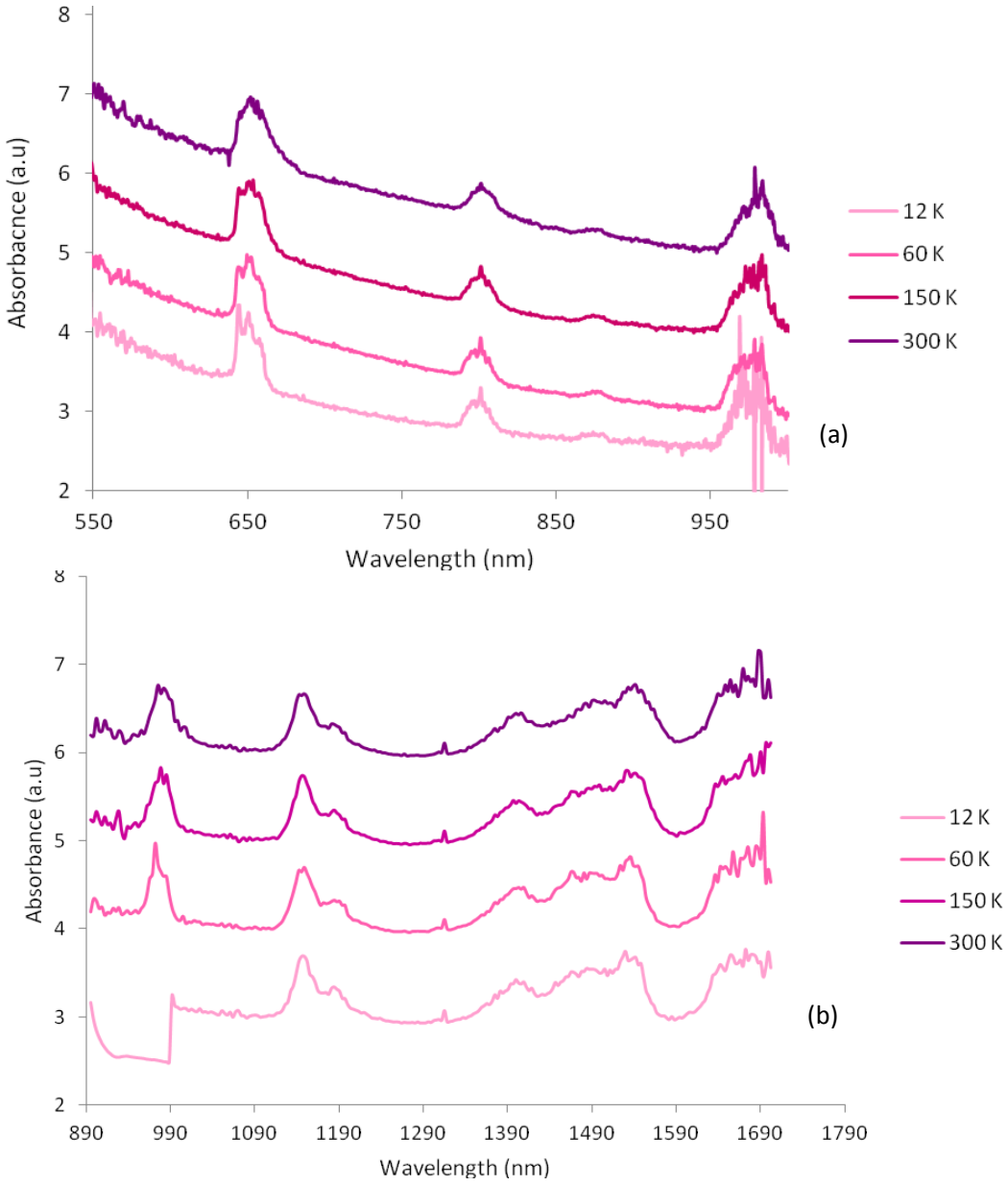

Figure 3.23 Variable temperature visible spectra for **3.5** (a) and variable temperature NIR spectra for **3.5**.

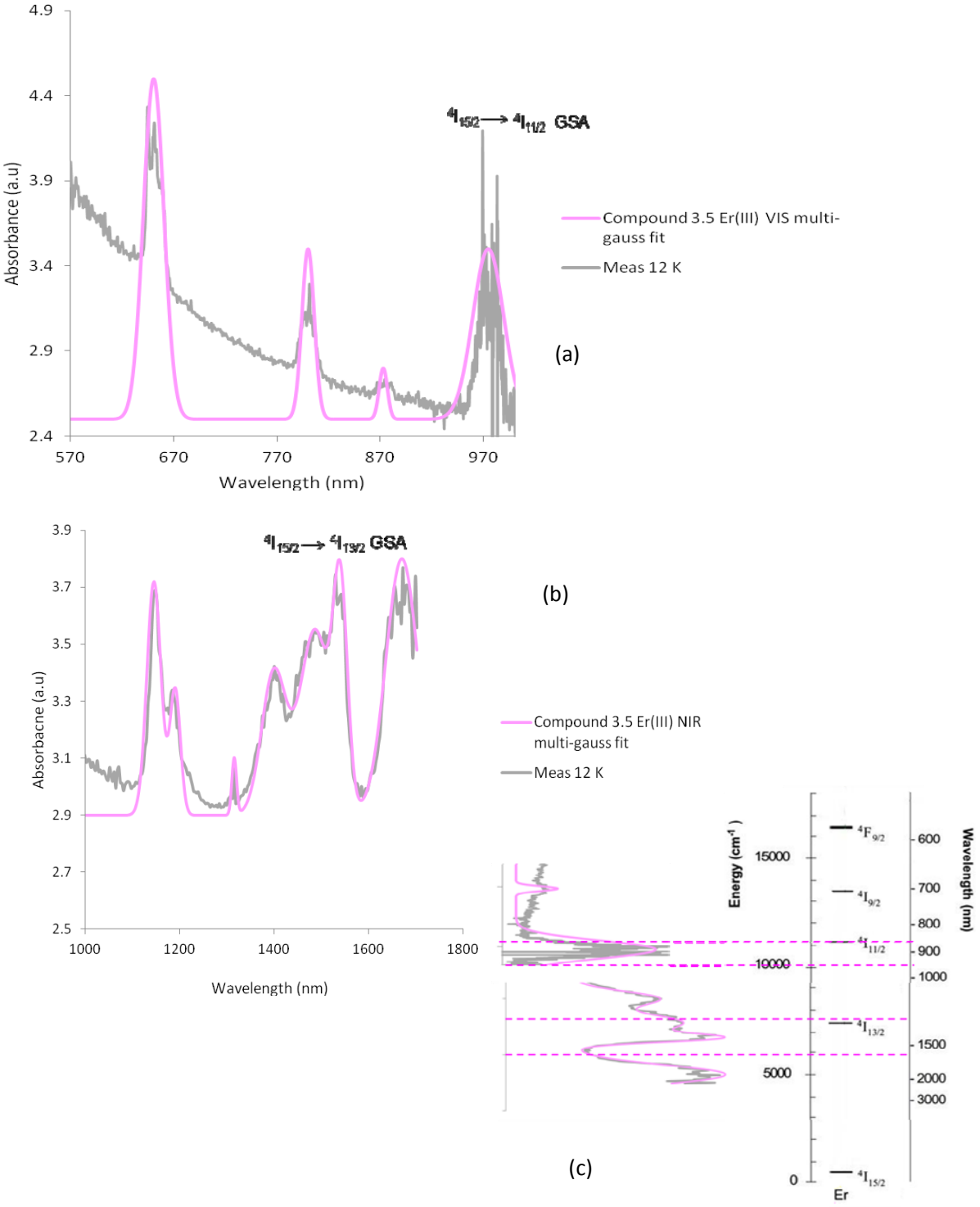

Figure 3.24 Multi-gauss fit data (pink) for compound **3.5** at 12 K in the visible region (a) and NIR region (b), indicating ground state absorption bands, (GSA). Observed absorption band for **3.5** simulated onto an energy level diagram for Er(III) (c).

It is apparent from Figure 3.23 that there is a small shift in the peaks, narrowing and increasing as the temperature is decreased, giving more resolved absorption bands. The peaks which appear at ~1145 and 1680 nm in the NIR spectrum, Figure 3.24 (b), were initially considered to be due to the excited-state absorption (ESA), of the Er(III) ion.[98,99] These excited state transitions would be expected to appear in the spectrum, since it is these strong transitions which have led to Er(III) based compounds being utilised in glass fibres (which have been erbium-doped) and in the telecommunications industry.[91-93,98,99] However, once NIR measurements were conducted on the Tb(III) compound **3.8**, at 12 K, the same transitions at ~1145 and 1680 nm were still present, Figure 3.25.

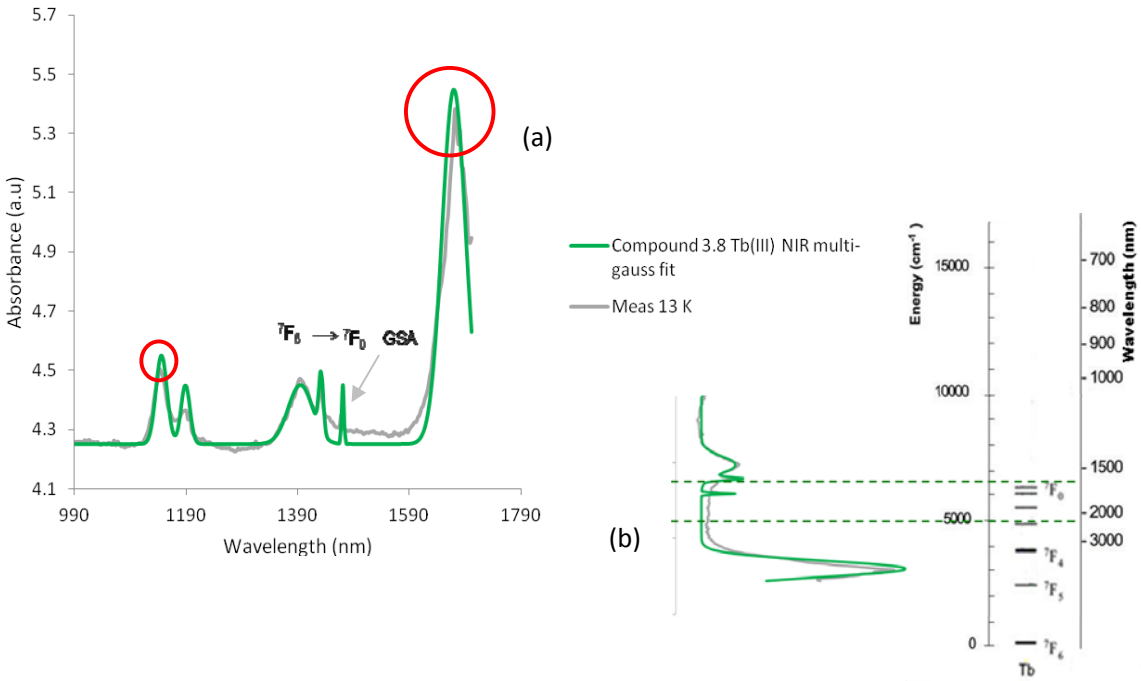

Figure 3.25 Multi-gauss fit (green) data for compound **3.8** in the NIR, showing absorption bands at 1145 and 1680 nm (circled in red). Observed absorption bands for **3.8** simulated onto a energy level diagram for Tb(III) (b).

These absorptions are seemingly as a result of the relatively small energy gap between excited state, $^4I_{13/2}$ and the ground state, $^4I_{15/2,}$ consequently resulting in the Er(III) excited state effectively being quenched by the vibronic coupling of high energy C-H stretching vibrations in the same regions as the Er(III) ion, overlapping the Er(III) transitions. This masking of ESA transitions from the central metal by vibronic C-H stretching is not uncommon and can also be seen for O-H and N-H stretching modes.[91] These C-H vibrations are derived from the coordinated THF and phenyl ligands for **3.5** and **3.8.** Furthermore, the colourless appearance of compound **3.8** resulted in no apparent observed bands in the visible region of the spectrum.

Similarly, variable temperature optical measurements were conducted on the Dy(III) compound, **3.4** between 9-300 K, Figure 3.26. As a result of a combination of the low temperatures at which these measurements were performed and the homogeneous crystallinity of the sample consisting of compound **3.4**, gave even more resolution to both the visible and NIR spectrum. Sharp, defined absorption peaks in both the visible and NIR spectra are in good agreement with those bands associated with the Dy(III) ion, previously reported, Figure 3.27.[100] Furthermore, the absorption bands corresponding to the C-H stretch vibrations present in the NIR spectrum for compounds **3.5** and **3.8** are also present in the NIR spectrum for **3.4**, confirming that these are associated with the ligand, not the ESA of the central lanthanide(III) metal.

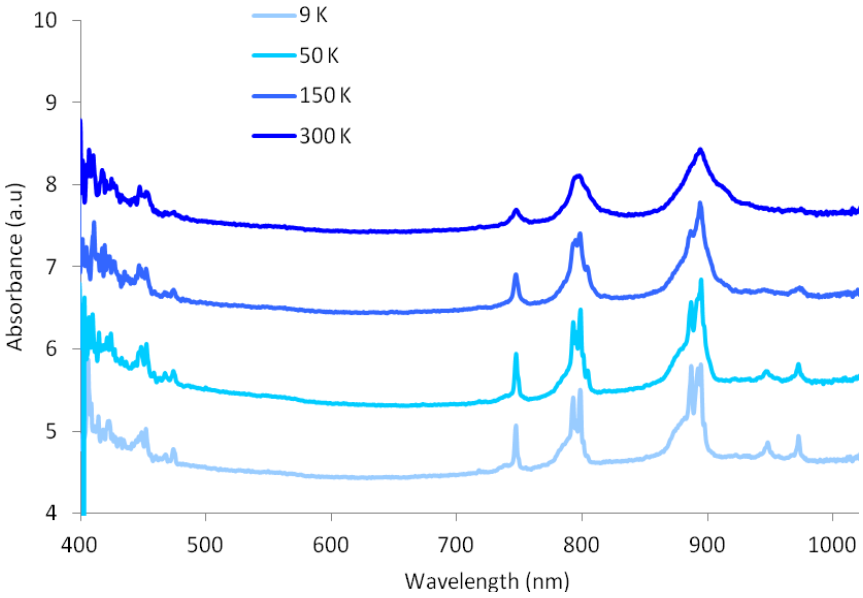

(a)

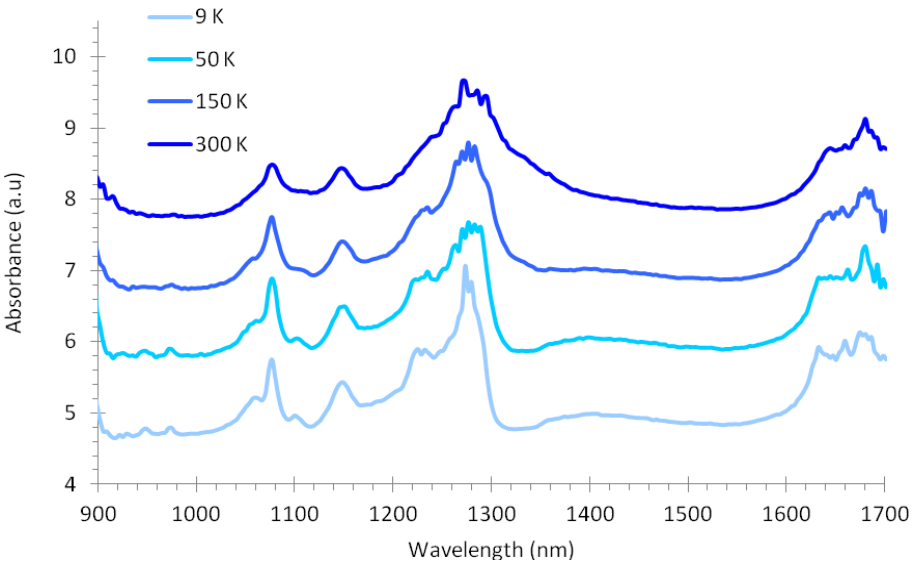

(b)

Figure 3.26 Variable temperature visible spectra for **3.4** (a) and variable temperature NIR spectra for **3.5** (b).

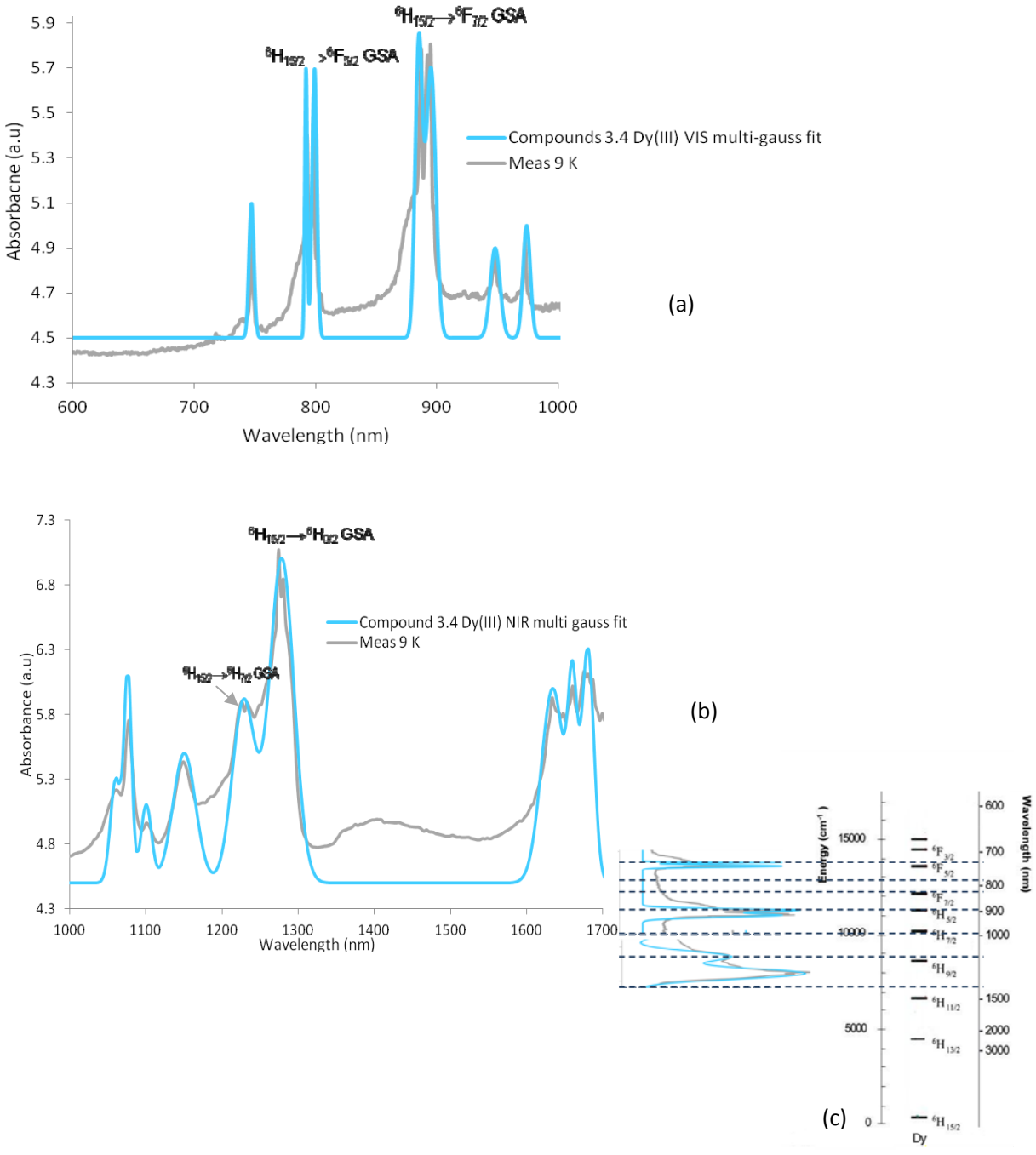

Figure 3.27 Multi–gauss fit data (blue) for compound **3.4** at 9 K in the visible region (a) and NIR (b), indicating ground state absorption bands. Observed absorption bands for **3.4** simulated onto an energy level diagram for Dy(III) (c).

To establish whether any ESA transition bands from the trivalent lanthanide ions for compound **3.5** are quenched by the presence of the C-H bonds, derived from the coordinated triphenylsiloxy ligand, NIR measurements were conducted on the unreacted triphenylsiloxide ligand Ph_3SiOH, alone, Figure 3.28. The C-H bond stretching overtones present at ~1145 and 1680 nm are distinctly observed in the NIR spectrum of Ph_3SiOH ligand, Figure 3.28. Consequently, these peaks can be excluded as ESA transitions from the rare earth metal of **3.5**.

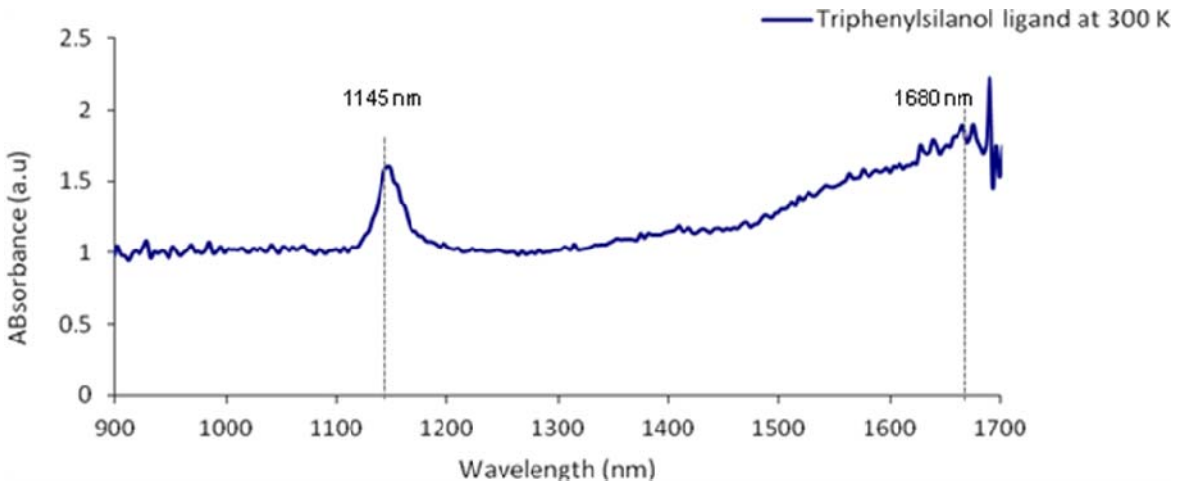

Figure 3.28 NIR spectrum for the triphenylsilanol pro-ligand Ph_3SiOH, showing the C-H absorptions at 1145 and 1680 nm.

Attempts were also made to perform visible and NIR absorption spectroscopy on the holmium compound **3.6**, however, it was found that the small quantity of sample available settled in the sample holder. Therefore, the sample was allowing too much

light to pass directly through, recording only a background spectrum rather than light being only absorbed by the sample.

The Gd(III) compound **3.7** is colourless and there are no energetically accessible excited states in the energy level diagram (Figure 3.18), therefore no absorption bands in either the NIR or visible region of the electronic spectrum were likely to be observed.

3.2.4 Conclusions to Variable Temperature Optical Spectroscopy and Further Discussion.

The optical spectroscopy data for compounds **3.4**(Er) and **3.5**(Dy) reveal a clear correlation between the electronic ground state transitions predicted in the general energy level diagram, Figure 3.20(b) and the absorption bands exhibited in both the visible and NIR spectra for both compounds. Direct evidence of this relationship is illustrated in the assignment of the relevant absorption bands to the corresponding ground state transitions in the energy level diagrams for compounds **3.4**, **3.5** and **3.8**(Tb). By placing the visible spectrum for compound **3.5** alongside a more detailed energy level diagram for the Er(III) ion in a known Er-doped glass fibre amplifier, labelled with the dominant Russell-Saunders $^{2S+1}L_J$ terms and the wavelength of the associated ground state absorption (GSA), it is apparent that there is good agreement between the principal absorbance peaks and the corresponding Er(III) levels as demonstrated by optical and magnetic studies conducted on the ethyl

sulfate compounds, Figure 3.29.[95-97]Consequently, these initial optical measurements may assist in validating the results of *ab initio* calculations used to determine the extent to which crystal field parameters influence the magnetic properties of high symmetry monometallic lanthanide compounds such as **3.4** and **3.5**, in addition to more complex polymetallic systems. Furthermore, conducting these optical experiments at low temperature increases the spectral resolution, presuming by decreasing the thermal motion of the ions.

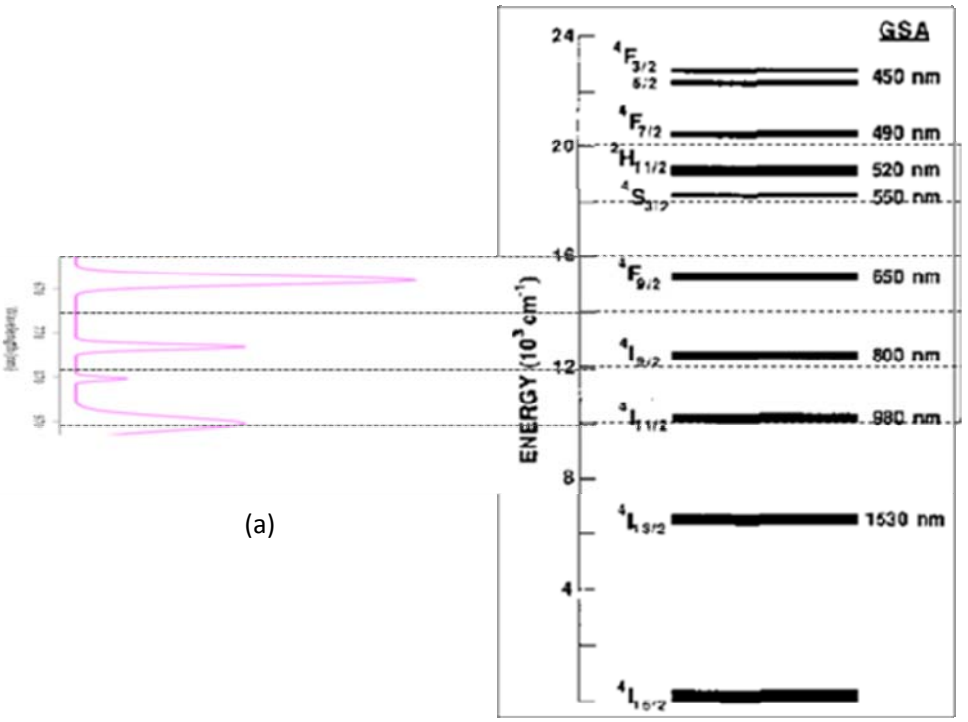

Figure 3.29 Visible spectra for compound 3.5 (a), simulated next to an energy level diagram for Er(III)-doped glass for fibre amplifers.[99]

Further evidence to support the assignment of the absorption bands corresponding to the appropriate energy level transitions, illustrated in Figure 3.20 can be observed

from the preliminary theoretical calculations for compound **3.5**, (Appendix Four). The theoretical calculations that give the energies (cm^{-1}) of the lowest spin-orbit Kramers doublets for **3.5**, appear to be in good agreement with the energy of the transitions expected for Er(III) ions**.** For instance, the selected energy values listed in Table 3.4 are transitioning for the Kramers doublets at values which correspond to the energy levels associated with the Er(III) ion, Figure 3.22, and therefore correspond to the detected absorption bands (see general energy level diagram in Figure 3.20(b)).

Dominant Term Symbols for Er(III).	**Corresponding absorption energy (cm^{-1}) for Er(III), Figure 3.20(b)**	**Selected Energies (cm^{-1}) of the lowest energy doublets in the group of Kramers doublets,(Appendix Three)**
$^4I_{13/2}$	~ 7000	**6872**
$^4I_{11/2}$	~ 10000	**10650**
$^4I_{9/2}$	~ 13000	**13415**
$^4S_{3/2}$	~ 19000	**19017**
$^4F_{7/2}$	~ 22000	**22624**
…	…	…

Table 3.4 Selected energies of the lowest spin-orbit Kramers doublets taken from the values which correspond to the electronic absorptions associated with the relevant energy level term symbol.

In Appendix Three there are much lower energy values given by the theoretical calculations and continue past what is observed in the spectra illustrated in Figures 3.23 and 3.24. This suggests that if the experiment was modified, using a higher resolution detector and the temperature at which these experiments were

conducted was lowered further, a much wider ranging and higher resolved spectrum may be observed, (Appendix Three). Hence, in principle the low-lying states may be detected in the emission spectroscopy.

Furthermore, it is common for Er(III) complexes to display hypersensitive transitions as a result of the interaction with the ligand or coordinating solvent molecules.[2,101] However, possibly as a result of the C-H vibronic stretching from the ligand, quenching the Er(III) ESA, hypersensitive transitions for **3.5** were not observed.

3.3 Overall Conclusions

The synthetic flexibility of the siloxide ligand, Ph_3SiOH, is demonstrated by the ease with which lanthanide precursors can react with these ligands not only from lanthanides towards the end the 4*f* series, but with early lanthanides too.[88] It would appear from the crystallographic information that the metal to ligand bond length decreases with decreasing cation size due to the lanthanide contraction, although there are only marginal differences in metal to ligand bond lengths between compounds **3.4**–**3.8**. Initial postulations for these reactions expected the formation of analogous structures to **2.2** and **2.3**, in the form of oxygen-bridged dimers. However, it would appear that partly due to the highly electronegative oxygen, which resides within these ligands, possessing much smaller covalent radius than sulfur, (66 ± 3 pm and 105 ± 2 pm respectively), sterically the preferred conformation of compounds **3.4**-**3.8** is to exhibit three bonded Ph_3SiO^- ligands and

three bonded THF ligands encapsulating the single lanthanide ion. This becomes more apparent when two synthetic routes are exploited (Scheme 3.7 and Scheme 3.8) to produce the same six coordinated octahedral complex, which in itself is highly unusual as the preferred coordination numbers in Ln(III) complexes are relatively high reaching, normally eight or nine coordinate (or more).

Furthermore, compounds **3.4** and **3.5** were the only two compounds of the series which were found to be SMMs, (albeit **3.5** a stronger SMM than **3.4**), whereas compounds **3.6** and **3.7** exhibit magnetic behaviour typically expected for single-ion lanthanide(III) complexes. Attempts to address the source of these observations were made through a series of theoretical calculations and optical absorption spectroscopy. Interestingly, compounds **3.4** and **3.5** were also the only two compounds to overtly exhibit optical activity in both the visible and the NIR regions of the absorption spectra. The extent to which these electronic transitions can be correlated with the crystal field and subsequently the magnetic data for these compounds, is yet to be determined. But, this preliminary data presents a strong insight into the differences in electronic properties between these compounds.

Overall, two novel synthetic routes led to the successful isolation of a family of monometallic lanthanide siloxide complexes **3.4**-**3.8**, which were structurally characterised by X-ray crystallography. Compounds **3.4** and **3.5** were found to be SMMs, with **3.5** exhibiting greater thermal activation barrier. Hence, even though

the general structural motif is known for other lanthanides including **3.4**,[88] there was no magnetic or electronic spectroscopy data, which has provided further insight into the chemical and physical properties of these compounds. In addition, developing two new accessible routes highlights the high reactivity of these siloxide ligands with lanthanide precursors.

Chapter Four

Synthesis, Structure and Magnetochemistry of 3*d* Transition Metal Compounds

4.1 Introduction to 3*d* Transition Metal Metallocenes

The world's first introduction to metallocenes came from the unanticipated discovery of the "dicyclopentadienyliron" complex, in 1951 by Kealy and Pauson, illustrated in Figure 4.1, as hybrid resonance structures.[102]

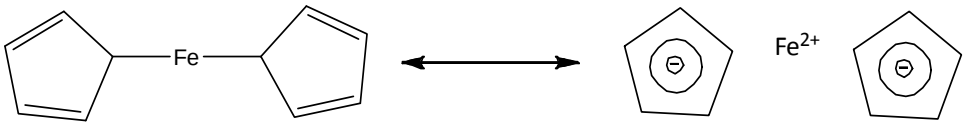

Figure 4.1 Scheme to show the proposed representation of dicyclopentadienyliron complex.

Whilst further reports on the structure were published by Miller, Tebboth and Tremaine in 1952,[103,104] it was not until 1954 that the more accurate model of the compound was revealed by Wilkinson and Fischer, exhibiting a "sandwich-like" structure along with a family of other transition metal sandwich complexes, (Figure 4.2).[4] It was these compounds that represent the name 'metallocenes' in their true form.

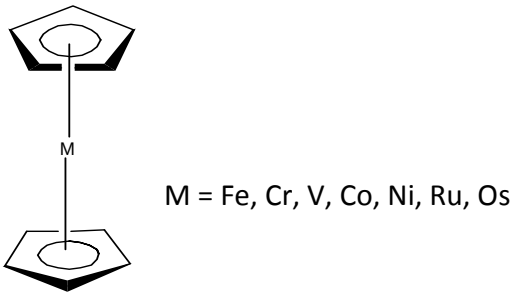

Figure 4.2 Representation of the sandwich metallocene complexes, $[(\eta^5\text{-}C_5H_5)_2M]$.

After Wilkinson identified the correct structural geometry of ferrocene, it was clear that the sandwich conformation was a result of good orbital overlap between the π–electrons in the *p* orbitals of the Cp rings and the *d* orbitals of the iron ion. In

addition, ferrocene is the only first row transition metal metallocene to possess no unpaired electrons and conforms to the 18-electron rule making this compound stable in air. Although this type of bonding had been considered before the discovery of the sandwich structure of ferrocene, this was the first experimental observation. The universal acceptance of this type of bonding (between metals and organic unsaturated molecules) laid the foundations for an abundance of organometallic chemistry with this type of complex.[105,106a]

The generic molecular orbital diagram, (MO) diagram for metallocenes, Cp_2M is illustrated in Figure 4.3. Here, there are three sets of π-orbitals, corresponding to the two staggered Cp rings to produce five molecular orbitals. There is a filled pair of low-lying orbitals of a_{1u} and a_{2u} symmetry and a filled set of e_{1g} and e_{1u} symmetry. In addition, there is an unfilled set of anti-bonding orbitals of e_{2g} and e_{2u} symmetry at higher energy. This occurs for a staggered D_{5d} symmetry molecule. Therefore, the molecular orbital bonding diagram can subsequently be simulated for the metallocene in question, with the appropriate symmetry, and is dependent on how these ligand orbitals overlap with the metal orbital. The molecular orbital diagram must also reflect the relative energies of the ligand orbitals and metal orbital components. For example Fe(II) exhibits d^6 $(e_{2g})^4$ $(a_{1g})^2$, however Mn(II) exhibits d^5 $(e_{2g})^2(a_{1g})^1$ $(e_{1g})^2$, which explains why the metallocenes are known for their range of *d*- electron counts.[106a]

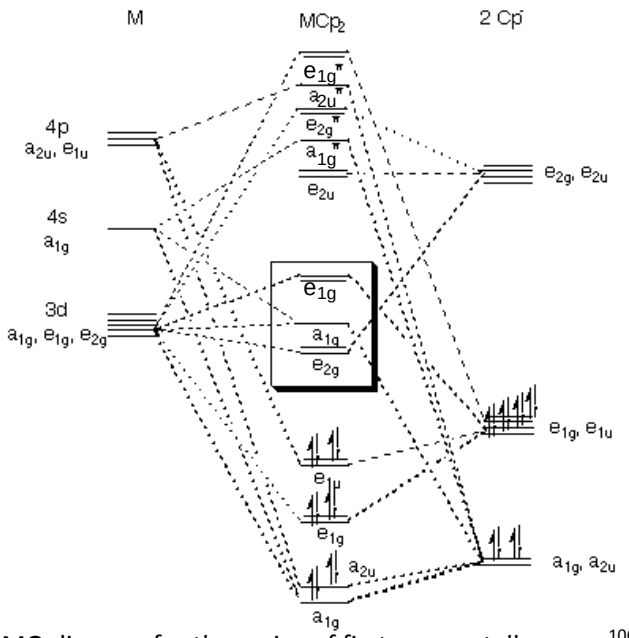

Figure 4.3 Generic MO diagram for the series of first row metallocenes.[106b]

The main focus of a majority of metallocene chemistry has been based on ferroecene because of its high stability and therefore relative ease of preparation.[106] The metallocenes of these heavier metals, such as ruthenocene and osmocene are much more costly to prepare, in addition to having less convenient and low yielding synthetic routes compared to that of ferrocene. As a result there are far fewer reports on these compounds. Much more prominently reported metallocenes however, are chromocene and manganocene.

Manganocene exhibits quite distinct differences with regard to its physical and chemical properties in comparison to those commonly observed in the rest of the family of 3*d* metallocenes Cp_2M (M = V, Cr, Fe, Co and Ni).[107] Manganocene is conveniently prepared by reacting manganese(II) halides with NaCp in THF and

isolated as very dark brown crystals. Cp_2Mn exhibits simple anti-ferromagnetic exchange below 432 K, which is thought to be caused by the intra-chain interactions between the Mn(II) ions of the unconventional zigzag crystal structure that manganocene adopts (Figure 4.4). Above 432 K, however, Cp_2Mn adopts the more commonly exhibited sandwich motif.[107]

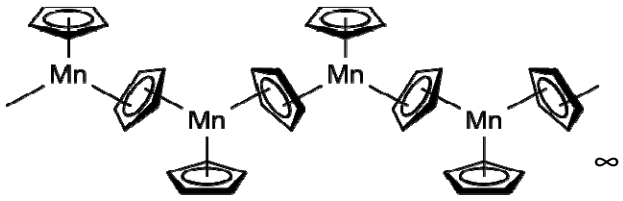

Figure 4.4 Atypical zig-zag structure adopted by manganocene.[107]

Furthermore, manganocene also displays unusual characteristics when compared to other organometallic metallocenes, because the manganese(II)-carbon bond is effectively ionic in nature. This distinct and crucial property is what largely separates manganocene and its derivatives from typical transition metal organometallics. The abnormal behaviour of Cp_2Mn has been attributed to the high stability associated with the high-spin S = 5/2, Mn(II) ion, in the which 3*d* valence orbitals are half-filled at room temperature.[106,107] Furthermore, the polar characteristic enables manganocene to act as a Brønsted base towards organic acids.[5,107]

All the bonding and non-bonding orbitals are filled for the Group 8 metallocenes (Fe, Ru, Os), therefore it is inevitable that these represent the most stable members of the series. Chromocene and vanadocene are paramagnetic, and because the valence

electron count is less than 18, they are quite susceptible to coordinate to additional ligands that will provide extra electrons. However, this makes them extremely air sensitive because oxygen can coordinate to them and oxidise the metal (i.e. Cr(II) oxidises to Cr(III) and V(II) can oxidise to V(III) and V(IV). Similarly, manganocene has only 17-electrons, hence is extremely reactive and is the only 3*d* metallocene to be readily hydrolysed by water and dilute hydrochloric acid.[106a,107c]

Analogously, to manganocene, chromocene is prepared generally by the reaction of chromium(III) halides with NaCp in THF, and isolated as very dark red chromium(II) d^4 crystals, which are soluble in THF. Although chromocene is paramagnetic, and highly reducing, the effective spin magnetic moment is significantly higher (μ_{eff} = 3.27 BM) than that of the expected spin only value for two unpaired electrons (μ_{eff} = 2.83 BM), which implies there is significant orbital contribution.[106] Consequently this results in a configuration which occurs from the removal of one electron from each completely filled e_{2g} and a_{1g} level's closed shell arrangement.

4.2 From Metal-Organic to Organometallic Cluster Chemistry.

There have been many reports on the development of oxygen-bridged manganese compounds that have utilised manganese carboxylate and β-diketonate-bridging ligands to produce single-molecule magnets.[108-110] Well established synthetic routes to developing molecules exhibiting slow magnetic relaxation commonly take the form of reacting an inorganic source material, usually metal salts, with bridging

oxygen donor ligand, alongside a capping co-ligand. The capping co-ligand serves the purpose of accommodating the co-ordination requirements of the metal ion. In addition, this reaction will take place in the presence of a non–innocent solvent, which in turn may coordinate to the cluster. A general scheme for reactions of this nature is illustrated in Scheme 4.1. An example of an oxygen-bridged manganese cluster that uses this style of synthesis is given in Figure 4.5.

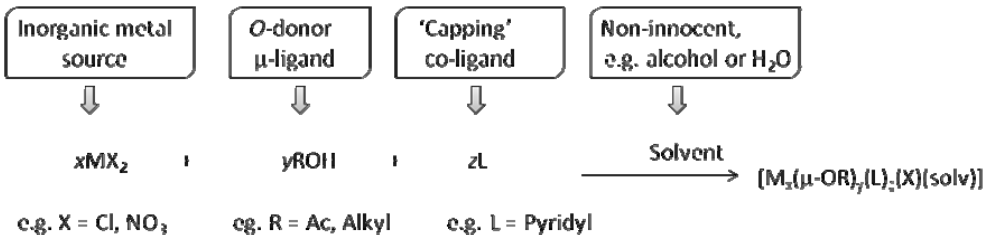

Scheme 4.1 Scheme to show the traditional synthetic route for developing oxygen-bridged metal clusters that are also SMMs.

There are many examples in the literature of manganese compounds where the metal centres bear +3 oxidation states and also mixed valence oxidation states, exhibiting one +2 oxidation state surrounded by two or more +3 oxidation state metal ions.[111] However, there are comparatively few compounds reported with three paramagnetic M(II) centres. These are more commonly known for iron,[112] nickel,[113] cobalt[114] and copper.[115] Figure 4.5 illustrates a Mn(II) pivalate cage, which emulates analogous cobalt(II) pivalate chemistry.[15] The synthesis of $[Mn_3(Me_3CCO_2)_6(Me_3CCO_2H)_5]\cdot 2(Me_3CCO_2H)$(**4.1**), directly addresses the gap in the development of trimetallic manganese(II) complexes compared with that of the previously mentioned transition metal complexes.

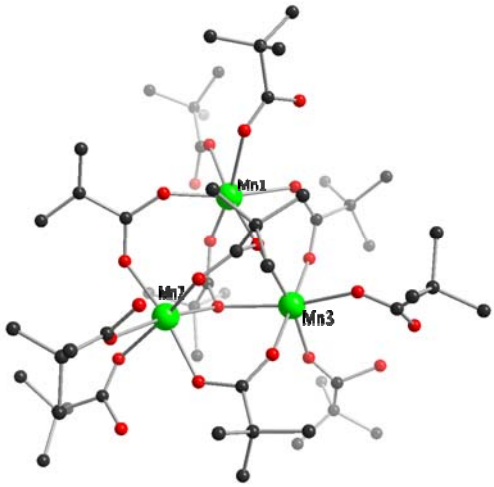

Figure 4.5 Structure of the trimetallic manganese(II) compound, $[Mn_3(Me_3CCO_2)_6(Me_3CCO_2H)_5]\cdot 2(Me_3CCO_2H)$ (**4.1**).[116]

Conversely, in recent years there has been great interest into developing new synthetic routes to developing SMMs. These incorporate organometallic precursors, utilising both oxygen-bridging ligands (which are prominent within this class of chemistry), and other organic non-oxygen bridging ligands, for instance chalcogen-based ligands such as those featuring sulfur. The synthetic template for reactions that follow by this method is illustrated in Scheme 4.2

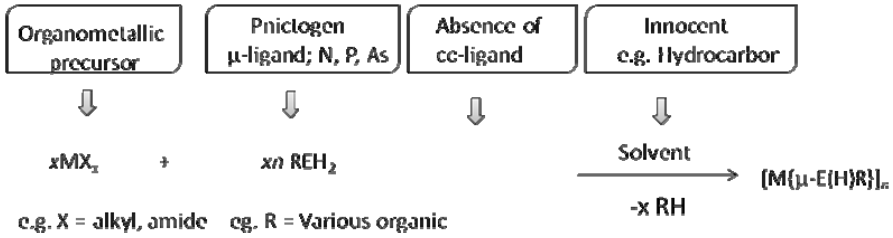

Scheme 4.2 A scheme to show the organometallic synthesis for developing SMM clusters.

A majority of the reactions of this nature has utilised nitrogen-based ligands to achieve higher blocking temperatures than the existing maxima. Scheme 4.3 outlines the synthesis of $[(Cp)Mn\{2\text{-}NH(4,6\text{-}Me_2pm)\}\cdot Mn\{2\text{-}N\text{-}(4,6\text{-}Me_2pm)\}]_4$ (**4.2**) reported by Layfield et al. and is generated by the reaction of an organometallic precursor, alongside a nitrogen-bridging ligand, in the absence of a traditional capping co-ligand.[117]

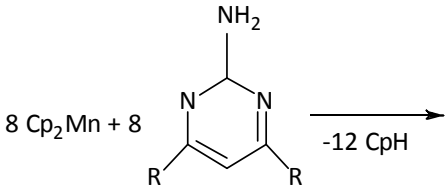

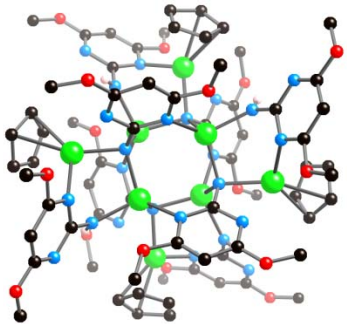

Scheme 4.3 A scheme to the reaction manganocene to yield $[(Cp)Mn\{2\text{-}NH(4,6\text{-}Me_2pm)\}\cdot Mn\{2\text{-}N\text{-}(4,6\text{-}Me_2pm)\}]_4$ (**4.2**)[117]

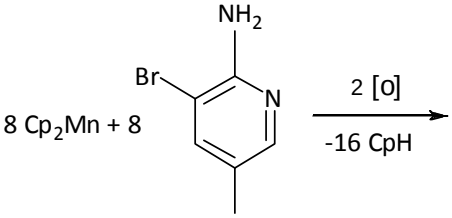

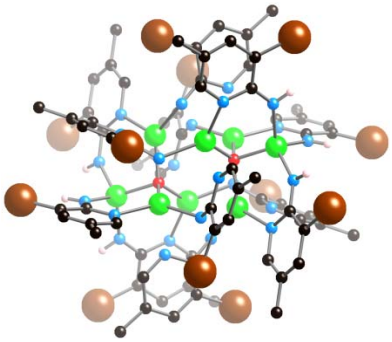

Scheme 4.4 A scheme to show the reaction of manganocene to yield $[Mn_4(\mu\text{-}O)\{N(H)Ar^2)_4]_2$ (**4.3**)[117]

Furthermore, there is no coordinating solvent within the framework of the structure, which makes it easier to control the coordination environments of the resulting compound. In addition, Scheme 4.2 also illustrates the utility of organometallic precursors to generate novel clusters which have no need to include

the capping co-ligand featured in the tradition framework illustrated in Scheme 4.1. The manganese(II) ions in **4.2** and **4.3** are high spin d^5, which typically results in an antiferromagnetic exchange. Although, these compounds do not reveal particularly interesting magnetic properties, they do demonstrate the utility of generating paramagnetic, organometallic compounds from atypical synthetic routes.

The preparation of **4.2** involves manganocene, which doubly deprotonates the NH_2 group of the moderately acidic 2-amino-4,6-dimethylpyrimidine, and so this general approach presents a potentially widely applicable synthetic route to high nuclearity Mn(II) imido cage compounds.[117,118] Consequency, these systems are intriguing and are worth exploring with respect to the prospect of remarkable magnetic interactions.

4.3 Organometallic Sulfur-Bridged Transition Metal Compounds

In contrast to the abundance of iron–sulfur cluster chemistry, there is considerably less reported on analogous manganese-sulfur cubane cluster chemistry. Holm, Berg et al. have made a significant contribution to the synthetic and structural analysis of sulfur-bridging iron compounds.[119a-b] In an attempt to address this lack of manganese–sulfur cluster chemistry Onaka and Katukawa have synthesised several sulfur-bridging manganese clusters.[119c] The 'cubane-like' tetramer $Mn_4(SPh)_{4(}CO)_{12}$ (**4.4**), was reacted with Me_3NO (trimethylamine *N*-oxide) alongside 1,1-bis(diphenylphosphino)ferrocene, (dppfe) to give $[Mn(CO)_3]_2(\mu\text{-}SPh)_2(\mu\text{-}dppfe)$(**4.5**),

Figure 4.6.[119c] The irregular octahedral arrangement around the Mn(II) atom stems from the acute S-Mn-S angle (75.8(2)°), as a result of steric repulsion between the phenyl groups. Compound **4.4** is prepared according to established literature procedure,[119e-g] where it was initially thought that upon the reaction of **4.4** with Me_3NO and dppfe, a dppfe-bridged dimer would be produced resembling a structure similar to $[Mn_4(SPh)_3(CO)_2](\mu$-dppfe). However, as compound **4.5** was generated, it was considered that compound **4.4** had degraded during the reaction to produce the intermediate dimer $Mn_2(SPh)_2(CO)_6$ upon addition of Me_3NO, and it is this dimer that reacts with dppfe to produce compound **4.5**.

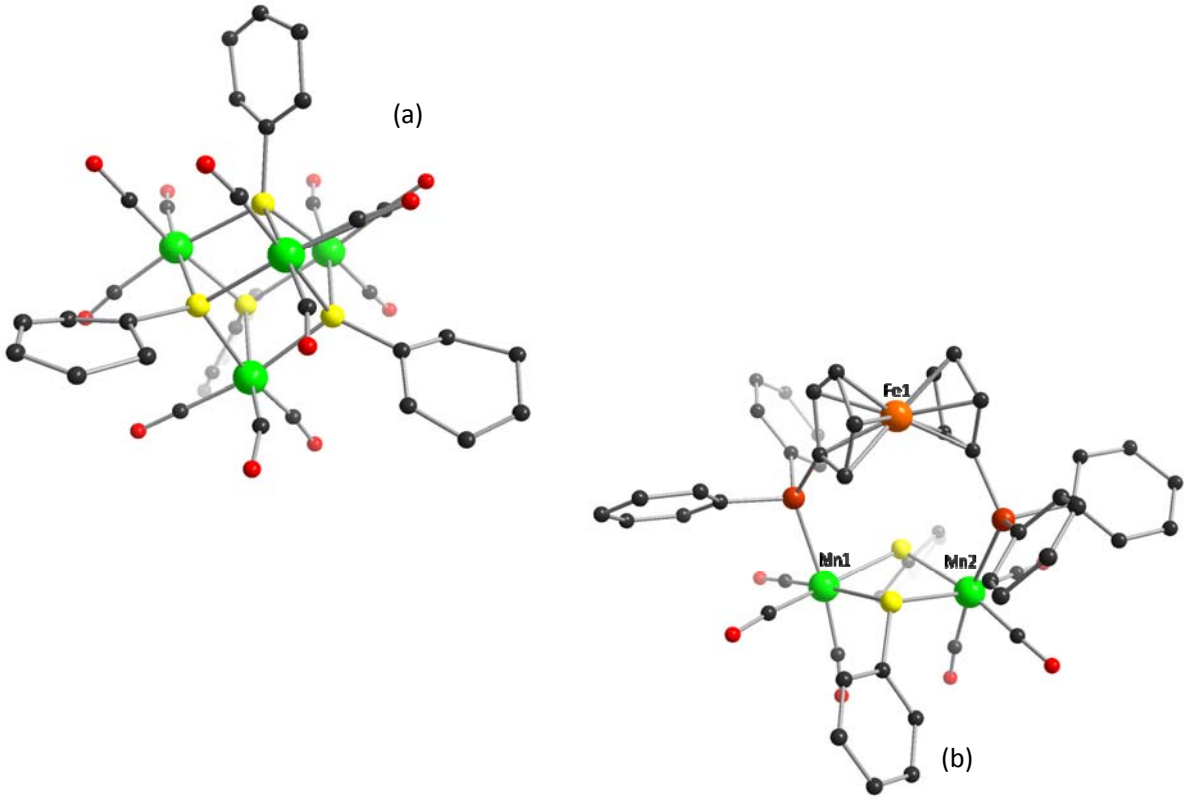

Figure 4.6 Molecular structures of compounds $Mn_4(SPh)_{4(}CO)_{12}$ (**4.4**)(a)[119e-g] and $[Mn(CO)_3]_2(\mu$-$SPh)_2(\mu$-dppfe)(**4.5**) (b).[119c] Hydrogen atoms have been omitted for clarity.

Similarly, whilst there have been some notable examples of sulfur-bridging chromium compounds,[120-122a] there are far fewer reports in the literature when compared to that of iron–sulfur cluster chemistry. The magnetic interactions between the Cr(II) ions within chromium-sulfur complexes, have been subject to growing interest over a number of years, commonly revealing antiferromagnetic behaviour.[120,121] The $Cr(NCS)_2(tu)_2$](**4.6**) (where tu = thiourea) complex (**4.6**), Figure 4.7, shows chains of directly interacting metal ions in a square planar conformation. Magnetic studies of the *trans*-planar stacked units of **4.6** exhibit a Cr···Cr separation of 3.97 Å and as a result of this large separation, compound **4.6** is only weakly antiferromagnetic.

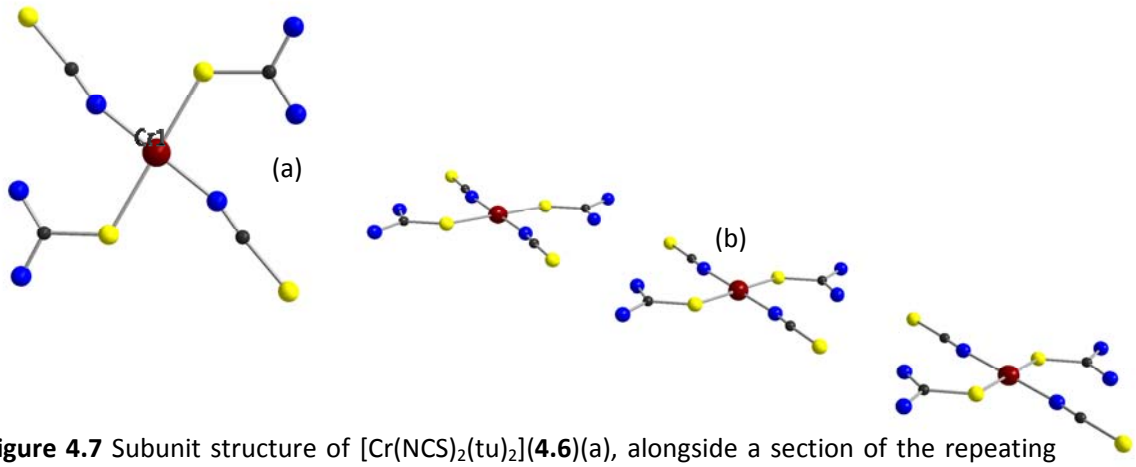

Figure 4.7 Subunit structure of $[Cr(NCS)_2(tu)_2]$(**4.6**)(a), alongside a section of the repeating units for compound **4.6**.[120]

4.4 Background and Aims

Whilst there are many examples of 3*d* transition metal complexes bridged by chalcogen-based ligands, the successes of reacting ligand, Ph_3SiS-Li (**2.1**) or Ph_3SiOH

with lanthanide precursors, (reported previously in Chapters Two and Three), led to the proposal of reacting these ligands with 3*d* transition metals too. Furthermore, distinct molecular cage compounds incorporating transition metals and ligands with Group 16-donor ligands are of particular significance due to their potential to be exploited as precursors for nano-scale metal-chalcogen clusters.[9,13] Consequently, the physical and magnetic properties of these compounds will also be an area of great interest as, specifically in the contexts of these Group 16 ligands, reports of reactions with transition metal precursors are somewhat rare. In particular, precursors incorporating manganese and chromium will be the main focus of this Chapter, namely manganocene and chromocene. The apparent differences between the chemical properties of these two potential precursors, (*vide supra*), will present some intriguing possibilities in terms of their reactivity and the effect this will have on their structure will be subject to crystallographic investigation. Hence, the reaction of manganocene with the siloxide ligand, Ph_3SiOH, and ligand (**2.1**) is reported, to produce the trimetallic $[Cp_2Mn_3(\mu\text{-}OSiPh_3)_4]$ (**4.7**) and the hetero-cubane $[CpMn(\mu\text{-}SSiPh_3)]_4$ (**4.8**) compounds respectively. Moreover, in a reaction of chromocene with ligand **2.1** the sulfur-bridged $[CpCr(\mu\text{-}SSiPh_3)]_2$ (**4.9**) dimer is generated. The magnetic properties of compounds **4.7**-**4.9**, which exhibit the general formula $[CpM\{\mu\text{-}(ER_x)\}]_n$ (where M = transition metal, E = chalcogen atom), are also reported.

4.5 Results and Discussion

4.5.1 The Synthesis and Structure of Trimetallic Manganese(II) Siloxide Complex.

The preparation of $[Cp_2Mn_3(\mu\text{-}OSiPh_3)_4]$(**4.7**), is illustrated in Scheme 4.5. The direct manganation of the O-H bond of the siloxide ligand in toluene, using either 1:1 or 3:4 (metal:ligand) stoichiometries, give the same outcome and produce a yield of 46% (based on manganese).

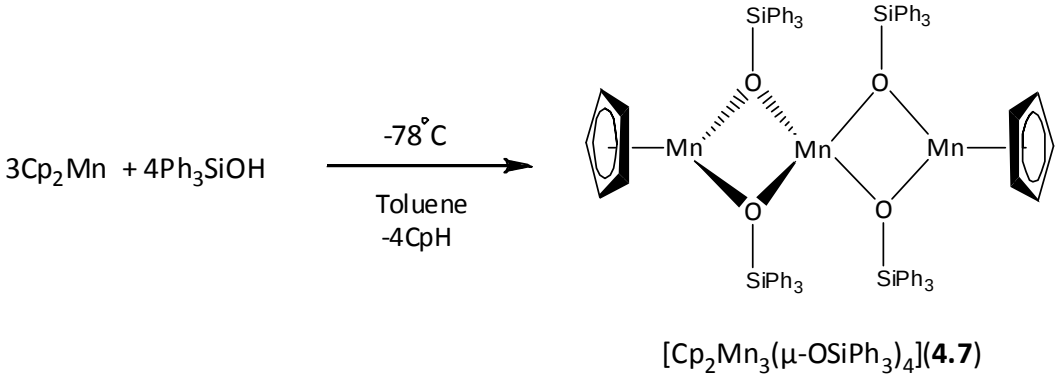

$[Cp_2Mn_3(\mu\text{-}OSiPh_3)_4]$(**4.7**)

Scheme 4.5 Synthesis of the trimetallic oxygen-bridged compound **4.7**.

The trimetallic manganese siloxide compound, **4.7** was crystallised at 4 °C in a saturated toluene solution to give colourless, rod-shaped single crystals of **4.7**.(2 toluene), suitable for X-ray crystallography. The toluene molecules present in the lattice are removed by prolonged drying *in vacuo*, where removal is confirmed by elemental analysis. Obtaining a good elemental analysis for compound **4.7**, proved difficult as a result of the high sensitivity to air and moisture commonly experienced when handling cyclopentadienyl Mn(II) compounds. However, after several attempts, isolation of a sample that proved to be suitable for elemental analysis was achieved and the results compared well with the calculated values (*vide infra*;

Chapter Six, 6.15). In addition, characterisation of **4.7** by solution phase ^{1}H NMR spectroscopy showed evidence of proton coupling patterns expected for the proton environments of the two Cp ligands (2.04 ppm, 10 ^{1}H, s, CpMn) and the twelve phenyl groups (6.23-7.28 ppm, 60 ^{1}H, m, phenyl, with a broad peak at 7.09 ppm), Figure 4.8 (*vide infra*; Chapter Six, 6.15). Furthermore, those peaks that are associated with the protons of the phenyl groups from the $OSiPh_3$ siloxide ligand compare well to the chemical shifts previously reported for the coordinated triphenylsiloxy groups (δ-7.09-7.44 ppm).[122b,c] However, broad range ^{1}H NMR experiments conducted on **4.7**, failed to detect peaks in the wider range paramagnetically shifted region of the spectrum (between −200 ppm to +200 ppm), even though **4.7** was found to be paramagnetic.

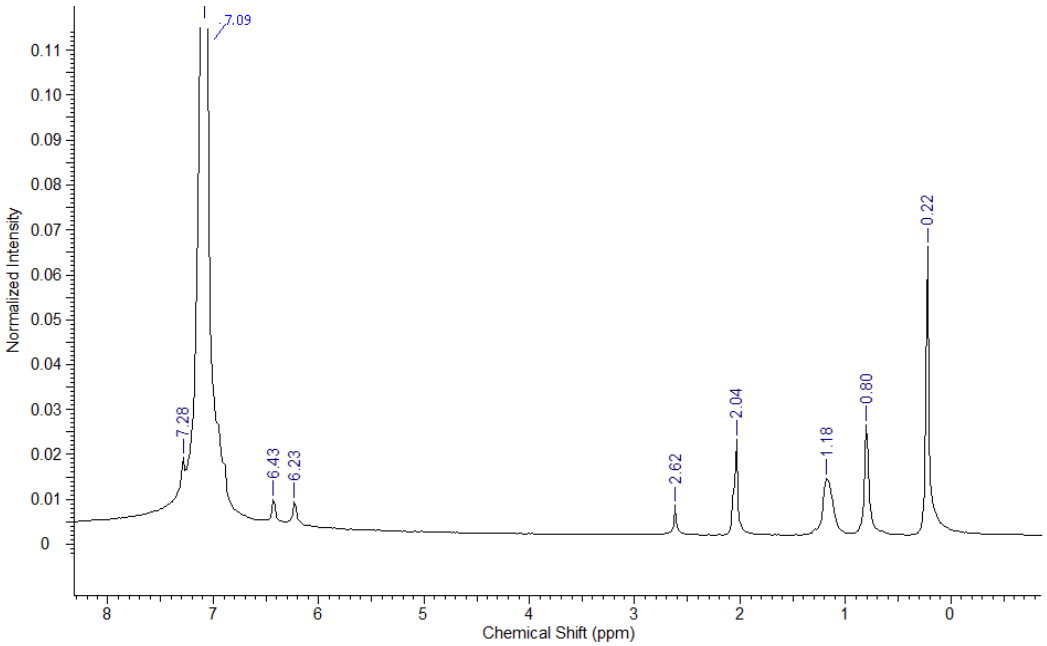

Figure 4.8 ^{1}H NMR spectrum for compound **4.7** in deuterated benzene, (d_6-C_6D_6).

Compound **4.7** crystallises in the centrosymmetric space group $P2_1/n$, with a molecular structure consisting of three manganese atoms that are bridged by four $[\mu\text{-}Ph_3SiO]^-$, with the two terminal manganese atoms being complexed by a single Cp ligand each, Figure 4.9. The bridging Mn-O bond lengths within complex **4.7**, range between 2.050(7)-2.076(7) Å, which results in a Mn1···Mn2 separation of 3.016(27) Å and a Mn2···Mn3 separation of 3.028(26) Å, which are typical for manganese-manganese separations in compounds with single atom bridges.[116,123a] The Mn-C distances of **4.7** are in the range of 2.376(13)-2.455(19) Å for Mn1 and 2.380(12)-2.445(12) Å for Mn3, which are expected bond lengths for manganese cyclopentadienides.[117] The terminal manganese sites are five coordinate, with the central manganese having a four coordinate geometry. Furthermore, the O-Si bonds lengths range between 1.634(7)-1.656(8) Å, which are relatively short considering the presence of the sterically bulky phenyl groups residing on the siloxide ligand.

The bond angles that exist between the two terminal CpMn and the oxygen-bridging siloxide ligands for the Mn1-O1-Mn2 and Mn3-O2-M2 core within compound **4.7** are slightly over 90° ranging between 93.98(3)°–94.98(3)°. Conversely, the bond angles that exist between the O2-Mn2-O4 and O1-Mn2-O3 are more obtuse ranging between 115.91(3)°–131.38(4)°, resulting in distortion around the central Mn(II) ion. Whilst there have been many examples of Mn(II) dimetallic complexes containing hard ligands such as the siloxides exhibited within this compound, there have not been any reports on linear trimetallic Mn(II) mono-

cyclopentadienyl compounds with manganese(II) to date. In addition, the magnetic exchanges that may occur within this compound are of particular interest.

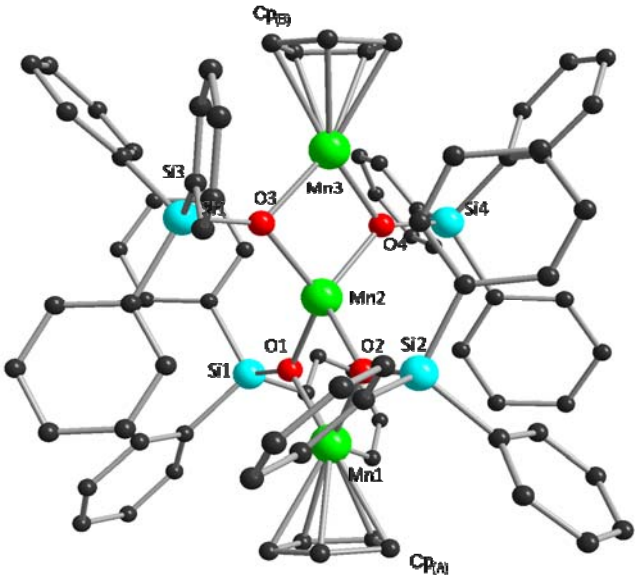

Figure 4.9 Molecular structure of **4.7**, with the hydrogen atoms omitted for clarity. Selected distances/Å and angles/°: Mn1-O3 2.053(7), Mn1-O4 2.058(7), Mn2-O3 2.073(7), Mn2-O4 2.050(7), Mn2-O1 2.057(7), Mn2-O2 2.053(7), Mn3-O1 2.076(7), Mn3-O2 2.064(7), Si1-O1 1.646(8), Si2-O2 1.645(8), Si3-O3 1.634(7), Si4-O4 1.656(8), Mn1-$Cp_{(A)}$ 2.376(13)-2.455(19), Mn3-$Cp_{(B)}$ 2.380(12)-2.445(12), Mn1-O4-Mn2 94.45(3), Mn1-O3-Mn2 93.98(3), Mn2-O1-Mn3 94.25(3), Mn2-O2-Mn3 94.39(3), Mn3-O1-Si1 130.14(4), Mn3-O2-Si2 129.11(4), Mn1-O4-Si4 129.51(4), Mn1-O3-Si3 131.38(4),O1-Mn2-O3 115.9(3), O4-Mn2-O2 122.01(3), O3-Mn1-O4 85.9, O2-Mn2-O1 129.4(3)

Table 4.1 Crystallographic data and summary of structural refinement for compound **4.7**

Empirical Formula	$C_{86}H_{86}Mn_3O_4Si_4$ (**4.7**)
Formula Weight (g mol^{-1})	1460.76
Temperature (K)	100(2)
Crystal System	Monoclinic
Space Group	$P2_1/n$
Colour	Colourless
a (Å)	14.632(4)
b (Å)	26.084(8)
c (Å)	20.375(6)
α (deg)	90
β (deg)	94.221(6)
γ (deg)	90
Volume ($Å^3$)	7755(4)
Z	4
ρ_{calcd} (kg m^{-3})	1.315
R1 [I>2.0 σ(I)][a]	0.0739
wR2 (all data) [a]	0.2478

[a] $R1 = \Sigma (||F_0| - |F_c|| / \Sigma|F_0|)$. [b] $wR2 = [\Sigma[w(F_0^2 - Fc^2)^2] / \Sigma[w(F_0^2)^2]]^{1/2}$

4.5.2 Magnetic Studies for Compound 4.7

4.5.2.1 d.c Magnetic Susceptibility Measurements

Direct current (d.c.) magnetic susceptibility measurements were conducted on a polycrystalline sample of compound **4.7**, which was prepared in a glove box, and within a temperature range of 2-300 K, in an applied field of 1 kG, Figure 4.10.

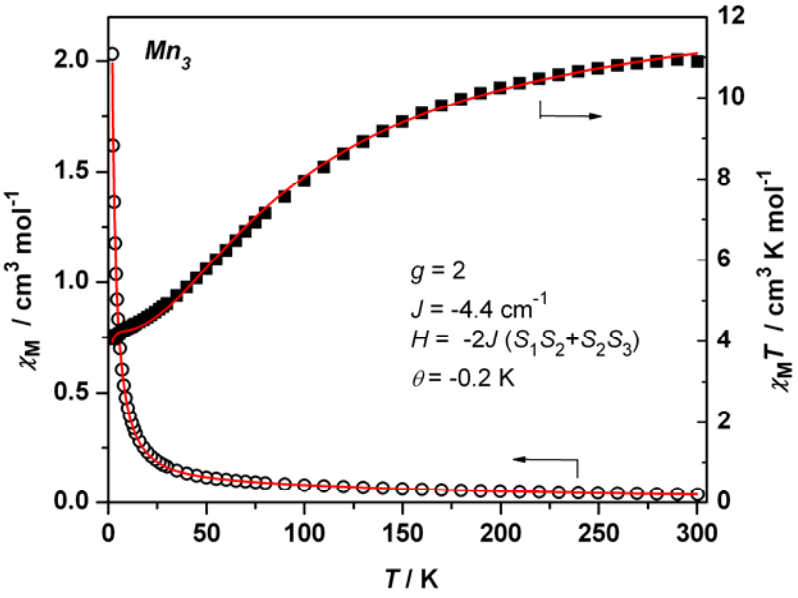

Figure 4.10 Magnetic data plot showing the temperature dependence of χ_M and $\chi_M T$ for compound **4.7** for the field strength H = 1 kG, with the red lines representing the fits to the experimental data using the parameters above.

The χ_M and $\chi_M T$ magnetic susceptibility data plots show weak antiferromagnetic exchange between the three high spin Mn(II) d^5, giving a $\chi_M T$ value of 11.0 cm^3 K mol^{-1} (S = 5/2 , L= 0, J = 5/2, g = 2; ground term symbol $^6S_{5/2}$). This value is lower than the expected value for three non-interacting Mn(II) ions of

13.13 cm^3 K mol^{-1}. Upon cooling, the $\chi_M T$ decreases steadily to 4.0 cm^3 K mol^{-1} at 2 K, which is consistent with that typically expected for a single Mn(II) ion of 4.38 cm^3 K mol^{-1} and indicative of a chain of three aniferromagnetically coupled Mn(II) ions. The susceptibility data for **4.7** can be modelled using the isotropic spin-Hamiltonian $H = -2J(S_1S_2 + S_2S_3)$, where S_x corresponds to the spins on the three Mn(II) ions (where, S_1 = Mn1, S_2 = Mn2 and S_3 = Mn3), Figure 4.11. This model allows for the exchange coupling constant J to be determined, where J = -4.4 cm^{-1}.

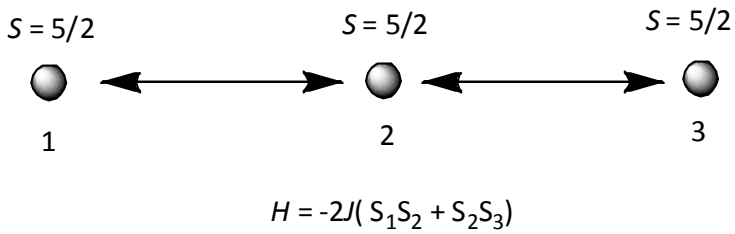

Figure 4.11 Spin-Hamiltonian model used to derive the exchange coupling constant *J*.

Furthermore, since the metal ions of **4.7** are aligned in linear chain, (Figure 4.11), the compound is not spin frustrated. Therefore, the antiferromagnetically interacting spins are able to minimise their energy, as each spin associated with the three metal ions can align itself oppositely with that of its neighbour leading to the antiferromagnetic coupled exchange.

4.5.3 The Synthesis and Structure of a Hetero-Cubane Manganese(II) Thiolate Complex.

The sulfur-bridged tetramer $[CpMn(\mu\text{-}SSiPh_3)]_4$ (**4.8**) was synthesised through transmetallation under the reaction conditions outlined in Scheme 4.6, to produce relatively low yields of 17 %.

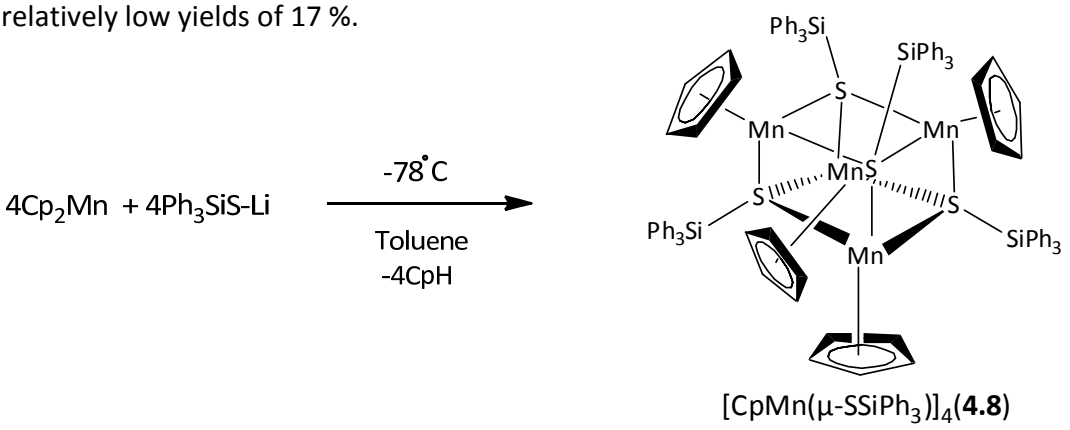

Scheme 4.6 Synthesis of the hetero-cubane$[CpMn(\mu\text{-}SSiPh_3)]_4$ (**4.8**) tetramer.

Compound **4.8**.(2 toluene) was synthesised utilising the lithiated thiolate ligand, **2.1**, also exploited in the production of compounds **2.2** and **2.3**. In the same manner as with compound **4.7**, the toluene molecules present in the lattice were removed by thoroughly drying *in vacuo*. The removal of lattice toluene was confirmed by elemental analysis, as the calculated elemental values were compatible with the experimental values, excluding the additional solvent toluene (*vide infra*; Chapter Six, Section 6.16). Furthermore, the proton coupling patterns from solution phase ^1H NMR spectroscopy exhibit chemical shifts, representative of the protons residing on the twelve phenyl groups, (6.89-7.77 ppm, m, 6 ^1H, phenyl; 6.06-6.45, m, 12 ^1H phenyl) and the proton environments on the four Cp ligands (2.04 ppm, 5 ^1H, s, CpMn), (*vide infra*; Section Six, 6.16). However, broad range ^1H NMR experiments

conducted on **4.8**, failed to detect peaks in the paramagnetic region of the spectrum (between −200ppm to +200ppm), similarly to compound **4.7**. This could possibly be as a result the weak magnetic interactions between the Mn(II) ions for these compounds (Section 4.5.4).

Compound **4.8** was crystallised by the slow cooling of a saturated toluene solution to give colourless block-shaped single crystals suitable for X- ray crystallography. Compound **4.8** crystallises in the centrosymmetric space group P-1 as a hetero-cubane tetramer, with the molecular structure consisting of four manganese atoms that are bridged by four $[\mu_3\text{-}SSiPh_3]^-$ ligands to from the Mn_4S_4 core, Figure 4.12. Each of the four manganese atoms are complexed by a Cp ligand, coordinated in a η^5-manner. All of the Mn-S bridging bond lengths of compound **4.8**, range between 2.5786(11) Å and 2.6795(11) Å, which results in Mn···Mn separation across the four Mn(II) ions ranging between 3.8072(8) Å –3.8321(9) Å. These Mn···Mn distances are relatively consistent with Mn···Mn separation distances previously reported for Mn(II) tetramers.[119] Interestingly, the Mn4-S4 bond distance is 0.06 Å longer the mean bond lengths for the other Mn-S bond distances which are all within 0.04 Å of each other. This slight extension could possibly be in order to accommodate the sterically bulky $SiPh_3$ groups. Consequently, the Mn(II) ions of compound **4.8** adopts a six-coordinate 'piano-stool' environment, with a formal valence count of 17-electrons. Furthermore, the Mn-Cp distances for each of the four metal ions are all relatively similar, ranging between 2.363(4) Å-2.543(4) Å, and are similar to that

expected for Mn(II) cyclopentadienides.[123a] All the Mn-S-Mn bond angles are slightly obtuse averaging at 94.37°, and exhibit acute angles between the S-Mn-S bonds averaging at 85.56°, therefore compound **4.8** is not quite by definition a cubane, rather it has a slightly distorted cubane structure.

Interestingly, the reaction conditions of $MnCp_2$ with Ph_3SiOH to give compound **4.7** and the reaction of $MnCp_2$ with Ph_3SSi-Li to yield **4.8** are very similar, therefore the initial postulation, when undertaking the reaction outlined in Scheme 4.6, was to essentially derive an analogous compound to that of **4.7**, (substituting the oxygen bonded ligand with sulfur). However, as a result of the bridging Mn-S bonds in **4.8** being considerably longer than that of the Mn-O bond lengths within **4.7**, structurally, this allows for an additional subunit to form part of **4.8**, creating a 'cubane-like' structure, with two further complexing Cp ligands. Consequently, this leads to the trimetallic, tetrahedral arrangement at the central Mn(II) ion, being more geometrically favourable for compounds **4.7** with the shorter Mn-O bond lengths.

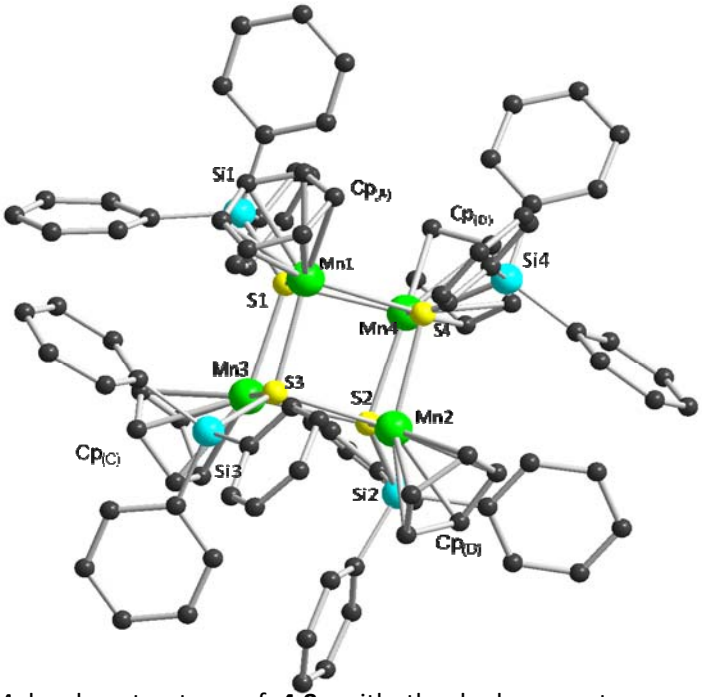

Figure 4.12 Molecular structure of **4.8**, with the hydrogen atoms omitted for clarity. Selected distances/Å and angles/°: Mn1-S1 2.6022(11), Mn1-S2 2.6181(11), Mn1-S4 2.5876(10), Mn2-S1 2.6013(10), Mn2-S2 2.5941(11), Mn1-S3 2.6096(10), Mn3-S4 2.5786(11), Mn3-S2 2.5950(11), Mn4-S1 2.5888(10), Mn4-S3 2.5812(10), Mn4-S4 2.6795(11), S1-Si1 2.156(14), S2-Si2 2.153(14), S3-Si3 2.146(13), S4-Si4 2.152(13), Mn1-$Cp_{(A)}$ 2.387(4)-2.487(4), Mn2- $Cp_{(B)}$ 2.397(4)- 2.543(4), Mn3- $Cp_{(c)}$ 2.363-2.458(5), Mn4-$Cp_{(D)}$ 2.372(4)-2.469(4), S4-Mn1-S1 86.77(3), S1-Mn1-S2 85.66(3), S2-Mn2-S1 86.17(3), S1-Mn2-S3 84.69(3), S2-Mn2-S3 85.69(3), S4-Mn3-S3 86.18(3), S4-Mn3-S2 85.81(3), S3-Mn3-S2 85.11(3), S3-Mn4-S4 84.39(3), S1-Mn4-S4 85.15(3)

Furthermore, the influence of the sterically crowded phenyl groups on the structural geometry of both compounds cannot be ignored. There are very few examples of oxygen-bridging tetramers exhibiting bulky ligand groups,[123b] as a result of the short

M-O bond. Those tetramers that do exist, possess far less cumbersome ligands than the triphenylsiloxy, $OSiPh_3$ ligands associated with **4.7**, and have to undergo severe distortion to accommodate the ligand. For example, the $[Cu_4(PPh_3)_4(OPh)_4]$ tetramer, reported by Lopes et al. distorts from a tetrahedral array of metals to a trigonal pyramidal array as a result of the triphenylphosphine groups having to bend away from the core in order to reduce steric crowding.[123b]

Similarly, with compounds **4.4** and **4.5** (Section 4.3), the longer Mn-S bonds (ranging between 2.395-2.415(6) Å for **4.4** and at 2.394(6) Å for **4.5**), allows for minimal steric repulsion between the four triphenylsilyl groups. Hence, the Mn-S bonds of **4.8** are long enough to accommodate a tetramer arrangement, preventing steric clashes from the phenyl groups, whilst the M-O bonds of **4.7** are not sufficiently long enough to adopt the cubane structure. Further determination of this is given by the space-filling diagrams for compounds **4.7** and **4.8**, Figure 4.13.

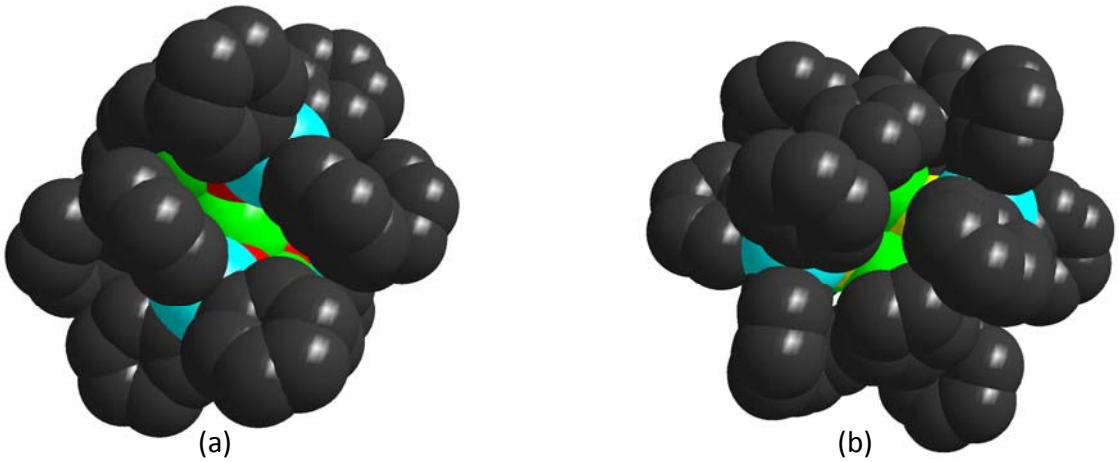

Figure 4.13 Space filling diagrams for compound **4.7** (a) and **4.8** (b), illustrating the steric bulk of the $SiPh_3$ groups.

Table 4.2 Crystallographic data and summary of structural refinement for compound **4.8**.

Empirical Formula	$C_{92}H_{88}Mn_4S_4Si_4$ (**4.8**)
Formula Weight (g mol^{-1})	1738.12
Temperature (K)	100(2)
Crystal System	Triclinic
Space Group	P-1
Colour	Colourless
a (Å)	14.5819(6)
b (Å)	19.0152(9)
c (Å)	20.4025(8)
α(deg)	101.673(4)
β(deg)	90.905(3)
γ(deg)	90.503(3)
Volume ($Å^3$)	5539.1(4)
Z	2
ρ_{calcd}, (kg m^{-3})	1.291
R1 [I>2.0 σ(I)][a]	0.1001
wR2 (all data) [a]	0.2674

[a] $R1 = \Sigma (||F_0| - |F_c||/ \Sigma|F_0|$.[b] $wR2 = [\Sigma[w(F_0^2 - Fc^2)^2]/ \Sigma[w(F_0^2)^2]]^{1/2}$

4.5.4 Magnetic Studies on Compound 4.8

4.5.4.1 d.c. Magnetic Susceptibility Measurements.

d.c. magnetic susceptibility measurements were conducted on a polycrystalline sample of compound **4.8**, which were prepared in a glove box, within a temperature range of 2-300 K, in an applied field of 1 kG, Figure 4.14.

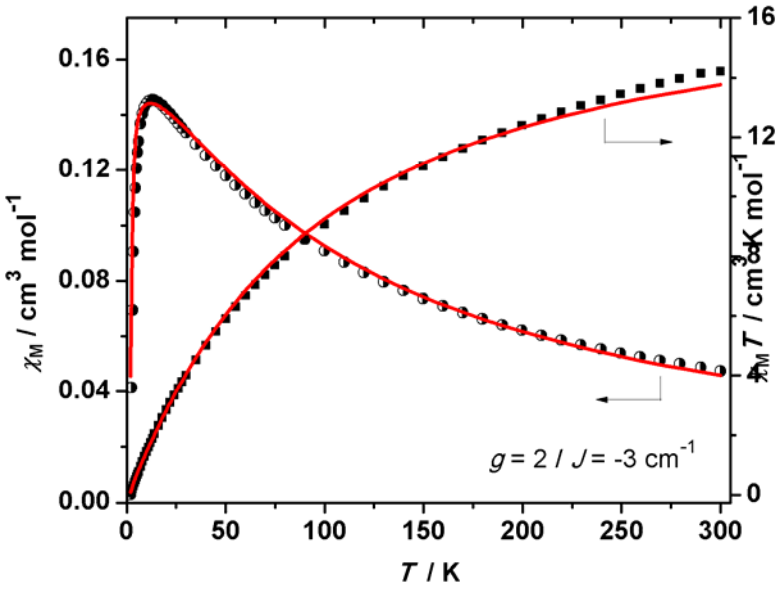

Figure 4.14 Magnetic data plot showing the temperature dependence of χ_M and $\chi_M T$ for compound **4.8** for the field strength H = 1 kG, with the red line representing the fit to the experimental data using the parameters above.

The $\chi_M T$ value for **4.8** at 300 K is 14.1 cm^3 K mol^{-1}, which is lower than typically expected for four non-interacting Mn(II) ions, normally observed at 17.5 cm^3 K mol^{-1}. This indicates weak anitiferromagnetic coupling between the Mn(II) in **4.8**, and there is a gradual decrease of $\chi_M T$ until approximately 100 K. $\chi_M T$ then begins a sharp

decent towards lower temperatures, until at 2 K where the $\chi_M T$ value is effectively zero, indicating the ground state to be diamagnetic.

The magnetic susceptibility data are modelled using the simplified spin-Hamiltonian formula $H = -2J(S_1S_{1A} + S_1S_{1B} + S_1S_2 + S_{1A}\,S_{1B} + S_1S_2 + S_{1B}\,S_2)$, where, S = 5/2, g = 2 for each Mn(II) ion in **4.8**, to give an exchange coupling constant value of J = - 3.0 cm^{-1}. The observed value for compound **4.8** indicates the exchange coupling residing in **4.8** is relatively weaker than that in **4.7**. Interestingly, the larger sulfur donor atom from the Ph_3SiS^- ligand has greater radially extended orbitals, than the oxygen donor ligand, Ph_3SiO^-, which should in turn provide better overlap for magnetic exchange. However, the exchange coupling constants show that **4.8** gives a weaker magnetic exchange than **4.7**, which is J = -4.4 cm^{-1}. This observation suggests that although S-donor ligands exhibit greater radial extension than O-donor ligands, the elongated Mn-S bond somewhat reduces the ability to transmit stronger exchange interactions between the metal ions, since the inter-nuclear separation, bridged by the Mn-S bonds, is significantly increased for compound **4.8** compared to **4.7**.[123c] However, it must be emphasised this value of J = -3.0 cm^{-1} is not particularly weak in the sole context of M-S bonds, (M = transition metal) and this observation is supported by exchange coupling studies on 3*d* metal compounds bridged by S-donor ligands.[123c]

4.5.5 The Synthesis and Structure of a Chromium(II) Thiolate-Bridged dimer.

The preparation of the dimetallic, chromium(II) thiolate-bridged dimer, **4.9** is outlined in Scheme 4.7, with a yield of 66 % (based on chromium).

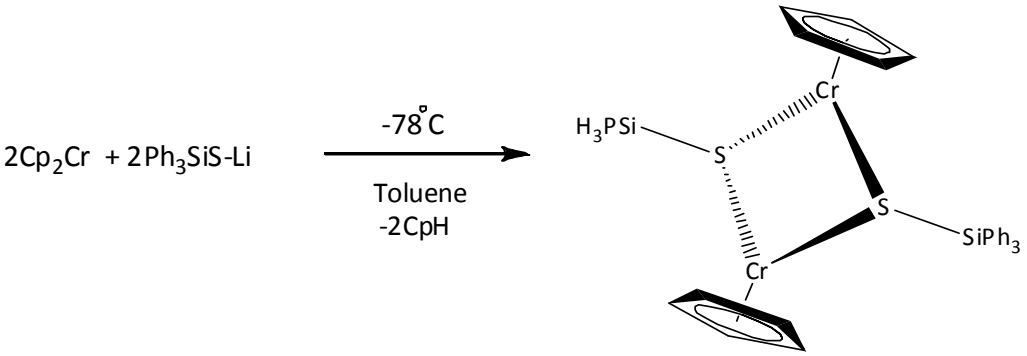

Scheme 4.7 Synthesis of the chromium(II) thiolate bridged dimer $[CpCr(\mu\text{-}SSiPh_3)]_2$ (**4.9**)

The lithiated triphenylsilylthiolate ligand **2.1** is utilised in a reaction with chromocene to produce compound **4.9**.(2 toluene), under the same reaction conditions as for the preparation of compound **4.8**. A direct 'one-pot' synthesis was adopted for the transmetalation reaction illustrated in Scheme 4.7, where the dimer was crystallised by slow cooling of a saturated toluene solution to result in the formation of black, block-shaped single-crystals suitable for X-ray crystallography. The 'one-pot' synthesis allowed for enhanced purity of the sample and without the possibility of contamination or oxidation as chromocene is very unstable in air. The additional toluene in the lattice was removed *in vacuo*, and removal of the additional lattice toluene was confirmed by elemental analysis, as the calculated elemental values were compatible with the experimental values, (*vide infra*; Chapter

Six, 6.17). Characterisation of **4.9** by elemental analysis compared very well to that of the calculated values, in addition to a compatible ^{1}H NMR spectrum to the expected coupling patterns associated with the two Cp groups residing on the chromiums (2.22 ppm, 5 ^{1}H, s, CpCr), and the set of six phenyl groups, (7.54-7.69 ppm, m, 6 ^{1}H, phenyl; 7.11-7.43 ppm, (9 ^{1}H, m, phenyl) (*vide infra;* Chapter Six, 6.17). Similarly to compound **4.7** and **4.8**, the chromium dimer **4.9**, failed to show any peaks in the wider paramagnetic region of the NMR spectrum.

Compound **4.9** crystallises in the centrosymmetric space group P-1, with an inversion centre, point group C_i, as a dimeric compound to give a molecular structure consisting of two chromium(II) ions that are bridged by two [μ-Ph_3SiS]$^{-}$ ligands, with each chromium ion being complexed by a terminal Cp ligand, Figure 4.15. The Cr-S bridging bond lengths range between 2.387(10) Å and 2.390(1) Å, which results in a $Cr_{(1A)}\cdots Cr_{(1B)}$ separation of 3.1262(9) Å, which is relatively long for Cr-Cr distances in related dimetallic complexes, but not uncommon.[124a] The Cr-C bond distances range between 2.280(3)- 2.3887(10) for both $Cr_{(1A)}$ and $Cr_{(1B)}$, which are typically expected for chromium cyclopentadienides.[124b] The bond angles between the two Cp_2Cr units and the bridging sulfur atoms are 98.28(3) °, with acute Cr-S-Cr bond angles giving 81.72(3)°, leading to distortion along these bonds. In addition, the $Si_{(1A)}$-$S_{(1A)}$-$Cr_{(1A)}$ and $Cr_{(1B)}$-$S_{(1B)}$-$Si_{(1B)}$ bond angles are 105.71(4)° and 109.02(5)° respectively. These angles are moderately obtuse considering the presence of sterically bulky phenyl groups, which result in the slight distortion along

the Cr-S bonds to give a zig-zag 'bent' orientation of these angles, common in dimetallic chromium complexes (inset Figure 4.15).[123c] The chromium sites in **4.9** are five coordinate, with each centroid Cr(II) ion residing in a trigonal coordination environment, resulting in the Cp ligands being situated above and below the plane in an apical position relative to the two chromium atoms, Figure 4.15. This consequently results in a mean Cp-Cr-S bond angle of 127.34 °, compared to a mean S-Cr-S bond angle of 98.28(3)°.

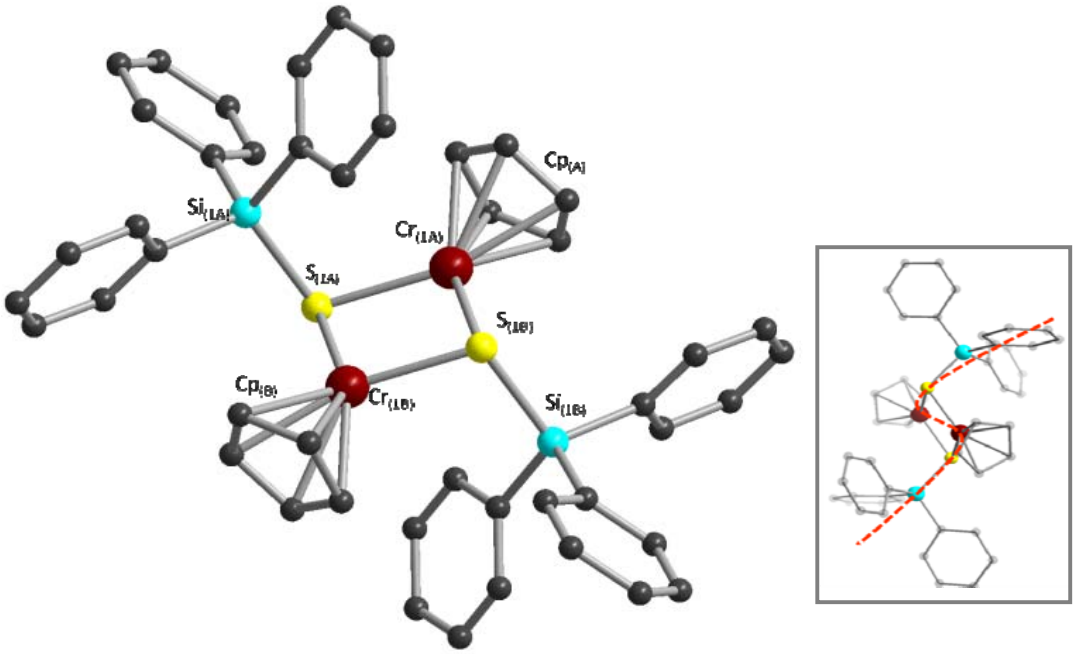

Figure 4.15 Molecular structure of **4.9**, with the hydrogen atoms omitted for clarity. Selected distances/Å and angles/°: $Cr_{(1A)}$-$S_{(1A)}$ 2.3887(10), $Cr_{(1A)}$-$S_{(1B)}$ 2.390(1), $Cr_{(1A)}$ -$Cp_{(A)}$ 2.280(3)-2.3887(10), $Cr_{(1B)}$-$Cp_{(B)}$ 2.282(3)-2.3887(10), $S_{(1A)}$-$Si_{(1A)}$ 2.1435(12), $S_{(1A)}$ -$Cr_{(1A)}$-$S_{(1B)}$ 98.28(3), $Cr_{(1A)}$ -$S_{(1A)}$-$Cr_{(1B)}$ 81.72(3), $Si_{(1A)}$- $S_{(1A)}$-$Cr_{(1A)}$ 105.71(4), $Cr_{(1B)}$- $S_{(1B)}$-$Si_{(1B)}$ 109.02(5).

Table 4.3 Crystallographic data and summary of structural refinement for compound **4.9**

Empirical Formula	$C_{53}H_{48}Cr_2S_2Si_2$ (**4.9**)
Formula Weight (g mol^{-1})	1001.35
Temperature (K)	100(2)
Crystal System	Triclinic
Space Group	P-1
Colour	Black
a (Å)	9.8478(7)
b (Å)	11.3103(7)
c (Å)	12.6382(13)
α (deg)	96.271(7)
β (deg)	112.568(8)
γ (deg)	98.013(6)
Volume ($Å^3$)	1266.64(18)
Z	1
ρ_{calcd}, (kg m^{-3})	1.313
R1 [I>2.0 σ(I)][a]	0.0587
wR2 (all data) [a]	0.1463

[a] $R1 = \Sigma (||F_0| - |F_c||/ \Sigma|F_0|$. [b] $wR2 = [\Sigma[w(F_0^2 - Fc^2)^2]/ \Sigma[w(F_0^2)^2]]^{1/2}$

4.5.6 Magnetic Studies for Compound 4.9

Attempts to conduct d.c. magnetic susceptibility measurements on a polycrystalline sample of compound **4.9**, within a temperature range of 2-300 K, in an applied field of 1 kG, were met by the severe instability of this compound. Although, the sample consistently produced a strong signal in the magnetometer, the final data for this experiment clearly showed evidence of decay and possibly oxidation of one or both of the metal ions from Cr(II) to Cr(III), during the magnetic susceptibility experiment.

Since SQUID measurements are conducted on bulk material of the sample, (unlike single crystal X-ray diffraction), there may be a lack of uniformity throughout compound **4.9** leading to errors in the final results caused by the air sensitive nature of the compound. Therefore, it was not possible to gain a true, representative magnetic susceptibility data plot $\chi_M T$, throughout the temperature range 2-300 K, in order to derive the exchange coupling constant for compound **4.9**. However, the d.c. magnetic susceptibility measurements performed on **4.9**, showed a decrease in $\chi_M T$ from 300 K to c.a. 100 K, and implies evidence of strong antiferromagnetic interaction

4.6 Organometallic Synthesis with Selenium-Bridging Ligands.

The diversity of chalcogenide complexes, incorporating either oxygen or sulfur based ligands, has prompted great interest into synthesising compounds that integrate selenium bridging ligands, not only within transition metal cluster chemistry, but within lanthanide metal cluster chemistry.[125-128]

Many of these complexes are generated by means of elemental insertion reactions of selenium, into either C-M or Si-M ligand bonds, or through the metallation of sterically bulky organic acids, RE-H (where E = Se), with organolithium reagents.[129] Elemental insertion reactions are thought to be the most advantageous over the latter synthetic route because it decreases the probability of forming intermediate organoselenides, therefore allowing for the possibility of gaining better access to species possessing uncomplicated organic groups, R.

In a bid to address the relative gap in fully characterised organometallic selenium-bridging compounds, several reactions were conducted, exploiting both transition and lanthanide metallocene precursors with a newly synthesised organolithiumsilyl-based selenium ligand. Ligand **4.10**, illustrated in Scheme 4.8, was synthesised by implementing the insertion of elemental selenium into a commercially available organolithium (trimethylsilylmethyl)lithium in pentane (1:1 equivalent), with a slight

excess of TMEDA. The solvent was then removed *in vacuo* to give a toffee-like textured product. Hence, the insertion of Se into the C-Li bond gave compound **4.10**.

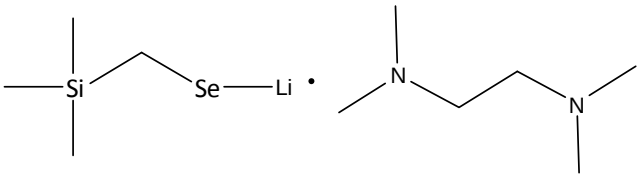

$Me_3SiCH_2Li + Se°$ —(TMEDA, Pentane, 0° C)→ $Me_3SiCH_2Se\text{-}Li$. (TMEDA) (**4.10**)

Scheme 4.8 Insertion reaction of elemental Se into the organic (trimethylsilyl)methyllithium organolithium .

Characterisation of lithium salt **4.10** through solution phase ^{1}H NMR and ^{77}Se NMR spectroscopy in distilled deuterated benzene, proved the only effective means of analysis due to the sticky texture and the sensitive nature of the compound, making it rather difficult to handle whilst in a glove box. The results of the ^{1}H NMR spectra showed proton coupling expected for the protons situated on the trimethylsilyl unit of the ligand, in addition the $–CH_2$ group residing between the inserted selenium and the silicon atoms. In conjunction with identifying accurate chemical shifts for the protons within **4.10**, the ^{77}Se NMR spectrum (Figure 4.16, *infra vide*; Section 6.23), displays a prominent peak at around 320.93 ppm,[129b,c] which is strongly indicative of the presence of the inserted Se atom, hence, providing clear evidence that the

insertion reaction, illustrated in Scheme 4.11, to yield the novel ligand, **4.10**, was a success .

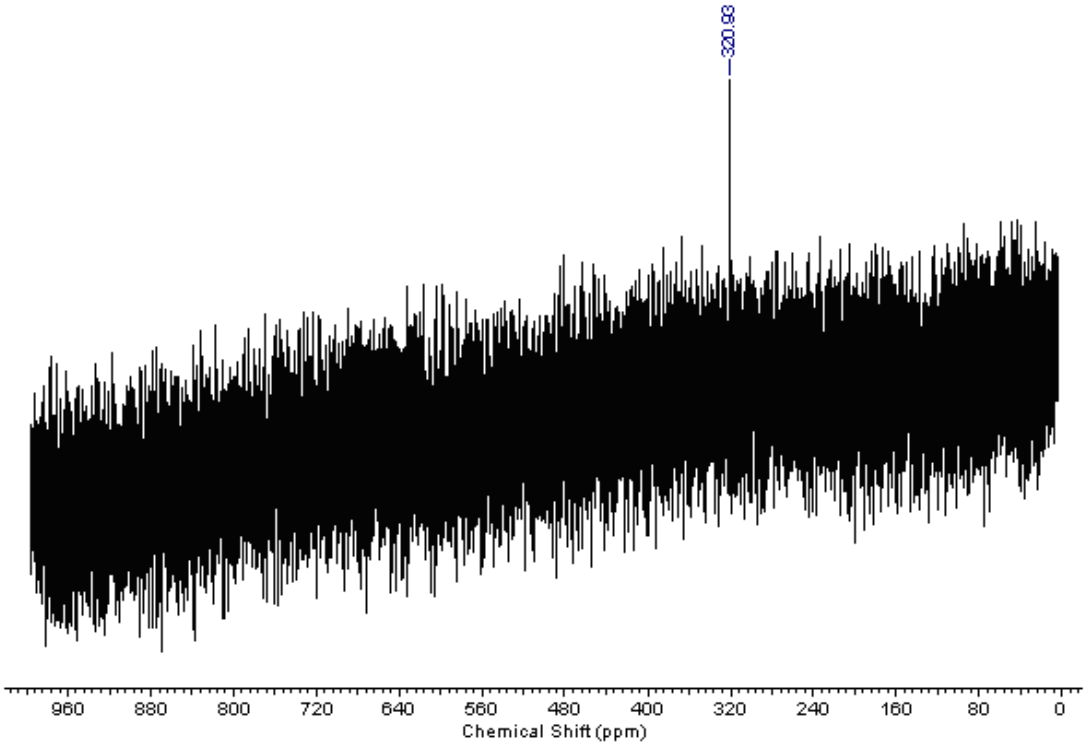

Figure 4.16 Solution phase ^{77}Se NMR spectrum of **4.11** in d_6-C_6D_6 indicating a prominent peak at 320.93 ppm.

Subsequently, **4.10** was initially utilised in 1:1 reactions with manganocene and chromocene in toluene or THF solvents, using standard Schlenk line techniques, Scheme 4.9. Upon reacting manganocene with **4.10** at -78°C, dark brown solutions were observed, which changed to an orange/amber colour when warmed to room temperature. Initially, manganocene reactions were stored at 4 °C, but proved unsuccessful because solutions appeared to show decomposition after no more than

24 hours, even though sealed under nitrogen. Similarly, the reactions with chromocene in either THF or toluene and mixed solvent solutions at -78°C gave green solutions, however upon warming to room temperature resulted in black solutions, clearly indicating reactions were taking place. However, only gel-like substances were formed at the bottom of the Schlenk tube when stored in environments of 4 °C. Therefore, various conditions of temperature were employed for both the manganocene and chromocene reactions to aid crystallisation, namely further cooling and storing at –10°C in addition to storing the reactions at of –30 °C. However, after several attempts to isolate crystalline samples from these reactions, the same unsuccessful outcome prevailed.

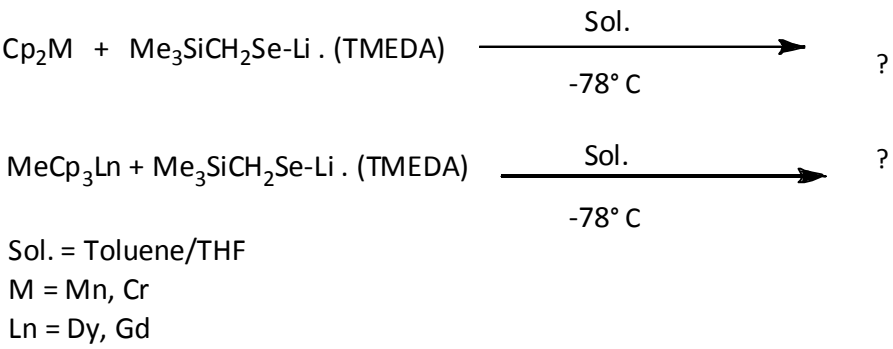

Scheme 4.9 Scheme outlining the reaction of transition and lanthanide metal precursors with ligand (**4.11**)

Furthermore, attempts were made to react the novel selenium based ligand with organolanthanide precursors ($MeCp_3$)Dy and ($MeCp_3$)Gd (see Chapter Two; Section 2.2). Distinct colour changes also took place during these reactions, from light yellow solutions upon addition at -78°C, to dark orange solutions upon warming to room

temperature (Scheme 4.9). Numerous efforts to isolate crystalline products from these reactions also came to no avail, after each reaction was treated to an array of conditions. Varying solvent quantities and polarity seem to have little to no effect on the final outcome of these reactions, neither did storing the resulting solutions in varying quantities of solvents and at various temperatures.

Due to the time constraints of this research, continued work on these reactions had to come to cease, and unfortunately attempts to isolate sufficient samples for X-ray crystallography and standard analytical characterisation were unsuccessful. However, there is still considerable scope for the development of organometallic species that incorporate selenium-bridging ligands, and therefore this research should be pursued further.

4.7 Organometallic Manganocene Reactions with Amido-Bridging Ligands

Alongside completing reactions involving 3*d* metallocenes with chalcogen ligands (detailed in Sections 4.4 and 4.5), attempts were also made to conduct reactions incorporating metallocenes with amido-bridging ligands, in order to advance on previous reports of synthesising 3*d* metallocenes with various amide ligands.[17,18] In addition, the intriguing magnetic communication within these complexes has led to the consideration of developing further examples for a more comprehensive study of their magnetic and spectroscopic properties.

In order to fulfil these preliminary aims, these amido reactions were initially conducted utilising the pro-ligand benzotriazole (btaH = 1*H*-1,2,3-benzotriazole), (this ligand also features in Section 1.8 when utilised with a 4*f* lanthanide metallocene, **1.17**). Benzotriazole and substituted benzotriazoles are well established corrosion inhibitors for copper and its alloys,[130] by bridging surface metal ions, and it is these properties that enable benzotriazole to be a prospective candidate for numerous 3*d* M^{2+} complexes, for which there have been many examples.[131] By far the most recognised example incorporating 3*d* transition metals is that of the family of pentametallic complexes exhibiting the general formula $[M_5(OH)_x(R)_{6-x}(L)_4(H_2O)_{4x}]$ (where M = Cu, Zn, Ni; R = Bta^-, Me_2Bta^- (5,6-Me_2-bta^-); L = β-diketonate, x = 0, 1).[132] Magnetic analysis conducted on these complexes revealed that weak antiferromagnetic exchange between the metals results in a spin ground state that is equivalent to that of the 'isolated' central ion. Although there has been an abundance of pentametallic 3*d* M(II) complexes synthesised and characterised,

there have been no reports of organometallic 3*d* metallocene complexes utilising BtaH. Therefore, initial reactions using manganocene with benzotriazole in the presence of toluene using standard Schlenk line techniques were implemented, Scheme 4.10).

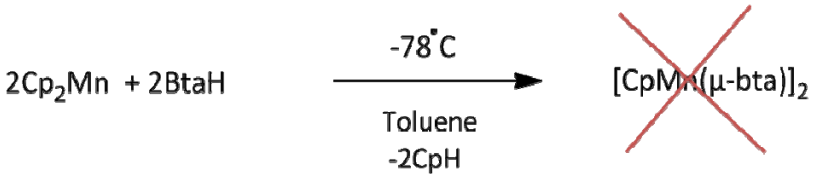

Scheme 4.10 General synthetic method implemented to conduct reactions of manganocene with benzotriazole

It was originally expected to observe a benzotriazolate-bridged dimer similar to that encountered in the previously reported dysprosium dimer **1.16**, through a N-H deprotonation reaction between [Cp_2Mn] and benzotriazole. However, numerous attempts to isolate a crystalline product suitable for X-ray crystallography proved difficult because of poor solubility in these reactions. In an attempt to improve the solubility of the benzotriazole products a change of solvent to THF was implemented. However, once in solution getting the products to remain soluble proved difficult and amorphous precipitates continued to form.

A range of alternative benzotriazole analogues were therefore considered to react with manganocene including the ligands 5-methylbenzotriazole (**1**) and 5,6-dimethylbenzotiazole (**2**) in both toluene and THF (Table 4.4). The aim of substituting the benzotriazole ligand with methyl groups was to further improve the

solubility in these reactions. Nevertheless, these reaction mixtures failed to crystallise forming either brown or yellow amorphous precipitates at -10°C, 4°C and at room temperature, which were difficult to handle in order to achieve any analysis including powder diffraction.

Reactions with manganocene were undertaken incorporating ligands (**1**), (**5**), (**7**) or (**8**), (see Table 4.4) that were lithiated using either butyllithium, (^{n}BuLi) or lithiumdiisopropylamide, (LDA) depending on the ligand substituent to enable deprotonation to occur at the active site, hence to aid metal to ligand coordination. Distinct colour changes occurred in these reactions from light brown to a vivid purple upon addition of the lithiated ligand in the presence of THF, but whether stored at room temperature, 4°C or -10°C conditions, these reaction solutions did not crystallise. The organic ligand tetramethylethylenediamine, TMEDA was also introduced into these reactions to bind to the metal in a further attempt to promote coordination of the benzotriazole ligand (**1**) and ultimately produce crystalline products, but yet again these attempts proved unsuccessful.

Structure Number	**Ligand**	**Pro- Ligand Name and Abbreviations**
(**1**)	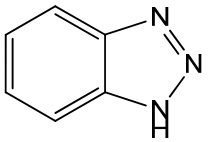	1*H*- Benzotriazole BtaH
(**2**)	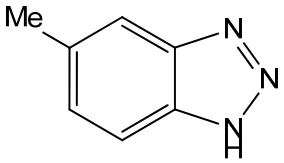	5-Methylbenzotriazole 5-MeBtaH
(**3**)	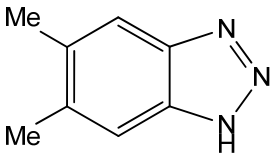	5,6-dimethylbenzotriazole 5,6-MebtaH
(**4**)	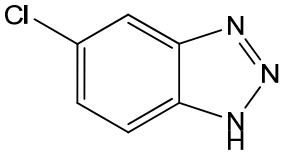	5-Chlorobenzotriazole 5-ClbtaH

(**5**)	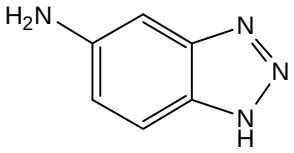	5-Aminobenzotriazole 5-NH_2btaH
(**6**)	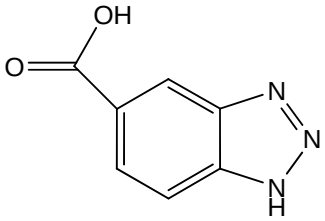	5-Carboxylicbenzotriazole 5-COOHbtaH
(**7**)	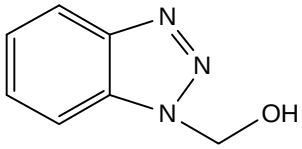	Benzotriazole-1*H*-Methanol 1-MeOHbtaH
(**8**)	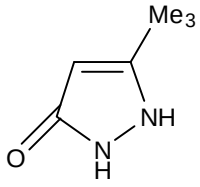	3- methyl-3-pyrazolin-5-one 3Me-3-Py-5-one

Table 4.4 List of amido- bridging benzotriazoles and pyrazoles utilised.

4.9 Conclusions

Reactions exploiting organometallic lanthanide precursors with the lithiated sulfur-bridging pro-ligand, Ph_3SiS-Li (**2.1**), along with its siloxide analogue, Ph_3SiOH (Chapters Two and Three), gave strong precedence for utilising these ligands in conjunction with organometallic 3*d* transition metal precursors. While the reaction of manganocene and Ph_3SiOH produced the trimetallic compound **4.7**, the reaction of manganocene with **2.1** under the same conditions gave the sulfur-bridged hetero-cubane compound **4.8**. The bridging Mn-S bonds are longer for compound **4.8** averaging at 2.6032 Å, compared to the bridging Mn-O bonds in compound **4.7** averaging at 2.0605 Å. The resulting structure of **4.8** is less structurally compact than that of **4.7**, subsequently allowing for an additional sub-unit to form, ultimately creating a more structurally extended compound. Furthermore, the long Mn-S bonds reduce any steric repulsion that may result from the bulky phenyl groups on the triphenylsilyl ligand, whereas the close proximity of the bulky $SiPh_3$ groups to one another hinder the ability of an additional Ph_3SiO^- to coordinate to compound **4.7**. These variations in bond lengths are consequently responsible for the lower coordination numbers and valence electron counts observed in **4.7** (9 and 15 for the central Mn(II) and the two terminal Mn(II) ions respectively), which would typically be expected for a molecule with a thermodynamically stable 17-electron configuration. Furthermore, there is some degree of variation between the C-Mn bond lengths when comparing **4.7** and **4.8**. These differences are not an unexpected observation, because Cp-Mn bonding is known to be very flexible in high-spin

manganocene derivatives, (derived from the metal–ligand bond possessing largely electrostatic character).[123]

In the reaction of chromocene with **2.1**, illustrated in Scheme 4.7, black, block-shaped single crystals were produced at -10° C and when subjected to analysis by X-ray crystallography a centrosymmetric dimer was observed, **4.9**. Identical reaction conditions were employed to those implemented to produce compound **4.8**, however, due to the contrasting chemical characteristics of the two precursors, the two resulting compounds are structurally different. Both manganocene and chromocene are exceptions to the eighteen electron rule, where manganocene possesses 17-electrons whereas the highly reducing chromocene only has 16-electrons, and therefore proceeds to produce the five coordinate dimetallic compound **4.9,** Scheme 4.7.

Compounds **4.7** and **4.8** exhibit expected antiferromagnetic coupling interactions, whilst **4.9** shows evidence of antiferromagnetism. The Cr-Cr bond distances in **4.9** are typically expected lengths for Cr(II) displaying strong antiferromagnetic coupling interactions, however as a result of the decomposition of **4.9** during the SQUID measurements this data cannot be deemed as truly representative of this compound. In addition, the extent of the magnetic exchange interactions is clearly determined by the influence of the bridging ligand. Compounds **4.8** clearly show that although the presence of the radially extended S-donor ligands transmit strong

exchange interactions, the long M-S bonds lessens the interaction to that observed by **4.7** (exhibiting Mn-O bonds).

Unfortunately, the reactions conducted with the various derivatives of benzotriazole in an attempt to produce amido-bridged organometallic compounds, were unsuccessful. Similarly, attempts to expand the family of chalcogen-bridged compounds, to include those utilising selenium-bridging ligands such as the organolithium Me_3SiCH_2Se-Li (**4.10**) complex came to no avail. The inability to negotiate suitable reaction conditions for crystallisation proved a dominating factor for the lack of success with these reactions. However, distinct colour changes were observed during the reaction of the metallocene precursors outlined in Section 4.6; Scheme 4.9, indicating a form of reaction took place.

The isolation of three distinct 3*d* transition metal compounds demonstrate the great flexibility of both the siloxide ligand, Ph_3SiOH, and its lithiated sulfur-bridging, Ph_3SiS-Li counterpart. Furthermore, compounds **4.7** and **4.8** are the first chalcogen-bridged mono-cyclopentadienyl compounds with a +2 oxidation state. Complete structural characterisation by X-ray crystallography, shows interesting structural variations between **4.7**, **4.8** and **4.9**. Antiferromagnetic couplings observed for compounds **4.7** and **4.8** were expected for the interacting 3*d* metals in each complex. However, there is clearly further scope for the expansion of this series of

compounds, particularly exploiting other chalcogen-based ligands, which incorporate selenium or even tellurium-bridging atoms.

Chapter Five

Thesis Review and Future Work

5.1 Thesis Review

The comprehensive introduction and review of prominent lanthanide complexes, alongside their magnetic properties (outlined in Chapter One), clearly highlights the scope of these complexes for the development of novel 4*f* lanthanide complexes, not only for the advancement on what is known about their chemical properties, but to develop molecules with extended slow relaxation of magnetisation properties. In particular, the growing interest in the utility of organometallic lanthanide precursors for the production of novel SMM compounds was encouraged by the development of the amido-bridged dysprosium dimer, $[Cp_2Dy(\mu\text{-bta})]_2$[39] featured in Chapter One; 1.5.4. However, the main focus of Chapter Two was to exploit more unconventional ligands to the commonly used hard oxygen or nitrogen donor ligands, when considering the augmentation of novel SMMs, which may have favourable effects on their magnetic properties. Through the implementation of soft donor ligands, namely the novel lithiated thiolate bridging ligand, Ph_3SSi-Li (**2.1**), sulfur-bridged dimers $[(MeCp)_2Dy(\mu\text{-}SSiPh_3)]_2$ (**2.2**) and $[(MeCp)_2Gd(\mu\text{-}SSiPh_3)]_2$ (**2.3**) were synthesised. The results of numerous magnetic studies conducted on compound **2.2** revealed that this molecule was the first sulfur-bridged SMM, displaying a higher reversal barrier of magnetisation than any other reported $\{Dy_2\}$ SMM, $U_{eff} = 133 \pm 3.5$ cm^{-1} (or 192 ± 5 K). The inherent chemical attributes of soft donor ligands are thought to be significantly responsible for the impressive SMM behaviour observed within compound **2.2**, since it appears that the magnetic exchange between Ln(III) ions are readily enhanced. In addition, as crystal field effects are the most pivotal

influence in determining the slow relaxation of magnetisation observed within lanthanide containing SMMs, alternative crystal field effects may also be accessible whilst exploiting these sulfur-bridging soft donor ligands, which further justifies the results of the magnetic data offered by compound **2.2**. Hence, there is clearly further scope for the exploration soft ligands especially when incorporated with lanthanide-containing complexes.

The exploration of single-ion magnets (SIMs), have been spurred by the discovery of Ishikawa's family of SIM sandwich complexes, in particular the terbium(III), $[Tb^{i}Pc_2]$ complex which currently holds the record for the highest anisotropy barrier of U_{eff} = 566 cm^{-1}. Due to the flexibility of the siloxide ligand and its variety of derivatives, Chapter Three initially outlines a comprehensive analysis of the applications of siloxide ligands in the context of monolanthanide complexes. Preliminary aims for Chapter Three were to develop a series of siloxy, oxygen-bridged dimers, utilising the widely reported pro-ligand triphenylsilanol, Ph_3SiOH, which were analogous to the dimers observed in Chapter Two. Although Ph_3SiOH has been exploited extensively in the literature, the versatility of this pro-ligand made it an ideal candidate to attempt the development of novel complexes, through organometallic synthesis, utilising cyclopentadienyl precursors. Instead of oxo-bridged dimetallic lanthanide dimers, the reaction scheme outlined in Section 3.2.1 of Chapter Three resulted in the formation of a series of octahedral monometallic siloxide complexes. The susceptibility for the formation of these complexes is illustrated by the ability to

employ a combination of synthetic routes to result in the same structural outcome. Furthermore, although the general structures for these complexes have been sporadically reported before (for the dysprosium complex **3.4** and various other lanthanides),[88] there have been little or no magnetic or electronic spectral studies conducted on these systems. In an attempt to address this gap, a series of magnetic studies were performed. These complexes are particular interesting due to their three-fold, C_{3v} symmetry, which are thought to provide ideal conditions to achieve slow relaxation, when combined with crystal field effects (Chapter Three; Section 3.2.2.1). The results of the a.c. and d.c. magnetic susceptibility measurements, revealed only compounds **3.4** and **3.5** were SMMs, with compound **3.5** displaying greater thermal energy barrier for magnetisation reversal, (U_{eff} = ~ 28 K), than **3.4** in an applied field.

Furthermore, preliminary low temperature, optical spectroscopy conducted on compounds **3.4**, **3.5** and **3.8,** emphasise how the energies of the electronic 4*f*-4*f* absorption spectra can fit crystal field parameters, which can be later be modelled by theoreticians to provide more advanced physical and electronic studies on these high symmetry C_{3v}, compounds.

The application of the of the two analogous triphenylsilyl ligands exploited in Chapter Two and Three, subsequently led to the exploration of the utility of these ligands when used in conjunction with organometallic transition 3*d* metal precursors

to produce three novel chalcogen-bridged compounds, $Cp_2Mn_3(\mu\text{-}OSiPh_3)_4$](**4.7**) $[CpMn(\mu\text{-}SSiPh_3)]_4$ (**4.8**) and $[CpCr(\mu\text{-}SSiPh_3)]_2$ (**4.9**). Compound **4.8**, illustrated in Chapter Four; Section 4.5.3, is bridged by the sulfur atoms derived from ligand **2.1**, and it is these bridging M-S (M = transition metal), bonds which play an instrumental role in the context of the comparing the differences between the resulting structure of compound **4.8** with the oxygen-bridged **4.7** cage compounds. Since the Mn-S bond lengths residing in **4.8** are considerably greater than that of the Mn-O bond lengths in **4.7**, the presence of an additional sub-unit as part of **4.8** is formed to result in more cumbersome cubane-like structure, as opposed to the more compact trimetallic geometrical arrangement of compound **4.7**. Although, another possible explanation for these structural differences could derive from the different manganese:chalcogen stoichiometric ratios, as they were synthesised using different types of reactivity (Chapter 4; Sections 4.5.1 and 4.5.3), the presence of the sterically bulky $SiPh_3$ groups are significantly more influential. Furthermore, the dimetallic sulfur-bridged compound **4.9**, illustrated in Chapter 4; Section 4.5.5., is not dissimilar to that of the methylated cyclopentadienyl lanthanide dimers reported in Chapter Two; Section 2.2 and also presents typical extensive M-S bonds, however not as prominent as **4.8**, since the steric constraints of **4.8** are not as influential in **4.9**.

Direct current magnetic susceptibility measurements conducted for compounds **4.7**, and **4.8** reveal that both these compound display typical antiferromagnetic behaviour in an applied field. The weak antiferromagnetic exchange interaction

between the high spin Mn(II) d^5 within compounds **4.7** and **4.8** show comparable magnetic susceptibility $\chi_M T$, values of 11.0 cm^3 K mol^{-1} and 14.1 cm^3 K mol^{-1} respectively, whereas the high instability of **4.9** resulted in deterioration of the sample with evidence of oxidation taking places whilst undertaking SQUID measurements.

To summarise, the successful isolation of the first sulfur-bridged SMM in the form of compound **2.2** alongside its gadolinium(III) analogue, **2.3** was achieved, utilising organometallic lanthanide air sensitive synthetic techniques, which is fundamentally significant in this area of chemical study. In addition, the synthesis and comprehensive magnetic and electronic study of a series of intriguing monometallic lanthanide alkoxide complexes, where two systems, compounds **3.4** and **3.5** were found to be SIMs, albeit presenting relaxation times which still leave Ishikawa's sandwich SIM complexes unrivalled. Furthermore, organometallic *3d* transition metal chemistry was revisited through the exploitation of the highly versatile triphenylsilanol and lithium triphenylsilylthiolate ligands to present a range of distinct chalcogenide bridged manganocene and chromocene compounds.

5.2 Future Work

Although, the series of compounds presented throughout this body of work display some groundbreaking and intriguing results, it is clear there is still great scope to develop this work even further. It has not gone unnoticed that throughout the

literature the one lanthanide that appears most frequently and subsequently appears to be the most popular to work with, is that of compounds possessing dysprosium(III) atoms. Besides most dysprosium(III) precursors being relatively affordable commercially, making it attainable to buy in bulk, dysprosium has a very large (J) value, with a large energy gap to the first excited state as a result of the large spin-orbit coupling (Section 3.2.2.1, Figure 3.9), therefore it is widely seen as the most favourable lanthanide atom to incorporate into synthetic procedures in order to produce comparable magnetic studies to those compounds reported which display impressive magnetisation reversal barriers, U_{eff} and blocking temperature, T_B. However, the dysprosium(III) and gadolinium(III) thiolate-bridged dimers produced in Chapter Two could be built upon and a series of lanthanide thiolate-bridged dimers could be synthesised similarly to that of the family of monomers presented in Chapter Three, especially with terbium(III). However, due to the high sensitivity of these compounds and the complicated solubility issues, experienced when developing **2.2** and **2.3** this may prove more difficult in practice then in theory. In addition, with reference to the existing dimers **2.2** and **2.3**, attempts to isolate samples in order to perform low temperature, single crystal Micro-Squid measurements proved unsuccessful, as after several attempts the highly unstable compounds were unable to survive the journey to the Néel Institute in France where the measurements were to be performed. The samples that seemed to survive gave fairly obscure results, which were signs of possible deterioration. Therefore, due to time constraints, these measurements had to be abandoned, however further

attempts in the future could be reinstated as these results would enhance the existing magnetic data and provide evidence of hysteresis.

Furthermore, expansion of the range chalcogen-bridging ligands to include either selenium or tellurium atoms could be worked on further, in conjunction with both transition and lanthanide metal precursors. The implications on the varying bridging atoms could subsequently be investigated through a series of quantitative magnetic studies.

In addition, expanding the family of lanthanide and transition metal chalcogen-bridged compounds may be achieved through the use of varying the substituents on the cyclopentadienyl precursor. For instance, pentamethyl-cyclopentadienyl lanthanide and transition metal precursors may be used in conjunction with the appropriate ligand. Compounds exploiting linked Cp rings could be also be used as precursors, in addition to those cyclopentadienyl precursors which incorporate ligand substituents.

Whilst preliminary EPR measurements have been conducted for compound **3.7**, EPR measurements at higher fields should also be run in order to resolve the EPR transitions and provide improved simulations for **3.7.** Continuations into comprehensive theoretical calculations also should be performed on compounds **3.4** and **3.5** to give further insight into their magnetisation reversal properties, which may also give further quantitative analysis as to why the Er(III) complex, **3.5** has a slower relaxation than the Dy(III) complex **3.4**, in an applied field.

Chapter Six

Experimental

6.1 General Considerations

All air sensitive synthetic procedures were carried out under a dinitrogen atmosphere using standard Schlenk and vacuum-line techniques in addition to a dinitrogen-filled MBraun glovebox. All glassware was dried thoroughly in an oven kept at 150°C for several hours before storing at room temperature and further rigorous drying by pumping and heating *in vacuo* before use. Toluene and pentane were acquired from a solvent purification system, (Innovation Technology Inc), and stored over molecular sieves, grade type 4A. THF and diethyl ether were pre-dried over sodium wire then distilled off sodium benzophenone, with diethyl ether being stored over molecular sieves. Hexane was also pre-dried and distilled over sodium wire. Deuterated solvents for NMR spectroscopy were supplied by the chemical supplies company Sigma-Aldrich in sealed ampoules. However, due to the air/moisture sensitive nature of the compounds reported in this thesis, the solvents were pre-dried before use by refluxing over potassium, and then distilled before storing in a glovebox over molecular sieves.

X-ray crystallographic data were obtained on either an Oxford X-Calibur 2 or Bruker AXS SMART APEX diffractometer. Air sensitive samples retained stability through coating in Fomblin crystallography oil until mounted onto the goniometer and were placed under a stream of cold dinitrogen gas using an Oxford Cryostream. Crystallographic data were solved using ShelXTL or WinGX software.

Solution-phase ^{1}H NMR spectra were recorded on a Bruker DPX300 NMR spectrometer or a Bruker DPX400 NMR at 300 and 400 MHz respectively, whilst ^{7}Li

and ^{77}Se NMR spectra were recorded on a Bruker DPX400 NMR spectrometer at 155.51 and 77.34 MHz respectively. Elemental analyses were performed on an Exeter Analytical CE-400 Elemental Analyser (C, H, N), where air sensitive samples were packaged in small vials, placed inside larger vials surrounded by cotton wool to avoid breakages, sealed with parafilm to ensure air tightness before sending to Stephen Boyer at the Science Centre, London Metropolitan University, for measurements to be made.

Magnetic susceptibility measurements were performed using a Quantum Design Superconducting Quantum Interference Device (SQUID), MPMS-XL magnometer at varying frequencies and temperatures under an applied field. Samples were prepared in a glovebox and contained in a Teflon capsule. The magnometer output was corrected for the diamagnetism of the sample holder and the underlying diamagnetism of the constituent using Pascal's constants for the compound in question. EPR spectra were recorded at Q-band on a Bruker ESP 300E-12/15Z EPR spectrometer at room temperature.

Variable temperature optical spectroscopy measurements were conducted using visible (VIS-BWTEK BTC11TE cooled CCD array) and near-Infrared (Bayspec Super Gamut™) spectrometers within a temperatures range of 9-300 K. Samples were inserted into a novel copper disk sample-holder and secured in place between two optical sapphire windows, (UQG optics) with silver dag adhesive, then mounted onto a cold-finger, cooled by a closed-cycle helium recycling cryostat. A tungsten filament

lamp was to used conduct the spectroscopy measurements and the amount of light transmitted was controlled by neutral density filters.

6.2 Synthesis of tris-(methylcylopentadienyl) dysprosium $(MeCp)_3Dy$

$(MeCp)_3Dy$ was prepared in the same manner as outlined in literature procedures.[1c,6b] Methylcyclopentadiene (MeCpH), (36 ml, 449.3 mmol) in its dimeric form was distilled and collected into a 100 ml round bottomed flask. After degassing under nitrogen for 10-12 m the MeCpH was added drop-wise to a solution of sodium hydride, NaH (6.0 g, 260.9 mmol) in THF (120 ml) to give a light purple solution and stirred for 2 h. The resulting MeCpNa solution was added to a suspension of $DyCl_3$ (15.0 g, 56.1 mmol) in THF (100 ml) at 0°C, and refluxed for 4 h, then cooled to room temperature to give a suspension of NaCl and $(MeCp)_3Dy(THF)$. The solvent was removed by evaporation under reduced pressure *in vacuo* and prepared for sublimation, in order to separate the resulting product from the residual NaCl. Bright yellow crystals of $(MeCp)_3Dy$ were formed on the sublimation cold finger and isolated away from the NaCl in a glovebox. Yield 9.24 g, (41 %)

6.3 Synthesis of tris-(methylcylopentadienyl) gadolinium, $(MeCp)_3Gd$

$(MeCp)_3Gd$ was prepared in the same manner as outlined in a literature procedure.[1c,6b] Methylcyclopentadiene (MeCpH), (4.97 ml, 62.4 mmol) in its dimeric form was distilled and collected into a 50 ml round bottomed flask. After degassing

under dinitrogen for 10-12 m the MeCpH was added drop-wise to a solution of sodium hydride, NaH (2.0 g, 87 mmol) in THF (50 ml) to give a pink/purple solution and stirred for 2 h. The resulting MeCpNa solution was added to a suspension of $GdCl_3$ (5.0 g, 19.1 mmol) in THF (60 ml) at 0°C, and refluxed for 4 h, then cooled to room temperature to give a suspension of NaCl and $(MeCp)_3Gd(THF)$. The solvent was removed by evaporation under reduced pressure *in vacuo* and prepared for sublimation, in order to separate the resulting product from the residual NaCl. Pale yellow crystals of $(MeCp)_3Gd$ were formed on the sublimation cold finger and isolated away from the NaCl in a glovebox. Yield 3.61 g, (48 %)

6.4 Synthesis of tris-(methylcylopentadienyl) erbium, $(MeCp)_3Er$

$(MeCp)_3Er$ was prepared in the same manner outlined in a literature procedure.[1c,6b] Methylcyclopentadiene (MeCpH), (4.70 ml, 61.2 mmol) in its dimeric form was distilled and collected into a 50 ml round bottomed flask. After degassing under dinitrogen for 10-12 mthe MeCpH was added drop-wise to a solution of sodium hydride, NaH (0.66 g, 28.7 mmol) in THF (50 ml) to give a light pink solution and stirred for 2 h. The resulting MeCpNa solution was added to a suspension of $ErCl_3$ (2.5 g, 9.2 mmol) in THF (25 ml) at 0°C, and refluxed for 4 h, then cooled to room temperature to give a suspension of NaCl and $(MeCp)_3Er(THF)$. The solvent was removed by evaporation under reduced pressure *in vacuo* and prepared for sublimation, in order to separate the resulting product from the residual NaCl.

Bright pink crystals of $(MeCp)_3Er$ were formed on the sublimation cold finger and isolated away from the NaCl in a glovebox. Yield 0.88g, (24 %)

6.5 Synthesis of Manganocene, Cp_2Mn

Cp_2Mn was prepared according to a literature procedure.[5a] Cyclopentadiene (CpH), (13.5 ml, 202 mmol) in its dimeric form was distilled and collected into a 50 ml round bottomed flask. After degassing under dinitrogen for 10-12 m the CpH was added drop-wise to a solution of sodium hydride, NaH (1.36 g, 7.0 mmol) in THF (120 ml) to give a purple solution and stirred for 2 h. The resulting CpNa solution was added to a suspension of $MnCl_2$ (3.53 g, 28 mmol) in THF (20 ml) at 0°C, and refluxed for 4 h, then cooled to room temperature to give a suspension of NaCl and $Cp_2Mn(THF)$. The solvent was removed by evaporation under reduced pressure *in vacuo* and for prepared sublimation, in order to separate the resulting product from the residual NaCl. Dark brown crystals of Cp_2Mn were formed on the sublimation cold finger and isolated away from the NaCl in a glovebox. Yield 3.28 g, (63 %)

6.6 Synthesis of Chromocene, Cp_2Cr

Cp_2Cr was prepared according to a literature procedure.[5a] Cyclopentadiene (CpH), (23 ml, 378.2 mmol) in its dimeric form was distilled and collected into a 50 ml round bottomed flask. After degassing under dinitrogen for 10-12 m the CpH was added drop-wise to a solution of sodium hydride, NaH (5.86 ml, 260.9 mmol) in THF (70 ml) to give a pink/purple solution and stirred for 2 h. The resulting CpNa solution

was added to a suspension of $CrCl_3$ (9.8 g, 62.4 mmol) in THF (50 ml) at 0°C, then stirred at to room temperature for 16 h to give a suspension of NaCl and $Cp_2Cr(THF)$. The solvent was removed by evaporation under reduced pressure *in vacuo* and prepared for sublimation, in order to separate the resulting product from the residual NaCl. Bright yellow crystals of Cp_2Cr were formed on the sublimation cold finger and isolated away from the NaCl in a glovebox. Yield 5.82 g, (52 %)

6.7 Synthesis of Ph_3SiS-Li (**2.1**)

To a stirred suspension of Ph_3SiS-H (5.0 g, 17.1 mmol) in hexane (50 ml), ^{n}Buli (11.2 ml, 1.6 M) was added slowly at -78°C and stirred for 30 m. The suspension then warmed to room temperature and left to stir for 16 h. The solid was filtered, washed with hexane and dried under vacuum for 2 h. The resulting white precipitate, lithium triphenylsilylthiolate, Ph_3SiS-Li, was isolated and stored in the glove box. Yield 4.44 g, (87 %), Elemental analysis calculated for $C_{18}H_{15}SiS$-Li (%): C 72.45, H 5.07; Found: C 72.30, H 4.90. ^{1}H NMR (d_6-C_6D_6, 400.13 MHz, 298 K, δ/ppm) 7.70-7.72, (6 ^{1}H, m, phenyl) and 7.11-7.15, (9 ^{1}H, m, phenyl), ^{7}Li NMR (d_6-C_6D_6 155.51 MHz, 298 K, δ/ppm) 0.57 ppm.

6.8 Synthesis of $[(MeCp)_2Dy(\mu\text{-}SSiPh_3)]_2$, (**2.2**)

A solution of $(CpMe)_3Dy$ (0.1 g, 0.25 mmol) with Ph_3SiS-Li (0.076 g, 0.25 mmol) in toluene (20 ml) was stirred for 30 m at -78°C. The solution was then warmed to room temperature and left to stir for 16 h, to give a pale yellow solution. The solution was filtered through celite and the volume reduced under vacuum before storing at -30°C overnight to produce fragile, colourless, needle-like crystals of $[(MeCp)_2Dy(\mu\text{-}SSiPh_3)]_2$(tol). Thorough drying of the crystals under vacuum for approximately 30-45 m subsequently removes the lattice toluene to give **2.2**. Yield 0.097 g, (64 %), Elemental analysis calculated for $C_{60}H_{58}Dy_2S_2Si_2$: C 58.86, H 4.77; Found: C 58.71, H 4.69.

6.9 Synthesis of $[(MeCp)_2Gd(\mu\text{-}SSiPh_3)]_2$, (**2.3**)

A solution of $(CpMe)_3Gd$ (0.1 g, 0.25 mmol) with Ph_3SiS-Li (0.076 g, 0.25 mmol) in toluene (20 ml) was stirred for 30 m at -78°C. The solution was then warmed to room temperature and left to stir for 16 h, to give a pale yellow solution. The solution was filtered through celite and the volume reduced under vacuum before storing at -30°C overnight, producing fragile, colourless, needle-like crystals of $[(MeCp)_2Gd(\mu\text{-}SSiPh_3)]_2$(tol). Thorough drying of the crystals under vacuum for approximately 30-45 m subsequently removes the lattice toluene to give **2.3**. Yield 0.120 g, (70 %) Elemental analysis calculated for $C_{60}H_{58}Gd_2S_2Si_2$: C 59.37, H 4.82; Found: C 59.03, H 4.77.

6.10 Synthesis of $[Dy(OSiPh_3)_3(THF)_3]$ (**3.4**)

A solution of Ph_3SiOH (0.16 g, 0.58 mmol) in THF (8 ml) was added to a solution of $(MeCp)_3Dy$ (0.1 g, 0.25 mmol) in THF (10 ml) at room temperature. The solution was left to stir for 4 h, and then filtered through celite. The volume was reduced then stored at 4°C overnight to produce yellow crystalline blocks of $[Dy(OSiPh_3)_3(THF)_3](THF)$. Thorough drying of the crystals under vacuum for approximately 30-45 m subsequently removes the additional THF in the lattice to give **3.4**. Yield 0.058 g, (55 %). Elemental analysis calculated for $C_{66}H_{69}O_6Si_3Dy_1$: C 65.78, H 5.77; Found: C 65.82, H 5.95.

6.11 Synthesis of $[Er(OSiPh_3)_3(THF)_3]$ (**3.5**)

A solution of Ph_3SiOH (0.16 g, 0.58 mmol) in THF (8 ml) was added to a solution of $(MeCp)_3Er$ (0.1 g, 0.25 mmol) in THF (10 ml) at room temperature. The solution was left to stir for 4 h, and then filtered through celite. The volume was reduced then stored at 4°C overnight to produce pink crystalline blocks of $[Er(OSiPh_3)_3(THF)_3](THF)$. Thorough drying of the crystals under vacuum for approximately 30-45 m subsequently removes the additional THF in the lattice to give **3.5**. Yield 0.036 g, (34 %). Elemental analysis calculated for $C_{66}H_{69}O_6Si_3Er_1$: C 65.53, H 5.75; Found: C 65.70, H 5.93.

6.12 Synthesis of [Ho(OSiPh$_3$)$_3$(THF)$_3$] (**3.6**)

A solution of NaO^{t}Bu (0.128 g, 1.60 mmol) with Ph$_3$SiOH (0.315 g, 1.14 mmol) in THF (20 ml) was added to a solution of HoCl$_3$ (0.1 g, 0.38 mmol) in THF (15 ml) and stirred at room temperature for 30 m to give an off white solution. The solution was then refluxed for 16 h, before cooling back to room temperature as a cream coloured solution. The solution was then filtered through celite and volume reduced by evaporation, then stored at 4°C overnight to produce pale pink crystalline blocks of [Ho(OSiPh$_3$)$_3$(THF)$_3$](THF). Thorough drying of the crystals under vacuum for approximately 30-45 m subsequently removes the additional THF in the lattice to give **3.6**. Yield 0.030 g, (28 %). Elemental analysis calculated for $C_{66}H_{69}O_6Si_3Ho_1$: C 65.71, H 6.07; Found: C 65.65, H 5.94.

6.13 Synthesis of [Gd(OSiPh$_3$)$_3$(THF)$_3$] (**3.7**)

A solution of Ph$_3$SiOH (0.16 g, 0.58 mmol) in THF (8 ml) was added to a solution of (MeCp)$_3$Gd (0.1 g, 0.25 mmol) in THF (10 ml) at room temperature. The solution was left to stir for 4 h, and then filtered through celite. The volume was reduced then stored at 4°C overnight to produce colourless crystalline blocks of [Gd(OSiPh$_3$)$_3$(THF)$_3$](THF). Thorough drying of the crystals under reduced pressure for approximately 30-45 m subsequently removes the additional THF in the lattice to give **3.7** Yield 0.025 g, (23 %). Elemental analysis calculated for $C_{66}H_{69}O_6Si_3Gd_1$: C 66.10, H 6.11; Found: C 65.93, H 5.99.

6.14 Synthesis of $[Tb(OSiPh_3)_3(THF)_3]$ (**3.8**)

A solution of NaO^tBu (0.128 g, 1.60 mmol) with Ph_3SiOH (0.315 g, 1.14 mmol) in THF (20 ml) was added to a solution of $TbCl_3$ (0.1 g, 0.38 mmol) in THF (15 ml) and stirred at room temperature for 30 m to give an off white suspension. The solution was then set to reflux for 16 h, before cooling to back to room temperature to give a cream coloured solution. The solution was then filtered through celite and volume reduced by evaporation then stored at 4°C overnight to produce colourless crystalline blocks of $[Tb(OSiPh_3)_3(THF)_3](THF)$. Thorough drying of the crystals under vacuum for approximately 30-45 m subsequently removes the additional THF in the lattice to give **3.8**. Yield 0.022 g (21 %). Elemental analysis calculated for $C_{66}H_{69}O_6Si_3Tb_1$: C 66.02, H 6.09; Found: C 65.90, H 5.93.

6.15 Preparation of $[Cp_2Mn_3(OSiPh_3)_4]$ (**4.7**)

A solution of $MnCp_2$ (0.1 g, 0.55 mmol) in toluene (10 ml) was added to a solution of Ph_3SiOH (0.152 g, 0.55 mmol) in toluene (10 ml) at -78°C and stirred for 30 m. The solution was then warmed to room temperature and left to stir for 16 h, to give a light green solution with a pale yellow precipitate. The mixture was gently heated and the precipitate redissolved, which turned a light brown/amber colour, and was then filtered through celite. The solution was reduced in volume by evaporation under reduced pressure and then set aside at room temperature overnight to produce colourless crystalline rods of $[Cp_2Mn_3(OSiPh_3)_4](tol)$. Thorough drying of the

crystals *in vacuo* under reduced pressure for approximately 30-45 m subsequently removes the toluene in the lattice to give **4.7**. Yield: 0.138 g, (46 %) Elemental analysis calculated for $C_{79}H_{78}Mn_3O_4Si_4$ (%): C 67.75, H 5.53; Found: C 67.59, H 5.65. ^{1}H NMR (d_6-C_6D_6, 400.23 MHz, 296.4 K, δ/ppm). 6.23-7.28, (60 ^{1}H, m, phenyl) and 2.04, (10 ^{1}H, s, CpMn). There were no peaks found in the wider paramagnetic region, (-200 to +200 ppm).

6.16 Preparation of [CpMn(SSiPh$_3$)]$_4$ (**4.8**)

A solution of $MnCp_2$ (0.1 g, 0.55 mmol) and Ph_3SiS-Li (0.16 g, 0.55 mmol) in toluene (15 ml) was stirred for 30 m at -78°C, warmed to room temperature and left to stir for 16 h. The resulting light brown solution was filtered through celite and the volume reduced in volume under vacuum before storing at -4 °C overnight to produce colourless crystalline blocks of [CpMn(SSiPh$_3$)]$_4$(tol). Thorough drying of the crystals *in vacuo* under reduced pressure for approximately 30-45 m subsequently removed the additional toluene in the lattice to give **4.8**. Yield 0.085 g, (17 %). Elemental analysis calculated for $C_{92}H_{80}Mn_4S_4Si_4$ (%): C 67.13, H 4.90; Found: C 66.95, H 4.85. ^{1}H NMR (d_6-C_6D_6, 400.23 MHz, 296.4 K, δ/ppm), 6.89-7.77, (20 ^{1}H, m, phenyl), 6.06-6.45, (40 ^{1}H, m, phenyl) and 2.04, (20 ^{1}H, s, CpMn). There were no peaks found in the wider paramagnetically shifted region, (-200 to +200 ppm).

6.17 Preparation of $[CpCr(SSiPh_3)]_2$ (**4.9**)

A solution of Cp_2Cr (0.1 g, 0.55 mmol) with Ph_3SiS-Li (0.16 g, 0.55 mmol) in toluene (15 ml) was stirred for 30 m at -78°C. The solution was then warmed to room temperature and left to stir for 16 h, to give a dark brown/black solution. The solution was filtered through celite and the volume reduced under vacuum before storing at -10°C over 3 d to produce black crystalline blocks of $[CpCr(SSiPh_3)]_2$(tol). Thorough drying of the crystals *in vacuo* under reduced pressure for approximately 30-45 m subsequently removes the additional toluene in the lattice to give **4.9**. Yield: 0.115 g, (66%). Elemental analysis calculated for $C_{46}H_{40}Cr_2S_2Si_2$ (%): C 67.13, H 4.90; Found: C 66.95, H 4.85. ^{1}H NMR (d_6-C_6D_6, 400.23 MHz, 293 K, δ/ppm), 7.54-7.69, (6 ^{1}H, m, phenyl), 7.11-7.43, (30 ^{1}H, m, phenyl) and 2.22, (10 ^{1}H, s, CpCr). There were no peaks found in the wider paramagnetically shifted region (-100 to +100 ppm).

6.18 Preparation of Me_3SiCH_2Se-Li·(TMEDA)(**4.11**)

A solution of trimethyl(silylmethyl)lithium, Me_3SiCH_2-Li (in pentane), (25 ml, 1.0 M) with TMEDA (2.56 ml), was transferred by cannula to a round bottomed flask charged with Se (2.0 g, 25.3 mmol) at 0°C and stirred for 30 m. The suspension was then warmed to room temperature and left to stir for a further 1 h. The orange/red solution was then dried by evaporation under reduced pressure to produce a thick, toffee-like wax of Me_3SiCH_2Se-Li and stored in a glove box. Due to the toffee-like

texture of this compound, preparation of a sample for elemental analysis proved difficult. However, ^{1}H NMR and ^{77}Se NMR were conducted after the agitation of the sample in deuterated benzene. Yield 1.54 g, (42 % based on selenium). ^{1}H NMR, (d_6-C_6D_6, 300 MHz, 299.95 K, δ/ppm) 0.06, (9 ^{1}H, s, CH_3) 0.26 (2 ^{1}H, s, $SiCH_2$), 2.3, (12 ^{1}H, s, NCH_3) and 1.65 (4 ^{1}H, s, NCH_2), ^{77}Se NMR (d_6-C_6D_6, 294 K, 77.34 MHz, δ/ppm) 320.90 ppm.

6.19 Reaction of $MnCp_2$ with Me_3SiCH_2Se-Li·(TMEDA) (in toluene)

A solution of $MnCp_2$ (0.1 g, 0.55 mmol) with Me_3SiCH_2Se-Li·(TMEDA), (0.12 g, 0.55 mmol) in toluene (20 ml) was stirred for 30 m at -78°C. The solution was then warmed to room temperature and left to stir for 16 h, resulting in an amber solution. The solution was filtered and the volume reduced under vacuum before storing at -30°C overnight. The reaction solutions failed to crystallise, producing dark brown residues.

6.20 Reaction of $MnCp_2$ with Me_3SiCH_2Se-Li·(TMEDA) (in THF)

A solution of $MnCp_2$ (0.1 g, 0.55 mmol) with Me_3SiCH_2Se-Li·(TMEDA), (0.12 g, 0.55 mmol) in THF (15 ml) was stirred for 30 m at -78°C to give a brown solution. The solution was then warmed to room temperature and left to stir for 16 h, to give a dark amber solution. The solution was filtered and the volume reduced under

vacuum before storing at -30 °C overnight. The reaction solutions failed to crystallise, producing dark brown residues, similarly to the reactions in toluene.

6.21 Reaction of $CrCp_2$ with Me_3SiCH_2Se-Li·(TMEDA)

A solution of $CrCp_2$ (0.1 g, 0.55 mmol) with Me_3SiCH_2Se-Li·(TMEDA), (0.12 g, 0.55 mmol) in toluene (15 ml) was stirred for 30 m at -78°C to give a green solution. The solution was then warmed to room temperature and left to stir for 16 h, resulting in a black solution. The solution was filtered and the volume reduced under vacuum before storing at -30 °C overnight. Black solutions were obtained, from which no crystals were obtained.

6.22 Reaction of $(Me_3Cp)Ln$ (Ln = Dy, Gd) with Me_3SiCH_2Se-Li·(TMEDA)

A solution of $(CpMe)_3Ln$ (Ln = Dy, Gd) (0.1 g, 0.25 mmol) with Me_3SiCH_2Se-Li·(TMEDA), (0.053 g, 0.25 mmol) in toluene (15 ml) was stirred for 30 m at -78°C to give pale yellow solutions. The solution was then warmed to room temperature and left to stir for 16 h, to give a deep yellow/orange solution. The solution was filtered through celite and the volume reduced under vacuum before storing at -30°C overnight. These solutions proved extremely sensitive to air and highly unstable. Subsequently, these solutions did not produce a crystalline product.

6.23 Reaction of Cp_2Mn with btaH

Cp_2Mn (0.1 g, 0.55 mmol), in toluene (10 ml) was added at -78°C to a solution of benzotriazole (0.07 g, 0.55 mmol) in toluene (10 ml) and stirred for 30 m. The pale brown solution was then warmed to room temperature and left to stir for 16 h. The resulting brown solution formed a brown precipitate, which was dried *in vacuo* and redissolved in THF (15 ml), followed by a filtration. The volume of the solution was then reduced *in vacuo* and stored at 4° C. The solutions failed to produce crystalline material.

6.24 Reaction of Cp_2Mn with 5-MebtaH

Cp_2Mn (0.1 g, 0.55 mmol), in THF (10 ml) was added at -78°C to a solution of 5-methylbenzotriazole (0.07g, 0.5 mmol) in THF (10 ml) and stirred for 30 m. The brown solution was then warmed to room temperature and left to stir for 16 h. The resulting dark brown solution formed a brown precipitate, which was heated to redissolve, followed by a filtration. The volume of the solution was then reduced under vacuum and stored at 4° C. The solution did not produce crystals.

6.25 Reaction of Cp_2Mn with 5,6-Me_2btaH

Cp_2Mn (0.1 g, 0.55 mmol), in THF (10 ml) was added at -78°C to a solution of 5,6-methylbenzotriazole (0.08 g, 0.55 mmol) in THF (10 ml) and stirred for 30 m. The brown solution was then warmed to room temperature and left to stir for 16 h. The

resulting brown solution formed a brown precipitate, which was redissolved on heating, followed by a filtration. The volume of the solution was then reduced under vaccum and stored at -10° C, but no crystals were formed.

6.26 Reaction of Cp_2Mn with 5-ClbtaH

Cp_2Mn (0.1 g, 0.55 mmol), in THF (10 ml) was added at -78°C to a solution of 5-chlorobenzotriazole (0.08 g, 0.55 mmol) in THF (15 ml) and stirred for 30 m. The dark green solution was then warmed to room temperature and left to stir for 16 h. The resulting dark green solution was then filtered and the volume reduced under vacuum. The green solution was then stored at -10° C, but no crystals were produced.

6.27 Reaction of Cp_2Mn with 5-NH_2btaH

Cp_2Mn (0.1 g, 0.55 mmol), in THF (10 ml) was added at -78°C to a solution of 5-aminobenzotriazole (0.07 g, 0.55 mmol) in THF (10 ml) and stirred for 30 m. The pale brown solution was then warmed to room temperature and left to stir for 16 h. The resulting brown solution was filtered and the volume reduced. The brown solution was then stored at 4° C. No crystals were produced, although precipitation occurred. However, further analysis of the precipitate was not obtained, as the precipitate was essentially a mixture of the separated starting reactants.

6.28 Reaction of Cp_2Mn with 5-COOHbtaH

Cp_2Mn (0.1 g, 0.55 mmol), in THF (8 ml) was added at -78°C to a solution of 5-carboxylic-benzotriazole (0.08 g, 0.55 mmol) with LDA (0.27 ml, 0.55 mmol) in THF (10 ml) and stirred for 30 m. The green/brown solution was then warmed to room temperature and left to stir for 16 h. The resulting dark green/brown oily solution formed a brown precipitate, which was dried under vacuum, washed with pentane and the redissolved in THF (10 ml). The solution was then filtered and the volume reduced. The green/brown solution was stored at -10° C, but no crystals were obtained.

6.29 Reaction of Cp_2Mn with 1-MeOHbtaH

Cp_2Mn (0.1 g, 0.55 mmol), in THF (15 ml) was added at -78° C to a solution of benzotriazole-1-methanol (0.08 g, 0.55 mmol) with (0.27 ml, 0.55 mmol) with LDA (0.27 ml, 0.55 mmol) in THF (12 ml) and stirred for 30 m. The red/orange solution was then warmed to room temperature and left to stir for 16 h. The resulting red/orange solution was filtered and the volume reduced and stored at -30° C. Small red crystals formed, however attempts to analyse the crystals through X-ray diffraction were unsuccessful, because the crystals did not diffract adequately enough to pursue a full scan of the crystal, possibly due to prolonged contact with air, subsequently disintegrating into powders. Attempts were made to conduct powder diffraction patterns of the resulting powders, however due to the air

sensitive nature of these reactions; the powders were unable to refrain from deteriorating long enough to provide an adequate and reliable powder pattern.

6.30 Reaction of Cp_2Mn with 3-Me-3-Py-5-one with LDA.

Cp_2Mn (0.1 g, 0.55 mmol), in THF (10 ml) was added at -78°C to a solution of 3-methyl-3-pyrazolin-5-one (0.09 g, 0.55 mmol) with LDA (0.27 ml, 0.55 mmol) in THF (8 ml) and stirred for 30 m. The pale brown solution was then warmed to room temperature and left to stir for 16 h. The resulting brown solution was then filtered and the volume reduced under vacuum. The brown solution was stored at -4° C. No crystals were obtained from the solution.

6.31 Reaction of Cp_2Mn with 3-Me-3-Py-5-one in the presence of butyllithium.

Cp_2Mn (0.1 g, 0.55 mmol), in toluene (10 ml) was added at -78°C to a solution of 3-methyl-3-pyrazolin-5-one (0.09 g, 0.55 mmol) with ^{n}Buli (0.31 ml, 0.55 mmol) in THF (15 ml) and stirred for 30 m. The dark brown solution was then warmed to room temperature and left to stir for 16 h. The resulting dark brown solution was filtered reduced and stored at -10° C, but no crystals were obtained.

6.32 Reaction of Cp_2Mn with 5-NH_2btaH in the presence of butyllithium.

Cp_2Mn (0.1 g, 0.55 mmol), in THF (10 ml) was added at -78°C to a solution of 5-aminobenzotriazole (0.07 g, 0.55 mmol) with ^{n}Buli (0.27 ml, 0.55 mmol) in THF (10 ml) and stirred for 30 m. The purple was then warmed to room temperature and left

to stir for 16 h. The resulting vivid purple solution was filtered and the volume reduced by evaporation. The solution was then stored at 4° C, but no crystals were produced.

Chapter Seven

References

1. R. Anwander in "*Principles in Organolanthanide Chemistry*", 1st Edition, Volume 2, Chapter 1 pp. 1-61, S. Kobayashi, Springer-Velag Berlin Heidelberg, 1999.

2. H. C. Aspinall, "*Chemistry of the f-Block Elements"*, Gordon and Breach Science Publishers, Amsterdam, 2001.

3. N. Kaltsoyannis and P. Scott, "*The f Elements"*, Oxford Science Publications, Oxford, 1999.

4. (a) F. A. Hart and F. P. Laming, J*. Inorg. Nucl. Chem.,* 1965, **27**, 1605.

(b) http://www.sciencephoto.com, 2012, Science Photo Library Ltd.

5. (a) G. Wilkinson and F. A. Cotton, *Chem. Ind.,* 1954, **11**, 307. (b) G. Wilkinson, F. A. Cotton and J. M. Birmingham, *J. Inorg. Nucl. Chem.,* 1956, **2**, 95.

6. (a) F. A. Cotton and G. Wilkinson, *J. Inorg. Nucl. Chem.*, 1955*,* **1**, 165. (b) L. T. Reynolds and G. Wilkinson, *J. Inorg. Nucl. Chem*., 1959, **9**, 86. (c) J. M. Birmingham, G. Wilkinson, *J. Am. Soc*., 1956, **78**, 42.

7. (a) T. J. Marks and R. D. Ernst, in *"Comprehensive Organometallic Chemistry"*, 1st Edition, Volume 3, Chapter 21, pp. 173-270. G. A. Wilkinson, F. G. A. Stone, E. W. Abel (eds), Pergamon Press, Oxford, 1982. (b) F. T. Edelman in *"Comprehensive Organometallic Chemistry"*, 2nd Edition, Volume 4, Chapter 2. pp. 11-212. G. A. Wilkinson and F. G. A. Stone, E. W. Abel (Eds.), Pergamon, Oxford, 1995.

8. R. E. Maginn, S. Manastyrskyj, and M. Dubeck, *J. Am. Chem. Soc*., 1963, **85**, 672

9. (a) R. Sessoli, H.-L. Tsai, A. R. Schake, S. Wang, J. B. Vincent, K. Folting, D. Gatteschi, G. Christou and D. N. Hendrickson, *J. Am. Chem. Soc.,* 1993, **115**, 1804. (b) R. E. P. Winpenny, *Adv. Inorg. Chem.,* 2001, **52**, 1.

10. G. Aromı´ and E. K. Brechin, *Struct. Bonding.,* 2006*,* **122**, 1.

11. G. Christou, D. Gatteschi, D. N. Hendrickson and R. Sessoli, *MRS Bull.,* 2000, **25**, 66.

12. D. Gatteschi and R. Sessoli, *Angew. Chem. Int. Ed.,* 2003*,* **42**, 26.

13. C. J. Milios A. Vinslava, W. Wernsdorfer, S. Moggach, S. Parsons, S. P. Perlepes, G. Christou, and E. K. Brechin, *J. Am. Chem. Soc*., 2007, **129**, 2754.

14. (a) N. Ishikawa, M. Sugita, T. Ishikawa, S. Y. Koshihara and Y. Kaizu, *J. Am. Chem*. *Soc*., 2003, **125***,* 8694. (b) N. Ishikawa, M. Sugita, N. Tanaka, T. Ishikawa, S.-Y. Koshihara and Y. Kaizu, *Inorg. Chem.,* 2004, **43**, 5498 (c) S. Takamatsu, T. Ishikawa, S.-Y. Koshihara and N. Ishikawa, *Inorg. Chem*. 2007, **46**, 7250. (d) J. D. Rinehart and J. R. Long, *Chem. Sci.,* 2011, **2**, 2078.

15. (a) N. Ishikawa, *Polyhedron,* 2007, ***26,*** 2147. (b) S. Jank, H. Reddmann and H.-D. Amberger, *Inorg. Chim. Acta*, 2008, **361**, 2154. (c) L. Sorace, C. Benelli and Dante Gatteschi*, Chem. Soc. Rev*., 2011, **40**, 3092.

16. R. J. Blagg, C. A. Muryn, E. J. L. McInnes, F. Tuna and R. E. P. Winpenny, *Angew. Chem. Int. Ed.,* 2011, **50**, 6530.

17. M. Kritikos, M. Moustiakimov, M. Wijk and G. Westin, *J. Chem. Soc. Dalton. Trans.* 2001, 1931.

18. G. Helgesson, S. Jagner, O. Poncelet and L. G. Hubert-Pfalzgraf, *Polyhedron*, 1991, **10**, 1559.

19. G. Westin, M. Moustiakimov and M. Kritikos, *Inorg. Chem.,* 2002, **41**, 3249.

20. G. Westin, M. Kritikos and M. Wijk, *J. Solid State Chem.*, 1998, **141**, 168.

21. D. C. Bradley, H. Chudzynska, D. M. Frigo, M. E. Hammond, M. B. Hursthouse and M. A. Mazid, *Polyhedron*, 1990, **9**, 719.

22. S. Daniele, L. G. Hubert-Pfalzgraf, P. B. Hitchcock and M. F. Lappert, *Inorg. Chem. Commun.,* 2000, **3**, 218.

23. J. Gromada, A. Mortreux, T. Chenal, J. W. Ziller, F. Leising and J.-F. Carpentier, *Chem. Eur. J*., 2002, **8**, 3773.

24. I. J. Hewitt, J. Tang, N. T. Madhu, C. E. Anson, Y. Lan, J. Luzon, M. Etienne, R. Sessoli and A. K. Powell, *Angew. Chem*., 2010, **122**, 6496.

25. (a) J. D. Rinehart, M. Fang, W. J. Evans and J. R. Long, *Nature Chemistry*, 2011, **3**, 538. (b) T. Rajeskumar and G. Rajaraman, *Chem. Commun*., 2012, **48**, 7856.

26. (a) R. Sessoli, D. Gatteschi, A. Caneschi and M. A. Novak, *Nature.*, 1993, **365**, 141. (b) L. Thomas, F. Lionti, R. Ballou, D. Gatteschi, R. Sessoli and B. Barbara*, Nature.,* 1996 **383**, 145. (c) J. R. Friedman and M. P. Sarachik, *Phys. Rev. Lett.,*

1996 **76** , 3830. (d) H. J. Eppley, H.-L. Tsai, N. de Vries, K. Folting, G. Christou and D. N. Hendrickson, *J. Am. Chem. Soc.,* 1995, **117** 301. (e) S. M. J. Aubin, S. Spagna, H. J. Eppley, R. E. Sager, G. Christou and D. N. Hendrickson, *Chem. Commun.,* 1998, **803**. (f) S. M. J. Aubin, Z. Sun, L. Pardi, J. Krzystek, K. Folting, L.-C. Brunel, A. L. Rheingold, G. Christou and D. N. Hendrickson, *Inorg. Chem.,* 1999, **38**, 5329. (g) M. Soler, S. K. Chandra, D. Ruiz, E. R. Davidson, D. N. Hendrickson and G. Christou, *Chem. Commun.*, 2000, 2417. (h) C. Boskovic, M. Pink, J. C. Huffman, D. N. Hendrickson and G. Christou, *J. Am. Chem. Soc.,* 2001, **123**, 9914. (i) M. A. AlDamen, J. M. Clemente-Juan, E. Coronado, C. Martı´-Gastaldo and A. Gaita-Arino, *J. Am. Chem. Soc*., 2008, **130**, 8874. (j) N. Magnani, R. Caciuffo, E. Colineau, F. Wastin, A. Baraldi, E. Buffagni, R. Capelletti, S. Carretta, M. Mazzera, D. T. Adroja, M. Watanabe and A. Nakamura, Physical Review, B, 2009, **79**, 104407.

27. S. Bertaina, S. Gambarelli, A. Tkachuk, I. N. Kurkin, B. Malkin, A. Stepanov and B. Barbara, *Nat. Nanotechnol*., 2007, **2**, 39.

28. (a) C. Benelli and D. Gatteschi, *Chem. Rev*., 2002, **102***,* 2369. (b) Y.-N. Guo, G.-F. Xu, Y. Guo and J. Tang, *Dalton Trans.*, 2011, **40**, 9953.

29. (a) M. Ferbinteanu, T. Kajiwara, K.-Y. Choi, H. Nojiri, A. Nakamoto, N. Kojima, F. Cimpoesu, Y. Fujimura, S. Takaishi and M. Yamashita, *J. Am. Chem. Soc*., 2006, **128**, 9008. (b) T. Kajiwara, M. Nakano, K. Takahashi, Shinya Takaishi, and M. Yamashita*, Chem. Eur. J.,* 2011, **17**, 196.

30. G. Poneti, K. Bernot, L. Bogani, A. Caneschi, R. Sessoli, W. Wernsdorfer and D. Gatteschi, *Chem. Commun*., 2007, 1807.

31. J.-P. Costes, S. Shova and W. Wernsdorfer, *Dalton Trans.,* 2008, 1843.

32. A. Mishra, W. Wernsdorfer, K. A. Abboud and G. Christou, *J. Am. Chem. Soc.,* 2004, **126**, 15648.

33. (a) J. Tang, I. J. Hewitt, N. T. Madhu, G. Chastanet, W. Wernsdorfer, C. E. Anson, C. Benelli, R. Sessoli and A. K. Powell, *Angew. Chem*. 2006, **118**, 1761. (b) J. Tang, I. J. Hewitt, N. T. Madhu, G. Chastanet, W. Wernsdorfer, C. E. Anson, C. Benelli, R. Sessoli and A. K. Powell, *Angew. Chem. Int. Ed.,* 2006, **45***,* 1729.

34. P. H. Lin, T. J. Burchell, R. Clérac and M. Murugesu, *Angew. Chem. Int. Ed*., 2008, **47**, 8848.

35. M. Diop, F. B. Tamboura, M. Gaye, A. S. Sall, A. H. Barry, T. Jouini and D. Senegal, *Bull. Chem. Soc. Ethiop.*, 2003, **17**, 167.

36. X-H. Bu, M. Du, L. Zhang, X-B. Song, R-U. Zhang and T. Clifford, *Inorg. Chim. Acta,* 2000, **308**, 143.

37. A. Panagiotopoulos, T. F. Zafiropoulos, S. P. Perlepes, E. Bakalbassis, I. Masson-Ramade, O. Kahn, A. Terzis and C. P. Raptopolou, *Inorg. Chem.*, 1995, **34**, 4918.

38. R. A. Layfield, A. Bashall, M. McPartlin, J. M. Rawson and D. S. Wright, *Dalton Trans.*, 2006, 1660.

39. R. A. Layfield, J. J. W. McDouall, S. A. Sulway, F. Tuna, D. Collison and R. E. P. Winpenny, *Chem. Eur*. J., 2010, **16***,* 4442.

40. P.- H. Lin, T. J. Burchell, R. Clérac and M. Murugesu, *Angew. Chem*., 2008, **120**, 8980.

41. (a) V. Lozan, C. Loose, J. Kortus and B. Kersting, *Coord. Chem. Rev*., 2009, **253**, 2244. (b) G. Henkel and B. Krebs, *Chem. Rev.,* 2004, **104**, 801. (c) A. C. Marr, D. J. E. Spencer and M. Schröder. *Coord. Chem. Rev.* 2001, **1055**, 219-221. (d) D. Sellmann and J. Sutter*, Acc. Chem. Res.* 1997, **30**, 460.

42. (a) T. Liu, B. Li, M. L. Singleton, M. B. Hall and M. Y. Darensbourg, *J. Am. Chem. Soc*., 2009, **131**, 8296. (b) H. Petzold, J. Xu and P. J. Sadler, *Angew. Chem. Int.* Ed., 2008, **47**, 3008. (c) D. C. Fox, A. T. Fiedler, H. L. Halfen, T. C. Brunold and J. A. Halfen, *J. Am. Chem. Soc*., 2004, **126**, 7627. (d) X. G. Zhou, M. Zhu, L. B. Zhang, Z.Y. Zhu, C. F. Pi, Z. Pang, L. H. Weng and R. F. Cai, *Chem. Commun.,* 2005, 2342. (e) S. P. Jeffery, J. Lee and M. Y. Darensbourg, *Chem. Commun.,* 2005, 1122. (f) A. T. Fiedler, P. A. Bryngelson, M. J. Maroney and T. C. Brunold, *J. Am. Chem. Soc.* 2005, **127**, 5449. (g) E. Bourles, R. Alves de Sousa, E. Galardon, M. Giorgi and I. Artaud, *Angew. Chem., Int. Ed.,* 2005, **44**, 6162. (h) B. Hernandez, Y. Wang, D. Zhang and M. Selke, *Chem. Commun.,* 2006, **997**.

43. (a) J. H. Melman, T. J. Emge and J. G. Brennan, *Chem. Commun*., 1997, 2269. (b) Y. Misumi, H. Seino and Y. Mizobe, *J. Am. Chem. Soc.,* 2009, **131**, 14636. (c) E. Alvaro and J. F. Hartwig, *J. Am. Chem. Soc.,* 2009, **131**, 7858. (d) S. C. Ammal, N. Yoshikai, Y. Inada, Y. Nishibayashi and E. Nakamura, *J. Am. Chem. Soc.,* 2005, **127**, 9428.

44. (a) Y.-F. Han, Y.-J. Lin, W.-G Jia and G.-X. Jin, *Dalton Trans.,* 2009, 2077. (b) J. Ruiz Aranzaes, C. Belin and D. Astruc, *Chem. Commun.,* 2007, 3456. (c) M. Bardaji, M. J. Calhorda, P. J. Costa, P. G. Jones, A. Laguna, M. R. Perez and M. D. Villacampa, *Inorg. Chem.,* 2006, **45**, 1059. (d) T. Glaser, T. Beissel, E. Bill, T. Weyhermueller, V. Schuenemann, W. Meyer-Klaucke, A. X. Trautwein and K. Wieghardt, *J. Am. Chem. Soc.,* 1999, 121, 2193. (e) H. J. Kruger and R. H. Holm, *J. Am. Chem. Soc.,* 1990, **112**, 2955. (f) P. M. Treichel, L. D. Rosenhein and M. S. Schmidt, *Inorg. Chem.,* 1983, **22**, 3960.

45. D. Brown, D. G. Holah, and C. E. F. Rickard, *J. Chem.* Soc., 1970, **786**.

46. S. Spiliadis, A. A. Pinkerton, and D. Schwarzenbach, *J. Chem. Soc., Dalton Trans.,* 1982, 1809.

47. H. C. Aspinall, D. C. Bradley, M. B. Hursthouse, K. D. Sales and N. P. C. Walker, *J. Chem. Soc. Chem., Commun.,* 1985, 1585. (b) H. C. Aspinall, and S. A. Cunningham, *Inorg. Chem.* **1998**, 37*,* 5396.

48. H. C. Aspinall, D. C. Bradley, M. B. Hursthouse, K. D. Sales, N. P. C. Walker and B. Hussain, *J. Chem. Soc., Dalton Trans.,* 1989, 623.

49. (a) J. Zhang, L. Ma, Y. Han, F. H. Z. Zhang, R. Cai, Z. Chen and X. Zhou., *Dalton Trans.*, 2009, 3298–3305 (b) Z. Zhang, L. Zhang, Y. Li, L. Hong, Z. Chen and X. Zhou*, Inorg. Chem.*, 2010, **49**, 5715-5722 (c) L. Ma, J. Zhang, Z. Zhang, R. Cai, Z. Chen and X. Zhou., *Organometallics,* 2006, **25**, 4571.

50. Z. Zhang, L. Zhang, Y. Li, L. Hong, Z. Chen and X. Zhou*, Inorg. Chem.*, 2010, **49**, 5715.

51. L. Ma, J. Zhang, Z. Zhang, R. Cai, Z. Chen and X. Zhou, *Organometallics*, 2006, **25**, 4571.

52. (a) K. S. Cole and R. H. Cole, *J. Chem. Soc.* 1941, **9**, 341.

53. S. M. Fang, E. C. Sañudo, M. Hu, Q. Zhang, S. T. Ma, L. R. Jia, C. Wang, J. Y. Tang, M. Du and C. S. Liu, *Crystal Growth and Design*, 2011, **11**, 811.

54. (a) Y. N. Guo, G. F. Xu, W. Wernsdorfer, L. Ungur, Y. Guo, J. Tang, H. J. Zhang, L. F. Chibotaru and A. K. Powell, *J. Am. Chem. Soc.*, 2011, **133**, 11948. (b) P. H. Lin, T. J. Burchell, L. Ungur, L. F. Chibotaru, W. Wernsdorfer and M. Murugesu, *Angew. Chem. Int. Ed.,* 2009, **48**, 9489. (c) L. F. Chibotaru, L. Ungur and L. Soncini, *Angew. Chem. Int. Ed.,* 2008, **47**, 4126.

55. F. Aquilante, L. De Vico, N. Ferre, G. Ghigo, P. A. Malmqvist, P. Neogrady, T. B. Pedersen, M. Pitonak, M. Reiher, B. O. Roos, L. Serrano-Andres, M. Urban, V. Veryazov and R. Lindh, *J. Comput. Chem*., 2010, **31**, 224.

56. (a) S. A. Sulway, R. A. Layfield, F. Tuna, W. Wernsdorfer and R. E. P. Winpenny, *Chem. Commun*., 2012, **47**, 1508. (b) F. Tuna, C. A. Smith, M.

Bodensteiner, L. Ungur, L. F. Chibotaru, E. J. L. McInnes, R. E. P. Winpenny, D. Collison, and R. A. Layfield, *Angew. Chem. Int. Ed.,* 2012, **51**, 6976.

57. For SINGLE_ANISO module, see http://www.molcas.org/documentation/manual/node95.html

58. L. Ungur and L. F. Chibotaru, Program POLY_ANISO, University of Leuven, 2006-2012.

59. (a) R. Anwander in "*Organolanthanoid Chemistry: Synthesis, Structure, Catalysis*", Springer-Verlag Berlin Heidelberg, Volume 179, pp 151-200, 1996. (b) D. C. Bradley, R. C. Mehrotra and D. P. Gauer, "*Metal Alkoxides*", Academic Press, London, 1978. (c) R. C. Mehrotra, *Adv. Inorg. Chem., Radiochem.,* 1983, **26,** 269. (d) K. C. Malhotra, and R. L. Martin, *J. Organomet. Chem.,* 1982. **239**, 159.

60. G. A. Molander, *Chem Rev*, 1992, **92**, 29.

61. (a) T. J. Marks, *Prog. Inorg. Chem.,* 1978, **24**, 51. (b) W. J. Evans, *Adv. Organomet. Chem.,* 1985, **24,** 131.

62. (a) H. Arm, K. Hochstrasser and P. W. Schnidler, *Chimia*, 1978, **28**, 237. (b) L. A. Cohen and W. M. Jones, *J. Am. Chem. Soc.,* 1963, **85**, 3397.

63. (a) O. Poncelet, W. J. Sartain, L. G. Hubert-Pflazgraf, K. Folting and K. G Caulton, *Inorg. Chem.*, 1989, **28**, 263. (b) D. C. Bradley, H. Chudzynska, D. M. Frigo, M. E. Hammond, M. B. Hursthouse and M. A. Mazid, *Polyhedron,* **9**,

719. (c) G. Helgesson, S. Jagner, O. Poncelet and L. G. Hubert-Pflazgraf, *ipid,* **10**, 1559.

64. D. C. Bradley, H. Chudzynska and M. B. Hursthouse, *Polyhedron*, **1991**, 10, 1049.

65. C. Eaborn, *J. Chem. Soc*, 1952, 2840.

66. P. D. Lickiss, *J. Organomet. Chem.,* 1986, **308**, 261.

67. (a) M. Weidenbruch, H. Pesel, W. Peter and R. Steichen, *J. Organomet. Chem*, 1977, **141**, 9 , (b) M. Weidenbruch, H. Pesel and D. Van Hieu, *Z. Naturforsch*, B35, 31.

68. E. M. Dexheimer, L. Spialter and L. D. Smithson, *J. Organomet. Chem.*, 1975, **102**, 21

69. F. A. Cotton, G. Wilkinson, C. A. Murillo and M. Bochmann "*Advanced Inorganic Chemistry*", 6th ed., John Wiley & Sons Ltd, New York, 1999.

70. C. Airoldi and R. F. de Farias, *Quim. Nova,* 2004, **27**, 84.

71. G. B. Deacon, T. Feng, P. Mackinnon, R. H. Newnham, S. Nickel, B. W. Skelton and A. H. White, *Aust. J. Chem.,* 1993, **46**, 387.

72. G. B. Deacon, G. D. Fallon, C. M. Forsyth, S. C. Harris, P. C. Junk, B. Skelton and A. H. White, *Dalton Trans.,* 2006, 802.

73. G. B. Deacon, P. E. Fanwick, A. Gitlits, I. P. Rothwell, B. W. Skelton and A. H. White, *Eur. J. Inorg. Chem.,* 2001, 1505

74. W. J. Evans, M. A. Greci and J. W. Ziller, *Chem. Commun.,* 1998, 2367.

75. G. B. Deacon, C. M. Forsyth, P. C. Junk, B. W. Skelton and A. H. White, *Chem.-Eur. J.* 1999, **5**, 1452.

76. W. J. Evans, M. A. Greci and J. W. Ziller, *Chem. Commun.,* 1998, 2367.

77. L.-L. Zhang, Y.-M. Yao, Y.-J. Luo, Q. Shen and J. Sun, *Polyhedron,* 2000, **19**, 2243.

78. F. A. Carey, "*Advanced Organic Chemistry",* 4th Edition, Kluwer Academic/Plenum Publishers, New York, 2001.

79. D. Astruc, "*Organometallic Chemistry and Catalysis*", Springer-Verlag, Berlin, 2007.

80. R. C. Mehrotra, A. Singh and U. M. Tripathi, *Chem. Rev.,* 1991, **91**, 1287.

81. L. G. Hubert-Pfalzgraf, *New J. Chem.,* 1995, **19**, 727.

82. R. Anwander, *Top. Curr. Chem.,* 1996, **179**, 149.

83. D. C. Bradley, R. C. Mehrotra, I. P. Rothwell and A. Singh, "*Alkoxo and Aryloxo Derivatives of Metals"*, Academic Press, New York, 2001.

84. N. Y. Turova, E. P. Turevskaya, V. G Kessler and M. I. Yanovskaya in "*The Chemistry of Metal Alkoxide*", Kluwer Academic Publishers, Boston, 2002.

85. (a) W. J. Evans, R. Anwander, V. H. Berlekamp and J. W. Ziller, *Inorg. Chem,* 1995, **34**, 3583. (b) W. J. Evans, R. E. Golden and J. W. Ziller, *Inorg. Chem.,* 1991, **30**, 4963. (c) W. J. Evans, J. M. Olofson and J. W. Ziller, *Inorg. Chem.,* 1989, **28**, 4308. (d) L. G. Hubert-Pfalzgraf, S. Morlens, S. Daniele and A. Thozet, *Inorg. Chem. Commun.,* 2004, **7**, 751. (e) O. Poncelet, L. G. Hubert-

Pfalzgraf, J.-C. Daran and R. Astier, *Chem. Commun.,* 1989, 1846. (f) L. G. Westin, M. Kritikos, and A. Caneschi, *Chem. Commun.,* 2003, 1012.

86. (a) W. J. Evans, M. A. Greci and J. W. Ziller, *Inorg. Chem.,* 1998, **37**, 5221. (b) W. J. Evans, M. A Greci and J. W. Ziller, *Inorg. Chem.,* 2000, **39**, 3213.

87. T. J. Boyle and L. A. M. Ottley, *Chem. Rev.,* 2008, **108***,* 1896.

88. P. S**.** Gradeff, J. K. Yunlu, T. J. Deming, J. M. Olofson, R. J. Doedens, and W. J. Evans, *Inorg. Chem.,* 1990, **29,** 420.

89. R. G. Gerkin and W. J. Reppart, *Acta Cryst.,* 1984, **40**, 78.

90. (a) D. M. L. Goodgame, D. Williams and R. E. P. Winpenny, *J. Chem. Soc. Dalton. Trans*., 1989, 1439. (b) A. Abragam and B. Bleaney, "*Electron Paramagnetic Resonance of Transition Ions"*, Oxford University Press, Oxford, England, 1970. (c) A. Priem, P. J. M. van Bentum, W. R. Hagen, and E. J. Reijerse, *Appl. Magn. Reson.,* 2001, **21**, 535. (d) M. Arakawa, H Ebisu and H Takeuchi, *J. Phys.: Condens. Matter,* 1997, **9***,* 5193. (e) H. Takeuchi, H. Ebisu and M. Arakawa, *J Phys.: Condens. Matter*, 1995, **7**. (f) C. Legein, J. Y. Buzaré, G. Silly and C. Jacoboni, *J. Phys.: Condens. Matter*, 1996, **8**. (g) H. Takeuchi, M. Arakawa and H. Ebisu, *J. Phys.: Condens. Matter,* 1991, **3**, 4405. (h) C.-C. Yang, S. Lee, and A. J. Bevolo, *Physical Review* B, 1976, **13**.

91. R. Van Deun, P. Nockemann, C. Göller-Walrand and K. Binnemans, *Chemical Physics Letters,* 2004, **397,** 447.

92. K. Kuriki, Y. Koike and Y. Okamoto, *Chem. Rev.*, 2002, **102**, 2347.

93. L. H. Slooff, A. van Blaaderen, A. Polman, G. A. Hebbink, S. I. Klink, F. C. J. M. van Veggel, D. N. Reinhoudt and J. W. Hofstraat, *J. Appl. Phys.,* 2002, **91**, 3955.

94. M. J. Dejneka, A. Streltsov, S. Pal, A. G. Frutos, C. L. Powell, K. Yost, P. K. Yuen, U. Müller, and J. Lahiri, *PNAS.*, 2003, **100**, 393.

95. W. F. Krupket, *Phys. Rev.,* 1965, **139**.

96. J. B. Gruber and R. A. Satten *J. Chem. Phys.,* 1963, **39**, 1455

97. J. C. Hill and R. G. Wheeler, *Phys. Rev.,* 1966, **152**, 482

98. N. K. Al-Rasbi, S. Derossi, D. Sykes, S. Faulkner and M. D. Ward, *Polyhedron,* 2009, **28**, 227.

99. W. J. Miniscalo, *J. Lightwave. Tech.*, 1991*,* **9**, 234

100. (a) H. L. Liu, Y. Wang, C. Hou, W. Li, M. Lu, K. Zou and B. Peng, *Optics Express*, 2009, **17** 15351. (b) M. Seshadri, K. Venkata Rao J. Lakshmana Rao, K. S. R. Koteswara Rao and Y. C. Ratnakaram*, Journal of Luminescence,* **130,** 2010, 536

101. (a) H. A. Hussain, A. A. Ansari and K. Iftikhar, *Spectrochimica Acta*, 2004, **60**, 873. (b) M. Irfanullah & K. Iftikhar, *J Fluoresc*., 2011, **21**, 81.

102. (a) D. M. P. Mingos in *"Comprehensive Organometallic Chemistry"*, 1st Edition, Volume 3, Chapter 19, pp. 1-63. G. Wilkinson, F. G. A. Stone, E. W. Abel (Eds.), Pergamon Press, Oxford, 1982. (b) F. T. Eldelman in *"Comprehensive Organometallic Chemistry"*, 2nd Edition, Volumes 1-12. G. Wilkinson, F. G. A. Stone, E. W. Abel (Eds.), Pergamon, Oxford, 1995.

103. T. J. Kealy and P. L. Pauson, *Nature,* 1951, **168**, 1039

104. S. A. Miller, J. A. Tebboth and J. F. Tremaine, *J. Chem. Soc.,* 1952, 632

105. G. Wilkinson, *J. Am. Chem. Soc.,* 1952, **74**, 2125

106. (a) N. Long, "*Metallocenes: An introduction to Sandwich Complexes"* 1st Edition, Blackwell Science Ltd., London, 1998.(b) www.ilpi.com/organomet/Cp.htm/

107. (a) W. Bünder and E. Weiss, *Z. Naturforsch., B: Anorg. Chem. Org. Chem.,* 1978, **33,** 1235. (b) P. Coppens, *Nature*, 1964, **204**, 1298. (c) R. A. Layfield, *Chem. Soc. Rev.,* 2008, **37**, 1098.

108. G. Christou, "*Magnetism: A Supramolecular Function"*, ed. O. Kahn, NATO ASI. Series, Kluwer, Dordrecht, The Netherlands, 1996, **383.**

109. G. Aromí, S. M. J. Aubin, M. A. Bolcar, G. Christou and H. J. Eppley, *Chem. Commun.*, 1999, 1973.

110. K. Folting, D. N. Hendrickson, J. C. Huffman, R. C. Squire, H.-L. Tsai, S. Wang and M. W. Wemple, *Polyhedron*, 1998, **17**.

111. (a) R. D. Cannon and R. P. White, *Prog. Inorg. Chem*, 1988, **36,** 195. (b) S. P. Palii, D. E. Richardson, M. L. Hansen, B. B. Iversen, F. K. Larsen, L. Singerean, G. A. Timco, N. V. Gerbeleu, K. R. Jennings and J. R. Eyler, *Inorg. Chim. Acta*., 2000, **319**, 23.

112. (a) S. K. Mandal, V. G Young Jr. and L. Que Jr., *Inorg. Chem.,* 2000, **39**, 1831.

(b) C. Boskovic, E. Rusanov, H. Stoeckli-Evans and H. U. Güdel, *Inorg. Chem.*

Commun., 2002, **5**, 881. (c) S. A. Sulway, D. Collison, J. J. W. McDouall, F. Tuna and R. A. Layfield, *Inorg. Chem.,* 2011, **50**, 2521-2526.

113. R. Kempe, J. Sieler, D. Walther, J. Reinhold and K. Rommel, *Z. Allorg. Allg. Chem*.,1993, **619**, 1105.

114. J. Estienne and R. Weiss, *J. Chem. Soc. Chem. Commun.,* 1972, **862.**

115. R. Clérac, F. A. Cotton, K. R. Dunbar, E. M. Hillard, M. A. Petrukhina and B. W. Smucker, *C. R. Acard. Sci. Ser II Chim.*, 2001, **4**.

116. G. Aromi, A. S. Batsanov, P. Christian, M. Helliwell, A. Parkin, S. Parsons, A. A. Smith, G. A. Timco and R. E. P. Winpenny*, Chem.Eur. J.,* 2003, **9**, 5147.

117. C. S. Alvarez, A. Bashall, A. D. Bond, D. Cave, E. A. Harron, R. A. Layfield, M. E. G. Mosquera, M. McPartlin, J. M. Rawson, P. T. Wood and D. S. Wright, *Dalton Trans*., 2003, 3002.

118. M. A. Beswick, J. S. Palmer and D. S. Wright, *Chem. Soc. Rev.*, 1998, **27***,* 225.

119. (a) R. H. Holm, *Chem. Soc. Rev.*, 1981, **10,** 455. (b) J. M. Berg, K. O. Hodgson and R. H. Holm, *J. Am. Chem. Soc.*, 1979, **101**, 4586 (c) S. Onaka, Y. Katukawa, *J. Coord. Chem,* 1996, **39**, 135-146 (d) E. W Abel and B. C. Crosse, *J. Chem. Soc. (A).,* 1966, 1141, (e) B. F. G. Johnson, P. J. Pollick, I. G. William and A. Wojcicki, *Inorg. Chem.,* **7**, 831, 1968. (f) C. R. Jenkins, *J. Organomet. Chem.,* **15**, 441, 1968 (g) P. M. Treichel and M. H. Tegan*, Inorg. Synthesis*, H. R.

Allcock, ed. John Wiley & Sons, New York, 1989, **25**, 115 and references therein.

120. J. Jubb, L. F. Larkworthy, G. A. Leonard, D. C. Povey and B. Joly-Tucker, *J. Chem. Soc. Dalton Trans.,* 1989, 1631.

121. L. F. Larkworthy, G. A. Leonard, D. C. Povey, S. S. Tandon, B. Joly-Tucker and G. W. Smith, *J. Chem. Soc. Dalton Trans*., 1994, 1425.

122. (a) A. M. Arif, J. G. Hefner, R. A. Jones and S. U. Koshmieder, *J. Coord. Chem*., 1991, **23**, 13. (b) P. Sobota, S. Przybylak, J. Ejfler, M. Kobyl ka and L. B. Jerzykiewicz, *Inorganica Chimica Acta*., 2002, **334** 159. (c) M. J. McGeary, K. Folting, W. E. Streib, J. C. Huffman and K. G. Caulton, Polyhedron, 1991, **10**, 2699.

123. (a) C. S. Alvarez, S. R. Boss, J. C. Burley, S. M. Humphrey, R. A. Layfield, R. A. Kowenicki, M. McPartlin, J. M. Rawson, A. E. H. Wheatley, P. T. Wood and D. S. Wright, *Dalton. Trans*., 2004, 3481. (b) C. Lopes, M. Håkansson and S. Jagner, *Inorganica Chimica Acta,* 1997, **254**, 361 (c) W. E. Hatfield, R. R. Weller and J. W. Hall, *Inorg. Chem*., 1980, **19**, 3825. (d) L. J. Batchelor, E. Fitzgerald, J. Wolowska, J. J. W. McDouall and E. J. L. McInnes*, Chem. Eur. J.,* 2010, **16**, 11082.

124. (a) L. Y. Goh and M. S. Tay, *Organometallics,* 1992, **11**, 1711. (b) L.-C. Song, H-W. Cheng, X. Chen, and Q.-M Hu, *Eur. J. Inorg. Chem.,* 2004, 3147. (c) K.

Sukcharoenphon, T. D. Ju K. A. Abboud, C. D. Hoff*, Inorg. Chem.,* 2002, **41**, 6769.

125. W. Evans, G. Rabe and J. Ziller, *J. Angew., Int. Ed. Engl.,* 1994, **33**, 2110

126. D. Cary, G. Ball and J. Arnold, *J. Am. Chem. Soc.*, 1995, **117**, 3492.

127. (a) D. Freedman, T. J. Emge and J. G. Brennan, *J. Am. Chem. Soc.,* 1997, **119**, 1112. (b) D. Freedman, J. H. Melman, T. J. Emge and J. G. Brennan*, Inorg. Chem.,* 1998, **37**, 4163.

128. J. H. Melman, T. J. Emge and J. G. Brennan, *Inorg. Chem.,* 1999, **38**, 211.

129. (a) M. A. Beswick, C. N Harmer, P. R. Raithby, A. Steiner, M. Tombul and D. S. Wright, *J. Organomet. Chem*., 1999, **573**, 267. (b) W. -H. Pan and J. P. Fackler Jr., *J. Am. Chem. Soc.,* 1978, 5183 (c) M. Lardon, *J. Am. Chem. Soc.*, 1970, **92**, 5063.

130. I. Dugdale and J. B. Cotton, *Corros. Sci.* 1963, ***3***, 69.

131. D. Collison, E. J. L. McInnes and E. K. Brechin, *Eur. J. Inorg. Chem.,* 2006, 2725–2733.

132. (a) J. H. Marshall, *Inorg. Chem.,* 1978, **17**, 3711. (b) M. Murrie, D. Collison, C. D. Garner, M. Helliwell, P. A. Tasker and S. S. Turner, *Polyhedron.,* 1998, **17**, 3031. (c) J. Handley, D. Collison, C. D. Garner, M. Helliwell, R. Docherty, J. R. Lawson and P. A. Tasker, *Angew. Chem. Int. Ed. Engl.,* 1993, ***32***, 1036. (d) E. G. Bakalbassis, E. Diamontopoulou, S. P. Perlepes, C. P. Raptopoulou, V. Tangoulis, A. Terzis and T. F. Zafiropoulos, *J. Chem.Soc., Chem. Commun.,*

1995, 1347. (e) V. Tangoulis, C. P. Raptopoulou, A. Terzis, E. G. Bakalbassis, E. Diamontopoulou and S. P. Perlepes, *Inorg. Chem.,* 1998, **37**, 3142.

APPENDICES

APPENDIX ONE

Single-Molecule Magnets

DOI: 10.1002/anie.201202497

A High Anisotropy Barrier in a Sulfur-Bridged Organodysprosium Single-Molecule Magnet**

Floriana Tuna, Charlene A. Smith, Michael Bodensteiner, Liviu Ungur, Liviu F. Chibotaru, Eric J. L. McInnes, Richard E. P. Winpenny, David Collison, and Richard A. Layfield**

Dedicated to Professor Dieter Fenske on the occasion of his 70th birthday

Following the discovery in the early 1990s that individual molecules can exhibit slow relaxation of magnetization and magnetic hysteresis,[1] studies of single-molecule magnets (SMMs) have been dominated by large-spin, exchange-coupled cages of 3d transition metals.[2] In addition to the intrinsic interest in the physics of SMMs, such compounds have been proposed for applications in molecular spintronics and in quantum computing.[3] However, a major obstacle to realizing the applications of SMMs is that energy barriers to magnetization reversal, U_{eff}, and blocking temperatures, T_B, lead to slow relaxation of magnetization only at liquid helium temperatures.

In recent years, there has been a growing realization that focusing on enhancements in magnetic anisotropy rather than on ever-larger spins may be a more effective strategy for increasing U_{eff} and T_B. Therefore, there has been a rise to prominence of the f elements in SMM studies,[4] and lanthanide-containing SMMs (Ln-SMMs) in particular have enabled many exciting developments. For example, in 2003 Ishikawa et al. reported that slow relaxation of magnetization is possible in molecules that contain a single lanthanide ion, namely the terbium(III) phthalocyanine sandwich complex $[TbPc_2]^-$, with $U_{eff} = 230\ cm^{-1}$.[5] The family of lanthanide single-ion magnets (SIMs) continues to grow,[6] and indeed the terbium(III) SIM $[Tb^iPc_2]$ (^iPc = isopropylidenedioxyphthalocyanine), has the highest anisotropy barrier of $U_{eff} = 556\ cm^{-1}$.[6e]

Many polymetallic Ln-SMMs, the majority based on dysprosium(III), have also been reported, some of which show impressive SMM properties, such as high values of U_{eff} and/or T_B.[7] The dilanthanide SMMs $[Ln_2\{N(SiMe_3)_2\}_4(thf)_2(\mu{:}\eta^2{:}\eta^2\text{-}N_2)]^-$ with Ln = Dy or Tb, reported by Evans, Long et al., are arguably the most notable recent examples because the Ln^{III} ions are strongly exchange-coupled by the radical $[N_2]^{3-}$ ligand.[8] In the case of the terbium derivative, hysteresis loops in the magnetization versus field plots were observed up to 14 K.

In the majority of Ln-SMMs, the Ln^{III} ions reside in environments that consist of hard oxygen or nitrogen donor ligands. Whereas the spin configurations of Ln^{III} ions are insensitive to their environment, their overall electronic structure may be very sensitive. We reasoned that using less-conventional ligands (in the context of SMMs) could be a route to modifying their properties. For example, using soft donors could have two effects: first, magnetic exhange between Ln^{III} ions could be enhanced; second, very different crystals fields could be generated. Thus, as crystal field effects are the main interactions that lead to slowly relaxing magnetization in Ln-SMMs, there is merit in exploring soft ligand environments. We now report the $\{Dy_2\}$ SMM $[\{Cp'_2Dy(\mu\text{-}SSiPh_3)\}_2]$ (**2**, $Cp' = \eta^5\text{-}C_5H_4Me$), in which the Dy ions are bridged by thiolate ligands. Compound **2** is the first sulfur-bridged SMM, and the magnetization reversal barrier is the highest yet reported for a $\{Dy_2\}$ SMM. Ab initio calculations on **2** and related compounds provide insight into the factors that influence the magnetization reversal barrier.

The sulfur-bridged dimers $[\{Cp'_2Ln(\mu\text{-}SSiPh_3)\}_2]$ (Ln = Gd (**1**), Dy (**2**)) were synthesized by the ligand substitution reactions of Cp'_3Ln with lithium triphenylsilylthiolate (Scheme 1).

The centrosymmetric dimers crystallize as **1**·(toluene) and **2**·(toluene), and are isostructural (Figure 1; Supporting Information, Figures S1,S2 and Tables S1,S2).

Each Ln^{III} ion in **1** and **2** is complexed by two η^5-Cp′ ligands and by the sulfur atoms of two μ-$SSiPh_3$ ligands,

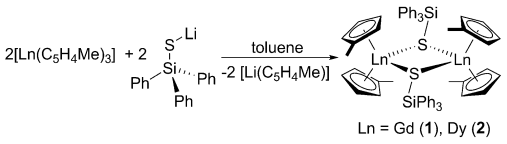

Scheme 1. Synthesis of **1** and **2**.

[*] Dr. F. Tuna, C. A. Smith, Prof. E. J. L. McInnes, Prof. R. E. P. Winpenny, Prof. D. Collison, Dr. R. A. Layfield
School of Chemistry and EPSRC UK National EPR Facility
The University of Manchester
Oxford Road, Manchester, M13 9PL (UK)
E-mail: richard.layfield@manchester.ac.uk
Dr. M. Bodensteiner
Institute of Inorganic Chemistry, University of Regensburg
93040 Regensburg (Germany)
Dr. L. Ungur, Prof. L. F. Chibotaru
Division of Quantum and Physical Chemistry
Katholieke Universiteit Leuven
Celestijenlaan 200F, 3001 Leuven (Belgium)

[**] R.A.L. thanks the Alexander von Humboldt Foundation (Fellowship for Experienced Researchers). The EPSRC (UK) are acknowledged. R.E.P.W. thanks The Royal Society for a Wolfson Merit Award. L.U. thanks the FWO-Vlaanderen (Flemish Science Foundation) for a post-doctoral fellowship.

Supporting information for this article is available on the WWW under http://dx.doi.org/10.1002/anie.201202497.

© 2012 Wiley-VCH Verlag GmbH & Co. KGaA, Weinheim

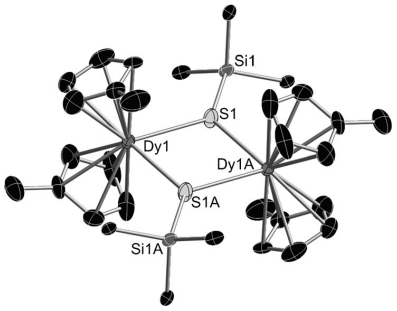

Figure 1. ORTEP representation (ellipsoids set at 50% probability) of the molecular structure of **2**. For clarity, only the *ipso* carbons of the phenyl rings are shown, and the hydrogen atoms are omitted.

resulting in formal coordination numbers of eight. Alternatively, with respect to Cp ligand centroids and the sulfur atoms, the Dy^{III} centers reside in pseudo tetrahedral geometries, with local C_2 symmetry at Ln (see Table 1 for bond lengths and angles). The asymmetric η^5-Cp coordination mode is reflected in the range of Ln–C distances, which are 2.622(7)–2.707(14) for **1** and 2.599(15)–2.693(10) Å for **2**. The Ln1–S1 and Ln1–S1A distances of 2.7755(14) and 2.7961(15) Å in **1** and 2.7500(15) and 2.7761(16) Å in **2**, combined with the Ln1-S1-Ln1A angles of 101.53(5) and 101.43(6) in **1** and **2**, respectively, show that the Ln_2S_2 rings are rhomboidal. The Ln–C and Ln–S bond lengths and angles in **1** and **2** are typical of compounds of the type $[\{Cp_2Ln(\mu\text{-}SR)\}_2]$ with Ln = Gd or Dy.[9]

Table 1: Selected bond lengths [Å] and angles [°] for **1** and **2**.

	1 (Ln = Gd)	**2** (Ln = Dy)
Ln–C	2.622(7)–2.707(14)	2.599(15)–2.693(10)
Ln1–S1	2.7755(14)	2.7500(15)
Ln1–S1A	2.7961(15)	2.7761(16)
S1-Ln1-S1A	78.47(4)	78.57(5)
Ln1-S1-Ln1A	101.53(5)	101.43(6)

Lanthanide chalcogenolate complexes have been extensively studied because of their applications in organic synthesis and in the catalytic ring-opening polymerization of ε-caprolactone.[10] However, the dynamic magnetic properties of such compounds have not, to the best of our knowledge, been studied previously.

Direct current (dc) magnetic susceptibility measurements on polycrystalline samples of **1** and **2** were carried out in the temperature range 2–300 K in an applied field of 1 kG. For **1**, the value of $\chi_M T$ (χ_M is the molar magnetic susceptibility) per Gd^{III} at 300 K is 15.5 $cm^3 K mol^{-1}$ (Supporting Information, Figure S3), which is in good agreement with the predicted value of $\chi_M T = 15.76\ cm^3 K mol^{-1}$ for two non-interacting Gd^{III} free ions ($^8S_{7/2}$ ground term, $g = 2$). On cooling, the value of $\chi_M T$ decreases very slowly until about 30 K, and then below 30 K $\chi_M T$ decreases rapidly to reach a value of 6.7 $cm^3 K mol^{-1}$ at 2 K. The absence of first-order spin–orbit coupling in Gd^{III} enables the exchange coupling constant, J, for **1** to be readily determined. Fitting the susceptibility data for **1** using the isotropic spin Hamiltonian $H = -2J[S_{Gd1} \cdot S_{Gd1A}]$, where S_{Gd1} and S_{Gd1A} denote the spins on Gd1 and Gd1A, respectively, produced an excellent fit for $J = -0.105\ cm^{-1}$. The same parameters also reproduced the field dependence of the isothermal magnetization of **1** measured at several temperatures between 2–9 K (Supporting Information, Figure S4). These data indicate that the Gd^{III} ions in **1** are weakly antiferromagnetically coupled by the μ-thiolate ligands, which is consistent with other exchange-coupled gadolinium compounds, and can be rationalized in terms of the core-like nature of their valence 4f orbitals.[11]

In **2**, the value of $\chi_M T$ at 300 K is 27.9 $cm^3 K mol^{-1}$, which agrees well with the expected value of 28.34 $cm^3 K mol^{-1}$ for two magnetically noninteracting Dy^{III} ions with a $^6H_{15/2}$ ground term ($g = 4/3$; Supporting Information, Figure S5). On lowering the temperature, $\chi_M T$ decreases gradually until about 70 K, and then more rapidly to reach 11.2 $cm^3 K mol^{-1}$ at 2 K; this decrease is likely to be due to depopulation of excited m_J sublevels and/or weak antiferromagnetic exchange. At low temperatures, the isothermal $M(H)$ data of **2** are far from reaching saturation under magnetic fields of 0–7 T, and the corresponding $M(H/T)$ curves do not superimpose (Supporting Information, Figure S6), indicating the presence of significant magnetic anisotropy and/or low-lying excited states. The value of the magnetization at 7 T and 1.8 K is 11.4 μ_B (5.7 per Dy^{III} ion), and is similar to that observed in other Dy complexes.[7]

Both the temperature dependence (Figure 2; Supporting Information, Figure S7) and the frequency dependence (Supporting Information, Figure S8) of the alternating current (ac) susceptibilities of **2** reveal features characteristic of an SMM. In zero dc field, the in-phase (χ') (Supporting Information, Figure S7) and the out-of-phase (χ'') components (Supporting Information, Figure 2) of the ac susceptibility show a frequency dependence up to about 40 K, and a single $\chi''(T,\nu)$ peak is observed below 32 K. Semicircular Cole–Cole plots of χ'' vs. χ' at several temperatures below 32 K were obtained

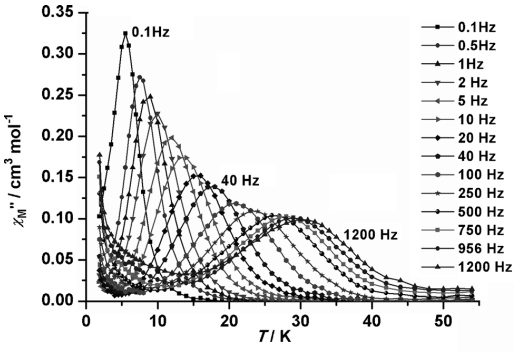

Figure 2. Temperature dependence of χ'' in **2** at various frequencies in zero applied dc field and an ac field of $H_{ac} = 1.55$ Oe.

 © 2012 Wiley-VCH Verlag GmbH & Co. KGaA, Weinheim

(Supporting Information, Figure S9), and were fitted by a generalized Debye model using α parameters in the range $\alpha = 0.01$–0.15. This indicates a narrow range of magnetization relaxation times in **2**. Above 20 K, the relaxation in **2** is thermally activated and the Arrhenius plot of $\ln\tau$ versus $1/T$, where τ is the relaxation time constant, is linear (Figure 3).

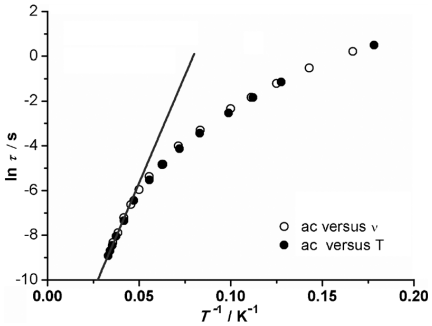

Figure 3. Arrhenius plot of ln τ versus $(1/T)$ for **2**. The solid line is the best fit of the data in the thermally activated regime ($T > 20$ K).

Fitting the higher-temperature data to the Arrhenius law $\tau = \tau_0 \exp(U_{\text{eff}}/k_B T)$ produced an effective energy barrier to magnetization reversal of $U_{\text{eff}} = (133 \pm 3.5)\ \text{cm}^{-1}$ (or (192 ± 5) K) and a pre-exponential factor of $\tau_0 = 2.38 \times 10^{-7}$ s. The SMM behavior of **2** was confirmed by the observation of a narrow hysteresis in magnetization versus field measurements on polycrystalline samples at 1.8 K (Supporting Information, Figure S10).

Compound **2** is the first sulfur-bridged SMM. Organometallic compounds are an interesting alternative chemical repertoire for developing SMMs with unusual physics and high magnetization reversal barriers. Notable recent SMMs based on the dianionic cyclooctatetraene ligand (C_8H_8, COT) include: $[Dy\{\eta^8\text{-}1,4\text{-}(Me_3Si)_2(COT)\}_2]^-$, which exhibits multiple relaxation modes;[6a] $[(\eta^5\text{-Cp*})Er(\eta^8\text{-COT})]$;[6b] and neptunocene, $[Np(\eta^8\text{-COT})_2]$.[6c] The SMMs most closely related to **2** are $[\{Cp_2Dy(\mu\text{-Cl})\}_n]$ ($n = 2$, **3a**; $n = \infty$, **3b**), $[Cp_2Dy(thf)(\mu\text{-Cl})]_2$ (**4**) and $[\{Cp_2Dy(\mu\text{-Bta})\}_2]$ (**5**; Bta = benzotriazolate), which have lower magnetization reversal barriers of $U_{\text{eff}} = 26$, 68, 34, and 33 cm^{-1}, respectively.[12]

Further insight into the magnetization reversal in **2**–**5** was obtained with ab initio calculations,[7b,d,g] using MOLCAS 7.6.[13a] Local magnetic properties on individual Dy ions were computed by the Single_Aniso module,[13b] while the magnetic properties of the dimers were simulated by the Poly_Aniso routine (Supporting Information).[13c] Table 2 shows the energies of the lowest Kramers doublets of the individual Dy ions in **2**–**5**.

The orientation of the main anisotropy axes of the Dy ions in **2**–**4** is close to perpendicular to the $\{Dy_2X_2\}$ planes (Figure 4; Supporting Information, Figures S17, S20, S21). The very anisotropic g matrices in the ground doublets (Table 3) mean that the magnetic interaction between Dy ions will be mostly of the Ising type, and so can be described

Table 2: Energies [cm^{-1}] of the lowest Kramers doublets in **2**–**5**.

No.	2	3a	3b	4	5
1	0	0	0	0	0
2	113	144	134	96	103
3	283	313	296	193	171
4	368	383	356	211	210
5	386	401	392	236	226
6	426	444	434	286	248
7	457	488	457	308	295
8	624	672	588	339	389

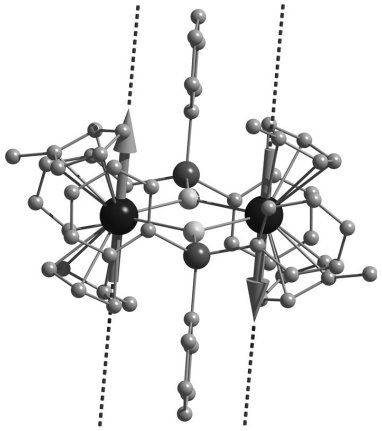

Figure 4. Orientation of the main anisotropy axes (dashed lines) of the ground Kramers doublets of the Dy^{III} ions (large spheres) in **2**.

Table 3: Principal g values of the ground Kramers doublets in **2**–**5.**

	2	3a	3b	4	5
g_x	0.0012	0.0004	0.0009	0.0224	0.0073
g_y	0.0019	0.0009	0.0015	0.0479	0.0884
g_z	19.3611	19.4090	19.3590	18.9208	19.0530

by $H = -J s_{1z_1} s_{2z_2}$ [Eq. (1)], where s_{1z_1} and s_{2z_2} are projections of the effective spin $\tilde{s} = 1/2$ of lowest Kramers doublets of the two Dy ions on the local anisotropy axes. The magnetic coupling parameter J is a sum of the exchange interaction (J_{exch}) and the magnetic dipole–dipole interaction (J_{dipolar}) between the Dy ions. Knowledge of the ground state g matrix on the Dy sites allows for exact calculations of J_{dipolar} (Table 4), so that the only unknown parameters are J_{exch}, which are derived by fitting the magnetic data (Supporting

Table 4: Dipolar and exchange parts [cm^{-1}] of the magnetic interaction between the Dy^{III} ions in complexes **2** and **4**.

	2	4
J_{exch}	−2.19475	0.08550
J_{dipolar}	−2.22550	−1.99075
$J = J_{\text{exch}} + J_{\text{dipolar}}$	−4.42025	−1.90525

© 2012 Wiley-VCH Verlag GmbH & Co. KGaA, Weinheim

Information, Figures S5, S18, S22). The intramolecular dipolar interaction favors antiferromagnetic coupling between magnetic moments, which is explained by the local anisotropy axes being almost perpendicular to the Dy1···Dy2 axis (Figure 4; Supporting Information, Figures S21 for **2** and **4**, respectively). While the dipolar couplings in **2** and **4** are similar, the exchange interaction in **2** is twice as large as that in **4** (Table 4). This is not unexpected, because the valence orbitals of sulfur are more diffuse than those of chloride.

The U_{eff} value of 133 cm^{-1} for **2** agrees well with the calculated energy of the first excited state on Dy sites (113 cm^{-1}). The U_{eff} value of 33 cm^{-1} for thf-solvated **4**, which was extracted in a similar way, does not agree well with the calculated energy of the first excited Kramers doublet (96 cm^{-1}). Analysis of the out-of-phase ac susceptibility of **4** in an applied dc field of 1200 Oe reveals an additional maximum, which is not reached at ac frequencies of less than 1000 Hz and, furthermore, this maximum is not detected in zero applied dc field.[12b] An explanation may be found by considering the two relaxation mechanisms possible in Ln-SMMs: first, a thermally activated (Orbach) mechanism via the first excited state, and; second, a direct mechanism via quantum tunneling of the magnetization (QTM) and/or a Raman process. The rate of the direct process generally correlates with the strength of QTM, and measurements on **4** show that this SMM is in a QTM regime already at $T \approx 5$ K.[12b] A dc field applied to **4** suppresses the QTM and other processes, and on this basis the activated relaxation becomes apparent. In **2**, the QTM and direct relaxation are much less prominent; QTM is not approached even at 2 K and, accordingly, the Orbach process involving the first excited state is measured in the ac susceptibility studies, hence the good match of the energy barriers determined by experiment and by computation.

This interpretation is supported by the calculated values of transverse *g* values on the Dy ions (g_x and g_y in Table 3), which are one order of magnitude larger in **4** relative to **2**. This implies more prominent QTM (and a larger rate of direct relaxation) in **4**. The same reasoning, based on the "axiality" of the ground Kramers doublet on the Dy sites, explains why the relaxation properties of **5** are similar to those of **4**, whereas the polymeric chains of **3b** behave in a similar manner to **2**. Spurious blocking barriers, which we find here for **4** and **5**, have been encountered in other Ln-SMMs. For instance, the Arrhenius fit of ac susceptibility for $\{Dy_3\}$ triangles gave a blocking barrier of 25 cm^{-1} in zero dc field, which increased to about 83 cm^{-1} in a dc field of 3 kOe.[7k] The only deviation from this model are the dimeric units of **3a**, which show relatively small transverse *g* factors on the Dy sites, yet at the same time their magnetization relaxes relatively quickly as in **4** and **5**. The reasons for this inconsistency are currently unclear.

These results illustrate the potential and the complexity of organolanthanide SMMs with soft ligands. Our calculations and most of our observations suggest that the symmetry at the individual Ln sites is crucial in determining the observed U_{eff} value. The transverse *g* values decide the quantum tunneling rate, and hence whether the complex will fall into an activated or a direct relaxation regime. In low-symmetry cases, with high *g* factors, it is probable that the direct process is observed.

Received: March 30, 2012
Revised: May 9, 2012
Published online: June 8, 2012

Keywords: ab initio calculations · dysprosium · organometallics · single-molecule magnets · sulfur

[1] a) A. Caneschi, D. Gatteschi, R. Sessoli, A. L. Barra, L. C. Brunel, M. Guillot, *J. Am. Chem. Soc.* **1991**, *113*, 5873; b) R. Sessoli, H. L. Tsai, A. R. Schake, S. Y. Wang, J. B. Vincent, K. Folting, D. Gatteschi, G. Christou, D. N. Hendrickson, *J. Am. Chem. Soc.* **1993**, *115*, 1804; c) R. Sessoli, D. Gatteschi, A. Caneschi, M. A. Novak, *Nature* **1993**, *365*, 141.

[2] G. Aromí, E. K. Brechin, *Struct. Bonding (Berlin)* **2006**, *122*, 1.

[3] a) S. Loth, S. Baumann, C. P. Lutz, D. M. Eigler, A. J. Heinrich, *Science* **2012**, *335*, 196; b) M. Mannini, F. Pineider, P. Sainctavit, C. Danieli, E. Otero, C. Sciancalepore, A. M. Talarico, M.-A. Arrio, A. Cornia, D. Gatteschi, R. Sessoli, *Nat. Mater.* **2009**, *8*, 194; c) L. Bogani, W. Wernsdorfer, *Nat. Mater.* **2008**, *7*, 179; d) A. Ardavan, O. Rival, J. J. L. Morton, S. J. Blundell, A. M. Tyryshkin, G. A. Timco, R. E. P. Winpenny, *Phys. Rev. Lett.* **2007**, *98*, 057201; e) M. N. Leuenberger, D. Loss, *Nature* **2001**, *410*, 789.

[4] a) J. D. Rinehart, J. R. Long, *Chem. Sci.* **2011**, *2*, 2078; b) L. Sorace, C. Benelli, D. Gatteschi, *Chem. Soc. Rev.* **2011**, *40*, 3092; c) Y.-N. Guo, G.-F. Xu, Y. Guo, J. Tang, *Dalton Trans.* **2011**, *40*, 9953; d) R. Sessoli, A. K. Powell, *Coord. Chem. Rev.* **2009**, *253*, 2328.

[5] N. Ishikawa, M. Sugita, T. Ishikawa, S. Koshihara, Y. Kaizu, *J. Am. Chem. Soc.* **2003**, *125*, 8694.

[6] a) M. Jeletic, P.-H. Lin, J. J. Le Roy, I. Korobkov, S. I. Gorelsky, M. Murugesu, *J. Am. Chem. Soc.* **2011**, *133*, 19286; b) S.-D. Jiang, B.-W. Wang, H. L. Sun, Z. M. Wang, S. Gao, *J. Am. Chem. Soc.* **2011**, *133*, 4730; c) N. Magnani, C. Apostolidis, A. Morgenstern, E. Colineau, J.-P. Griveau, H. Bolvin, O. Walter, R. Caciuffo, *Angew. Chem.* **2011**, *123*, 1734; *Angew. Chem. Int. Ed.* **2011**, *50*, 1696; d) M. A. AlDamen, J. M. Clemente-Juan, E. Coronado, C. Marti-Gastaldo, A. Gaita-Arino, *J. Am. Chem. Soc.* **2008**, *130*, 8874; e) M. Gonidec, R. Biagi, V. Corradini, F. Moro, V. De Renzi, U. del Pennino, D. Summa, L. Muccioli, C. Zannoni, D. B. Amabilino, J. Veciana, *J. Am. Chem. Soc.* **2011**, *133*, 6603.

[7] a) I. J. Hewitt, J. Tang, N. T. Madhu, C. E. Anson, Y. Lan, J. Luzon, M. Etienne, R. Sessoli, A. K. Powell, *Angew. Chem.* **2010**, *122*, 6496; *Angew. Chem. Int. Ed.* **2010**, *49*, 6352; b) Y.-N. Guo, G.-F. Xu, W. Wernsdorfer, L. Ungur, Y. Guo, J. Tang, H.-J. Zhang, L. F. Chibotaru, A. F. Powell, *J. Am. Chem. Soc.* **2011**, *133*, 11948; c) R. J. Blagg, C. A. Muryn, E. J. L. McInnes, F. Tuna, R. E. P. Winpenny, *Angew. Chem.* **2011**, *123*, 6660; *Angew. Chem. Int. Ed.* **2011**, *50*, 6530; d) P.-H. Lin, T. Burchell, L. Ungur, L. F. Chibotaru, W. Wernsdorfer, M. Murugesu, *Angew. Chem.* **2009**, *121*, 9653; *Angew. Chem. Int. Ed.* **2009**, *48*, 9489; e) Y.-Z. Zheng, Y. Lan, W. Wernsdorfer, C. E. Anson, A. K. Powell, *Chem. Eur. J.* **2009**, *15*, 12566; f) P. H. Lin, T. J. Burchell, R. Clérac, M. Murugesu, *Angew. Chem.* **2008**, *120*, 8980; *Angew. Chem. Int. Ed.* **2008**, *47*, 8848; g) L. F. Chibotaru, L. Ungur, L. Soncini, *Angew. Chem.* **2008**, *120*, 4194; *Angew. Chem. Int. Ed.* **2008**, *47*, 4126; h) C. Aronica, G. Pilet, G. Chastanet, W. Wernsdorfer, J.-F. Jacquot, D. Luneau, *Angew. Chem.* **2006**, *118*, 4775; *Angew. Chem. Int. Ed.* **2006**, *45*, 4659; i) J. Long, F. Habib, P.-H. Lin, I. Korobkov, G. Enright, L. Ungur, W. Wernsdorfer, L. F. Chibotaru, M. Murugesu, *J. Am. Chem. Soc.* **2011**, *133*, 5319; j) J. K. Tang, I. J. Hewitt, N. T. Madhu, G. Chastanet, W. Wernsdorfer, C. E. Anson, C. Benelli, R. Sessoli,

 © 2012 Wiley-VCH Verlag GmbH & Co. KGaA, Weinheim

A. K. Powell, *Angew. Chem.* **2006**, *118*, 1761; *Angew. Chem. Int. Ed.* **2006**, *45*, 1729; k) J. Luzon, K. Bernot, I. J. Hewitt, C. E. Anson, A. K. Powell, R. Sessoli, *Phys. Rev. Lett.* **2008**, *100*, 247205; l) J. W. Sharples, Y.-Z. Zheng, F. Tuna, E. J. L. McInnes, D. Collison, *Chem. Commun.* **2011**, *47*, 7650; m) F. Habib, P.-H. Lin, J. Long, I. Korobkov, W. Wernsdorfer, M. Murugesu, *J. Am. Chem. Soc.* **2011**, *133*, 8830.

[8] a) J. D. Rinehart, M. Fang, W. J. Evans, J. R. Long, *J. Am. Chem. Soc.* **2011**, *133*, 14236; b) J. D. Rinehart, M. Fang, W. J. Evans, J. R. Long, *Nat. Chem.* **2011**, *3*, 538.

[9] Cambridge Structural Database, ConQuest software, Version 1.14, accessed March **2012**.

[10] H.-X. Li, Y.-J. Zhu, M.-L. Cheng, Z.-G. Ren, J.-P. Lang, Q. Shen, *Coord. Chem. Rev.* **2006**, *250*, 2059.

[11] a) R. A. Layfield, A. Bashall, M. McPartlin, J. M. Rawson, D. S. Wright, *Dalton Trans.* **2006**, 1660; b) G. Champion, N. Lalioti, V. Tangoulis, M.-A. Arrio, P. Sainctavit, F. Villain, A. Caneschi, D. Gatteschi, C. Giorgetti, F. Baudelet, M. Verdaguer, C. Cartier dit Moulin, *J. Am. Chem. Soc.* **2003**, *125*, 8371.

[12] a) R. A. Layfield, J. J. W. McDouall, S. A. Sulway, F. Tuna, D. Collison, R. E. P. Winpenny, *Chem. Eur. J.* **2010**, *16*, 4442; b) S. A. Sulway, R. A. Layfield, F. Tuna, W. Wernsdorfer, R. E. P. Winpenny, *Chem. Commun.* **2012**, *48*, 1508.

[13] a) F. Aquilante, L. De Vico, N. Ferre, G. Ghigo, P. A. Malmqvist, P. Neogrady, T. B. Pedersen, M. Pitonak, M. Reiher, B. O. Roos, L. Serrano-Andres, M. Urban, V. Veryazov, R. Lindh, *J. Comput. Chem.* **2010**, *31*, 224; b) for SINGLE_ANISO, see: http://www.molcas.org/documentation/manual/node95.html; c) L. Ungur, L. F. Chibotaru, Program POLY_ANISO, University of Leuven, 2006 – 2012.

[14] a) A. Bhunia, M. T. Gamer, L. Ungur, L. F. Chibotaru, A. K. Powell, Y. Lan, P. W. Roesky, F. Menges, C. Riehn, G. Niedner-Schatteburg, *Inorg. Chem.* **2012**, DOI: 10.1021/ic300065x; b) H. L. C. Feltham, Y. Lan, F. Klöwer, L. Ungur, L. F. Chibotaru, A. K. Powell, S. Brooker, *Chem. Eur. J.* **2011**, *17*, 4362.

 © 2012 Wiley-VCH Verlag GmbH & Co. KGaA, Weinheim

Angewandte Chemie
Eine Zeitschrift der Gesellschaft Deutscher Chemiker

Supporting Information

© Wiley-VCH 2012

69451 Weinheim, Germany

A High Anisotropy Barrier in a Sulfur-Bridged Organodysprosium Single-Molecule Magnet**

Floriana Tuna, Charlene A. Smith, Michael Bodensteiner, Liviu Ungur, Liviu F. Chibotaru, Eric J. L. McInnes, Richard E. P. Winpenny, David Collison, and Richard A. Layfield**

anie_201202497_sm_miscellaneous_information.pdf

Section 1. Synthesis and X-ray crystallography: general considerations

Solvents were dried by refluxing under nitrogen over sodium-potassium alloy. Solids were manipulated using an MBraun LabMaster glovebox under an argon atmosphere, and solutions were transferred using a Schlenk line under nitrogen that had been passed through several columns of drying agents and a heated copper catalyst. Both *tris(*methylcyclopentadienyl)dysprosium and *tris(*methylcyclopentadienyl)gadolinium were synthesized according to literature procedures.[1] Single crystal X-ray diffraction data were collected either using an Oxford Diffraction Gemini R Ultra diffractometer (**1**) or an Oxford Instruments XCalibur2 diffractometer (**2**). Structures were solved and refined with SHELX.[2] For the refinement of the disordered phenyl and Cp parts of the structures, displacement parameter restraints were applied to the model. NMR spectra of lithium triphenylsilylthiolate were acquired using a Bruker Avance III spectrometer.

Synthesis of lithium triphenylsilylthiolate, Ph_3SiSLi. A stirred suspension of triphenylsilylthiol (Ph_3SiSH, 5.00 g, 17.1 mmol) in hexane (50 mL) was cooled to –78°C, and a solution of *n*-butyllithium in hexanes (1.6 M, 11.2 mL, 18.0 mmol, 5% excess) was added drop-wise over five minutes. The milky-white reaction mixture was warmed to room temperature and then treated with ultrasound for 15 minutes. Stirring the reaction overnight resulted in the formation of a colourless solid, which was collected on a porosity 3 frit, washed with hexane (3× 10 mL) and then dried *in vacuo*. Lithium triphenylsilylthiolate, Ph_3SiSLi, was obtained as a colourless solid (4.44 g, 87%). Elemental analysis calculated for $C_{18}H_{15}LiSiS$: C 72.45, H 5.07; found C 72.30, H 4.90. ^{1}H NMR (thf-d_8, 400.13 MHz, 298 K, δ/ppm): 7.698-7.722, multiplet, 6 ^{1}H, phenyl; 7.114-7.146, multiplet, 9 ^{1}H, phenyl. ^{7}Li NMR (thf-d_8, 155.51 MHz, 298 K): 0.567 ppm.

Synthesis of $[(C_5H_4Me)_2Gd(\mu\text{-}SSiPh_3)]_2\cdot$(toluene), 1·(toluene). A Schlenk tube was charged with $[(C_5H_4Me)_3Gd]$ (0.10 g, 0.25 mmol) and Ph_3SiSLi (0.076 g, 0.25 mmol) and cooled to –10°C. Toluene (20 mL) was added and the mixture warmed to room temperature and then stirred overnight, producing a light yellow solution with a gelatinous precipitate. The reaction mixture was filtered (Celite, porosity 3) and the frit then washed with toluene until the filtrate became colourless (5 mL). The solvent volume was reduced until copious amounts of a colourless precipitate had formed on the walls of the Schlenk tube, at which point the solution was gently heated until all the precipitate had re-dissolved. Storage of the light yellow solution at –30°C overnight produced colourless crystalline blocks, which X-ray crystallography subsequently revealed to be $[(C_5H_4Me)_2Gd(\mu\text{-}SSiPh_3)]_2\cdot$(toluene), **1**·(toluene). Placing **1**·(toluene) under vacuum for periods of about 30 minutes results in removal of the lattice toluene, giving **1** (0.097 g, 64% based on gadolinium). Elemental analysis calculated for $C_{60}H_{58}Si_2S_2Gd_2$: C 59.37, H 4.82; found C 59.03, H 4.77.

Synthesis of $[(C_5H_4Me)_2Dy(\mu\text{-}SSiPh_3)]_2\cdot$(toluene), 2·(toluene). The procedure used to synthesize **2·(toluene)** was identical to that used for the gadolinium analogue, with the following amounts: $[(C_5H_4Me)_3Dy]$ (0.10 g, 0.25 mmol), Ph_3SiSLi (0.076 g, 0.25 mmol) and toluene (20 mL). The bright yellow solution was stored at –30°C overnight, which produced yellow crystalline blocks, which X-ray crystallography subsequently revealed to be $[(C_5H_4Me)_2Dy(\mu\text{-}SSiPh_3)]_2\cdot$(toluene), **2**·(toluene). Placing **2**·(toluene) under vacuum for periods of about 30 minutes results in removal of the lattice toluene, giving **2** (0.120 g, 70% based on dysprosium). Elemental analysis calculated for $C_{60}H_{58}Si_2S_2Dy_2$: C 58.86, H 4.77; found C 58.71, H 4.69.

1. Wilkinson, G.; Birmingham, J. M. *J. Am. Chem. Soc*. **1954**, *76*, 6210.
2. Sheldrick, G. M. *Acta Cryst*. **2008**, *A64*, 112.

Table S1. Crystal data and structure refinement for **1**·(toluene)

Empirical formula	$C_{67}H_{66}Gd_2S_2Si_2$
Formula weight	1306.02
Temperature	123(1) K
Wavelength	1.54178 Å
Crystal system	Monoclinic
Space group	$P2_1/n$
Unit cell dimensions	a = 9.7437(2) Å
	b = 18.8921(6) Å β = 96.694(2)°
	c = 15.4871(5) Å
Volume	2831.41(14) Å^3
Z	2
Density (calculated)	1.532 Mg/m^3
Absorption coefficient	16.384 mm^{-1}
Crystal size	0.16 × 0.08 × 0.06 mm^3
Theta range for data collection	3.71 to 62.09°
Index ranges	-11<=h<=11, -21<=k<=20, -14<=l<=17
Reflections collected	11191
Independent reflections	4356 [R(int) = 0.0542]
Completeness to theta = 62.09°	97.8 %
Absorption correction	Semi-empirical from equivalents
Refinement method	Full-matrix least-squares on F^2
Data / restraints / parameters	4356 / 24 / 408
Goodness-of-fit on F^2	1.096
Final R indices [I>2σ(I)]	R_1 = 0.0469, wR_2 = 0.1222
R indices (all data)	R_1 = 0.0529, wR_2 = 0.1299
Largest diff. peak and hole	0.752 and -1.917 e.Å^{-3}

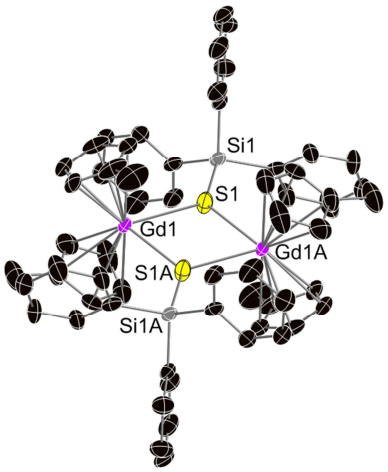

Figure S1. Thermal ellipsoid representation (50% probability) of the molecular structure of **1**.

Table S2. Crystal data and structure refinement for **2**·(toluene)

Empirical formula	$C_{67}H_{66}Dy_2S_2Si_2$
Formula weight	1316.52
Temperature	100(2) K
Wavelength	0.71073 Å
Crystal system	Monoclinic
Space group	$P2_1/n$
Unit cell dimensions	a = 9.7223(19) Å
	b = 18.864(4) Å β = 96.55(3)°
	c = 15.410(3) Å
Volume	2807.8(10) Å^3
Z	2
Density (calculated)	1.557 Mg/m^3
Absorption coefficient	2.799 mm^{-1}
Crystal size	0.70 × 0.10 × 0.10 mm^3
Theta range for data collection	1.71 to 28.83°.
Index ranges	-12<=h<=12, -24<=k<=24, -19<=l<=20
Reflections collected	24579
Independent reflections	6833 [R(int) = 0.0451]
Completeness to theta = 25.00°	100%
Absorption correction	Semi-empirical from equivalents
Refinement method	Full-matrix least-squares on F^2
Data / restraints / parameters	6833 / 36 / 407
Goodness-of-fit on F^2	1.127
Final R indices [I>2σ(I)]	R_1 = 0.0400, wR_2 = 0.0949
R indices (all data)	R_1 = 0.0559, wR_2 = 0.1183
Largest diff. peak and hole	1.327 and -1.125 e.Å^{-3}

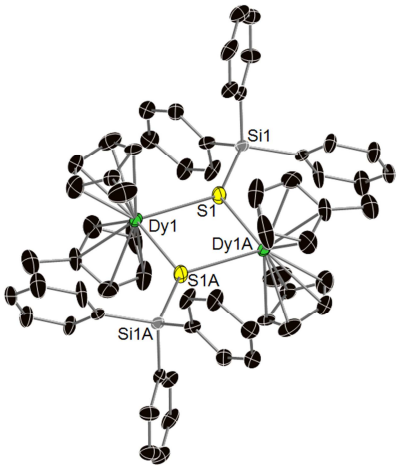

Figure S2. Thermal ellipsoid representation (50% probability) of the molecular structure of **2**.

Section 2. Magnetic susceptibility measurements on 1 and 2

The magnetic properties of polycrystalline samples of **1** and **2** were measured using a Quantum Design MPMS-7 SQUID magnetometer at temperatures in the range 1.8-300 K. In a glove box, the polycrystalline samples were transferred to Kel-F capsules, which were then sealed with an O-ring cap, and the capsules were then placed in plastic straws. One end of the straw was then sealed with a cap, and the other end was sealed with Blu-Tac. The straw was then sealed in a Schlenk tube and taken to the magnetometer. The straw was removed from the Schlenk tube and the Blu-Tac quickly replaced with the carbon fibre rod, and then the sample was quickly transferred to the purged sample space of the MPMS.

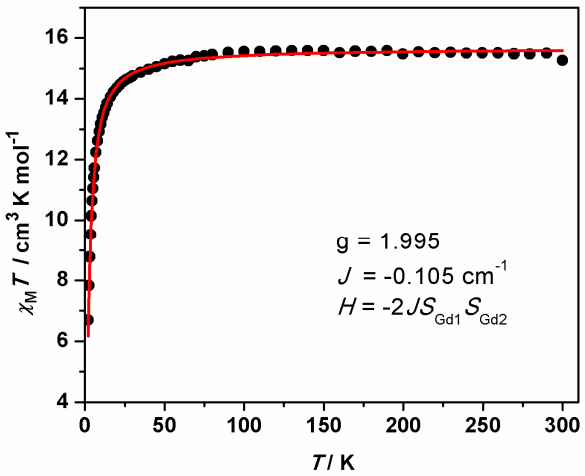

Figure S3. The product of molar magnetic susceptibility and temperature, $\chi_M T$, against temperature, T, for **1**. The red line is a theoretical fit of the experimental data using the spin Hamiltonian $H = -2J[S_{Gd1} \cdot S_{Gd1A}]$ and $g = 1.995$, which produced an exchange coupling constant of $J = -0.105$ cm^{-1}.

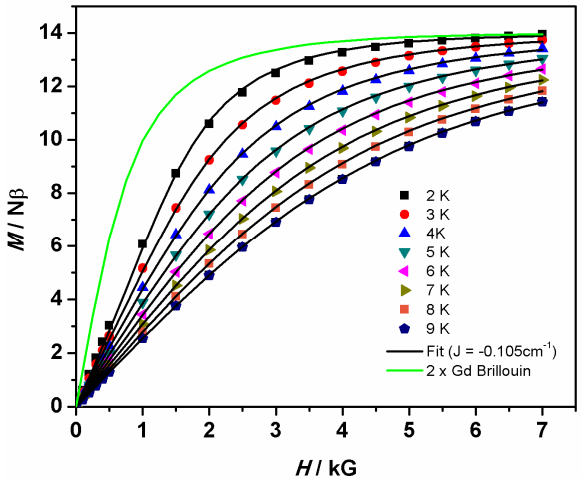

Figure S4. Plot of magnetization against field for **1** at various temperatures in the range 2-9 K. The solid lines are a theoretical fit of the experimental data using $J = -0.105$ cm^{-1}.

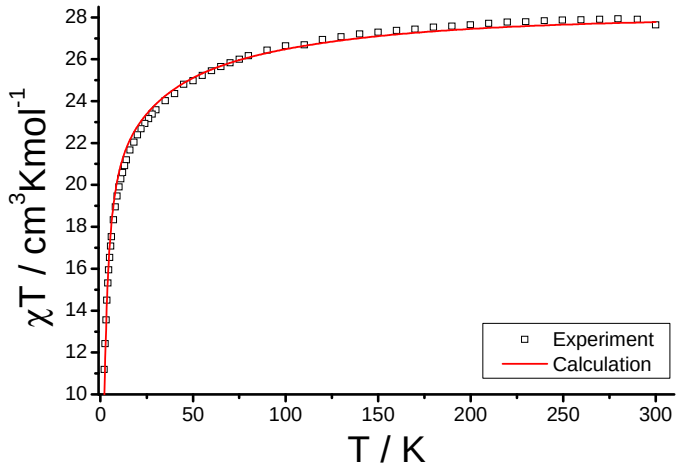

Figure S5. Product of molar magnetic susceptibility and temperature, $\chi_M T$, against temperature, T, for **2**. The red trace shows the calculated curve using the *ab initio* results in the computational model CB (see the details in Section 3 of the SI).

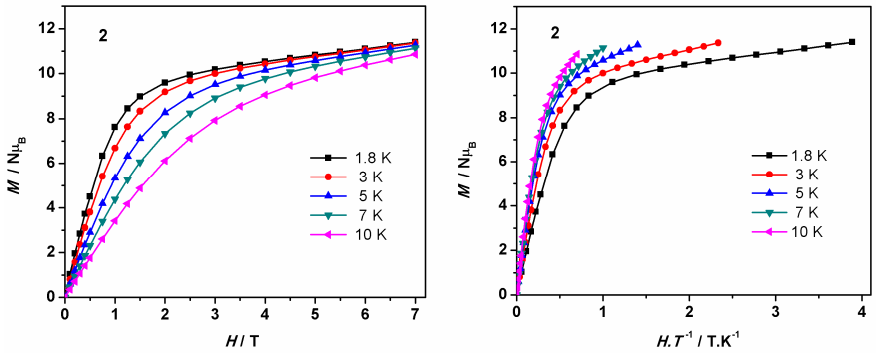

Figure S6. Left: M vs. H and; right, M vs. H/T for **2** at temperatures between 1.8 and 10 K.

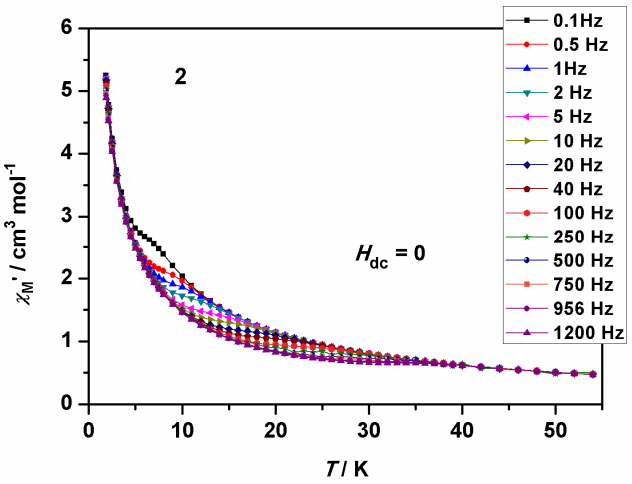

Figure S7. Temperature dependence of the in-phase ac susceptibility of **2** at zero-dc field and 1.55 Oe ac field, oscillating at the indicated frequencies.

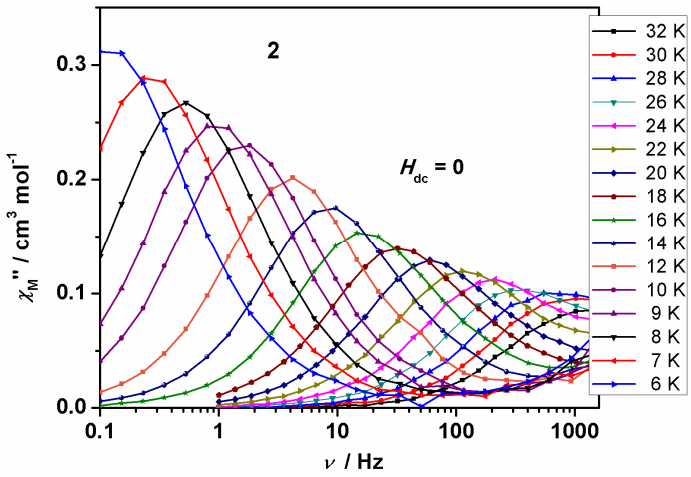

Figure S8. Frequency dependence in zero-dc-field of the out-of-phase (χ_M'') ac susceptibility of **2** at temperatures between 6 and 32 K.

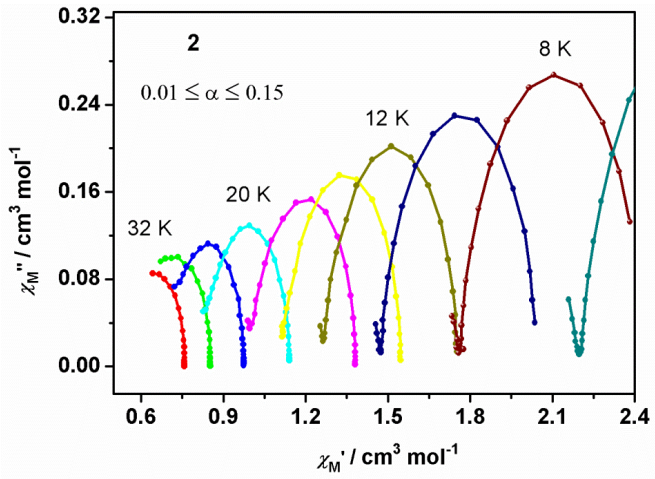

Figure S9. Cole-Cole diagram for **2** at temperatures in the range 28 and 18 K.

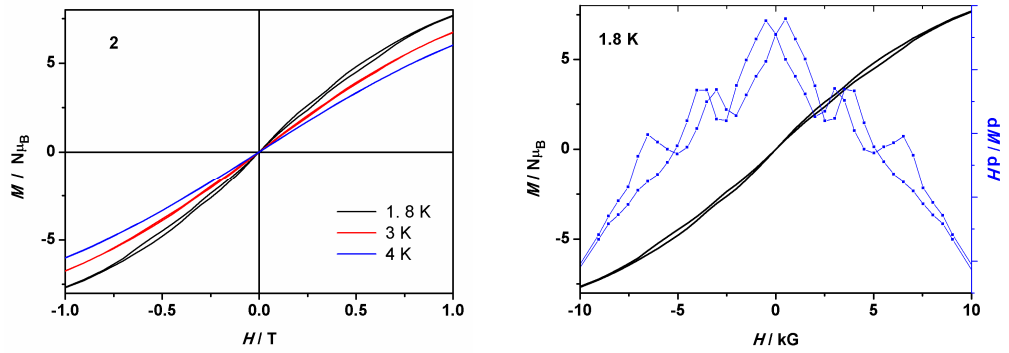

Figure S10. Left: magnetization versus field plots for **2** at T = 1.8, 3 and 4 K. Right: magnetization versus field plots for **2** at T = 1.8 K and plot of dM/dH *vs.* H.

Section 3. *Ab initio* Calculations of electronic and magnetic properties

Computational details: All calculations were done with MOLCAS 7.6 and are of the CASSCF/RASSI/SINGLE_ANISO type.

[$(C_5H_4Me)_2Ln(\mu\text{-}SSiPh_3)]_2$ (2)

We have employed three structural approximations: **A**, a reduced fragment of the molecule; **B**, a larger fragment, and; C, the entire molecule. Each structural approximation was calculated using two basis set approximations: **A** small, and **B** large. This results in six computational approximations for **2**, i.e. **AA**, **AB**, **BA**, **BB, CA** and **CB**.

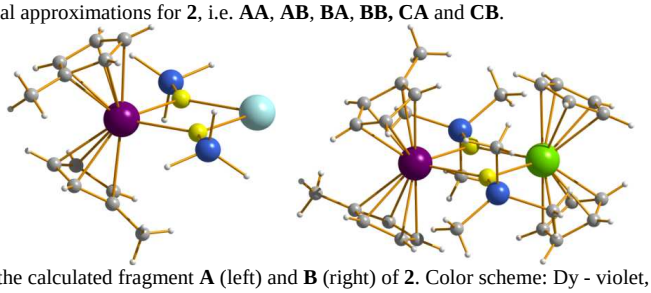

Figure S11. Structure of the calculated fragment **A** (left) and **B** (right) of **2**. Color scheme: Dy - violet, Lu – green, La – light turquoise, Si – blue, S – yellow, C – grey, H – white.

[$Cp_2Dy(\mu\text{-}Cl)]_2$ (3a)

We have employed two structural approximations: **A**, a reduced fragment of the molecule, and; **B**, the entire molecule. Each structural approximation was calculated using two basis set approximations: **A** small, and **B** large. This results in four computational approximations for **3a**, **AA**, **AB**, **BA**, and **BB**.

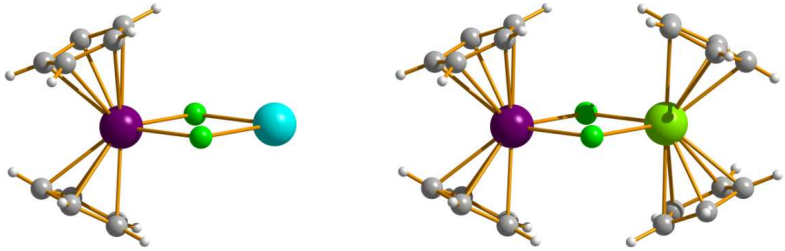

Figure S12. Structure of the calculated fragment **A** (left) and **B** (right) of the complex **3 –dimer**. Color scheme: Dy - violet, Lu – light green, La – green, Cl – yellow, O – red, C – grey, H – white.

[$Cp_2Dy(\mu\text{-}Cl)]_\infty$ (3b)

We have employed two structural approximations: **A**, a reduced fragment of the molecule, and; **B**, the entire molecule. Each structural approximation was calculated using two basis set approximations: **A** small, and **B** large. This results in four computational approximations for **3a**, **AA**, **AB**, **BA**, and **BB**.

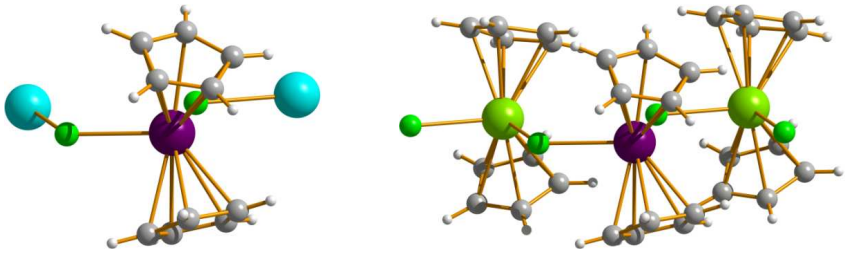

Figure S13. Structure of the calculated fragment **A** (left) and **B** (right) of the complex **3 – polymer**. Color scheme: Dy - violet, La – green, Lu – light green, Cl – yellow, O – red, C – grey, H – white.

[$Cp_2Dy(thf)(\mu\text{-}Cl)]_2$ (4)

We have employed two structural approximations: **A**, a reduced fragment of the molecule, and; **B**, the entire molecule. Each structural approximation was calculated using two basis set approximations: **A** small, and **B** large. This results in four computational approximations for **3a**, **AA**, **AB**, **BA**, and **BB**.

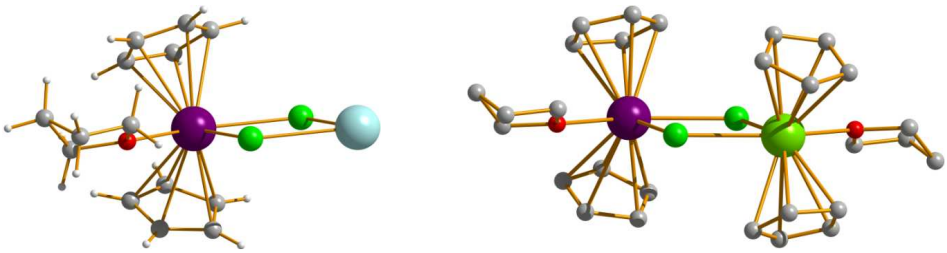

Figure S14. Structure of the fragment **A** (left) and B (right) of the complex **4**. Color scheme: Dy - violet, La – cyan, Lu – light green, Cl – green, O – red, C – grey, H – white.

[$Cp_2Dy(\mu$-Bta)]$_2$ (5)

We have employed two structural approximations: **A**, a reduced fragment of the molecule, and; **B**, the entire molecule. Each structural approximation was calculated using two basis set approximations: **A** small, and **B** large. This results in four computational approximations for **3a**, **AA**, **AB**, **BA**, and **BB**.

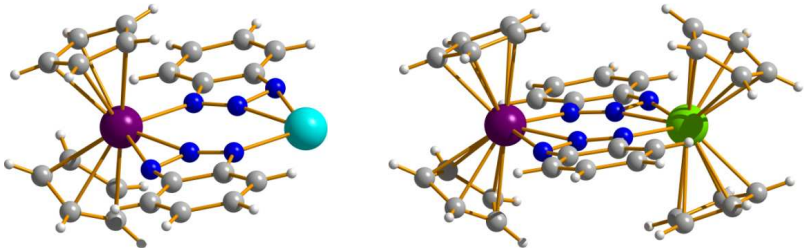

Figure S15. Structure of the calculated fragment **A** (left) and **B** (right) of the complex **5**. Color scheme: Dy - violet, La- cyan, Lu – green, N – blue, C – grey, H – white.

Table S3. Contractions of the employed basis sets in computational approximations **A** and **B**.

Basis A	Basis B
Dy.ANO-RCC...7s6p4d3f1g.	Dy.ANO-RCC...8s7p5d4f2g1h.
La.ECP.deGraaf.0s.0s.0e-La(LaMnO3).	La.ECP.deGraaf.0s.0s.0e-La(LaMnO3).
Lu.ANO-RCC...7s6p4d3f1g.	Lu.ANO-RCC...7s6p4d3f1g.
Si.ANO-RCC...4s3p.	Si.ANO-RCC...5s4p2d.
S.ANO-RCC...4s3p1d.	S.ANO-RCC...5s4p2d1f.
Cl.ANO-RCC...4s3p1d.	Cl.ANO-RCC...5s4p2d1f.
O.ANO-RCC...3s2p1d.	O.ANO-RCC...4s3p2d1f. (close)
C.ANO-RCC...3s2p.	O.ANO-RCC...4s3p2d. (distant)
H.ANO-RCC...2s.	C.ANO-RCC...4s3p1d. (close)
	C.ANO-RCC...3s2p. (distant)
	H.ANO-RCC...2s1p.

Electronic and magnetic properties of $[(C_5H_4Me)_2Dy(\mu\text{-}SSiPh_3)]_2$ (2)

Table S4. Energies of the lowest Kramers doublets (cm^{-1}) in **2**.

Kramers doublets (cm^{-1})					
AA	AB	BA	BB	CA	CB
0.000	0.000	0.000	0.000	0.000	0.000
158.894	187.514	83.079	106.676	88.201	113.151
333.452	383.642	240.288	279.464	241.151	283.888
448.781	516.897	276.716	350.322	292.568	367.884
533.825	606.289	310.780	370.651	319.373	385.991
558.447	618.388	338.173	409.524	352.575	426.208
581.103	660.793	368.637	451.587	373.706	456.957
714.687	828.920	527.048	629.611	515.884	624.035
3613.458	3627.429	3588.728	3596.413	3587.652	3596.823
3788.221	3816.493	3705.215	3733.246	3710.833	3739.744
3888.975	3930.665	3740.002	3782.724	3750.951	3795.463
3973.137	4030.448	3788.946	3845.844	3799.613	3859.633
4059.552	4126.940	3859.017	3923.702	3870.000	3938.205
4116.181	4188.245	3913.162	3988.652	3917.349	3996.091
4153.402	4253.084	3969.571	4062.097	3961.650	4059.212
6197.038	6220.773	6138.681	6157.516	6139.480	6160.070
6342.943	6372.436	6236.967	6269.878	6244.952	6278.623
6424.048	6466.366	6265.800	6309.266	6276.979	6322.479
6517.252	6574.768	6335.952	6390.286	6343.658	6402.107
6603.579	6676.340	6420.697	6487.363	6424.396	6495.737
6645.207	6728.268	6453.525	6538.178	6451.157	6538.895
8201.238	8231.971	8117.161	8143.859	8119.140	8147.932
8320.770	8353.059	8191.792	8230.027	8200.504	8240.195
8405.617	8450.215	8231.929	8277.158	8243.751	8291.414
8509.489	8579.165	8350.262	8409.053	8349.544	8414.498
8582.294	8653.777	8393.263	8467.328	8395.993	8471.681
9752.228	9783.879	9660.971	9686.961	9664.026	9692.289
9868.246	9900.570	9722.806	9761.482	9732.868	9773.636
9981.179	10043.370	9790.402	9850.645	9798.008	9861.683
10118.492	10187.185	9952.612	10018.883	9952.194	10021.689
…	…	…	…	…	…

Table S5. Energies (cm^{-1}) and *g* tensors of the lowest Kramers doublets (KD) in **2**.

KD		AA		AB		BA		BB		CA		CB	
		E	*g*	E	*g*	E	*g*	E	*g*	E	*g*	E	*g*
1	g_X		0.0000		0.0001		0.0029		0.0011		0.0031		0.0012
	g_Y	0.000	0.0005	0.000	0.0003	0.000	0.0056	0.000	0.0021	0.000	0.0050	0.000	0.0019
	g_Z		19.6856		19.7150		19.0827		19.2880		19.1740		19.3611
2	g_X		0.0025		0.0020		0.0022		0.0018		0.0037		0.0029
	g_Y	158.894	0.0032	187.514	0.0023	83.079	0.0082	106.676	0.0039	88.201	0.0094	113.151	0.0049
	g_Z		17.1491		17.1095		17.0666		17.0284		17.0928		17.0545
3	g_X		0.1432		0.0726		0.2870		0.0795		0.1878		0.0726
	g_Y	333.452	0.1844	383.642	0.0843	240.288	0.3526	279.464	0.0992	241.151	0.2597	283.888	0.0858
	g_Z		14.6263		14.6204		15.1700		15.0123		15.1391		14.9721
4	g_X		0.5212		0.5406		1.3632		0.6476		3.3772		8.7803
	g_Y	448.781	0.6543	516.897	0.6295	276.716	1.7863	350.322	1.7005	292.568	4.3149	367.884	6.8391
	g_Z		11.4535		11.7317		16.4165		16.7454		12.5142		1.8084
5	g_X		2.1236		0.1044		0.8760		1.0223		7.8279		0.2759
	g_Y	533.825	3.7318	606.289	1.1238	310.780	4.1547	370.651	3.7009	319.373	5.3026	385.991	4.6117
	g_Z		6.8870		11.8660		10.0511		10.4453		2.4932		11.8435
6	g_X		1.5240		2.1563		1.1825		3.8555		0.8819		2.3401
	g_Y	558.447	2.5609	618.388	2.7647	338.173	3.3415	409.524	4.8097	352.575	3.1923	426.208	5.1644
	g_Z		17.6417		11.5628		13.6435		11.7483		13.7867		11.0989
7	g_X		2.9191		11.6524		1.9407		0.9977		1.5548		1.0027
	g_Y	581.103	4.6242	660.793	7.5952	368.637	5.7089	451.587	2.8156	373.706	6.2898	456.957	3.8534
	g_Z		13.6088		2.6082		13.0187		15.1869		12.2011		13.8268
8	g_X		0.0376		0.0220		0.0971		0.0687		0.1325		0.0836
	g_Y	714.687	0.1471	828.920	0.0715	527.048	0.1322	629.611	0.0948	515.884	0.1932	624.035	0.1247
	g_Z		19.5754		19.6455		19.7197		19.7552		19.6713		19.7289

Table S6. Angles [°] between the main magnetic axes of the lowest Kramers doublet in **2**, obtained in different computational approximations.

	AA	AB	BA	BB	CA	CB
AA	0.000	0.182	3.007	2.291	2.234	1.657
AB	0.182	0.000	3.034	2.311	2.269	1.681
BA	3.007	3.034	0.000	0.727	0.779	1.353
BB	2.291	2.311	0.727	0.000	0.200	0.635
CA	2.234	2.269	0.779	0.200	0.000	0.594
CB	1.657	1.681	1.353	0.635	0.594	0.000

The main anisotropy axis of the ground state is almost perpendicular to the Dy_2S_2 plane (see Table S7).

Table S7. Angles [°] between the main magnetic axes of the lowest Kramers doublet in **2**, obtained in different computational approximations and the Dy_2S_2 plane (degrees).

	AA	AB	BA	BB	CA	CB
angle	86.232	86.308	83.317	84.043	84.059	84.653

The orientation of the main anisotropy axes in the ground Kramers doublet of **2**, with an illustration of the antiferromagnetic coupling of the local Dy magnetic moments, is shown in the main article (Figure 4).

Table S8. Exchange interactions between Dy ions in **2**.
Lines parameters (cm^{-1}):

	AA	AB	BA	BB	CA	CB
J_{exch}	-0.09234	-0.09177	-0.08569	-0.08704	-0.08649	-0.08779
$J_{dipolar}$	-0.09037	-0.09038	-0.08764	-0.08842	-0.08846	-0.08902
$J_{total}=J_{exch}+J_{dipolar}$	-0.18271	-0.18215	-0.17333	-0.17546	-0.17495	-0.17681

Ising parameters (cm^{-1}):

	AA	AB	BA	BB	CA	CB
J_{exch}	-2.30850	-2.29425	-2.14225	-2.17600	-2.16225	-2.19475
$J_{dipolar}$	-2.25925	-2.25950	-2.19100	-2.21050	-2.21150	-2.22550
$J_{total}=J_{exch}+J_{dipolar}$	-4.56775	-4.55375	-4.33325	-4.38650	-4.37375	-4.42025

Table S9. Energies and corresponding tunnelling gaps of the lowest five exchange doublet states of **2**.
Part 1:

AA		AB		BA	
energy	Δ_t	energy	Δ_t	energy	Δ_t
0.000000000 0.000000000	0.00000E+00	0.000000000 0.000000000	0.00000E+00	0.000000000 0.000000033	3.30000E-08
2.145312760 2.145313134	3.74000E-07	2.145050520 2.145051601	1.08100E-06	1.918489585 1.918489858	2.73000E-07
158.936768811 158.936768837	2.60000E-08	187.558754213 187.558754220	7.00001E-09	83.063830893 83.063831680	7.87000E-07
159.134766976 159.134766998	2.20000E-08	187.761670581 187.761670586	5.00000E-09	83.279366718 83.279367275	5.57000E-07
160.886202287 160.886203526	1.23900E-06	189.505048433 189.505048693	2.60000E-07	84.835466373 84.835467671	1.29800E-06

Part 2:

BB		CA		CB	
energy	Δ_t	energy	Δ_t	energy	Δ_t
0.000000000 0.000000005	5.00000E-09	0.000000000 0.000000007	7.00000E-09	0.000000000 0.000000001	1.00000E-09
1.982829107 1.982829965	8.58000E-07	1.954021209 1.954024704	3.49500E-06	2.012402293 2.012402371	7.80000E-08
106.680340911 106.680341051	1.40000E-07	88.196463276 88.196463890	6.14000E-07	113.163773254 113.163773370	1.16000E-07
106.892646092 106.892646201	1.09000E-07	88.406351627 88.406351987	3.60000E-07	113.372241800 113.372241876	7.60000E-08
108.493021565 108.493022023	4.58000E-07	89.992314081 89.992315957	1.87600E-06	114.998454316 114.998454636	3.20000E-07

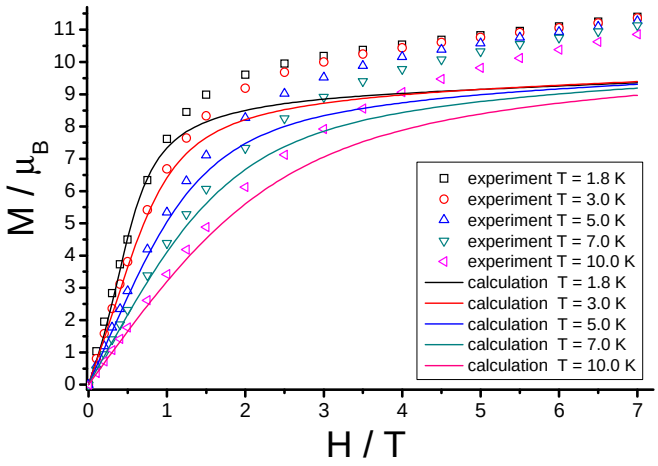

Figure S16. Measured and calculated molar magnetization of **2** at low temperatures (computational approximation CB).

Electronic and magnetic properties of $[Cp_2Dy(\mu\text{-}Cl)]_2$ (3a)

Table S10. Energies of the lowest Kramers doublets (cm^{-1}) on individual Dy ions.

Kramers doublets (cm^{-1})			
AA	AB	BA	BB
0.000	0.000	0.000	0.000
247.390	237.785	150.706	144.200
446.454	433.014	322.790	313.188
582.822	563.195	411.535	383.364
688.038	658.574	416.315	400.821
755.084	694.332	467.201	444.185
766.313	723.748	509.009	487.838
885.626	871.246	694.458	672.128
3661.795	3654.771	3619.668	3614.754
3856.114	3840.145	3762.374	3750.584
4011.291	3982.988	3832.255	3813.567
4130.583	4096.050	3906.541	3884.064
4227.292	4191.236	3984.472	3958.824
4289.538	4246.646	4049.832	4026.161
4319.032	4294.918	4125.584	4102.739
6272.790	6259.474	6194.594	6185.539
6420.768	6398.579	6303.352	6287.192
6551.821	6519.063	6360.696	6339.190
6677.226	6640.742	6452.884	6428.122
6765.720	6734.115	6549.839	6524.657
6811.856	6775.424	6602.286	6578.302
8294.988	8275.995	8188.961	8175.927
8411.363	8383.540	8268.498	8249.142
8549.181	8511.796	8337.402	8312.743
8667.740	8639.015	8472.310	8447.939
8739.831	8701.031	8529.291	8503.884
9850.461	9827.498	9731.794	9716.479
9971.381	9939.228	9807.262	9785.344
10151.807	10116.964	9926.471	9899.840
…	…	…	…

Table S11. Energies (cm^{-1}) and *g* tensors of the lowest Kramers doublets (KD) on individual Dy ions.

KD		AA		AB		BA		BB	
		E (cm^{-1})	*g*	E (cm^{-1})	*g*	E (cm^{-1})	*g*	E (cm^{-1})	*g*
1	g_X	0.000	0.0007	0.000	0.0005	0.000	0.0001	0.000	0.0004
	g_Y		0.0009		0.0008		0.0007		0.0009
	g_Z		19.7544		19.7260		19.4443		19.4090
2	g_X	247.390	0.0051	237.785	0.0006	150.706	0.0063	144.200	0.0066
	g_Y		0.0055		0.0010		0.0074		0.0078
	g_Z		17.0949		17.0777		16.9821		16.9597
3	g_X	446.454	0.1533	433.014	0.1477	322.790	0.0448	313.188	0.0050
	g_Y		0.1856		0.1750		0.0483		0.0097
	g_Z		14.4280		14.4867		14.7878		14.8008
4	g_X	582.822	0.2492	563.195	0.0502	411.535	0.0105	383.364	0.0372
	g_Y		0.5072		0.2636		1.5151		0.3037
	g_Z		11.5010		11.6394		15.5494		19.2969
5	g_X	688.038	3.7498	658.574	3.3567	416.315	1.1175	400.821	1.1703
	g_Y		4.6373		3.6838		2.0917		1.4729
	g_Z		8.1679		8.6381		9.9559		11.6236
6	g_X	755.084	0.9324	694.332	1.3817	467.201	5.2542	444.185	5.3295
	g_Y		3.1856		3.6405		5.9350		5.6150
	g_Z		12.6032		15.8790		9.2976		10.2589
7	g_X	766.313	10.1472	723.748	10.5685	509.009	0.7956	487.838	0.4729
	g_Y		7.8019		8.6765		1.5741		1.4056
	g_Z		1.2881		1.9286		15.4520		15.8294
8	g_X	885.626	0.1177	871.246	0.0451	694.458	0.0443	672.128	0.0443
	g_Y		0.1972		0.0597		0.0741		0.0677
	g_Z		19.3054		19.4715		19.7135		19.7336

Table S12. Angles between the main magnetic axes of the lowest Kramers doublet obtained in different computational approximations (degrees).

	AA	AB	BA	BB
AA	0.000	0.228	1.288	1.834
AB	0.228	0.000	1.082	1.622
BA	1.288	1.082	0.000	0.553
BB	1.834	1.622	0.553	0.000

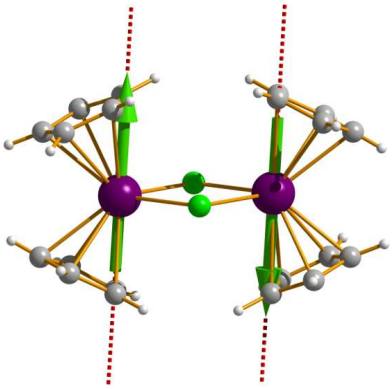

Figure S17. Orientation of the main anisotropy axes of the ground Kramers doublet of **3a**. Green arrows show the antiferromagnetic coupling of the local magnetic moments of the Dy ions in the ground state. The main anisotropy axis of the ground state is almost perpendicular to the Dy_2Cl_2 plane (see Table S13).

Table S13. Angles between the main magnetic axes of the lowest Kramers doublet, obtained in different computational approximations, and the Dy_2Cl_2 plane in **3a** [°].

	AA	AB	BA	BB
angle	87.424	87.251	86.185	85.672

Table S14. Exchange interactions between Dy ions in **3a**.

Lines parameters (cm^{-1}):

	AA	AB	BA	BB
J_{exch}	0.00000	0.00000	0.00000	0.00000
$J_{dipolar}$	-0.10526	-0.10506	-0.10267	-0.10268
$J_{total}=J_{exch}+J_{dipolar}$	-0.10526	-0.10506	-0.10267	-0.10268

Ising parameters (cm^{-1}):

	AA	AB	BA	BB
J_{exch}	0.00000	0.00000	0.00000	0.00000
$J_{dipolar}$	-2.63148	-2.62642	-2.56664	-2.56705
$J_{total}=J_{exch}+J_{dipolar}$	-2.63148	-2.62642	-2.56664	-2.56705

Only the intra-molecular dipolar interaction was considered.

Table S15. Energies and corresponding tunneling gaps of the lowest five exchange doublet states of **3a**.

AA		AB		BA		BB	
energy	Δ_t	energy	Δ_t	energy	Δ_t	energy	Δ_t
0.000000000 0.000000004	4.000E-09	0.000000000 0.000000004	4.000E-09	0.000000000 0.000000001	1.000E-09	0.000000000 0.000000001	1.000E-09
1.303359246 1.303360794	1.548E-06	1.298352720 1.298355544	2.824E-06	1.254173462 1.254177340	3.878E-06	1.244744735 1.244745246	5.110E-07
247.323142486 247.323142503	1.700E-08	237.713043881 237.713043907	2.600E-08	150.588507817 150.588507823	6.000E-09	144.075711941 144.075711942	1.000E-09
247.632211773 247.632211832	5.900E-08	238.030929182 238.030929214	3.200E-08	150.975157236 150.975157241	5.000E-09	144.470099170 144.470099178	8.000E-09
248.516176394 248.516178101	1.707E-06	238.899440511 238.899441083	5.720E-07	151.731882858 151.731884798	1.940E-06	145.214010194 145.214010454	2.600E-07

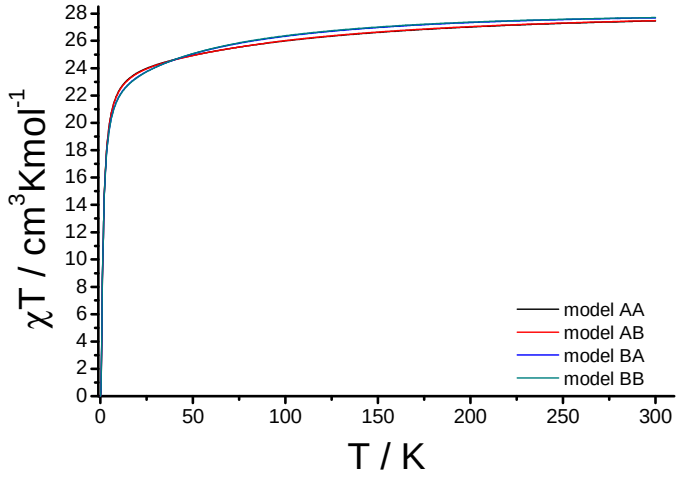

Figure S18. Calculated magnetic susceptibility of **3a**.

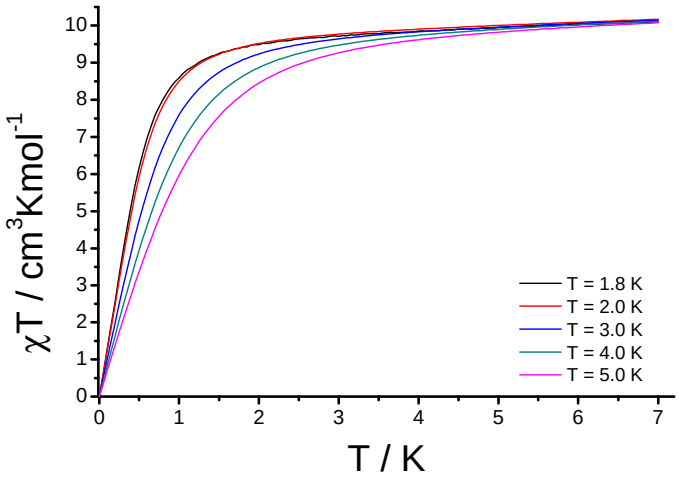

Figure S19. Calculated molar magnetization of **3a** at low temperatures (computational approximation BB).

Local electronic and magnetic properties of the chain $[Cp_2Dy(\mu\text{-}Cl)]_\infty$ (3b)

Table S16. Energies of the lowest Kramers doublets (cm^{-1}) on individual Dy ions in **3b**.

Kramers doublets (cm^{-1})			
AA	AB	BA	BB
0.000	0.000	0.000	0.000
280.148	272.508	136.272	134.432
516.890	500.919	300.671	296.615
680.076	656.399	365.031	356.800
778.127	748.084	399.656	392.299
846.915	810.952	444.274	434.601
939.038	897.205	467.611	457.868
1104.385	1061.111	599.178	588.890
3684.981	3676.574	3608.951	3605.449
3909.012	3891.514	3754.879	3748.329
4079.368	4054.963	3816.749	3808.024
4216.142	4186.377	3876.317	3866.286
4326.724	4292.373	3949.911	3938.218
4419.583	4379.792	3997.588	3985.289
4525.795	4480.535	4050.320	4038.416
6315.378	6300.084	6176.170	6170.279
6480.158	6457.496	6292.245	6283.151
6622.987	6594.787	6340.438	6329.671
6766.685	6733.459	6418.236	6405.978
6882.004	6844.657	6496.138	6482.992
6994.478	6948.279	6543.481	6529.916
8353.001	8331.546	8163.790	8155.597
8476.255	8449.631	8251.670	8240.784
8621.227	8589.573	8312.525	8299.949
8778.462	8742.755	8417.228	8403.856
8900.919	8855.144	8482.559	8467.672
9916.048	9890.803	9710.743	9701.030
10028.449	10000.240	9783.639	9771.676
10250.467	10214.894	9874.699	9861.103

Table S17. Energies (cm^{-1}) and *g* tensors of the lowest Kramers doublets (KD) on individual Dy ions in **3b**.

KD		AA		AB		BA		BB	
		E (cm^{-1})	*g*	E (cm^{-1})	*g*	E (cm^{-1})	*g*	E (cm^{-1})	*g*
1	g_X	0.000	0.0001	0.000	0.0001	0.000	0.0008	0.000	0.0009
	g_Y		0.0002		0.0002		0.0014		0.0015
	g_Z		19.7173		19.7088		19.3645		19.3590
2	g_X	280.148	0.0036	272.508	0.0031	136.272	0.0033	134.432	0.0032
	g_Y		0.0041		0.0035		0.0049		0.0049
	g_Z		16.9992		16.9988		17.0542		17.0444
3	g_X	516.890	0.0605	500.919	0.0516	300.671	0.2764	296.615	0.3412
	g_Y		0.0669		0.0570		0.4015		0.5087
	g_Z		14.2952		14.3148		14.7838		14.7502
4	g_X	680.076	1.0389	656.399	1.0290	365.031	3.6916	356.800	3.8036
	g_Y		1.4377		1.4235		5.6879		5.0426
	g_Z		11.0262		11.0598		10.6077		11.4057
5	g_X	778.127	4.9222	748.084	4.8129	399.656	2.0448	392.299	1.4211
	g_Y		5.3107		5.2718		3.6749		4.1913
	g_Z		9.2985		9.6030		9.4417		9.2551
6	g_X	846.915	0.0886	810.952	0.2568	444.274	2.0382	434.601	1.9024
	g_Y		1.1807		1.0256		3.9921		3.5564
	g_Z		13.1216		13.0862		14.1107		14.6637
7	g_X	939.038	0.5998	897.205	0.6578	467.611	0.3098	457.868	0.3156
	g_Y		0.9532		1.0781		2.1808		2.2447
	g_Z		16.8039		16.6697		14.8152		14.8224
8	g_X	1104.385	0.0176	1061.111	0.0147	599.178	0.1481	588.890	0.1435
	g_Y		0.0243		0.0218		0.2555		0.2358
	g_Z		19.4433		19.4516		19.5304		19.5528

Table S18. Angles between the main magnetic axes of the lowest Kramers doublet in **3b**, obtained in different computational approximations [°]

	AA	AB	BA	BB
AA	0.000	0.079	2.306	2.274
AB	0.079	0.000	2.368	2.336
BA	2.306	2.368	0.000	0.034
BB	2.274	2.336	0.034	0.000

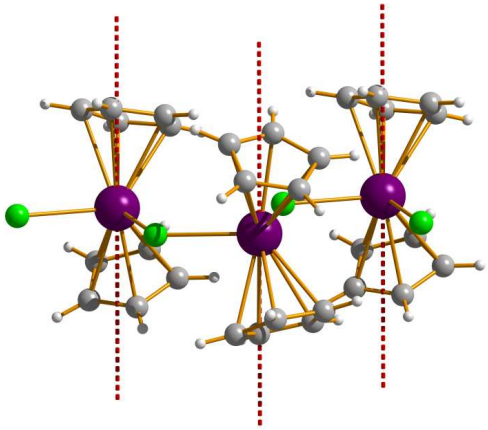

Figure S20. Orientation of the main anisotropy axes of the ground Kramers doublet of **3b**. The main anisotropy axis of the ground state is almost perpendicular to the Dy_2Cl_2 plane (see Table S19).

Table S19. Angles between the main magnetic axes of the lowest Kramers doublet, obtained in different computational approximations, and the Dy_2Cl_2 plane in **3b** [°].

	AA	AB	BA	BB
angle	86.730	86.809	84.737	84.763

Electronic and magnetic properties of $[Cp_2Dy(thf)(\mu\text{-}Cl)]_2$ (4)

Table S20. Energies of the lowest Kramers doublets (cm^{-1}) on individual Dy ions in **4**.

Kramers doublets (cm^{-1})			
AA	AB	BA	BB
0.000	0.000	0.000	0.000
161.847	159.094	97.646	95.851
290.283	286.670	199.378	192.583
359.280	352.868	217.607	211.385
431.146	424.226	239.960	235.811
480.015	464.923	293.116	285.788
540.820	511.156	316.491	308.481
593.619	561.349	347.899	338.596
3615.995	3612.236	3599.036	3597.358
3761.994	3753.888	3687.245	3680.693
3854.310	3842.610	3720.764	3711.712
3908.744	3896.987	3751.453	3741.328
3949.800	3934.302	3788.534	3781.157
4004.998	3984.065	3810.012	3798.763
4095.644	4061.705	3838.705	3827.819
6188.011	6180.611	6131.645	6127.080
6305.804	6294.212	6210.007	6201.593
6385.681	6370.802	6252.257	6241.480
6441.815	6426.223	6280.209	6268.865
6484.061	6465.088	6319.894	6310.546
6589.880	6557.781	6349.688	6336.395
8176.579	8166.047	8093.109	8086.191
8276.750	8261.820	8150.218	8139.828
8365.182	8347.640	8219.005	8206.755
8402.026	8384.866	8263.264	8253.370
8522.563	8492.202	8304.645	8290.177
9724.811	9712.908	9644.164	9636.018
9824.725	9807.215	9681.412	9669.924
9892.995	9875.198	9727.124	9715.189
10059.817	10030.842	9872.958	9858.250
…	…	…	…

Table S21. Energies (cm^{-1}) and *g* tensors of the lowest Kramers doublets (KD) on individual Dy ions in **4**.

KD		AA		AB		BA		BB	
		E (cm^{-1})	*g*	E (cm^{-1})	*g*	E (cm^{-1})	*g*	E (cm^{-1})	*g*
1	g_X	0.000	0.0015	0.000	0.0017	0.000	0.0183	0.000	0.0224
	g_Y		0.0020		0.0021		0.0377		0.0479
	g_Z		19.6482		19.6324		18.9781		18.9208
2	g_X	161.847	0.0681	159.094	0.0583	97.646	0.1143	95.851	0.1665
	g_Y		0.1111		0.0939		0.1475		0.1983
	g_Z		17.0341		17.0445		16.8076		16.6788
3	g_X	290.283	1.1845	286.670	1.1399	199.378	9.0406	192.583	2.4662
	g_Y		2.2599		2.2096		5.4273		5.4041
	g_Z		13.2484		13.3596		0.1321		11.2591
4	g_X	359.280	0.8859	352.868	0.9743	217.607	9.3602	211.385	3.0779
	g_Y		3.4859		3.4062		7.4808		3.4811
	g_Z		9.3764		9.5058		0.3755		11.4406
5	g_X	431.146	2.8740	424.226	2.3103	239.960	3.8305	235.811	4.1742
	g_Y		4.8932		5.3646		4.7976		4.7200
	g_Z		11.2780		10.3905		7.9796		7.7895
6	g_X	480.015	0.2629	464.923	0.3403	293.116	0.8327	285.788	0.8929
	g_Y		1.8441		2.3637		2.8442		3.0628
	g_Z		13.8972		14.0858		12.3145		12.2550
7	g_X	540.820	0.8505	511.156	1.1348	316.491	2.0970	308.481	2.1935
	g_Y		0.9930		1.3056		2.5583		3.7919
	g_Z		17.8734		17.7406		8.0156		7.2177
8	g_X	593.619	0.0836	561.349	0.1227	347.899	11.0588	338.596	10.9659
	g_Y		0.2718		0.4484		8.2791		8.3134
	g_Z		19.2422		18.9589		2.4657		2.6402

Table S22. Angles between the main magnetic axes of the lowest Kramers doublet obtained in different computational approximations (degrees)

	AA	AB	BA	BB
AA	0.000	0.202	5.312	4.860
AB	0.202	0.000	5.494	5.041
BA	5.312	5.494	0.000	0.462
BB	4.860	5.041	0.462	0.000

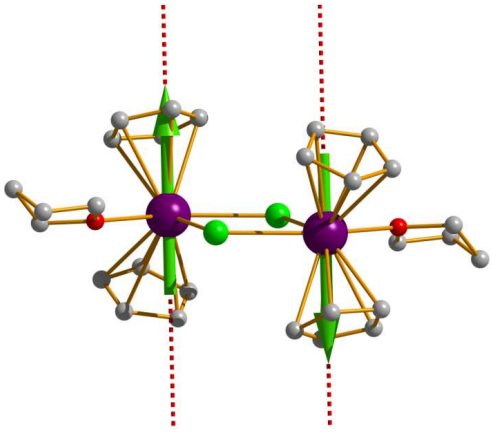

Figure S21. Orientation of the main anisotropy axes of the ground Kramers doublet of **4**. Green arrows show the antiferromagnetic coupling of the local magnetic moments of the Dy ions in the ground state. The main anisotropy axis of the ground state is almost perpendicular to the Dy_2Cl_2 plane (see Table S23).

Table S23. Angles between the main magnetic axes of the lowest Kramers doublet obtained in different computational approximations and the Dy_2Cl_2 plane [°].

	AA	AB	BA	BB
angle	85.918	86.122	80.806	81.268

Table S24. Exchange interactions between Dy ions in the complex **4**.

Lines parameters (cm^{-1}):

	AA	AB	BA	BB
J_{exch}	-0.01504	-0.01462	0.00131	0.00342
$J_{dipolar}$	-0.08264	-0.08267	-0.07933	-0.07963
$J_{total}=J_{exch}+J_{dipolar}$	-0.09768	-0.09729	-0.07802	-0.07621

Ising parameters (cm^{-1}):

	AA	AB	BA	BB
J_{exch}	-0.37600	-0.36550	0.03275	0.08550
$J_{dipolar}$	-2.06600	-2.06675	-1.98325	-1.99075
$J_{total}=J_{exch}+J_{dipolar}$	-2.44200	-2.43225	-1.95050	-1.90525

Table S25. Energies and corresponding tunnelling gaps of the lowest five exchange doublet states of **4**.

AA		AB		BA		BB	
energy	Δ_t	energy	Δ_t	energy	Δ_t	energy	Δ_t
0.000000000 0.000000000	0.000E+00	0.000000000 0.000000003	3.000E-09	0.000000000 0.000003809	3.809E-06	0.000000000 0.000006724	6.724E-06
1.144516713 1.144516735	2.200E-08	1.138163910 1.138164624	7.140E-07	0.856247453 0.856253840	6.387E-06	0.831590697 0.831601244	1.055E-05
161.833818440 161.833819021	5.810E-07	159.078690316 159.078690615	2.990E-07	97.574960436 97.574963186	2.750E-06	95.775407560 95.775412459	4.899E-06
162.015213255 162.015213320	6.500E-08	159.261972732 159.261972789	5.700E-08	97.784984811 97.785015989	3.118E-05	95.997731367 95.997785509	5.414E-05
162.896258908 162.896259848	9.400E-07	160.134086203 160.134087259	1.056E-06	98.386427995 98.386471070	4.308E-05	96.558291870 96.558367035	7.516E-05

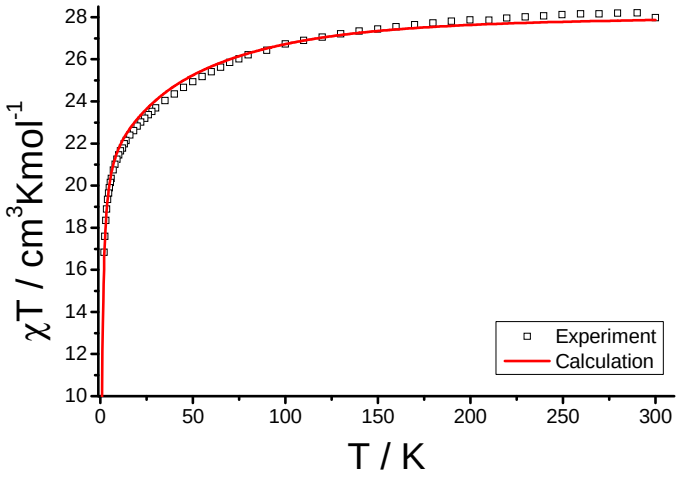

Figure S22. A comparison between measured and calculated magnetic susceptibility of **4** (computational approximation BB).

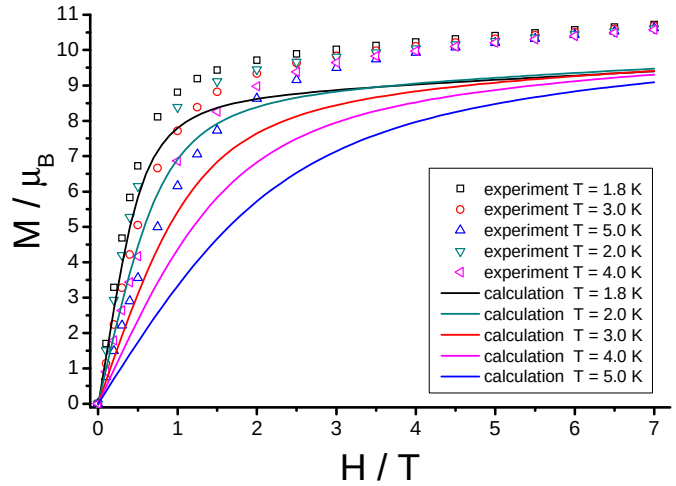

Figure S23. Measured and calculated molar magnetization of **4** at low temperature (computational approximation BB).

Local electronic and magnetic properties of the $[Cp_2Dy(\mu\text{-Bta})]_2$ (5).

Table S26. Energies of the lowest Kramers doublets (cm^{-1}) on individual Dy ions in **5**.

Kramers doublets (cm^{-1})			
AA	AB	BA	BB
0.000	0.000	0.000	0.000
156.787	154.838	103.453	103.949
286.117	283.001	171.433	171.728
328.107	322.147	207.302	210.283
355.178	344.782	227.282	226.287
380.156	371.282	246.530	248.792
430.299	421.406	296.143	295.570
537.679	523.073	395.202	389.575
3617.453	3614.105	3597.226	3595.429
3736.311	3729.905	3669.038	3666.461
3799.132	3789.703	3698.320	3695.629
3856.906	3846.516	3738.403	3735.886
3911.242	3901.116	3768.975	3768.123
3945.928	3933.490	3817.939	3813.477
3983.090	3967.130	3840.838	3834.661
6181.302	6175.449	6128.144	6125.860
6259.936	6250.634	6182.571	6178.272
6321.396	6310.094	6231.093	6226.065
6393.991	6381.639	6264.315	6260.832
6452.667	6440.032	6327.896	6322.725
6484.990	6468.141	6345.569	6338.358
8159.540	8151.391	8090.348	8086.865
8204.030	8192.764	8112.428	8107.462
8310.859	8297.583	8203.901	8198.039
8381.637	8368.288	8270.529	8264.138
8428.636	8411.327	8294.673	8286.489
9685.889	9676.239	9620.245	9615.586
9768.114	9755.253	9665.790	9659.986
9850.842	9836.894	9721.044	9714.652
9981.830	9964.249	9868.276	9858.955
…	…	…	…

Table S27. Energies (cm^{-1}) and g tensors of the lowest Kramers doublets (KD) on individual Dy ions in **5**.

KD		AA		AB		BA		BB	
		E (cm^{-1})	*g*	E (cm^{-1})	*g*	E (cm^{-1})	*g*	E (cm^{-1})	*g*
1	g_X	0.000	0.0128	0.000	0.0148	0.000	0.0038	0.000	0.0073
	g_Y		0.0347		0.0405		0.0761		0.0884
	g_Z		19.5065		19.5777		19.0472		19.0530
2	g_X	156.787	0.0011	154.838	0.0201	103.453	0.1313	103.949	0.1668
	g_Y		0.0437		0.0708		0.4598		0.5096
	g_Z		16.8989		16.9308		16.3546		16.2998
3	g_X	286.117	2.1375	283.001	2.5531	171.433	0.4593	171.728	0.4305
	g_Y		3.3995		3.8282		1.0073		0.8721
	g_Z		13.2048		12.8940		17.7649		17.7264
4	g_X	328.107	3.6333	322.147	3.2064	207.302	9.7942	210.283	9.9004
	g_Y		4.3517		3.9459		8.5526		8.0373
	g_Z		10.1635		10.9991		2.7509		3.0418
5	g_X	355.178	0.0411	344.782	0.1032	227.282	0.4708	226.287	1.0896
	g_Y		2.1565		1.9827		1.9148		2.0250
	g_Z		12.9548		13.6686		13.2599		13.2705
6	g_X	380.156	1.6707	371.282	1.8081	246.530	2.6683	248.792	3.2617
	g_Y		3.3537		2.9695		4.5624		4.4623
	g_Z		8.2917		9.2784		6.7181		6.5340
7	g_X	430.299	1.6805	421.406	1.8620	296.143	2.6553	295.570	2.6652
	g_Y		5.4708		5.1086		5.6856		5.4363
	g_Z		12.1073		12.3309		10.9842		11.1710
8	g_X	537.679	0.3154	523.073	0.3730	395.202	0.3517	389.575	0.3743
	g_Y		0.6361		0.7567		0.5007		0.5409
	g_Z		18.8516		18.8199		18.6041		18.5745

Table S28. Angles between the main magnetic axes of the lowest Kramers doublet obtained in different computational approximations [°].

	AA	AB	BA	BB
AA	0.000	0.053	3.626	3.407
AB	0.053	0.000	3.677	3.458
BA	3.626	3.677	0.000	0.225
BB	3.407	3.458	0.225	0.000

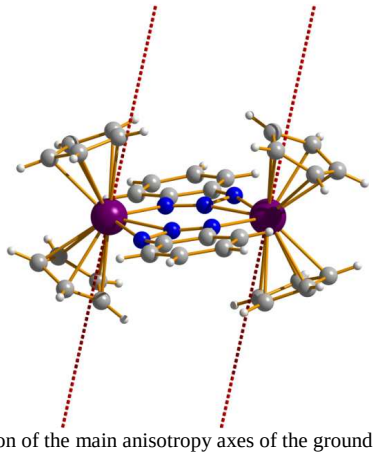

Figure S24. Orientation of the main anisotropy axes of the ground Kramers doublet of **5**.

APPENDIX TWO

Dalton Transactions

RSC Publishing

COMMUNICATION

Exchange-coupled oxygen- and sulfur-bridged cyclopentadienyl-manganese(II) cages†

Cite this: *Dalton Trans.*, 2013, **42**, 71

Received 26th September 2012,
Accepted 31st October 2012

DOI: 10.1039/c2dt32262e

www.rsc.org/dalton

Charlene A. Smith,[a] Floriana Tuna,[a,b] Michael Bodensteiner,[c] Madeleine Helliwell,[a] David Collison[a,b] and Richard A. Layfield*[a,c]

The trimetallic complex [{CpMn(μ-OSiPh$_3$)$_2$}$_2$Mn] (1) and the heterocubane [CpMn(μ$_3$-SSiPh$_3$)]$_4$ (2) are formed by deprotonation of Ph$_3$SiQH (Q = O, S) by manganocene, or by transmetallation of manganocene by Ph$_3$SiQLi. The Mn(II) centres in 1 and 2 are antiferromagnetically coupled, with J = −4.4 and −3.0 cm^{-1} in 1 and 2, respectively (−2J formalism).

Cage compounds based on transition metals and chalcogenolate ligands attract considerable interest, both from a fundamental perspective and also because of their potential use as precursors to metal–chalcogen nanometer-scale clusters, which can display desirable magnetic or optical properties.[1] Molecular precursors offer an attractive 'bottom–up' approach to the synthesis of nano-scale clusters because they often have good solubility in organic solvents, they can be manipulated using relatively mild conditions and, within certain limits, the metal-to-chalcogen ratio in the nano-cluster can be influenced.[2] Within this context, the diverse reactivity of manganese(II) bis(cyclopentadienide) (manganocene, Cp$_2$Mn) should provide a versatile organometallic route to manganese(II)–chalcogen cage compounds.[3] The appreciable ionic character of the cyclopentadienide ligands in manganocene enables the metallation (manganation) of acidic Q–H bonds (Q = heteroatom), and manganocene can be readily transmetallated by strong nucleophiles such as organolithiums: these types of reactivity ultimately provide reliable methods for synthesizing cage compounds of the type [CpMn{μ-(QR$_x$)}]$_n$, which may have potential to be developed as precursors to higher-nuclearity cages.

Although many examples of amido- and halide-bridged polymetallic cyclopentadienyl-manganese(II) compounds are known,[4–6] no compounds of the type [CpMn{μ-(QR)}]$_n$, in which Q is a Group 16 element, have been reported. We therefore now communicate the synthesis, structure and magnetic properties of the oxygen-bridged trimanganese compound [{CpMn(μ-OSiPh$_3$)$_2$}$_2$Mn] (**1**) and the tetrametallic manganese–sulfur heterocubane [CpMn(μ$_3$-SSiPh$_3$)]$_4$ (**2**).

Compound **1** was synthesized either by manganation of the O–H bond of triphenylsilanol or by transmetallation of Cp$_2$Mn by Ph$_3$SiOLi, in toluene solvent (Scheme 1). The outcome of the reaction is independent of the route and the Mn : O stoichiometry (1 : 1 and 3 : 4 were used). The direct manganation and the transmetallation methods were also used to synthesize the thiolate-bridged compound [CpMn(μ$_3$-SSiPh$_3$)]$_4$ (**2**) (Scheme 1).[7]

Single crystals of **1**·(1.5 toluene) and **2**·(3.5 toluene)·(pentane) were grown from saturated toluene solutions at 4 °C, and the structures of both were determined by X-ray crystallography. The asymmetric unit of **1**·(1.5 toluene) contains a relatively well-ordered toluene molecule and a toluene molecule at half occupancy, which is disordered about a crystallographic inversion centre. Molecules of **1** consist of a central manganese(II) cation, Mn(2), complexed by four [Ph$_3$SiO]$^-$ ligands that produce Mn(2)–O distances of 2.043(7)–2.078(7) Å, and O–Mn(2)–O angles in the range 85.9(3)–129.4(3)° (average 110.2°), resulting in a distorted tetrahedral coordination environment (Fig. 1). The [Ph$_3$SiO]$^-$ ligands containing O(1) and O(2) μ-bridge to Mn(1), and those containing O(3) and O(4) μ-bridge to Mn(3), with Mn–O bond distances in the

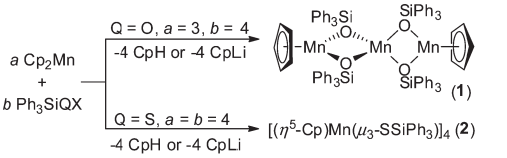

Scheme 1 Synthesis of **1** and **2**. X = H or Li.

[a]*School of Chemistry, The University of Manchester, Oxford Road, Manchester, M13 9PL, UK. E-mail: Richard.Layfield@manchester.ac.uk*
[b]*EPSRC U.K. National EPR Facility, Photon Science Institute, The University of Manchester, Oxford Road, Manchester, M13 9PL, UK*
[c]*Institute of Inorganic Chemistry, University of Regensburg, Regensburg, D-93040, Germany*

†Electronic supplementary information (ESI) available: Synthetic, analytical details. CCDC 884129 and 884130. For ESI and crystallographic data in CIF or other electronic format see DOI: 10.1039/c2dt32262e

This journal is © The Royal Society of Chemistry 2013

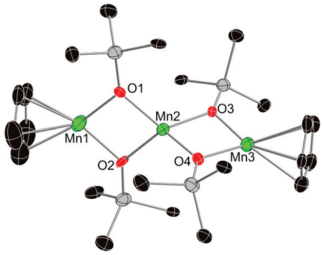

Fig. 1 Thermal ellipsoid representation (50% probability) of [{CpMn(μ-OSiPh$_3$)$_2$}$_2$Mn] (**1**). Unlabeled atoms are carbon (black) and silicon (grey). Hydrogen atoms are omitted for clarity, and only the *ipso* carbons of the phenyl substituents are shown.

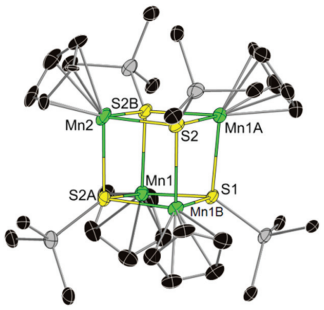

Fig. 2 Thermal ellipsoid representation (50% probability) of [CpMn(μ$_3$-SSiPh$_3$)]$_4$ (**2**). Unlabeled atoms are carbon (black) and silicon (grey). Hydrogen atoms are omitted for clarity. Only the *ipso* carbons of the phenyl substituents are shown.

narrow range of 2.054(7)–2.074(7) Å, and Mn–O–Mn bridging angles of 93.8(3)–94.7(3)°. A slight bending of the molecular structure of **1** is reflected in the Mn···Mn···Mn angle of 171.3(3)°. Both Mn(1) and Mn(3) are capped by an η^5-Cp ligand, with Mn(1)–C and Mn(3)–C bond lengths of 2.384(8)–2.427(9) Å and 2.403(8)–2.453(8) Å, respectively, meaning that these manganese centres are formally five-coordinate. The formal valence electron counts of Mn(2) and Mn(1/3) are 13 and 15, respectively.

Molecules of **2** adopt a hetero-cubane structure in which each manganese centre is complexed by three (μ$_3$-SSiPh$_3$) ligands and one η^5-Cp ligand. In **2**, Mn(1), Mn(1A) and Mn(1B) – and hence also S(2), S(2A) and S(2B) – are related by a crystallographic three-fold rotation axis that passes through Mn(2), S(1) and the centroid of the η^5-Cp ligand bonded to Mn(2), resulting in the Cp ligand being disordered. For Mn(1) and symmetry equivalents, the Mn(1)–S and Mn(1)–C distances are 2.5847(5)–2.6258(6) and 2.383(3)–2.450(3) Å, respectively, whereas for Mn(2) the three symmetry-related Mn(2)–S(1) distances are 2.5918(7) Å and the Mn(2)–C distances are 2.421(3)–2.433(3) Å, respectively. The three Mn–S–Mn μ-bridging angles subtended at S(2) are very similar at 93.42(2)–93.75(2)°, and are slightly more acute than the three analogous angles at S(1) of 95.42(2)°. Overall, each manganese centre in **2** resides in a six-coordinate 'piano-stool' environment, and has a formal valence electron count of 17 (Fig. 2).

The different outcomes of the reactions of manganocene with triphenylsilanol and lithium triphenylsilylthiolate are noteworthy. In the absence of steric constraints, manganese(II) mono(cyclopentadienyl) compounds are typically based on pseudo-octahedral 17-electron piano-stool units such as [(η^5-C$_5$H$_4$Me)Mn(PEt$_3$)(μ-X)]$_2$ (X = Cl, Br, I).[4] In the case of **1**, the coordination numbers of four and five, and their respective valence electron counts of 13 for Mn(2) and 15 for Mn(1/3), are therefore lower than would occur with the thermodynamically more stable 17-electron configuration. The reasons for the low coordination numbers and valence electron counts in **1** probably stem from the short Mn–O bonds, which bring the bulky SiPh$_3$ groups into close proximity with one another and so hinder coordination of additional μ-[Ph$_3$SiO]$^-$ ligands. In contrast, the Mn–S bonds in **2** are approximately 0.5 Å longer than the Mn–O bonds in **1**, hence the coordination environment around the manganese centres is less congested in **2**, and so it is possible for three μ$_3$-[Ph$_3$SiS]$^-$ ligands to coordinate to manganese and create a valence electron count of 17.

To the best of our knowledge, **1** and **2** are the first chalcogen-bridged mono-cyclopentadienyl compounds of manganese in the oxidation state +2. Oxygen-bridged manganese cages are a well-characterized family of compounds, due partly to the relevance of manganese–oxygen units to the oxygen-evolving complex of photosystem II,[8] and also to the development of the vast series of manganese-containing single-molecule magnets.[9] Many transition metal compounds containing [M$_4$S$_4$] structural units have been studied in detail, particularly in the case of iron because of their suitability as model compounds for iron–sulfur electron-transfer proteins.[10] In contrast, manganese thiolate chemistry is relatively underdeveloped,[11] and crystallographically characterized examples of manganese–sulfur cubanes are rare, being hitherto limited to diamagnetic manganese(I) compounds of the type [Mn(CO)$_3$(μ$_3$-SR)]$_4$ (R = Ph or 2-furanylmethyl).[12]

The paramagnetism of **1** and **2** affords an opportunity to investigate chalcogen-mediated magnetic exchange in mono(cyclopentadienyl)manganese compounds. Placing samples of **1**·(1.5 toluene) and **2**·(3.5 toluene)·(pentane) under a vacuum of approximately 10^{-3} mm Hg for one hour resulted in evaporation of the lattice solvation, as revealed by elemental analysis. Magnetic susceptibility measurements were therefore made on polycrystalline samples of **1** and **2**, using applied fields of 1000 G. For **1**, the temperature dependence of $\chi_M T$ (*i.e.* the product of the molar magnetic susceptibility, χ_M, and temperature) is shown in Fig. 3 and S3.† At 300 K, the value of $\chi_M T$ is 10.94 cm^3 K mol^{-1}, which is slightly less than the value of 13.13 cm^3 K mol^{-1} expected for three non-interacting Mn(II) ions each with S = 5/2 and g = 2.0,[13] and indicates weak antiferromagnetic exchange between the manganese centres. As the temperature is lowered, $\chi_M T$ gradually decreases to reach a value of 4.06 cm^3 K mol^{-1} at 2 K, which is very close to the value of 4.38 cm^3 K mol^{-1} expected for a single Mn(II) ion, and

 This journal is © The Royal Society of Chemistry 2013

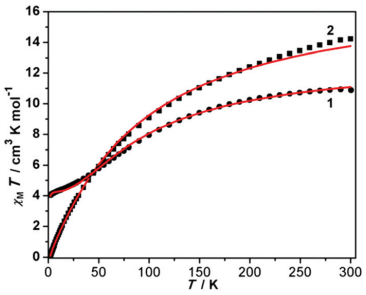

Fig. 3 Temperature dependence of $\chi_M T$ for **1** (circles) and **2** (squares). The red lines are theoretical fits of the experimental data.

is consistent with a chain of three antiferromagnetically coupled Mn(II) ions. A good fit of the experimental susceptibility data was obtained using the spin Hamiltonian $H = -2J(S_1S_2 + S_2S_3)$, where S_n represents the spin on the manganese (II) ions, labelled according to the molecular structure (Fig. 1). Each Mn(II) was assumed to be high-spin with $S = 5/2$ and $g = 2.0$. The fit of the magnetic susceptibility data for **1** (and **2**) was obtained by applying a matrix diagonalisation procedure to the spin Hamiltonian stated above, using the MAGPACK software,[14] which produced an exchange coupling constant of $J = -4.4$ cm^{-1}.

In **2**, $\chi_M T$ at 300 K is 14.21 cm^3 K mol^{-1}, whereas the expected value for four non-interacting Mn(II) ions is 17.51 cm^3 K mol^{-1}, hence weak antiferromagnetic coupling also occurs in **2**. The value of $\chi_M T$ decreases gradually down to about 100 K, and then more rapidly at lower temperatures (Fig. 3 and S4†). At 2 K $\chi_M T$ is zero and the ground state is diamagnetic. Fitting the magnetic susceptibility data in **2** using $H = -2J(S_1S_{1A} + S_1S_{1B} + S_1S_2 + S_{1A}S_{1B} + S_{1A}S_2 + S_{1B}S_2)$, with $S = 5/2$ and $g = 2.0$, gave $J = -3.0$ cm^{-1}, hence the exchange coupling in **2** is weaker than that in **1**.

Determinations of exchange coupling constants in polymetallic mono-cyclopentadienyl manganese(II) compounds are uncommon. In amido-bridged dimers of general formula $[CpMn(\mu\text{-}NR_2)]_2$ (NR_2 = primary or secondary amido ligand), weak antiferromagnetic coupling appears to be ubiquitous, with the magnitude of the exchange coupling constant typically in the range 2–15 cm^{-1}.[5] Similar observations have been made on the series of halide-bridged compounds $[CpMn(\mu\text{-}X)]_2$ (X = Cl, Br or I), for which the strength of the exchange coupling is apparently independent of the halide, with $J \approx -5$ cm^{-1}.[4] Exchange coupling mediated by phosphorus and arsenic has only been investigated by experiment in two instances (irrespective of the metal), namely $[CpMn\{E(SiMe_3)_2\}]_2$, which resulted in $J = -13.5$ cm^{-1} when E = P and $J = -1.5$ cm^{-1} when E = As.[15] Although factors such as coordination geometry and ligand substituent effects may influence exchange coupling, the *J*-values determined for **1** and **2** are therefore consistent with previous reports.

Conclusions

We have shown that exchange-coupled manganese(II)–chalcogenolate cages can be synthesized by direct metallation of Ph_3SiQH by manganocene, or by transmetallation of manganocene with Ph_3SiQLi (Q = O or S). The different aggregation states of **1** and **2** can be rationalized in terms of the much longer Mn–S bond in **2** leading to a sterically much less congested manganese coordination environment. The reactivity should be extendable to other oxygen- and sulfur-containing ligands, and to ligands based on the heavier chalcogens. Furthermore, it can be envisaged that varying the chalcogen and the steric demands of the ligand substituents may provide a means of influencing the manganese : chalcogen ratio in compounds of this type, which could in principle introduce a means of influencing the composition of larger nano-scale manganese–chalcogenide cages and nanoparticles.

Notes and references

1 (*a*) J. Zhou, G. Q. Bian and C. Y. Li, *Coord. Chem. Rev.*, 2009, **253**, 1221; (*b*) S. Dehnen and M. Melullis, *Coord. Chem. Rev.*, 2007, **251**, 1259.

2 (*a*) C. B. Khadka, A. Eichhöfer, F. Weigand and J. F. Corrigan, *Inorg. Chem.*, 2012, **51**, 2747; (*b*) C. B. Khadka, D. G. Macdonald, Y. Lan, A. K. Powell, D. Fenske and J. F. Corrigan, *Inorg. Chem.*, 2010, **49**, 7289; (*c*) M. L. Fu, I. Issac, D. Fenske and O. Fuhr, *Angew. Chem., Int. Ed.*, 2010, **49**, 6899; (*d*) C. E. Anson, A. Eichhöfer, I. Issac, D. Fenske, O. Fuhr, P. Sevillano, C. Persau, D. Stalke and J. Zhang, *Angew. Chem., Int. Ed.*, 2008, **47**, 1326.

3 R. A. Layfield, *Chem. Soc. Rev.*, 2008, **37**, 1098.

4 (*a*) F. H. Köhler, N. Hebendanz, G. Müller and U. Thewalt, *Organometallics*, 1987, **6**, 115; (*b*) F. H. Köhler, N. Hebendanz, U. Thewalt, B. Kanellakopulos and R. Klenze, *Angew. Chem., Int. Ed.*, 1984, **23**, 721.

5 (*a*) C. S. Alvarez, S. R. Boss, J. C. Burley, S. M. Humphrey, R. A. Layfield, R. A. Kowenicki, M. McPartlin, J. M. Rawson, A. E. H. Wheatley, P. T. Wood and D. S. Wright, *Dalton Trans.*, 2004, 3481; (*b*) C. S. Alvarez, A. D. Bond, E. A. Harron, R. A. Layfield, M. E. G. Mosquera, M. McPartlin, J. M. Rawson and D. S. Wright, *Dalton Trans.*, 2003, 3002; (*c*) C. S. Alvarez, A. D. Bond, D. Cave, M. E. G. Mosquera, E. A. Harron, R. A. Layfield, M. McPartlin, J. M. Rawson, P. T. Wood and D. S. Wright, *Chem. Commun.*, 2002, 2980; (*d*) C. S. Alvarez, A. D. Bond, E. A. Harron, R. A. Layfield, J. A. McAllister, C. M. Pask, J. M. Rawson and D. S. Wright, *Organometallics*, 2001, **20**, 4135.

6 (*a*) M. Maekawa, M. Römelt, C. G. Daniliuc, P. G. Jones, P. S. White, F. Neese and M. D. Walter, *Chem. Sci.*, 2012, **3**, 2972; (*b*) F. A. Stokes, R. J. Less, J. Haywood, R. L. Melen, R. I. Thompson, A. E. H. Wheatley and D. S. Wright, *Organometallics*, 2012, **31**, 23; (*c*) J. L. Krinsky, M. N. Stavis and

M. D. Walter, *Acta Crystallogr., Sect. E: Struct. Rep. Online*, 2003, **59**, m497; (*d*) A. Bashall, M. A. Beswick, H. Ehlenberg, S. J. Kidd, M. McPartlin, J. Palmer, P. R. Raithby, J. M. Rawson and D. S. Wright, *Chem. Commun.*, 2000, 749; (*e*) J. Heck, W. Massa and P. Weinig, *Angew. Chem., Int. Ed.*, 1984, **23**, 722.

7 F. Tuna, C. A. Smith, M. Bodensteiner, L. Ungur, L. Chibotaru, E. J. L. McInnes, R. E. P. Winpenny, D. Collison and R. A. Layfield, *Angew. Chem., Int. Ed.*, 2012, **51**, 6976.

8 Y. Umena, K. Kawakami, J. R. Shen and N. Kamiya, *Nature*, 2011, **473**, 55.

9 (*a*) R. Bagai and G. Christou, *Chem. Soc. Rev.*, 2009, **38**, 1011; (*b*) D. Gatteschi, R. Sessoli and J. Villain, *Molecular Nanomagnets*, Oxford University Press, New York, 2006; (*c*) G. Christou, *Polyhedron*, 2005, **24**, 2065; (*d*) G. Aromí and E. K. Brechin, *Struct. Bonding (Berlin)*, 2006, **122**, 1.

10 E. Münck and E. L. Bominaar, *Science*, 2008, **321**, 1452.

11 (*a*) T. Costa, J. R. Dorfman, K. S. Hagen and R. H. Holm, *Inorg. Chem.*, 1983, **22**, 4091; (*b*) T. Nguyen, A. Panda, M. M. Olmstead, A. F. Richards, M. Stender, M. Brynda and P. P. Power, *J. Am. Chem. Soc.*, 2005, **127**, 8545.

12 (*a*) D. S. Choi, S. H. Hong, S. S. Lee and Y. K. Chung, *J. Organomet. Chem.*, 1999, **579**, 385; (*b*) M. Reyes-Lazama, R. A. Toscano and N. Zúñiga-Villareal, *J. Organomet. Chem.*, 1996, **516**, 19; (*c*) S. Onaka and Y. Katukawa, *J. Coord. Chem.*, 1996, **39**, 135.

13 O. Kahn, *Molecular Magnetism*, VCH Publishers, New York, 1993.

14 J. J. Clemente-Juan, E. Coronado and B. S. Tsukerblat, *J. Comput. Chem.*, 2001, **22**, 985.

15 S. Scheuermayer, F. Tuna, M. Bodensteiner, M. Scheer and R. A. Layfield, *Chem. Commun.*, 2012, 8087.

 This journal is © The Royal Society of Chemistry 2013

Electronic Supplementary Information

Exchange-coupled oxygen- and sulfur-bridged cyclopentadienyl-manganese(II) cages

Charlene A. Smith, Floriana Tuna, Michael Bodensteiner, Madeleine Helliwell, David Collison and Richard A. Layfield

Page 1 Synthetic details
Page 2 Crystallographic details
Page 4 Magnetic susceptibility measurements

Synthetic details

General considerations. Toluene was dried by refluxing under nitrogen for several hours over sodium-potassium alloy. Benzene-d_6 was distilled from sodium-potassium alloy and stored over activated 4 Å molecular sieves. Solids were manipulated using an MBraun LabMaster glovebox under an argon atmosphere, and solutions were transferred using a Schlenk line under nitrogen that had been passed through several columns of various drying agents and a heated copper catalyst. Manganocene, Cp_2Mn[1] and lithium triphenthylsilylthiolate[2] were synthesized according to literature procedures, and triphenylsilanol was purchased from Aldrich and used as supplied. Paramagnetic ^{1}H NMR spectra were acquired using a Bruker Avance III 400 MHz spectrometer across a chemical shift range of 250 ppm. Elemental analysis results were obtained using the elemental analysis service of London Metropolitan University, U.K. (Mr. S. Boyer).

Compound 1: deprotonation route. A solution of Cp_2Mn (0.10 g, 0.55 mmol) in toluene (10 ml) was added to a stirred suspension of Ph_3SiOH (0.15 g, 0.55 mmol) at –78 C. The light green reaction mixture was warmed to room temperature and stirred overnight. The resulting amber solution was briefly heated to dissolve a pale yellow precipitate and then filtered (porosity 3). The volume of the filtrate was reduced until appreciable amounts of precipitate had formed on the walls of the reaction vessel, and then the mixture was gently heated until a homogeneous solution was obtained. Storage at room temperature produced a crop of large, colourless block-like crystals, which were subsequently identified by X-ray crystallography to be **1**·(1.5 toluene). Placing the crystals under vacuum for 30 minutes resulted in the formation of toluene-free **1** (isolated yield 0.14 g, 55% based on manganese). Analysis calculated for $C_{82}H_{70}O_4Si_4Mn_3$: C 70.52, H 5.05; found C 70.59, H 5.65. ^{1}H NMR (benzene-d_6, 400.13 MHz, 298 K, /ppm): 2.04, 1.18, 0.80, 2, 1 and 2 ^{1}H, respectively, phenyl. Cp protons not observed.

Compound **2** can be synthesized using this method, on the same scale, with typical yields of 40-45%.

Compound 2: transmetallation route. A solution of Cp_2Mn (0.10 g, 0.55 mmol) in toluene (10 ml) was added to a stirred suspension of Ph_3SiSLi (0.16 g, 0.55 mmol) in toluene (10 ml) at –78 C. The yellow reaction mixture was warmed to room temperature and stirred overnight, and then filtered (porosity 3) to remove a gelatinous precipitate of CpLi. The solvent was evaporated and the resulting yellow solid then washed with pentane (2 mL) and then dried. Toluene (5 mL) was and the dark yellow mixture was gently heated until a homogeneous solution was obtained. Storage at –28 C produced a crop of yellow crystals, which were subsequently identified by X-ray crystallography to be **2**·(3.5 toluene)·(1 toluene). Placing the crystals under vacuum for 60 minutes resulted in the formation of toluene-free **2** (isolated yield 0.12 g, 53% based on manganese). Analysis calculated for $C_{92}H_{80}S_4Si_4Mn_4$: C 67.13, H 4.90; found C 67.87, H 4.21. ^{1}H NMR (benzene-d_6, 400.13 MHz, 298 K, /ppm): 2.91, 2.62, 2.02, 2, 1 and 2 ^{1}H, respectively, phenyl. Cp protons not observed.

Compound **1** can be synthesized using this method, on the same scale, with typical yields of 55-60%.

X-ray crystallography

Data on **1**·(1.5 toluene) were collected using a Bruker APEX CCD diffractometer, and data on **2**·(3 toluene)·(*n*-pentane) were collected using an Agilent Technologies SuperNova CCD diffractometer. For **2**·(3 toluene)·(*n*-pentane), a multi-scan absorption correction was applied to the data.[3] The structures were solved with SHELXS, and SHELXL was used for the refinement.[4]

In **1**·(1.5 toluene), the asymmetric unit contains one molecule of **1** and 1.5 toluene solvent molecules, with the toluene at half occupancy disordered over a centre of symmetry. All non-H atoms were refined anisotropically with restraints on the adps of some of the carbon atoms, except the toluene at half-occupancy, which was refined isotropically with a common adp. All the phenyl groups were constrained to be regular hexagons and restraints were applied to the Ph–Me single bond lengths. The Cp rings were constrained to be regular pentagons. H-atoms were included in calculated positions. The crystals diffracted extremely weakly, which led to a high R_{int} value and a low percentage of data with $I > 2$ (*I*). It was also necessary to cut the data at 0.9 Å resolution because there was no diffraction beyond this point.

The crystal structure of **2** contains three toluene molecules and one *n*-pentane one which is located at the three-fold rotary-inversion axis. The disordered toluene molecule could be modelled with isotropic minor position. The *n*-pentane solvent was treated with the SQUEEZE function of the PLATON software.[5] The void contains 41 electrons (42 electrons for pentane) in a cavity of 188 Å^3.

Table S1. Crystal data and structure refinement for **1**·(1.5 toluene) and **2**·(3 toluene)·(pentane)[a]

	1·(1.5 toluene)	**2·(3 toluene)·(pentane)**
Empirical formula	$C_{92.5}H_{82}Mn_3O_4Si_4$	$C_{119}H_{117}Mn_4S_4Si_4$
Formula weight	1534.76	1935.38
T/K	100(2)	123(1)
/Å	0.71073	1.54178
Crystal system	monoclinic	trigonal
Space group	$P2_1/n$	$P\bar{3}$
a/Å	14.632(4)	20.0897(2)
b/Å	26.084(8)	20.0897(2)
c/Å	20.375(6)	14.0486(2)
/°	90	90
/°	94.221(6)	90
/°	90	120
V/Å^3	7755(4)	4910.33(14)
Z	4	2
Density (calculated)/Mg m^{-3}	1.315	1.339
Crystal size/mm^3	0.45 0.17 0.11	0.42 0.28 0.24
range for data collection/°	2.09-23.26	3.15-74.20
Reflections collected	46182	24724
Independent reflections	11108 [*R*(int) = 0.3053]	6497 [R_{int} = 0.0351]
Completeness/%	99.7 %	97.3 %
Data / restraints / parameters	11108 / 681 / 740	6497 / 0 / 408
Goodness-of-fit on F^2	0.734	1.033
Final *R* indices [$I>2$ (*I*)]	$R_1 = 0.0777$, $wR_2 = 0.1479$	$R_1 = 0.0402$, $wR_2 = 0.1094$
R indices (all data)	$R_1 = 0.2669$, $wR_2 = 0.1899$	$R_1 = 0.0423$, $wR_2 = 0.1106$
Largest diff. peak and hole/e.Å^{-3}	0.785 and -0.477	0.796 and -0.558

[a]Full-matrix least-squares on F^2 used as structure refinement for both compounds.

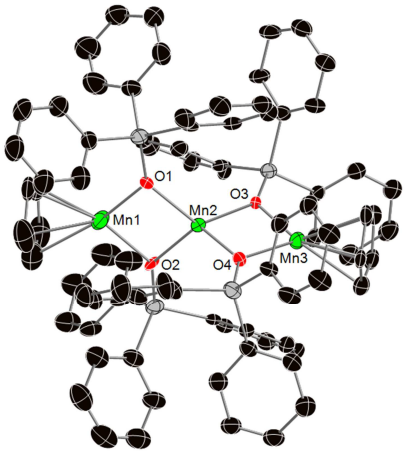

Figure S1. Thermal ellipsoid plots (50% probability) of the molecular structures of **1**. Unlabelled atoms are carbon (black) and silicon (grey). Hydrogen atoms not shown.

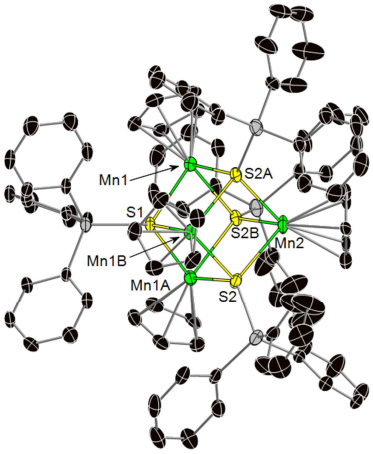

Figure S2. Thermal ellipsoid plots (50% probability) of the molecular structure of **2**, viewed along the crystallographic *b*-axis. Unlabelled atoms are carbon (black) and silicon (grey). The "A"and "B" atom labels indicates that these atoms are at equivalent positions. Hydrogen atoms are not shown.

Magnetic susceptibility measurements on 1 and **2**

The magnetic properties of polycrystalline samples of **1** and **2** were measured using a Quantum Design MPMS-7 SQUID magnetometer at temperatures in the range 2-300 K. In a glove box, the polycrystalline samples were transferred to Kel-F capsules, which were then sealed with an O-ring cap, and the capsules were then placed in plastic straws. One end of the straw was then sealed with a cap, and the other end was sealed with Blu-Tac. The straw was then sealed in a Schlenk tube and taken to the magnetometer. The straw was removed from the Schlenk tube and the Blu-Tac quickly replaced with the carbon fibre rod, and then the sample was quickly transferred to the purged sample space of the MPMS.

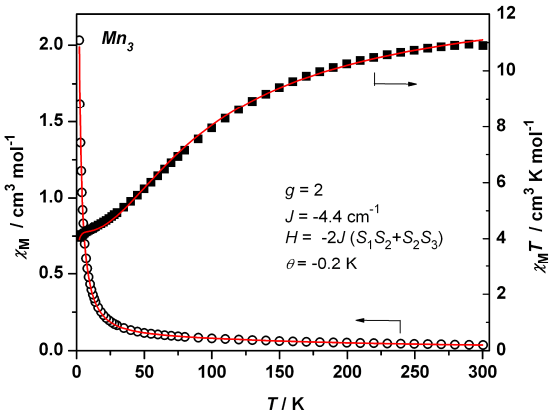

Figure S3. Temperature dependence of χ_M (squares) and $\chi_M T$ (circles) of **1**.

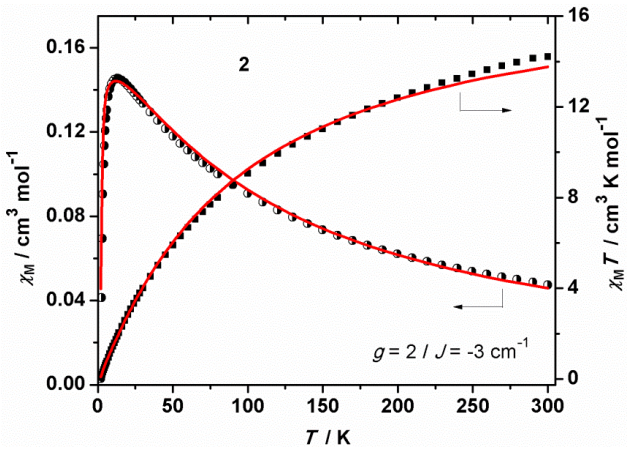

Figure S4. Temperature dependence of χ_M (squares) and $\chi_M T$ (circles) of **2**.

References

1. G. Wilkinson, F. A. Cotton, J. M. Birmingham, *J.Jnorg. Nucl. Chem.* 1956, **2,** 95.
2. F. Tuna, C. A. Smith, M. Bodensteiner, L. Ungur, L. F. Chibotaru, E. J. L. Mcinnes, R. E. P. Winpenny, D. Collison and R. A. Layfield, *Angew. Chem. Int. Ed.* 2012, **51,** 6976.
3. Agilent Technologies Inc., *SCALE3ABSPACK, CrysAlisPm Version 1.171.36.202012.*
4. G. M. Sheldrick, *Acta Cryst.* 2008, **A64,** 112.
5. P. Sluis, A. L. Spek, *Acta Cryst.* 1990, **A46,** 194.

APPENDIX THREE

The **Stevens operators** can be written in terms of polynomials of the spin operators, $\hat{S}_x$, $\hat{S}_y$, and $\hat{S}_z$:

$$\hat{O}_2^0 = 3\hat{S}_z^2 + S(S+1)$$

$$\hat{O}_4^0 = 35\hat{S}_z^4 - 30S(S+1)\hat{S}_z^2 + 25\hat{S}_z^2 - 6S(S+1) + 3S^2(S+1)^2$$

$$\hat{O}_4^3 = \frac{1}{4}[\hat{S}_z(\hat{S}_x^3 + \hat{S}_y^3)]$$

$$\hat{O}_6^0 = 231\hat{S}_z^6 - 105(3S^2(S+1)^2 - 7)\hat{S}_z^4 + (105S^4(S+1)^4 - 25S^2(S+1)^2 + 294)\hat{S}_z^2 - 5S^6(S+1)^6 - 40S^4(S+1)^4 - 60S^2(S+1)^2$$

$$\hat{O}_6^3 = \frac{1}{4}[(11\hat{S}_z^3 - (3S^2(S+1)^2 - 59)\hat{S}_z)(\hat{S}_x^3 + \hat{S}_y^3)]$$

$$\hat{O}_6^6 = \frac{1}{2}(\hat{S}_x^6 + \hat{S}_y^6)$$

APPENDIX FOUR

Ab initio study of the magnetic properties of the Er^{3+} complex

Computational details:

Structural approximations:

Three structural approximations have been employed denoted **A**, **B** and **C**. In all structural approximations the THF molecules have been preserved as in the experimental structure.

In approximation **A**, all nine benzene rings attached to the Si atoms were substituted by H atoms. (see Figure 1, left)

In approximation **B**, all nine benzene rings attached to the Si atoms were substituted by CH_3 groups. (see Figure 1, right)

In approximation **C**, the entire experimental structure was considered in the *ab initio* calculations.

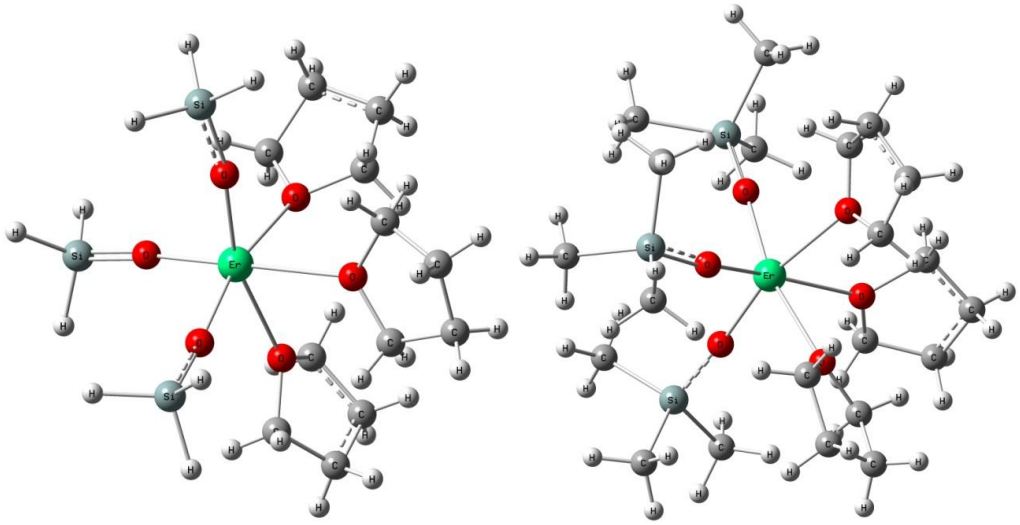

A **B**

Figure 1. The structure of the Er^{3+} model fragment in structural approximation **A**(left) and **B**(right).

Basis Set approximations:

Two basis set approximations have been employed denoted **A** (smaller) and **B** (larger).

Basis Sets of the approximation **A:** All employed basis sets were taken from the standard ANO-RCC basis set library from MOLCAS. The following contractions were used for the atoms:

Er – 7s6p4d3f1g.

Si – 4s3p1d.

O – 3s2p1d.

C – 3s2p.

H – 2s.

Basis Sets of the approximation **B**: All employed basis sets were taken from the standard ANO-RCC basis set library from MOLCAS. The following contractions were used for the atoms:
Er – 8s7p5d4f2g1h.
Si – 5s4p2d.
O – 4s3p2d.
C – 3s2p.
H – 2s.

Active space of the CASSCF method included 11 electrons in 7 orbitals.
The **spin orbit interaction** was computed by mixing of 35 (all) quartets and 112 (all) doublet spin free states.

In the following tables the first letter denotes the "structure" and the second letter denotes the "basis set" approximation.

Table 1. Energies (cm^{-1}) of the lowest spin-free states on Er^{3+} site (CASSCF).

Spin multiplicity	AA	AB	BA	BB	CA	CB
4	0.000	0.000	0.000	0.000	0.000	0.000
	23.867	24.059	24.180	24.001	23.979	24.333
	52.339	59.329	55.710	61.309	50.551	55.289
	55.119	60.796	57.768	62.928	53.991	57.793
	115.108	127.125	121.227	131.068	111.234	119.037
	129.624	142.158	137.045	147.528	128.191	136.928
	139.378	153.770	147.171	159.348	134.312	144.131
	321.707	330.166	325.292	332.663	321.563	328.114
	353.134	361.484	357.131	364.201	356.561	362.454
	366.126	373.166	370.867	377.006	369.717	375.397
	388.242	394.402	392.757	397.964	391.624	395.769
	414.148	421.853	419.065	426.114	422.330	428.577
	461.012	464.725	464.488	467.688	467.263	469.902
	18110.858	18105.338	18111.310	18105.171	18106.171	18099.256
	18225.689	18221.533	18226.278	18221.572	18225.195	18219.778
	18237.274	18231.258	18236.998	18230.446	18236.178	18229.744
	18348.560	18348.409	18351.104	18349.916	18347.967	18346.005
	18376.186	18385.586	18382.030	18389.663	18372.892	18378.060
	18493.686	18492.198	18494.568	18492.139	18495.130	18492.228
	18512.568	18510.593	18516.659	18513.732	18521.167	18517.599
	18613.345	18616.805	18617.245	18620.109	18617.466	18619.415
	…	…	…	…	…	…
2	18028.848	18027.507	18030.792	18028.252	18027.952	18024.469
	18038.965	18037.637	18040.980	18038.377	18037.352	18033.764
	18047.549	18046.606	18050.333	18048.110	18047.958	18044.659
	18076.462	18074.740	18078.641	18075.770	18076.268	18072.402
	18083.435	18081.677	18086.215	18083.260	18084.455	18080.367
	18089.187	18087.126	18091.722	18088.559	18089.622	18085.424

	18132.501	18130.884	18134.758	18132.062	18132.683	18128.928
	18135.608	18133.463	18138.236	18135.002	18136.886	18132.614
	18139.246	18137.479	18142.057	18139.218	18140.745	18136.826
	18171.195	18169.498	18174.558	18171.634	18172.424	18168.259
	18172.831	18171.046	18176.257	18173.248	18174.273	18170.023
	23881.938	23874.046	23881.324	23872.473	23878.364	23868.985
	23892.519	23883.845	23891.273	23881.713	23887.435	23877.373
	23914.049	23907.046	23915.170	23907.465	23917.412	23909.164
	23934.609	23928.986	23934.963	23928.527	23932.357	23925.309
	23948.449	23941.672	23950.709	23943.157	23951.226	23942.842
	23995.213	23993.137	23998.796	23995.497	23994.776	23990.051
	24050.068	24045.068	24052.104	24046.277	24049.796	24042.863
	24122.081	24122.820	24127.100	24126.305	24121.678	24118.734
	24123.169	24124.185	24128.357	24127.862	24123.693	24121.024
	26806.291	26783.989	26799.175	26777.527	26804.095	26784.171
	26806.505	26784.228	26799.387	26777.774	26804.446	26784.552
	26970.659	26958.797	26968.942	26956.468	26970.443	26958.116
	26984.870	26971.285	26982.195	26968.246	26984.821	26971.217
	27069.072	27064.860	27070.381	27064.822	27066.161	27059.573
	27081.896	27075.512	27084.297	27076.686	27083.445	27074.528
	27142.799	27141.764	27145.633	27142.941	27135.704	27131.255
	27166.403	27165.989	27172.400	27170.523	27171.149	27167.456
	27199.957	27201.120	27205.599	27205.310	27199.857	27197.474
	27345.018	27342.045	27343.762	27339.390	27333.305	27327.934
	27355.504	27354.282	27353.752	27350.798	27341.410	27337.038
	27399.369	27394.307	27407.630	27401.450	27408.686	27400.780
	27404.219	27400.421	27411.527	27406.257	27410.372	27403.125
	27449.912	27452.326	27457.829	27459.108	27465.437	27464.872
	27450.376	27452.869	27458.202	27459.546	27465.575	27464.916
	33012.071	32995.245	33007.982	32990.970	33008.589	32991.947
	33022.588	33004.985	33020.087	33002.446	33025.195	33008.065
	33061.333	33042.142	33058.294	33038.932	33061.808	33042.940
	33163.569	33147.165	33161.656	33144.768	33161.759	33144.973
	33241.185	33242.166	33245.600	33245.177	33240.273	33237.769
	33259.022	33258.854	33264.626	33263.067	33263.203	33259.427
	33324.150	33322.852	33329.230	33326.378	33324.218	33319.385
	33331.632	33330.579	33337.469	33334.884	33333.737	33329.009
	…	…	…	…	…	…

Table 2. Energies (cm^{-1}) of the lowest spin-orbit Kramers doublets (RASSI).

AA	AB	BA	BB	CA	CB
0.000	0.000	0.000	0.000	0.000	0.000
32.332	37.814	34.629	39.378	31.889	35.772
100.535	108.848	104.357	111.541	100.418	106.289
129.302	144.203	136.287	149.035	126.276	136.731
145.231	157.766	151.940	163.055	143.904	152.972
316.483	325.489	319.630	327.567	316.189	322.978
344.713	351.554	349.332	355.348	349.155	354.149
374.995	384.127	380.206	388.671	383.561	391.023

6586.611	6591.204	6587.317	6591.555	6585.943	6590.066
6639.283	6648.988	6642.103	6650.865	6639.134	6647.049
6676.750	6690.081	6681.223	6693.191	6675.694	6686.189
6700.386	6716.071	6706.299	6720.443	6699.219	6711.617
6822.160	6835.167	6824.246	6835.960	6818.407	6828.963
6833.898	6845.403	6839.919	6850.438	6838.607	6848.007
6853.185	6867.493	6858.705	6872.080	6860.277	6872.444
10646.068	10652.149	10647.440	10652.900	10645.707	10650.826
10694.344	10705.217	10697.671	10707.413	10694.175	10702.920
10718.114	10732.145	10722.924	10735.543	10717.496	10728.626
10795.570	10807.749	10798.237	10809.298	10793.209	10803.201
10805.901	10818.120	10810.960	10821.954	10808.476	10818.120
10819.694	10833.861	10824.803	10837.894	10824.522	10836.343
13410.280	13417.364	13411.907	13418.316	13409.781	13415.575
13449.381	13461.916	13454.103	13464.974	13447.442	13456.711
13564.575	13577.298	13568.496	13579.927	13564.744	13574.994
13619.514	13628.231	13622.501	13630.428	13621.854	13628.876
13627.655	13638.403	13631.888	13641.508	13630.701	13639.147
18981.957	18978.021	18982.262	18977.777	18981.078	18975.911
19020.600	19018.443	19021.676	19018.839	19020.578	19017.106
19089.536	19089.458	19091.310	19090.356	19090.125	19088.296
19158.588	19164.195	19161.633	19165.844	19155.957	19159.021
19181.597	19186.402	19187.163	19191.073	19187.346	19189.081
22624.790	22628.269	22627.097	22629.454	22623.107	22624.127
22635.687	22638.834	22638.453	22640.368	22633.937	22634.446
22699.841	22702.511	22702.474	22704.035	22699.790	22700.061
22763.827	22766.621	22766.552	22768.281	22765.161	22765.737
22767.493	22770.254	22770.348	22772.018	22768.953	22769.381
22792.535	22794.593	22795.195	22796.256	22794.637	22794.556
23611.081	23608.825	23612.108	23609.191	23611.761	23608.148
23670.489	23673.364	23673.870	23675.698	23671.493	23671.907
25162.239	25162.112	25162.422	25161.563	25160.740	25159.373
25213.915	25214.054	25214.732	25214.389	25215.411	25214.679
25243.471	25247.210	25246.079	25248.864	25243.792	25245.441
25322.986	25332.347	25327.694	25335.774	25323.601	25329.835
27248.894	27249.915	27249.993	27250.197	27247.964	27247.395
27262.556	27264.019	27264.030	27264.691	27262.133	27262.054
27367.504	27371.722	27369.875	27373.211	27369.144	27371.422
27576.119	27575.117	27576.502	27574.902	27576.444	27574.442
27668.150	27675.831	27672.608	27679.094	27669.827	27674.541
27804.707	27809.125	27806.742	27809.950	27803.004	27805.102
27838.860	27843.132	27840.678	27844.150	27839.487	27841.992
27854.876	27861.809	27857.621	27863.306	27855.223	27859.933
27913.323	27916.957	27914.645	27917.504	27913.532	27915.674
27931.672	27937.786	27934.868	27939.846	27932.932	27936.585
31777.718	31758.554	31770.212	31751.767	31774.486	31757.577
31960.308	31951.632	31957.994	31948.802	31959.472	31950.430
…	…	…	…	…	…

Table 2. Main values of the *g*-tensor for the lowest Kramers doublets.

KD		Main values of the g-tensor					
		AA	**AB**	**BA**	**BB**	**CA**	**CB**
1	g_X	0.1350	0.1076	0.1440	0.1215	0.1824	0.1661
	g_Y	0.3692	0.2661	0.3428	0.2621	0.4056	0.3293
	g_Z	16.3044	16.4421	16.3595	16.4752	16.2919	16.3965
2	g_X	2.4601	2.3267	2.3743	2.2403	2.5204	2.3839
	g_Y	2.5725	2.3410	2.4532	2.2713	2.5577	2.4645
	g_Z	13.2080	13.2794	13.2502	13.3219	13.1754	13.2072
3	g_X	1.8253	1.6783	1.8458	1.7301	1.5257	1.5020
	g_Y	2.2417	2.0683	2.0189	1.8633	2.5788	2.4107
	g_Z	8.9682	9.2051	9.0596	9.2652	8.7024	8.9146
4	g_X	1.3831	1.1984	1.2421	1.2085	1.1536	1.0141
	g_Y	3.9689	3.4948	3.9683	3.8879	4.9577	4.4396
	g_Z	11.7321	12.3612	11.9560	12.3442	11.1208	11.7443
5	g_X	2.5702	2.6972	2.5981	2.5729	2.3827	2.6157
	g_Y	3.6398	4.1428	3.7153	3.9918	2.9040	3.4227
	g_Z	9.4171	10.3139	10.2480	11.2583	10.0207	10.7269
6	g_X	1.3402	1.1879	1.1586	1.0220	1.0224	0.9121
	g_Y	4.0730	4.0871	3.2446	3.1884	2.6777	2.6156
	g_Z	11.8839	11.9447	12.8894	13.0172	13.6444	13.7787
7	g_X	0.8080	0.8561	0.6256	0.6866	0.4661	0.5170
	g_Y	5.0195	4.8725	4.0927	3.8782	3.4398	3.2551
	g_Z	11.5572	11.7144	12.4640	12.7209	13.3665	13.6065
8	g_X	0.6438	0.5692	0.5677	0.4943	0.3638	0.3158
	g_Y	1.0789	0.8875	1.0893	0.8817	0.9205	0.7494
	g_Z	15.8716	16.1576	15.9553	16.2458	16.2750	16.5069

a) b)

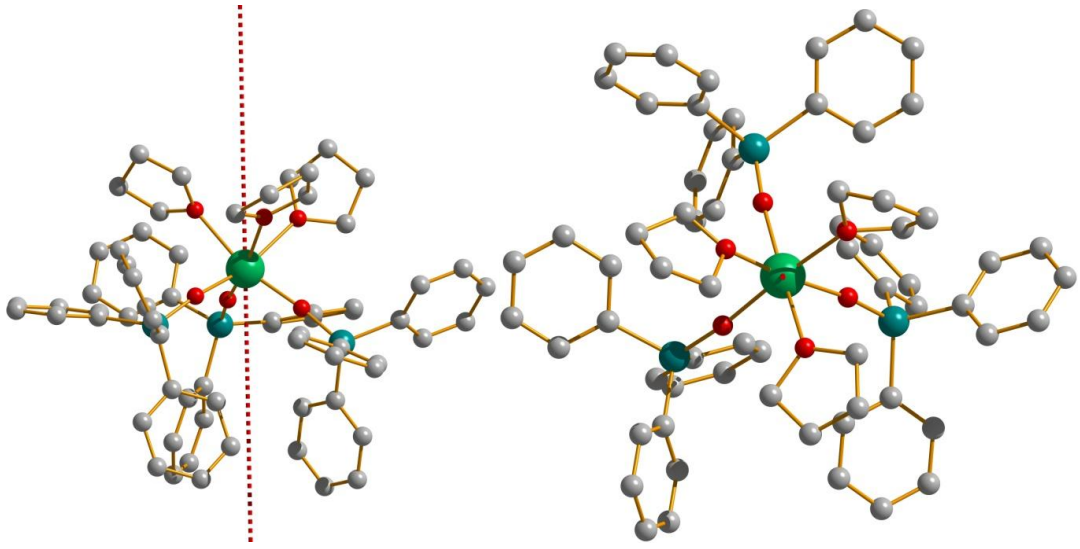

Figure 2. Two views of the orientation of the main anisotropy axis in the ground state of the Er^{3+} complex in the largest computational approximation **CB**.

Although the molecule doesn't have an exact C_3 symmetry, the orientation of the main magnetic axis of the ground state with respect to the molecular structure is almost parallel to the C_3 symmetry axis. The angle between the main magnetic axes of the ground state calculated in all computational approximations is max. 2.11°. The difference in the calculated magnetic properties is negligible.

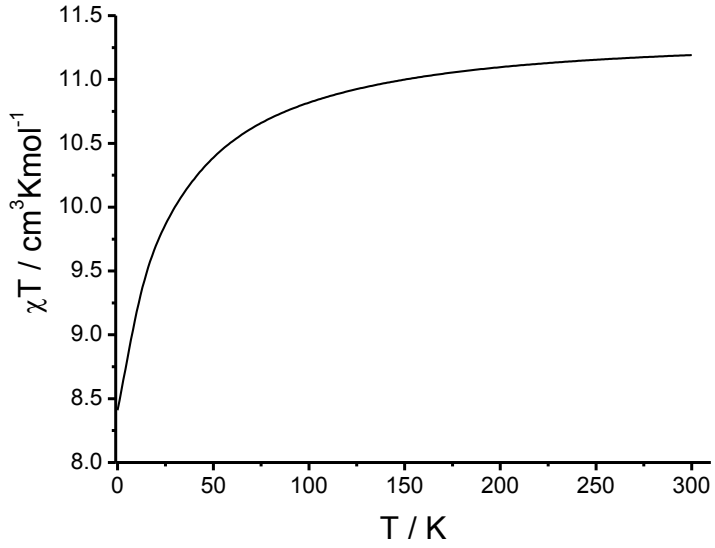

Figure 3. Temperature dependence of the χT of the Er^{3+} complex calculated in the computational approximation **CB**.

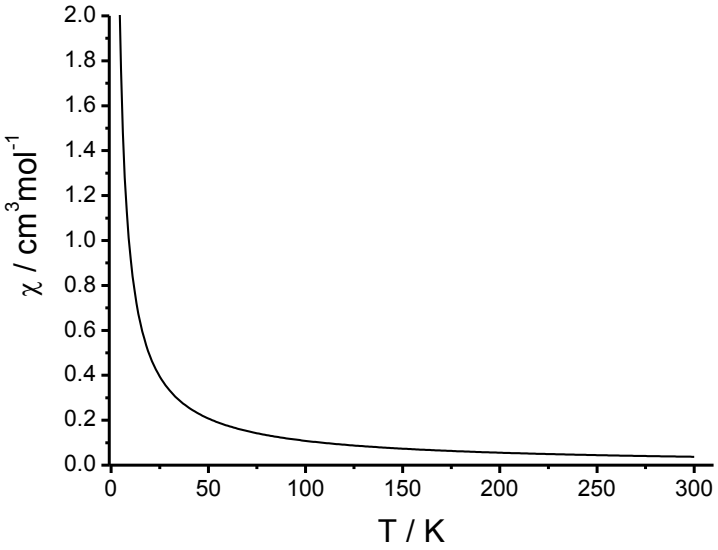

Figure 4. Temperature dependence of the χ of the Er^{3+} complex calculated in the computational approximation **CB**.

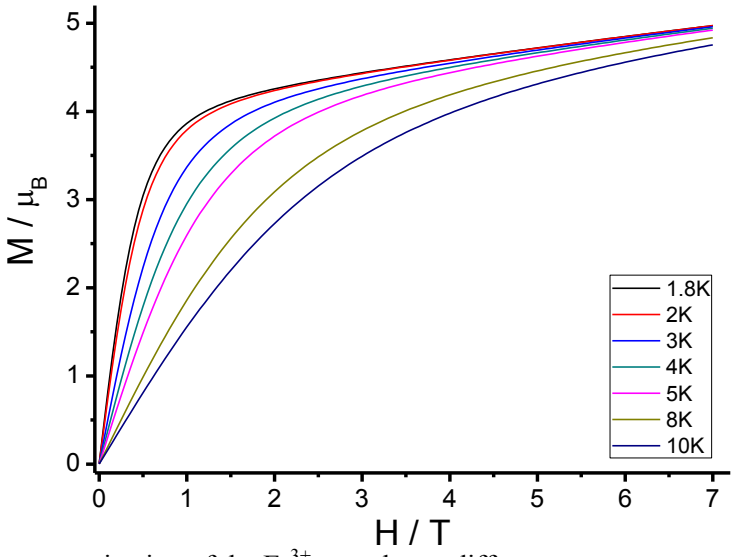

Figure 5. Molar magnetization of the Er^{3+} complex at different temperatures calculated in the computational approximation **CB**.

Comparison of the experimental and calculated magnetism of the Er3+ complex in the CB computational approximation

In all figures below *zJ* is the parameter of the intermolecular interaction, simulated in the mean field approximation.

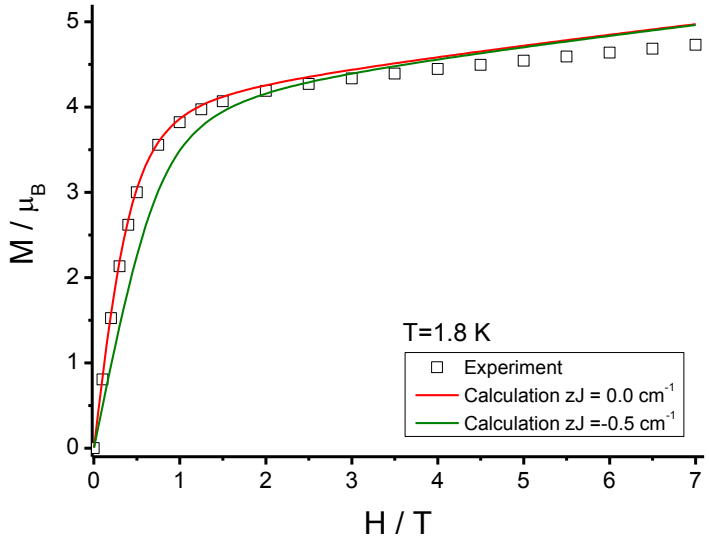

Figure 6. Molar magnetization at 1.8K.

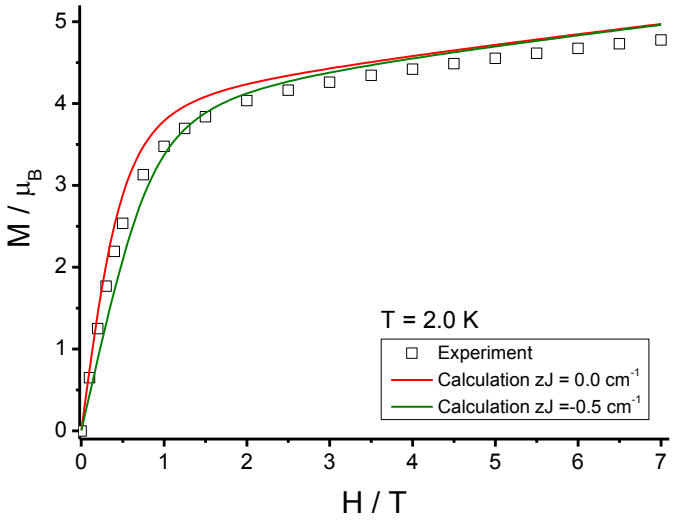

Figure 7. Molar magnetization at 2.0K.

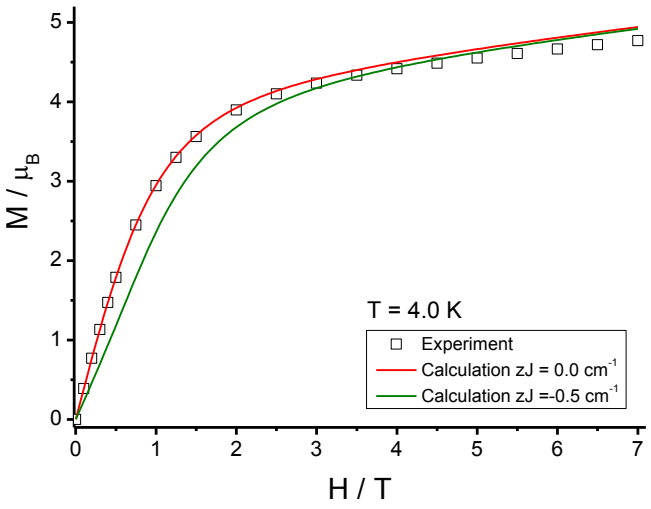

Figure 8. Molar magnetization at 4.0K.

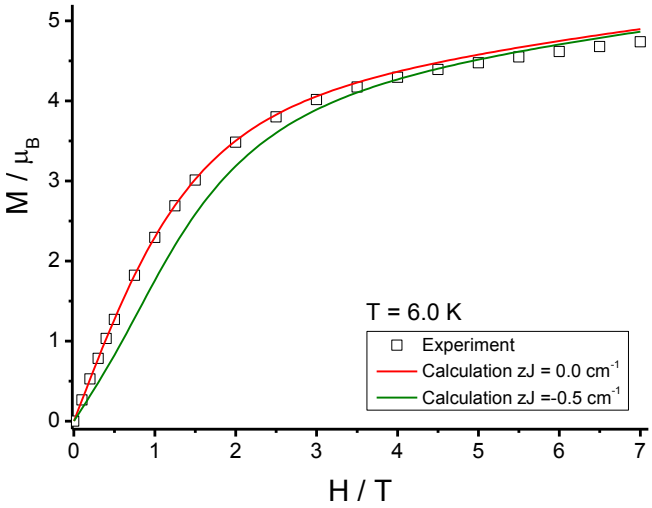

Figure 9. Molar magnetization at 6.0K.

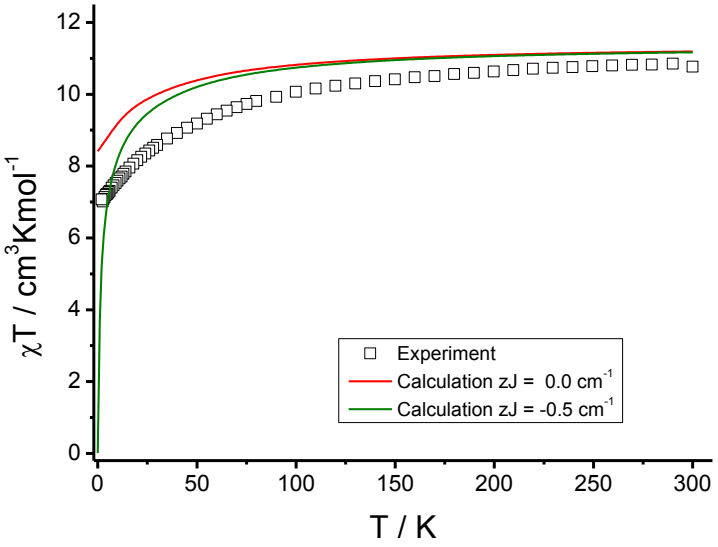

Figure 10. Temperature dependence of the magnetic susceptibility.

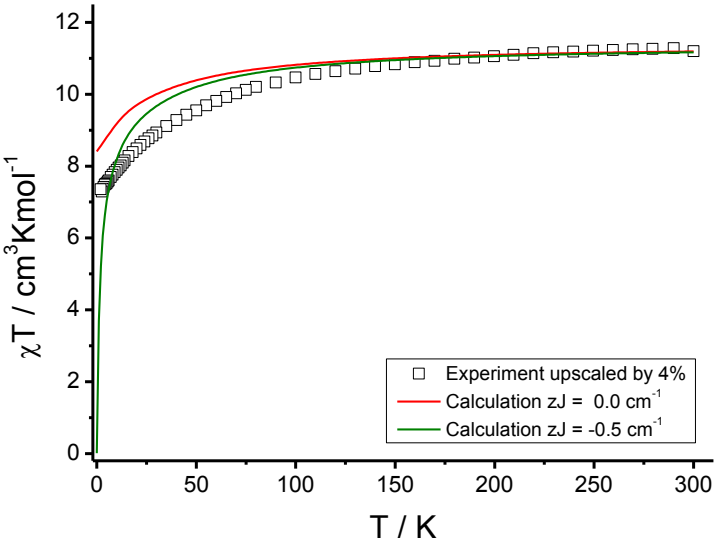

Figure 11. Temperature dependence of the magnetic susceptibility (experiment upscaled by 4%).

Some preliminary conclusions:

The experimental blocking barrier of 28 K is in a reasonable agreement with the energy of the first excited Kramers doublet (Table 2), while the magnitude of the perpendicular components of the *g* tensor (g_X and g_Y) are a sign of important quantum tunneling already in the ground state. Therefore it is possible that the SMM state has a short lifetime.